THE SIGNALLING PROPERTIES OF A_1:$P2Y_1$ RECEPTOR HETEROMERS FORMED AT PHYSIOLOGICAL EXPRESSION LEVELS

Qing Cai

Thesis submitted for the Degree of

Doctor of Philosophy in Biochemistry and Molecular Biology

Research Department of Structural and Molecular Biology

University College London

Gower Street

London

WC1E 6BT

London

October 2011

DECLARATION

I, **Qing Cai**, declare that all work presented in this thesis is the result of my own work. Where information has been derived from other sources, I confirm that this has been mentioned in the thesis. The work herein was carried out while I was a post-graduate student at the University College London, Research Department of Structural and Molecular Biology under the supervision of Dr Andrea Townsend-Nicholson.

ACKNOWLEDGMENTS

I would like to first thank my great supervisor Andrea, whose energetic spirits, brilliant mind, wonderful humours, and all the 'technical terms' inspired me profoundly throughout the my entire PhD years. Thank you for being so patient with such a stubborn me, pointing me in the right direction, and always being there when I needed help, especially your encouragement and support during those difficult times. Thank you for being such an excellent supervisor, I really enjoyed the project.

I would also like to thank all of my friends, in particular, Dipali, Batoul, Rumeza, Marilia, and Carmen, all the girls in the 'Beast Team', you supported me like family. I had the most wonderful times of my PhD. Also, a big thanks to Yuan and all the friends I happened to live with during these years.

Finally, the most emotional thanks goes to my most beloved parents, whose birthdays happen to be in the same month as my thesis submission day. Thank you so much for supporting me and encouraging me all the time, even from thousands of miles away, to you I dedicate this thesis as a gift. ^_^

ABSTRACT

Extracellular purine and pyrimidine nucleosides and nucleotides stimulate signalling responses via a family of G protein-coupled receptors (GPCR), known as purinergic receptors, to play essential roles in a diverse range of vital physiological functions. A heteromeric purinergic receptor, comprising the A_1 adenosine and $P2Y_1$ receptor subtypes has previously been reported in an overexpressing recombinant system using human embryonic kidney 293T cells, where activation by a $P2Y_1R$ agonist (ADPβS) induced an A_1R-mediated G_{ai} signalling response. In this thesis I present the first characterisation of the signalling properties of the recombinant human A_1R:$P2Y_1R$ heteromeric receptor expressed at physiological expression levels, which was achieved by selecting a clonal cell line stably expressing the human A_1 adenosine receptor in the Chinese hamster ovary cell line, CHO.K1, which expresses an endogenous $P2Y_1$ receptor. In addition to demonstrating that the A_1R:$P2Y_1R$ is activated by the endogenous $P2Y_1$ agonist ADP to produce a G_{ai} response, I have shown that ADP also elicits a biphasic calcium (G_{aq}) response, with the lower affinity site corresponding to the A_1R:$P2Y_1R$. The G_{ai} response requires a constitutively active A_1R and is inhibited by both A_1R and $P2Y_1R$ antagonists. The G_{aq} response of the heteromeric receptor is elicited by both wild type and constitutively active A_1 receptors and is not inhibited by any of the antagonists tested. Preliminary experiments to use Bimolecular Fluorescence Complementation to investigate the formation of A_1R:$P2Y_1R$ *in vivo* were initiated.

CONTENTS

List of Figures

List of Tables

ABBREVIATIONS

2-CADO	2-chloroadenosine
2-MeSATP	2-Methylthioadenosine-5'-O-triphosphate
2-MeSADP	2-Methylthioadenosine-5'-O-diphosphate
aa	amino acid
A_1R	adenosine A_1 receptor
AC	adenylyl cyclase
AMP	adenosine 5'-monophosphate
ADP	adenosine 5'-diphosphate
ADPβS	adenosine 5'-O-(2-thiodiphosphate)
APNEA	N6-2-(4-Aminophyl)ethyl-adenosine
ATP	adenosine 5'-triphosphate
ATPγS	adenosine 5'-O-(3-thiodiphosphate)
BiFC	bimolecular fluorescent complementation
bp	base pairs
BSA	bovine serum albumen
$CaCl_2$	calcium chloride
CaM	calmodulin/ calcium-modulated protein
CaMK	Ca^{2+}/calmodulin-dependent protein kinase
cAMP	cyclic adenosine 3',5,-monophosphate
CaN	calcineurin
CCD	charged coupled device
cDNA	complementary DNA
CPA	N^6-cyclopentyladenosine
CCPA	2-chloro-N^6-cyclopentyladenosine
CsCl	caesium chloride
dH_2O	distilled water
DMSO	dimethyl sulphoxide
DMEM	Dulbecco's Modified Eagle's Medium
DNA	deoxyribonucleic acid
dNTPs	deoxynucleotide triphosphates

DPBS	Dulbecco's phosphate buffered saline
DPCPX	8-cyclopentyl-1,3-dipropylxanthine
EC_{50}	half effective agonist-concentration
E.coli	*Escherichia coli*
EDTA	ethylene diamine tetraacetic acid
EtOH	ethanol
FBS	foetal bovine serum
FLIPR	fluorometric image plate reader
fmol	femtomoles
GPCR	G protein-coupled receptor
IC_{50}	half inhibitory concentration
IP_3	inositol (3,4,5-)triphosphate
KAc	potassium acetate
LASER	light amplicifaction by stimulated emission of radiation
LB	Luria-Bertani broth
LED	light-emitted diode
M	molar
Mg	milligrams
MG 50-3-1	1-amino-4-4-[4-chloro-6-(2-sulfonatophenylamino) [1,3,5]triazine-2-ylamino]-2-sulfonatophenylamino} -9,10-dioxo-9,10-dihydroanthracene-2-sulfonic acid trisodium salt
mL	millilitres
mM	millimolar
mm^2	millimetres squared
M-PER®	Mammalian Protein Extraction Reagent
MRS 2179	2'-Deoxy-N^6-methyladenosine 3',5'-bisphosphate tetrasodium salt
NaAc	sodium acetate
NaCl	sodium chloride
NaOH	sodium hydroxide
NECA	adenosine-5'-N-ethylcarboxamide
nM	nanomolar

nm	nanometres
OD	optical density
P2Y$_1$R	P2Y$_1$ receptor
P2Y$_2$R	P2Y$_2$ receptor
PCR	polymerase chain reaction
PKA	protein kinase A
PKC	protein kinase C
PLC	phospholipase C
pmol	picomoles
RNA	ribonucleic acid
R-PIA	*R*(–)-N^6-(2-phenylisopropyl)adenosine
RT-PCR	reverse transcriptase polymerase chain reaction
SDS	sodium dodecyl sulphate
SOC	salt optimised broth with carbon
TAE	Tris-acetate-EDTA
TE	Tris-HCl-EDTA
TRIZMA®	base Tris-(hydroxymethyl)-aminomethane
UTP	uridine (5'-)triphosphate
UV	ultraviolet
***µ*g**	micrograms
***µ*l**	microlitres
***µ*m**	micrometers
***µ*M**	micromolar
v/v	volume per volume
w/v	weight per volume

Chapter 1

Introduction

1.1 Introduction

G-protein coupled receptors (GPCRs), also known as the seven-transmembrane receptors, constitute the largest family of signalling proteins, as they comprise of approximately 3-5%[1] of total cellular protein and encode over 1000 genes[2,3] in mammals. Due to their functional properties and their widespread distribution in mammalian tissues and organs as well as the peculiar feature of their conformational 'instability', which ultimately leads to the equilibrium of the receptor activity states, this family of proteins has attracted significant attention for researchers interested in characterising their signal transduction properties and resolving the mysteries underlying their structure. Recently, these proteins have been shown to undergo protein-protein interactions with both GPCRs and with other protein types, resulting in changes to their functional properties[4]. All of these features have great potential for the exploitation of GPCRs as therapeutic targets.

This PhD project focuses on two particular members of the GPCR family, and this chapter will provide general background information about GPCRs, including a brief introduction about their structure,

classification, and about the G-proteins, which, if coupled to the receptor can, initiate signal transduction processes. GPCR oligomerisation and the functional significance of this oligomerisation will also be presented. Furthermore, the purinergic receptor family, to which the two GPCRs studied belong, will also be introduced. Finally, an overview of the signal transduction pathways elicited by the specific G-proteins coupled to these two receptors, and the aims and objectives of the PhD project will be described.

1.2 G PROTEIN-COUPLED RECEPTORS

1.2.1 Seven-Transmembrane Receptors

1.2.1.1 The Structures

GPCRs possess a characteristic structure of seven transmembrane α-helices[5,6] of varying lengths[7,8,9,10 11,12], arranged in an anticlock-wise direction[13,14], and are frequently referred to as seven-transmembrane (7TM) receptors. Significant research has been carried out in order to reveal the structure of a GPCR, using a wide array of techniques, from cryoelectron microscopy[15] and electron density mapping[5], to the more recently acquired X-ray crystallography structures[8]. Although the detailed structures differ from one another, the 7TM domains share common features such that they are not straight α-helices and are arranged in an orientation that enables the conserved and polar residues fto ace inwards[16]. For

example, in the bovine rhodopsin protein, six out of seven transmembrane helices are kinked, mostly due to the presence of a proline residue[17]. Furthermore, the second transmembrane helix is bent by 30 degrees from a vertical axis across the membrane[12],. These transmembrane helices are connected by 3 loops at both the intracellular and extracellular sides[5,2,11,12]. The NH_2 – terminal (N-terminal) is located at the extracellular side, whereas the COOH – terminal (C-terminal) is facing the intracellular side[5]. The three intracellular loops are responsible for interactions with the G-Proteins[5]. A representative two dimensional model is shown in Figure 1.

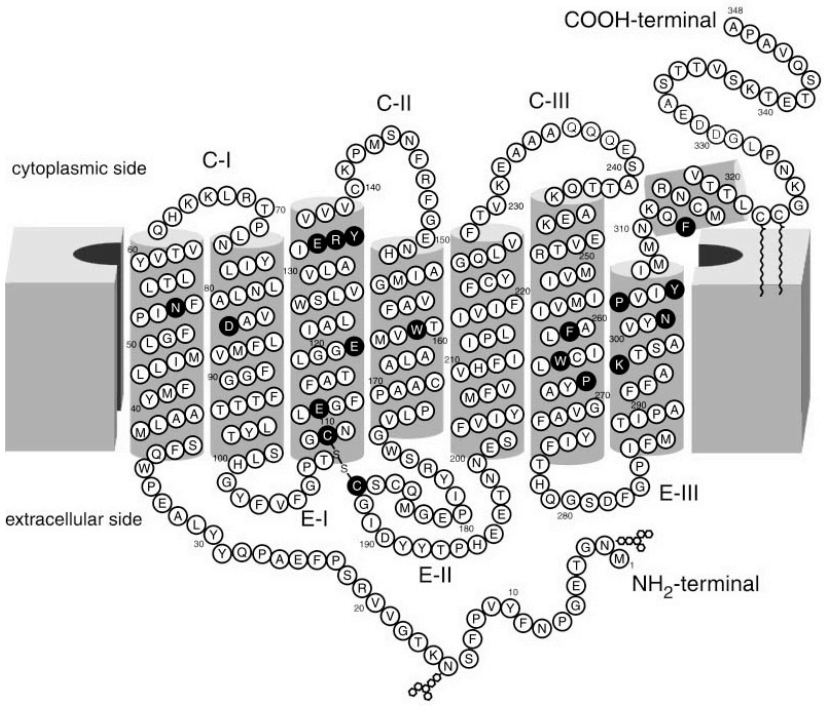

Figure 1. Two-dimensional structural model of a bovine rhodopsin receptor (figure referenced[11])

The GPCR consists of seven transmembrane helices, with the NH2-terminal facing the extracellular side and the COOH-terminal facing the intracellular side. Some of the key amino acid residues are highlighted.

1.2.1.2 GPCR Ligand-Binding Pocket

The locations of ligand binding sites on the receptors differ slightly between classes of GPCRs[1,10,18]. For most receptors, and Class A Rhodopsin-like receptors, the ligand binding sites were initially thought to be within the transmembrane domain[1,11,12], but have recently been shown to be on the extracellular loops as well as the upper segment of the transmembrane helices[19,20]. The Class C receptors have an alternate location for the ligand-binding site, which is located on the extracellular element formed by the extremely large N-terminus, which is often referred to as the venus flytrap domain (VFT)[1,18].

1.2.1.3 The Two-State Model

The GPCRs have been said to exist as a two-state model of activation[21]: they are in equilibrium between the active (R^*) and resting (R) states, which, upon binding of an agonist, will shift towards the active state. However, unique features of these receptors complicate an understanding of the mechanism of receptor activation. The overall affinity of the agonist, with respect to the response, depends not only on the equilibrium constant between the R^* and R states, but also upon the dissociation equilibrium constant of the agonist for receptors at both states[14,22]. For example, an agonist may bind to both R^* and R states of the receptor, with varying affinities

(determined by the dissociation equilibrium constant), and a higher affinity for the R^{*}[23] results in an increase in the concentration response for the receptor. This is the simplest model, without considering other factors, such as the G-proteins, which play a pivotal role in the GPCR signalling, and can be coupled to the activated receptors. The interaction of the G-protein to the receptors will be explained in detail later.

1.2.2 GPCR Classification

Based on primary amino acid sequence identity, GPCRs are grouped into five classes (A-E)[24]. Each of these classes share over 25% sequence identity in the transmembrane core region, where a set of highly conserved residues and motifs are usually seen[3]. The most commonly studied classes are class A-C. Class D and E on the other hand, are much smaller classes compared with the previous three. Class D is the fungal pheromone receptors, consisting of fungal pheromone A / B factor-like proteins, as well as the M and P factors. Class E is comprised solely from the dictyostelium cAMP receptors. Some examples of receptors in Class A–C are shown below, detailed descriptions can be found in the community-maintained online G Protein-Coupled Receptor Database (GPCRDB)[24]. This is the most commonly used classification system. In the recent years, different methods have been developed for a more comprehensive classification system[25-27]. In this section, a short description will be

presented for each class, including a brief description of the most commonly studied receptors.

Class A – Rhodopsin-like Receptors

This is by far the largest group of receptors in terms of abundance[3], which bind small molecules and peptide agonists[1]. The structure of rhodopsin receptors in this group has been widely studied using various techniques. The ligand-binding pocket is generally formed between the transmembrane domains and the extracellular loops; others like some glycoprotein hormone receptors, have the binding site located at the extracellular N-terminal domain[1]. The receptors in this class include amongst others, the rhodopsin, muscarinic, purinergic, opioid, dopaminergic, serotoninergic, prostaglandin and adrenergic receptors.

Class B – Secretin-like Receptors

This small group of receptors contain approximately 25 members[2]. Receptors in this family have a relatively large extracellular N-terminal hormone-binding domain[1,2]. They couple mainly to $G_{\alpha s}$ activating adenylyl cyclase[1], and include glucagon receptors, secretin and vasoactive intestinal peptide (VIP) receptors, and the growth-hormone-releasing hormone receptors.

Class C – Metabotropic Glutamate Receptors

Class C receptors are also called 'obligatory dimers', as they very frequently function as dimers[2]. Their ligand-binding domain is located on the Venus flytrap domain, which is formed by an extremely large extracellular domain on the N-terminal[2]. Receptors in the class include the $GABA_B$ receptors, metabotropic glutamate receptors, calcium sensing receptors, and the taste and odorant receptors.

Class D and E

As mentioned previously, Class D and E comprise mainly the fungal pheromone receptors and the dictyostelium cAMP receptors respectively.

1.2.3 The Guanine Nucleotide Binding Protein (G-Protein)

1.2.3.1 The Heterotrimeric G-Protein

The Guanine-nucleotide binding proteins (G-proteins) are heteromers consisting of α, β, and γ subunits[2,28], and are most often referred to by their G_α subunits, which comprise four distinct subfamilies[2,28]. The $G_{\beta\gamma}$ subunit has recently been acknowledged for its importance in the structural and signalling properties of GPCRs[28]. The heterotrimeric G-protein anchors to the plasma membrane via the N-terminal and C-terminal regions of the α, and γ subunits[9,29] and all three subunits are involved in interacting with the intracellular face of the

receptors[9,10,28,29]. Upon receptor activation[2,10], the G-proteins, with a bound GDP molecule[29], couple to the receptors which function as a Guanine-nucleotide Exchange Factor (GEF) to facilitate exchange GDP for GTP[30]. Following GTP-binding, the heteromeric G protein dissociate into a $G_{\alpha GTP}$ and a $G_{\beta\gamma}$ subunit[31]. After GTP hydrolysis, which is achieved by the G_{α} subunit's intrinsic GTPase[32] activity, the $G_{\beta\gamma}$ subunit comes into position and the whole GDP-bound structure is reassembled[10].

1.2.3.2 The G_{α}-Subunit and Intracellular Signalling

The G_{α} subunits, according to their sequence similarity, and their receptor and effector specificity and selectivities, are sub-divided into four main classes: the $G_{\alpha s}$, $G_{\alpha i}$, $G_{\alpha q}$, and $G_{\alpha 12/13}$, constituting of 20 known types of G_{α} subunits[33]. Amongst these four classes, the $G_{\alpha s}$ and $G_{\alpha i}$ subunits are coupled to the stimulation or inhibition of the enzyme adenylyl cyclase, resulting in the accumulation or reduction in intracellular cAMP levels. The $G_{\alpha q}$ subunit is coupled to the calcium-signalling pathway via phospholipase C, which hydrolyses phosphatidyl inositol 4,5-bisphosphate (PIP_2) into 1,2-diacyleglycerol (DAG) and inositol 1,4,5-triphosphotate (IP_3). The hydrolysis product IP_3, in turn, stimulates the IP_3-sensitive calcium channel resulting in

intracellular calcium mobilisation from endoplasmic reticulum (ER) stores. The $G_{\alpha 12/13}$ subunit is known to be coupled to the stimulation of small GTPase Rho Guanine-nucleotide Exchange Factors (Rho GEFs), the cellular response of which can be quite divergent involving both cytoplasmic and nuclear aspects, and is associated mainly with cell growth and differentiation[34-36]. All G_{α} subunits undergo a post-translational dual acylation (myristoylation and palmitoylation) at the N-terminal site for membrane anchorage and effector activation[36,37].

1.2.3.3 The $G_{\beta\gamma}$-Subunit and Signalling

The $G_{\beta\gamma}$ dimer functions as a monomeric subunit of G protein[33]. Although not as abundant as the G_{α} subunit, there are 6 and 14 known members of the G_{β} and G_{γ} families respectively[35,36]. This subunit not only contributes towards receptor coupling[37] and specificity[38,39], it directly or in complex with the G_{α} subunit, plays a significant role in the regulation of signal transduction pathways[28,33], such as adenylyl cyclase, phospholipase C, ion channels, and GPCR kinases.

1.2.4 G Protein-Coupled Receptor Interactions

1.2.4.1 GPCR Oligomerisation

Very frequently, the GPCR-mediated signal transduction process is being portrayed by an over-simplified model that only describes the interaction mechanism between the ligand, receptor and the G-protein in a 1:1:1 stoichiometry[3,40]. However, it is slowly being unravelled, that GPCRs form oligomers with each other and complexes with other proteins *in vivo* [3,41,42-45]. There has not been any conclusive evidence so far for a specific oligomeric state or size that all GPCRs attain for function. The extent of oligomerisation characterised this far, ranges from smaller dimers to larger octamers[3]. Such oligomerisation of GPCRs may not always be an artefact caused by over-expression of the receptor[46,47] or the methods of transfection[4] (transient or stable). However, it remains controversial as to where the oligomerisation occurs. Some studies indicate the formation of oligomers is an early step in GPCR maturation and cell surface delivery[4,48,49], others suggest that it takes place at the cell surface[50,51].

GPCR oligomerisation can occur between different ligand families and even between receptors from a different class. Hetero-oligomerisation between closely related GPCR subtypes appears to form more efficiently than between more distantly related GPCRs[4,52]. The oligomerisation process can be constitutive[53,54] and the presence of a ligand, usually an agonist, may facilitate[55,56] or even be

required for the oligomerisation[57,58]. In contrast, a number of studies have suggested that the addition of agonist may cause dissociation of certain preformed oligomers[59,60]. The formation of an oligomeric receptor may be obligatory for receptor signalling[61-65]. For example the $GABA_B$-1 and $GABA_B$-2 receptors are commonly being referred to as obligate heteromers, where the co-expression and association of both is an essential requirement for a functional $GABA_B$. Neither receptor expressed alone was functionally active.

1.2.4.2 Pharmacological Significance of GPCR Oligomerisation

There is no universally defined condition for GPCR oligomerisation[3,4,13,66], as the oligomerisation may require agonist induction, or over-expression of receptors, as well as being constitutive oligomers at physiological levels. Even though the interactions may not be obligatory, the resulting oligomers frequently possess altered pharmacological profiles. are frequently having significant augment or alteration on the pharmacological profiles[4,67-69]. The rhodopsin receptors provide a good example of this phenomenon. rhodopsin receptors as an example, Although the receptor exists as a mix of functional monomers and dimers, it was observed that the dimers activate G-proteins and transducins at a much faster reaction speed[70]. Functional GPCR oligomers, in general, ensure protein folding, maturation and cell surface delivery of the

receptors[48,49,71] (e.g. homodimers of β_2-adrenergic receptor for cell surface targetting) and the co–expression of a pair of GPCRs can modify the potency and the signal transduction properties[61,72,73] of the resulting receptor complex (e.g. somatosatin receptor sst_3 inactivation by sst_3:sst_{2A} heteromer). Some heterodimers can offer a docking interface with differential G-protein selectivity from their corresponding GPCR homodimers. For instance, the opioid receptor mu-delta functional heteromer showed reduced potency level for each of the individual receptors' highly selective agonist, but enhanced affinity for endomorphin-1 and Leu-eukephalin. The distal carboxyl tail of both receptors may be involved in the formation of the novel docking face, as truncation of either receptor leads to a modification of the selective binding pocket on the other receptor[62-65]. As mentioned above, some oligomeric receptors may have more efficient signal transduction properties than the monomers[70,74] several GPCR heterodimers have been shown to be required for various physiological functions[48,75,76].

On the other hand, oligomerisation of GPCRs exhibits great potential in pharmaceutical development, mainly due to its significant clinical relevance. A large number of studies have provedthe involvement of cross-talk between oligomeric receptors and receptor-specific drugs in diseases and their treatment. For example, the adenosine A_{2A} receptor attenuates the Parkinsonism treatment using the dopamine D_2 receptor agonist, levodopa, because of a chronic activation of

both A_{2A} and D_2 receptors in the heteromeric form[77]. As oligomeric GPCRs are gradually considered for their potential as novel drug targets, analysis of the physiological conditions required for receptor activity becomes crucial in the drug optimisation process, since an isolated receptor system no longer accurately represents the summed signalling events, nor does an overly expressed recombinant cell system[3]. The development of novel therapies using existing drugs may allow for a more effective treatment as has been proposed[3,77].

1.3 PURINERGIC RECEPTORS

1.3.1 Purinergic Receptor History And Nomenclature

The effect of purines was first noticed in the mammalian cardiovascular system. In 1929, Drury and Szent-Gyürgyi[78] purified substances from an extract of fresh minced bullock's heart, and identified an adenylic acid (adenosine 5'-monophosphate / AMP) consisting of adenine, a pentose and phosphoric acid. Such an adenylic acid-containing extract, when administered intravenously into other animals, transiently disturbed the cardiac rhythm, as well as the arterial pressure and skeletal muscle contractility, in a constant and defined manner indistinguishable from an adenosine-mediated response. Since then, research for over a number of decades has gradually come to demonstrate the importance of

adenosine nucleosides and nucleotides, as well as pyrimidines such as UTP, as vasodilators in the regulation of coronary blood flow[79-81].

In 1954, ATP was identified in extracts from the rabbit spinal root, inducing the antidromic vasodilatory activity in the rabbit ear artery. It was suspected that ATP may play a neurotransmitter role after its release was observed from the auricular nerve following antidromic stimulation, and its abolishment resulted from sympathectomy[82,83]. Since the response could not be inhibited by neither adrenergic (guanethidine) nor cholinergic (atropine) neuron blocking agents, a 'purinergic nerve' theory was proposed, which postulated the existence of a third component of the autonomic nervous system distinct from the adrenergic and cholinergic components[84-86]. This hypothesis has since then ibeen proved and supported by numerous experiments[87-90]. Historically,the term 'purinergic receptor' was first used in 1972[85] and later evolved to 'purinoceptor'[86].

Purinergic receptors belong to the class A family of GPCRs and are divided into P1 and P2 receptors, which bind ligands such as adenosine and nucleotides respectively[91,92]. P1 receptors, also called adenosine receptors, include the A_1, A_{2A}, A_{2B}, and A_3 receptor subtypes, all of which are coupled to G-proteins[93]. The sub-classification of these adenosine receptors is primarily based on their structural and pharmacological characteristics, hence the first identification of A_1[94,95] and A_2[96] subtypes, which demonstrated

opposite effects on adenylyl cyclase activity.These receptors have been shown to couple to $G_{\alpha i}$ and $G_{\alpha s}$ respectively. Further subdivision of the A_2 receptors was based on the evidence that these receptors showed differential affinity for adenosine in the central nervous system[97]. In addition, the fourth member of the P1 family, the A_3 receptor, is also coupled to the inhibition of adenylyl cyclase via the pertussis toxin (PTX)-sensitive $G_{i/0}$ subunit.

The members of the P2 receptors subtype include 7 P2X receptors ($P2X_{1\text{-}7}R$) and 8 mammalian G protein-coupled P2Y receptors ($P2Y_{1, 2, 4, 6, 11, 12, 13, 14}$)[92]. Unlike the P2Y receptorss, the P2X receptors are non-selective ATP-gated cation channels that allow the influx of Na^+, K^+ and Ca^{2+}. The fast excitatory response to ATP stimulation resultsin the direct influx of extracellular Ca^{2+}, casuing the depolarisation of the cell membrane which in turn leads to a secondary increase in the intracellular calcium concentration due to the activation of voltage-gated Ca^{2+} channels[98-100].

The P2Y receptors, in contrast, are GPCRs most of which are coupled to phospholipase C (PLC) via PTX-insensitive $G_{q/11}$ proteins, with the exception of $P2Y_{11}$ which is also coupled positively to adenylyl cyclase and $P2Y_{12\text{-}14}$, which are negatively coupled to adenylyl cyclase and do not couple to PLC[91,101]. These receptor proteins contain approximately 308 to 377 amino acids, with a molecular mass of approximately 41 to 53 kDa after glycosylation[92].

P2Y receptors respond to purine nucleotides such as ADP and ATP.$P2Y_{2,4}$ and $P2Y_6$ are also sensitive to the pyrimidine nucleotides UDP and UTP;, whereas$P2Y_{14}$ is only activated by UDP and UDP-based analogues[102].

1.3.2 Physiological Significance And Receptor Heteromerisation

Purinergic receptors are widely distributed throughout the body and participate in a diversity of physiological processes. Apart from the intensively studied cardiovascular responses mentioned above, purinergic receptors play key roles in a number of important physiological processes, including smooth muscle contraction, immune responses, platelet aggregation, pain, cardioprotection, and neurotransmission[101,103]. Signalling through purinergic receptors comprises a range of biological tasks, such as survival, repair, remodelling during development and involvement in injury, and plays a role in several pathological conditions such as metabolic impairment, excitotoxicity and acute and chronic neurodegenerative conditions[101].

As with many other GPCRs, the purinergic receptors GPCRs have also been identified in receptor heteromers, interacting both with receptors from the same purinergic family as well as other classes of

GPCRs. Table 1 shows a list of purinergic receptors for which functional GPCR heteromers have been characterised.

Purinergic Receptors	Interacting Partners	Detection Methods	Functional Significance
P1	A_1R : $A_{2A}R$[75]	Co-IP, FRET	-Altered A_1R agonist affinity modulating presynaptic striatal glutamate release -unique caffeine target
P2Y	$P2Y_1R$: $P2Y_{11}R$[104]	Co-IP, FRET	Promotes agonist-induced $P2Y_{11}R$ internalisation
P1 : P2Y	A_1R : $P2Y_1R$[103]	Co-IP	Altered A_1R pharmacology, altered signalling response via $P2Y_1R$ agonist activation
	A_1R : $P2Y_2R$[105]	Co-IP	Co-stimulation leads to decreased $G_{\alpha i}$ response via A_1R and synergistic increase of $G_{\alpha q}$ via $P2Y_2R$
P1 : Others	A_1R : D_1R[106]	Co-IP	Agonist-induced heterodimer, co-stimulation results in reduction of D_1R response and A_1R agonist-induced co-aggregation
	A_1R : mGlu1α[107]	Co-IP	Synergistic increase in Ca^{2+} signalling pathway
	$A_{2A}R$: D_2R[77]	Co-IP	Long-term co-stimulation leads to co-aggregation, co-internalisation, and co-desensitisation
	$A_{2A}R$: CB_1R[108]	Co-IP, BRET	$A_{2A}R$-dependent CB_1R signal transductions

Table 1. Purinergic receptor heteromerisation and its functional consequences

The P1 and P2Y GPCRs form heteromers with receptors from the same family as well as other GPCRs to alter pharmacological and signal transduction responses.

1.3.3 The Adenosine A_1 and $P2Y_1$ Receptors

In this section, descriptions of purinergic receptor signalling and heteromerisation will be provided in greater detail, including the receptor structure, tissue distribution, functional properties and significance of each identified example of heteromerisation. The adenosine A_1 receptor (A_1R) and $P2Y_1$ receptors ($P2Y_1R$) will be used as examples.

In a biological system, ATP is readily hydrolysed to ADP, AMP, and adenosine. Further hydrolysis leads to the production of inosine, hypoxanthine and, finally, uric acid. The nucleoside, adenosine, is found to stimulate the A_1R response whilst the nucleotides, ATP, ADP and AMP, target the $P2Y_1R$. It is worth mentioning that cytosolic ATP also exists in complex with Mg^{2+} ions as an $MgATP^{2-}$ and ATP^{4-} mixture[109] and it has been suggested that the $MgATP^{2-}$ might be an inactive form of ATP[110], with the addition of Mg^{2+} ions leading to an increase in $MgATP^{2-}$ and a reduction in the concentration of ATP^{4-}.

Adenosine is the principle endogenous agonist of A_1R. However, the metabolic product of adenosine, inosine, has also been shown to activate certain adenosine receptors and, in some occasions, may elicit a higher response than adenosine[111,112]. Adenosine comes from both intracellular and extracellular sources. Intracellular adenosine can be achieved via AMP dephosphorylation or S-adenosyl-homocystein hydrolysis[113-115] and is released into the extracellular

space by a specific bi-directional transporter. It has also been shown that the release of adenosine can also be mediated by some neurotransmitters, for example, NMDA and kainate, as well as nitric oxide[93,116,117]. At the extracellular side, various adenylyl nucleotides constitute precursors for the synthesis of adenosine. ATP, ADP and AMP are hydrolysed and dephosphorylated by ectonucleotidases, whilst cAMP is first converted into AMP by phosphodiesterases prior to ectonucleotidase action[93,115,118,119].

The A_1R is distributed all over the body with the highest expression found in brain cortex, cerebellum, and in hippocampus. In the spinal cord, eyes, adrenal gland and atria, this receptor is also highly expressed. In other tissues, such as skeletal muscle, adipose tissue, liver, kidney, oesophagus, colon and testis, as well as in bronchi and pancreas, A_1R is also expressed, but at relatively moderate levels[93].

At the present, all four types of adenosine receptors have been cloned. The A_1R, in particular, has been cloned from human, rat, mouse, dog, cow, rabbit, guinea pig, and chick[93]. These species show degrees of similarities in their amino acid sequences. For example, the human A_1R is most related to the guinea pig receptor, sharing about 95% identity at the amino acid level. In rat, the sequence only differs about 5 to 10%.However, when compared with chick A_1R, the difference is much larger, and is over 20%. Within the same species, the adenosine receptor may share high degrees of

sequence identities. For example, the human A_1R is most closely related to the $A_{2A}R$; A_3R is only about less than 10% different from the A_1R; and $A_{2B}R$ also shares approximately 10% sequence identity with the A_1R[93]. The crystal structure of A_1R has not yet been determined but pharmacological studies using chimeric receptors have provided valuable insights into the ligand binding and G-protein interaction sites[120,121]. The G-protein coupling site is believed to be near the third intracellular loop and the carboxyl terminal, as suggested by a study using A_1R/ $A_{2A}R$ chimeric receptors. Moreover, the agonist and antagonist binding sites are likely to be located at the distal 11-amino acid site on the second extracelluar loop and adjacent regions in TM6 and TM7, as shown using a chimeric A_1R/ A_3R receptor model[120]. Intensive site-directed mutagenesis studies have also identified a number of important amino acid residues for agonist and antagonist binding in TM3, 5, 6, and 7, as reviewed by Fredholm et al[93]. On the other hand, the crystal structure of a human $A_{2A}R$ has been solved with a bound agonist, revealing that agonist binding involves the movement of TM3, 5 and cytoplasmic part of TM6, with an additional coordinated movement between TM7 and extracellular loop 3. The latter is considered more specific for $A_{2A}R$ and its interaction with ligands[122]. This may also provide structural references for modelling the A_1R, considering the high degree of sequence identity between these two receptor subtypes.

Pharmacological studies using human A_1Rs stably transfected into Chinese hamster ovary (CHO) cells[123] have revealed that the A_1R is most effectively bound by CCPA at a subnanomolar concentration as compared to CPA and other commonly used A_1R agonist. CPA is a reasonably selective A_1R agonist with a slightly lower affinity than CCPA, followed by R-PIA, which showed a much greater affinity than its stereoisoform S-PIA. NECA also binds to the A_1R with a relatively lower affinity. However, despite this, it canalso activate the other members of the adenosine receptor subfamily. The most potent antagonist of the A_1R is DPCPX, which binds with nanomolar affinity, although it has also been shown to bind to the other three members of the adenosine receptors at much lower affinities. For example, the affinity at A_{2A}R is approximately a hundred nanomolar, and at A_{2B}R and A_3R, the number is about 10 and 40 times higher. In addition DPCPX had been observed to have inverse agonist properties[124].

$P2Y_1$R, on the other hand, is activated solely by adenylyl nucleotides. It is also called an ATP receptor although it exhibits a higher affinity for ADP and its analogues as opposed to ATP[125]. The receptor has been successfully cloned from human, bovine, rat and mouse[92], and the receptor's expression has been detected in the brain and spinal cord, gastrointestinal tract, liver, stomach, and spleen, as well as in heart, lung, kidney, smooth/ skeletal muscles and some blood cells[92]. Like many other GPCRs, the structural mysteries of the $P2Y_1$R remain to be elucidated. At present, there is still no X-ray

crystallography data for this receptor. Nevertheless, numerous studies using a number of alternative approaches have been carried out, including sequence analysis and homologous modelling using rhodopsin, molecular modelling of ligand analogues, and site-directed mutagenesis to provide further information on the structural determination. So far, the results have provided information relating to the ligand-binding pocket, and indicate that the ATP binding site may be located between TM3, 6 and TM 7, as crucial amino acid residues responsible for interactions with the adenosine and α-phosphate moiety of ATP have been identified at the exofacial side of TM3 and TM7[126].TM6 and TM7 are close to the adenine ring whilst the ribose is likely to be positioned near the TM3 and TM7[127].

As previously mentioned, $P2Y_1R$ is coupled to the $G_{\alpha q}$ protein signalling pathway which activates PLCβ and increases the concentration of intracellular calcium. Agonists for this receptor are mainly ADP, ATP and analogues. ADP is more potent than ATP. 2-MeSATP and 2-MeSADP have much higher affinity than ADP[125,128,129]. In some instances, ATP shows an antagonistic effect[130-132]. On the other hand, MRS 2179, a structural analogue of ADP, is a selective and potent $P2Y_1R$ antagonist, and only interacted with one other receptor, $P2X_1R$ with 20 to 40-fold lower affinity[133,134]. Other non-selective antagonists include suramin, which was reported to cause inhibitory effect on the turkey P2Y receptor 2MeSATP

responses, as well as the UTP response through the human P2U receptors[135].

Previous research has identified heteromer formation A_1R and $P2Y_1R$ d[103]. For instance, experiments conducted by Yoshioka et al. found that A_1R and $P2Y_1R$ co-immunoprecipitated in co-transfected HEK293T cells, suggesting a formation of an oligomeric complex. A similar interaction was detected between the A_1R and $P2Y_2R$ receptors. The oligomeric association between A_1R and $P2Y_1R$ created a new A_1 receptor that elicited $P2Y_1R$-like agonistic pharmacology[103], with the oligomer showing a reduction in both A_1R agonist and antagonist binding affinity as well as a significant increase in potency of a $P2Y_1R$ agonist (ADPβS). In addition, ADPβS inhibited the forskolin-dependent cAMP accumulation via the A_1R-coupled PTX-sensitive $G_{i/0}$, thus representing a novel purinergic receptor phenotype exhibiting both the ligand pharmacology of $P2Y_1$ and the signalling properties of the A_1 adenosine receptor. Further research confirmed the formation of hetero-oligomeric A_1R:$P2Y_1R$ in rat cortex, hippocampus and cerebellum[91]. The mechanistic details of receptor dimerisation and conformational changes have not yet been experimentally confirmed. On the other hand, the dimerisation process inevitably brought these two receptors into close contact. It is not clear whether this interaction resulted in a novel ADPβS binding pocket, or if the interaction of $P2Y_1R$ with the agonist led to a conformational change of the A_1R. Nevertheless, this novel

pharmacology was only observed in cells that co-expressed both receptors.As Figure 2 illustrates, A_1R is coupled to the $G_{\alpha i}$, which regulates the inhibition of the adenylyl cyclase protein, thus causing a reduction in intracellular cAMP concentrations. The $P2Y_1R$, on the other hand, is coupled to the $G_{\alpha q}$ protein, which regulates a completely different pathway that results in the accumulation of intracellular calcium levels. Therefore, in the case of A_1R:$P2Y_1R$ dimerization, it is highly possible that a $P2Y_1R$ agonist might be able to stimulate the dissociation of a $G_{\alpha i}$ protein, and hence the inhibition of forskolin-induced cAMP production.

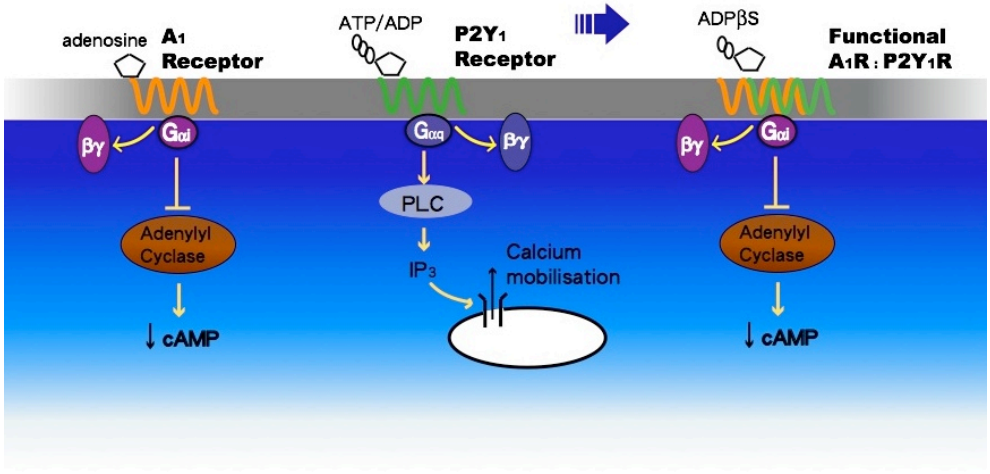

Figure 2. Schematic diagram representation of a functional A_1R:$P2Y_1R$ heteromeric receptor signal transduction events

Homomeric A_1R and $P2Y_1R$ are coupled to the $G_{\alpha}i$- and $G_{\alpha}q$-pathways respectively. Upon agonists activations, A_1R signals leading to decrease in the intracellular cAMP level, whilst $P2Y_1R$ causes intracellular calcium mobilisations. Heteromeric receptors formed between the two produced a functional signal, which stimulated an A_1R-coupled cAMP response when activated by a $P2Y_1R$ agonist ADPβS.

1.4 The Regulation of Purinergic Receptor Signalling Pathways

As discussed in the previous section, purinergic receptors are significant in the G protein-mediated regulation of intracellular cAMP and calcium levels. This project focuses mainly on two particular purinergic receptors, the adenosine A_1R and the $P2Y_1R$, which are coupled to inhibition of adenylyl cyclase and the activation of PLCβ, respectively, and lead to reduced cAMP levels as well as an increase in the intracellular calcium concentration. Therefore, this section will provide a brief introduction to the regulatory components involved in these two signalling pathways, especially concerning the Chinese hamster ovary cell (CHO.K1) expression system, in order to provide a useful background for placing the results of the functional assays into context.

Cyclic AMP and calcium have been described as the "only true ubiquitous second messengers"[136]. It is essential to understand that these two secondary messengers form a complex and interdependent signalling network[136,137], such that the impact of one exerts an effect on the other, and vice versa. As an example of this, cAMP directly operates on the cyclic nucleotide-gated Ca^{2+} channel[138], and activates the cAMP-dependent protein kinase A (PKA), which in turn phosphorylates and regulates IP_3 receptors[139] and voltage-gated Ca^{2+} channels[140]. Conversely, the elevation of intracellular calcium levels can also regulate cAMP levels directly by

acting on isoforms of adenylyl cyclase[141], or by interacting with calmodulin[141,142], the calcium-dependent phosphodiesterase that can lead to hydrolysis of cAMP[143,144]. It is the harmonious interaction between the two signalling pathways that ensures the regulation of both.

1.4.1 Adenylyl Cyclase and the cAMP Pathway

1.4.1.1 Cellular Control of cAMP Level by Adenylyl Cyclase

Cyclic adenosine 3',5'-monophosphate (cAMP) is synthesised by the enzyme adenylyl cyclase, which catalyses the cleavage of a diphosphate group from ATP and the formation of the cyclic adenosine nucleotide (cAMP) and an inorganic pyrophosphate. Cyclic AMP is a second messenger able to regulate a series of downstream effectors[145]. Since the activation and inhibition of the enzyme (adenylyl cyclase?) is achieved by a G_α subunit of a heteromeric G-protein which couples specifically to an activated GPCR, the alteration in the concentration of intracellular cAMP levels is often used as a means of measuring the signalling property of the upstreeam GPCR receptor, the activiation of which leads to the stimulation of an adenylyl cyclase-sensitive G_α subunit. There are currently at least nine distinctive isoforms of mammalian adenylyl cyclase that have been cloned, and these possess differential tissue distribution and functions[137,145]. According to their sequence

similarities and relatedness, these isoforms are grouped into four families: 1, 3 and 8; 2, 4 and 7; 5 and 6; and 9[136].

Adenylyl cyclase is anchored to the membrane via two transmembrane domains, M1 and M2 and has two catalytic cores (C1 and C2) that interact with a number of regulatory ligands and proteins as well as distinguish between the $G_{\alpha s}$ and $G_{\alpha i}$ subunits[137]. The C1 (C1a and C1b) interconnects the two transmembrane-domains, whereas the C2 domain (C2a and C2b) extends from the C-terminal side of the M2 domain[137]. Whilst the $G_{\alpha s}$ binds to the enzyme at C2a domain[146,147], the interaction site for $G_{\alpha i}$ is located on the C1a domain[148,149].

It is the fine regulation of adenylyl cyclase that leads to the control of cAMP synthesis. However, activation or inhibition of the adenylyl cyclase enzyme can be either dependent or independent of a GPCR. For example, the signal transduction processes of the adenosine A_1 and A_{2A} receptors[75], dopamine D_1 and D_2 receptors[63] and M_2 mascarinic receptor[150], are all coupled to the adenylyl cyclase pathways. In contrast, there are a variety of ligands[151] and proteins that are able to interact directly with the enzyme to exert a regulatory effect. Sodium Floride[152], divalent cations such as manganese[153,154] and calcium[155], cholera toxin and other enterotoxins[156] as well as forskolin[151] influences adenylyl cyclase activity directly. Proteins that are able to act directly at adenylyl cyclase are usually located

downstream of the signalling pathway. They operate as a feedback mechanism and include calmodulin, $G_{\beta\gamma}$ subunits[157,158] and some protein kinases[159].

Isoforms	GPCR-Dependent Regulation			GPCR-Independent Regulation		
	$G_{\alpha s}$	$G_{\alpha i}$	$G_{\beta\gamma}$	PKA	PKC	Ca^{2+} [a]
AC I	⇑		⇓		⇑ (weak)	⇑ (CaM)
AC II	⇑		⇑		⇑	
AC III	⇑	⇓			⇑	⇓ (CaMKII)
AC IV	⇑		⇑		? [c]	
AC V	⇑	⇓		⇓	⇑	⇓ (≤1μM)
AC VI	***⇑***	***⇓***		***⇓***	***⇓***	***⇓ (≥1μM)***
AC VII	***⇑***		***(⇑)*** [b]		***⇑***	
AC VIII	⇑					⇑ (CaM)
AC IX	⇑	⇓				⇓ (CaN)

a. Ca^{2+} regulation includes effects from $Ca^{2+,}$ CaM, CaMK and CaN.

b. Stimulation detected in over-expressed cells by one well-cited paper[160], not sufficient literature evidence.

c. Conflicting results[136].

Table 2. Adenylyl cyclase isoforms and their regulatory factors[136,137]

Isoforms of adenylyl cyclases are differentially regulated, either dependent on the GPCR activation, or independently via the intracellular enzymes and ions. Isoforms VI and VII, expressed in CHO cells are highlighted.

1.4.1.2 Adenylyl Cyclase Regulation in Chinese Hamster Ovary Cells

The mammalian adenylyl cyclase reaction rate is the result of the integration of the effect of a pool of enzyme modulators including the enzyme-specific G_{α} proteins, the $G_{\beta\gamma}$ subunit, the protein kinases A and C, the intracellular calcium/ calmodulin concentrations, as well as the presence of agonist ligand such as forskolin[161]. Depending on the tissue-specific expressions of the enzyme isoform and the concentration of modulator, the cAMP responses may differ upon stimulation of a GPCR in different tissue and cell lines. Therefore, a more detailed explanation of the regulatory processes for this enzyme will be discussed with reference to the Chinese Hamster Ovary (CHO.K1) cell line as this was the base for all the cell lines used in this project were established.

Identification of the adenylyl cyclase isoforms expressed in CHO using reverse transcriptase polymerase chain reaction (RT-PCR) revealed two isoenzyme types, VI and VII (AC VI and AC VII)[162]. As shown in Table 2, AC VI is regulated by both $G_{\alpha s}$ and $G_{\alpha i}$, whilst AC VII is activated by $G_{\alpha s}$. In addition, forskolin, calcium, PKA, PKC, and $G_{\beta\gamma}$ proteins all play roles as important endogenous regulatory components, apart from forskolin for these two adenylyl cyclase isoforms.

Forskolin, an extract from the roots of Coleus *forskohlii*[163], has been shown to be a potent activator of all types of adenylyl cyclase in membrane preparations as well as intact cells[151]. It is, therefore, readily applied in the functional characterisation of signalling pathways relating to cAMP level fluctuations.

Calcium, on the other hand, directly inhibits AC VI at submicromolar concentrations[141], independently of calmodulin. This has been proved in a whole cell system[136], where this inhibitory response has been shown to be attenuated by pertussis toxin[164]. The specific location at which calcium binds to AC VI has not been clearly identified yet. However, for AC V, which is in the same family as AC VI, it has been proposed that the binding site is located on the C1b domain[165]. The source of the cytosolic calcium by which the AC VI activity is regulated comes from extracellular influx through the CRAC-channels[141] during depletion of intracellular Ca^{2+} stores, or through cyclic nucleotide-gated Ca^{2+} channels[138]. Moreover, calcium mobilised via the PLC pathway also contributes towards the cytosolic accumulation of Ca^{2+} [166] which in turn inhibits AC VI activity. In CHO cells, this process may be achieved by PLCβ, which is coupled to $P2Y_1R$.

Both adenylyl cyclase isoforms in CHO.K1 cells are regulated by protein kinases. PKA and PKC exert inhibitory effects on AC VI[137], whilst PKC activates the AC VII isoform[136]. It is curious how PKC

exerts opposite regulatory effects on AC VI and VII. In general, the activation of PKC itself is achieved through the PLC pathway, in which the formation of DAG, from PIP_2 hydrolysis to IP_3, directly stimulates the kinase. Although, the evidence for PKC binding and phosphorylation is quite firm[136,167-169], there is, so far, only a small, but consistent amount of evidence for the stimulatory phosphorylation of AC VII by PKC. Moreover, evidence for the inhibitory control of AC VI by this kinase is still controversial, as activation of the isoform by PKC has also been observed[136]. PKA is a tetrameric holoenzyme consisting of two regulatory and two catalytic subunits. When cAMP binds to the regulatory subunit, the catalytic moiety is then released for phosphorylation of target proteins[170-172]. The isoform AC VI can also be regulated by a cAMP-dependent PKA phosphorylation[173], whose effect leads to an inhibition of the isoenzyme via a negative feedback mechanism.

Furthermore, AC VII can also be activated by the $G_{\beta\gamma}$ proteins, the intracellular concentration of which is approximately nanomolar, as opposed to subnanomolar for the $G_{\alpha s}$ subunit. Even then, the effect of $G_{\beta\gamma}$ is only substantial when $G_{\alpha s}$ is co-stimulated[158]. Due to the relative lack of expression, the G_i and G_o-proteins have become possible donors for $G_{\beta\gamma}$ subunits, rather than G_s[174]. In other words, the cross talk between G_s and $G_{i/0}$ leads to the AC VII activation by $G_{\beta\gamma}$. Prolonged activation of $G_{\alpha q}$ or $G_{\alpha i}$-coupled receptors will also

result into an accummulation of $G_{\beta\gamma}$[137,175]. In CHO.K1 cells, $G_{\alpha q}$ is coupled to the endogenously-expressed $P2Y_1R$, and the stably transfected A_1R has been shown to couple to $G_{\alpha i}$[176].

Another method of maintaining the level of cAMP in cells is through the hydrolysis of cAMP to AMP by phosphodiesterase (PDE). There are currently eight identified subfamilies of this enzyme, seven of which (PDE 1-7) catalyse the hydrolysis of cAMP[177]. In CHO cells, four types, PDE 1-4, have been identified[178,179]. These PDEs show differential cAMP specificities, and respond to distinctive regulatory signals such as calcium/ calmodulin complexes and protein phosphorylation via PKA, etc[137].

1.4.2 The Calcium Signalling Pathway

Mammalian cells have a calcium concentration gradient across the membrane that is about 100nM intracellularly and 1mM extracellularly. Calcium, which constitutues one of the most abundant second messengers, participates in a large range of essential physiological roles, from fertilisation to neurotransmission to skeletal muscle contractility[180-182]. Nevertheless, unregulated calcium in cells will have a cytotoxic effect, leading to apoptosis and necrosis[183]. The regulation of intracellular calcium concentration is achieved via calcium ion transporters and channels. Certain phosphoinositides,

such as the IP_3 formed from PIP_2 hydrolysis by PLCβ have been shown to play an important role in calcium mobilisation from intracellular stores[184]. Therefore, the regulation of PLCβserves in turn to balance the intracellular calcium concentration. In addition, this enzyme is activated by GPCRs. The $P2Y_1R$ endogenously expressed in CHO cells is coupled to the activation of PLCβ.

1.4.2.1 Phospoholipase C Isoenzymes

As a part of the GPCR signalling pathway, the regulation of PLC is a key aspect in modulating intracellular calcium mobilisation. The PLC enzymes consist of six classes with a total of thirteen members identified thus far. The structure of this enzyme is composed of an N-terminal pleckstrin homology (PH) domain, an EF-hand motif, and C-terminal C2 domain, all of which contribute to the regulatory part of the enzyme, whilst the catalytic part is located between the EF-hand and C2 domain, including an X domain with more conserved catalytic residues, and a Y domain for substrate recognition[185,186]. It is a soluble enzyme located in the cytosol and translocated to the cell membrane upon recognition of PIP_2, where it becomes tethered to the membrane[186]. Although the PLCβ isoform is activated through G_q proteins, different subtypes respond differentially to G proteins. The PLCβ1 and PLCβ4 are regulated by $G_{\alpha q}$ mainly, while PLCβ2 and PLCβ3 can be regulated by both $G_{\alpha q}$ and $G_{\beta\gamma}$ subunits[183]. CHO.K1 cells express PLCβ3 exclusively[187,188], which means that the

stimulation of the PLCβ pathway can also be the result of receptor cross-talk via an activated $G_{i\beta\gamma}$ subunit[189].

1.4.2.2 GPCR Activation Of PLCβ And Downstream Signalling

As mentioned earlier, the activation of PLCβ leads to the hydrolysis of PIP_2, producing IP_3 and DAG. IP_3 will bind to the IP_3-sensitive calcium channel, resulting in the release of calcium from the endoplasmic reticulum (ER) store[190,191] and increasing the cytosolic calcium concentration from nanomolar to micromolar[192]. The DAG molecule, on the other hand, can either work alone or in conjunction with calcium, activating the enzyme PKC. The net increase of intracellular calcium in turn triggers further release of calcium via the IP_3-senstive calcium channel and the ryanodine channel[193].

Following the increase in the cytosolic calcium level, a rapid mechanism is employed in order to maintain intracellular calcium homeostasis. Direct removal of calcium is achieved by efficient efflux from the cytosol via a Ca^{2+}-ATPase on the ER and plasma membranes and by a Na^{+}/Ca^{2+} exchanger[193]. The Ca^{2+}-ATPase pump has an extended C-terminal tail that allows interaction sites for calmodulin (which acts as a calcium sensor, binding to calcium during the increase), PKC and PKA. Therefore, it can be modulated by phosphorylation. When phosphorylated, the pump exhibits high

calcium-binding affinity and lowers the calcium concentrations to below micromolar level. Whilst this pump system shows a great affinity for calcium, its transport capacity is relatively low compared to the electrogenic Na^+/Ca^{2+} exchanger system, which operates using the energy of the Na^+ gradient across the membrane. In addition to acting as a regulatory tool for AC and Ca^{2+}-ATPase pump, PKC also controls the voltage-gated calcium channels (Ca_v), such as the $Ca_v1.2$. The effect of such regulation can induce a complex effect on the calcium current, causing it to increase, decrease or even become biphasic[194,195].

In addition, the control of the calcium level can be achieved by direct inhibition on the PLCβ3 activation pathway. Once PLCβ3 is phosphorylated by PKA, it leads to an inhibition of PIP_2 hydrolysis. This results in a reduction in the IP_3 concentration, which in turn, deactivates the IP_3-sensitive Ca^{2+} channels. The remaining DAG is either hydrolysed to glycerol and fatty acid, or phosphorylated to diacylglycerol-3-phosphate[196].

The rapid loss of calcium through a series of removal mechanisms occurs during the first few minutes until an equilibrium is re-established between the rate of calcium efflux and influx resulting from agonist stimulation[197,198].

1.5 PROJECT AIMS AND OBJECTIVES

Recent studies have identified that the A_1R and $P2Y_1R$ physically form a heteromeric receptor complex with altered signalling properties[103]. The aim of this project is to confirm the heteromerisation process in CHO cells, as well as to investigate the signalling properties of the heteromeric A_1R:$P2Y_1R$ when each of the receptor subtypes is expressed at a physiological level.

Previous work in the laboratory has allowed the establishment of two stably-transfected clonal cell lines based on the parental CHO.K1 cell line which expresses an endogenous hamster $P2Y_1$ receptor. One of the recombinant cell lines expresses a wild type human A_1 adenosine receptor at physiological levels while the other cell line expresses a constitutively active mutant form of the human A_1 adenosine receptor. Using a range of agonists and antagonists, these cell lines have been used for the functional characterization of heteromeric A_1R:$P2Y_1R$ signalling responses through the G_i and G_q pathways (using Fluorescent Imaging Plate Reader, or FLIPR?) The work presented in this thesis extends the current pharmacological and functional profile of the A_1R:$P2Y_1R$ heteromer and identifies a role for this heteromeric receptor in the production of both cAMP and calcium second messengers.

This work also describes the experiments performed in order to characterise the physical interactions between these two purinergic

receptors using co-immunoprecipitation of native receptors from the clonal cell lines used in the functional assays. In addition, it describes the development of an additional method for the identification of heteromeric interactions in living cells, namely Bimolecular Fluorescent Complementation (BiFC), which serves as analternative approach to co-immunoprecipitation as it allows the visualisation of receptor interactions in living cells

Chapter 2

Materials and Methods

2.1 MOLECULAR BIOLOGY TECHNIQUES

2.1.1 Restriction Enzyme Digestion of Plasmid DNA

Restriction endonuclease digestions were performed with approximately 1 unit of enzyme (New England Biolabs or Promega) per μg of DNA in the appropriate reaction buffer diluted to a final reaction concentration of 1X. In some cases, bovine serum albumin (BSA) was added in order to maintain enzyme stability. The restriction enzyme(s), together with the 10X buffer and BSA (10mg/mL) stock solutions, were typically added at 10% of the total reaction volume and the reactions were carried out at an appropriate temperature, usually at 37°C for 2-3 hours.

2.1.2 DNA Electrophoresis

DNA electrophoresis was used to confirm the DNA size and integrity after restriction endonuclease digestions. The use of the technique is based on the principle that DNA is negatively charged and able to migrate towards the positively charged electrodes through the gel

matrix, achieving separation of DNA fragments by their size. Typically, 1% agarose gels containing 1ug/mL Ethidium Bromide (EtBr, Promega) were used. For improved resolution of small DNA fragments however, 2% gels were used. Agarose gels were made by melting agarose powder (Sigma) in 1X TAE buffer (Promega). Before loading, DNA samples were mixed with 5X DNA loading buffer (Bioline), to give a final concentration of 1X loading buffer. Electrophoresis was performed at a constant voltage of 100V using horizontal gel tanks and a power supply EPS301 (GE Healthcare). Molecular weight DNA markers (Invitrogen) were run alongside the samples to enable the determination of fragment size.

2.1.3 DNA Fragment Purification

Restriction digestions (100-200μL) were loaded onto 1% agarose gels containing EtBr after confiming complete restriction in a pilot run. After electrophoresis, the desired DNA fragments were visualized over a UV transilluminator excised from the gel using a scalpel. The DNA was extracted from the gel slice using the Wizard® PCR Prep DNA Purification System (Promega) according to the manufacturer's protocol.

The purification of vectors for ligations was conducted by phenol: chloroform extraction, followed by ethanol precipitation. 200μL of the digest (approximately 20μg of plasmid vector DNA) was mixed with

100μL of phenol: chloroform: isoamyl alcohol (25:24:1, saturated with 10mM Tris, pH 8.0, 1mM EDTA, Sigma). The mixture was centrifuged at 13,200 rpm at 4°C for 5 minutes. The upper aqueous layer containing the DNA fragment was transferred into a clean 1.5mL Eppendorf test tube and the extraction process repeated.

After the phenol: chloroform extraction, 20μL of 3M Sodium Acetate (Sigma) and three volumes of 100% ethanol were added. The solution was further mixed and incubated at -20°C for 20-30 minutes to allow the DNA to precipitate. The mixture was then centrifuged at 13,200 rpm at 4°C for 20 minutes. The pellet was resuspended in 1X TE pH8.0 at an approximate concentration of 100ng/μL.

2.1.4 Ligation

After purification of the DNA fragments, the DNA was quantified on a 1% agarose gel containing EtBr. For ligations, the plasmid vector and DNA inserts were mixed in an approximately 1:1 ratio, with a minimum of 100ng of vector DNA per reaction, using 400U T4 DNA ligase and 1X T4 DNA ligase buffer containing 1mM ATP (New England Biolabs), in a total reaction volume of 20μL. A control ligation reaction of vector only was also prepared. Ligations were carried out in a 0.2mL flat cap PCR tubes (Molecular BioProducts) at 10°C overnight.

2.1.5 Transformation

Aliquots of the ligationswere used to transform One Shot® TOP10F' chemically competent *Escherichia coli* cells (Invitrogen) as follows. For each transformation, the ligation mixture was added directly into the competent cells and mixed by gentle pipetting. The cells were incubated on ice for 30 minutes, followed by heat shock at 42°C for 90 seconds, and then incubated on ice for a 2 minutes. SOC medium was added to the cells and incubated for 1hr at 37oC to allow antibiotic gene expression. The cells were then spread on antibiotic-containing LB agar plates and incubated at 37°C overnight. Single colonies were picked, and grown in LB broth to identify recombinant clones, as described in Section 2.1.7.

2.1.6 LB Stocks and Agar Plates for Bacterial Growth

LB Broth (Lennox L Broth, Invitrogen) and LB Agar (Lennox L Agar, Invitrogen) were made according to manufacturer's instruction and autoclaved at 121°C for 15 minutes, and cooled to below 50°C before the addition of antibiotics. The antibiotic used for most experiments was ampicillin (Roche-Diagnostics), which was added to a final concentration of 100μg/mL. LB agar plates were poured into 10cm Petri dishes and left at room temperature to solidify before being used or stored at 4°. Ampicillin was added to LB broth immediately prior to inoculation.

2.1.7 Small scale preparation of plasmid DNA (Miniprep)

The miniprep DNA purification technique was used to screen for recombinants. Single isolated colonies picked from the LB/Amp agar plates, and used to inoculate 2mL of LB broth medium containing 100μg/mL ampicillin. The culture was grown to saturation in a 14mL Falcon 2059 Polypropylene round-bottom tube (Becton Dickinson), in a 37°C shaking incubator at 250 rpm overnight.

One millilitre of the bacterial culture was transferred to a 1.5mL Eppendorf tube and centrifuged for 1 minute at 4°C and 13,200 rpm. The pellet was resuspended in 100μL of Solution I (50mM glucose, 25mM Tris-HCl pH8.0, 10mM EDTA pH 8.0) containing 50mg/mL lysozyme (Roche Diagnostics) for five minutes at room temperature. 200μL of Solution II (0.2N NaOH, 1% SDS) was added to the tube, and mixed by inversion. After a 5-minute incubation at room temperature, 150μL ice-cold Solution III (3M KAc, 11.5% glacial acetic acid) was added to the tube and left on ice for a further 10 minutes. The mixture was then centrifuged for 5 minutes, at 4°C at 13,200 rpm.

After centrifugation, the supernatant was transferred into a clean 1.5mL Eppendorf tube. The DNA was extracted from the supernatant phenol:chloroform extraction as described above (2.1.3). The DNA pellet was resuspended in 50μL TE buffer.

Recombinant plasmids (those with inserts) were verified by restriction digestion of the purified DNA and gel electrophoresis. Glycerol stocks of (positives) recombinants were prepared by mixing bacterial cultures of the positive clones and sterile glycerol in a 1:1 v/v ratio. This mixture was then stored at -80°C.

2.1.8 Large scale preparation of plasmid DNA (Maxiprep)

After identifying recombinant plasmids by the miniprep method, 500μL of positive clones was used to inoculate 500mL of LB broth containing 100μg/mL ampicillin, in a 2-litre Erlenmeyer flask. The culture was grown overnight in a 37°C incubator, shaking at 180 rpm.

The culture was then transferred into 500 mL centrifuge bottles, balanced and spun at 7000rpm, 4°C for 10 minutes in Sorvall high speed centrifuge usinga GSA rotor. The resulting pellets were resuspended in 18mL Solution I (as defined in 2.1.7), followed by the addition of a further 2mL of Solution I that contained 10mg/mL lysozyme. The mixture was incubated at room temperature for 10 minutes before adding 40mL of Solution II (lysis solution) and mixing by inversion. The bacterial lysate was incubated for 5 minutes at room temperature; 20mL of ice-cold Solution III was then added and the mixture was incubated on ice for 15 minutes before adding 5mL of dH_2O and centrifugation of the mixture at 7000 rpm and 4°C, for 15 minutes.

Following centrifugation, the supernatant was filtered through a gauze; 45mL of propan-2-ol was added to the filtered solution, mixed gently and incubated for xxxminutes to precipitate the DNA. After centrifugation at 7000 rpm for 20-30 minutes,the DNA pellet was resuspended in 6.5mL of TE buffer and an additional 150μL of 0.5M EDTA was added. Approximately 100μL of 2M TRIZMA®Base (Sigma) was added carefully in a step-wise manner until the pH level of the mixture reached approximately 7.5. The final volume of the mixture was adjusted to 10mL with 1X TE buffer and 12g of Caesium Chloride (CsCl, Sigma) was added to the solution and dissolved with gentle mixing. Meanwhile, a Quick-Seal ultracentrifugation tube (Beckman) was prepared with 250μL of 10mg/mL EtBr and the entire volume of the DNA/CsCl mixture was transferred into the NVT tube. After heat-sealing using the Beckman tube-sealer (Beckman, Palo Alto, California), samples were centrifuged in a Beckman Coulter OPTIMA L-100 XP ultra-centrifuge for 24hours at 60,000 rpm at 20°C. Two distinct and closely positioned bands of plasmid DNA were obtained, usually towards the upper part of the tube. The higher band represents the open linear form of DNA, whereas the lower band contains the supercoiled close-circular plasmid DNA. In order to extract this lower band, the top of the tube was first pierced using an 18-gauge (18G) needle. The band was then carefully removed using a syringe with an 18G needle inserted into directly below the DNA

band. The extract was transferred into a 14mL Falcon tube for butanol extraction.

EtBr was removed from the DNA by extraction with 2 to 3mL of 100% butan-1-ol. After mixing, the solution spontaneously separated into a top organic phase and a lower aqueous phase. The aqueous layer was carefully removed and transferred into a clean 14mL Falcon 2059 tube. The extraction process was repeated until the lower phase was colourless indicating that the EtBr had been completely removed. The clear aqueous phase was transferred and clip-sealed into a 15.9mm dialysis tubing (Medicell). CsCl was removed by dialysis in 2L of 1X TE at room temperature for 2 -3 hours. Following dialysis, the DNA solution was transferred into a clean 14mL Falcon tube, incubated with 10μg/mL RNaseA for 60 minutes in a 65°C water bath, followed by a further 60 minute incubation at 37°C with proteinase K (Roche-Diagnostics) and SDS at a final concentration of 100μg/mL and 0.2%, respectively. After this, the DNA was purified by phenol:chloroform extraction as described above. The plasmid DNA was precipitated in a 30mL Corex tube with 250mM NaCl and 3volumes of 100% ethanol; afterincubation at -20°C for 20 minutes samples were centrifuged for 20 minutes at 8000 rpm,4°C. The DNA pellet was resuspended in 1mL of 1X TE and the concentration of the DNA was determined as described in Section 2.1.9

2.1.9 Quantification of DNA

DNA was quantified using a Nanodrop machine (supplier) . The concentration and purity of the DNA were determined at $OD_{260/280}$. This ratio indicates the purity of the plasmid DNA: pure DNA has an $OD_{260/280}$ ratio of approximately >1.80, although contamination with proteins reduces this figure and contamination with phenol can augment it. When plasmid DNA was quantified, 1 OD_{260} corresponded to a concentration of 50μg/mL. The concentrations of 1 OD_{260} for oligonucleotides and RNA used were 37μg/mL and 40μg/mL, respectively.

2.1.10 Dideoxy DNA Sequencing

Both plasmid and PCR-derived DNA were sequenced using the dideoxy sequencing method (Sanger, xx), by the UCL DNA sequencing facility the . For PCR, DNA was amplified using a Hybaid PCR Express® Thermocycler and vector-specific primers. PCR reactions used the ABI PRISM® BigDye™ Terminator Cycle Sequencing Kit (version 3.1, supplier?) according to the manufacturer's instructions: 10μL reactions in 0.2mL PCR tubes contained 500ng of template DNA, 2μL of BigDye 3.1, 2μL of dilution buffer, 2μL of 2μM sequencing primer and 0.5μL of DMSO. Polymerase chain reaction amplification was carried out in three stages. The DNA was denatured for 5 minutes at 98°C, followed by a second stage of 25 cycles comprising: 30 seconds of denaturation

at 96°C, 20 seconds of primer annealing at 50°C and 4 minutes of extension at 60°C. The final stage was a 5 minute extension at 60°C for a single cycle.

After the PCR , the DNA was precipitated on ice for 15 minutes with 20μL 3M Sodium Acetate, 2μL 125μM EDTA (pH 8.0) and 50μL ice-cold 100% ethanol. The DNA was then centrifuged at 13,000 rpm at 4°C for 30minutes. Following centrifugation, the supernatant was aspirated off, and the DNA was washed with 50μL of 70% ethanol, followed by centrifugation at 13,000 rpm for 10 minutes. The DNA pellet was air-dried on a heat block at 50°C and then sent for sequencing. Sequencing data was analyzed using the 4Peaks program (version 1.7.2) to read the chromatogram and MacVector® (version 12.0.1).

2.2 PROTEIN BIOCHEMISTRY

The techniques used in this section were developed for the identification of the physical interactions between the A_1R and $P2Y_1R$ receptors. These methods include membrane extraction from frozen mammalian cell pellets, solubilisation of the native receptors A_1R and $P2Y_1R$, SDS-PAGE gel electrophoresis, Western blot transfer of the proteins from the SDS-PAGE gel to nitrocellulose membranes, immunoprecipitation of the native receptor proteins using a primary

antibody directed against the receptor and immunodetection of the receptor signals.

2.2.1 Choice of Detergent for Solubilisation

Detergents are can be broadly classified into 4 groups[198,199,200]: -

i. Anionic, e.g. sodium dodecyle sulphate (SDS), some bile salts such as cholate and deoxycholate;
ii. Cationic, e.g. CTAB (cetyltrimethylammonium bromide);
iii. Zwitterionic, e.g.3-[(3-cholamidopropyl)-dimethylammonio]-1-propanesulfonate (CHAPS);
iv. Non-ionic, e.g. Triton X-100.

When choosing detergents, several crucial factors are usually considered in order to achieve functional solubilisation:

1) <u>Critical Micelle Concentration (CMC).</u>

At low concentrations, detergent molecules exist as monomers in a pure aqueous solution. As the concentration increases above a critical range (a narrow range), which is referred to as the CMC, they form non covalent and thermodynamically-stable aggregates called micelles[199,200]. Past studies suggested that one should aim to use a detergent with high CMC (>1mM) at concentrations below the CMC[199] to prevent the loss of protein functions[199,200]. Salt[199,201] is often used to reduce the CMC, which is of particular relevance for bile acid-derived detergents such as CHAPS and

cholate and also for ionic detergents, where salts tend to reduce the repulsion between the charged head groups[199]. For example, it has been experimentally proved[201] that the logarithm of the CMC of CHAPS decreases linearly with the salt concentration up to 1.5M.

2) Detergent – Lipid – Protein Ratio

The amount of detergent required for functional solubilisation is largely dependent on the amount and nature of membrane proteins / lipids present. Although it is not essential to measure the optimal detergent to lipid ratio[199,202,203], choosing the most suitable detergent and the amount required for solubilisation of A_1:P2Y_1 heteromers involves a lot of trial-and-error.

3) Lipid Environment

During membrane solubilisation, sometimes a selective or differential solubilisation of membrane lipids may occur. Under such conditions, not only does it become impossible to determine the extent of solubilisation but, more importantly, the loss of essential protein-lipid interactions can result in the loss of protein functions[199,202], underlining the importance of the membrane lipid environment. For example, after the solubilisation of bovine hippocampal 5-HT_{1A} receptors using CHAPS[202], the G protein-coupling and ligand-binding abilities of the receptor were significantly reduced. Interestingly, the membrane cholesterols

were also lost and recovery of the ligand binding properties was obtained when cholesterols were reintroduced into the purified solubilised receptors[202].

In Table 3 below, some of the most commonly used detergents are listed, and the examples include all four types of detergents. The table also included the detergent's physical properties and functional preferences. It showed that some detergents are good for membrane protein solubilisation providing a mild and non-denaturing condition. The functional properties of the receptors can be retained with certain detergents; others are also recommended for immunoprecipitation. In addition to solubilising membrane proteins, some detergents are used in the gel electrophoresis.

Detergent	Type	Aggregation Number	Critical Micelle Concentration (CMC) mM	Micellar Weight	Additional Notes
Sodium n-Dodecyl Sulfate (SDS)	Ionic	62	7-10	18,000	electrophoretic separation (proteins and lipids)
Cholic Acid, Sodium Salt	Ionic	2	9-15	900	purification of functional membrane protein complexes; two-dimensional gel electrophoresis
Deoxycholic Acid, Sodium Salt	Ionic	4-10	4-8	1600-4100	membrane-bound proteins
Digitonin, High Purity	Non-Ionic	5-6	-	7000	solubilise membrane-bound proteins
Nonidet™ P 40	Non-Ionic	-	0.05-0.3	-	solubilise receptors; permeabilise cellular /nuclear membranes under mild conditions
Nonidet™ P 40 Substitute	Non-Ionic	-	0.059	-	solubilise cerebral GABA receptors, proteins and lipids of the scallop gill ciliary and breast cancer cell membranes
TRITON® X-100	Non-Ionic	100 - 155	0.2 - 0.9	80,000	solubilisation of membrane proteins under mild non-denaturing conditions
TWEEN® 20	Non-Ionic	-	0.059	-	Immuno-precipitation and solubilisation of membrane-bound proteins
CHAPS	Zwitterionic	4-14	6-10	6000	Non-denaturing; better than structurally-related carboxylic acid anions; effective at breaking protein-protein interactions

Table 3.Examples of some most commonly used commercially available detergents. The four main classes are represented and physical properties associated with each detergent such as aggregation number, the critical micelle concentration, and the micellar weights are shown. The functional advantages or disadvantages are stated for each detergent.

2.2.2 Membrane Preparation and Solubilisation

Chinese Hamster Ovary (CHO) cells (ECACC) were cultured ir tissue culture flasks (175cm^2 surface area, BD Falcon™) until confluent, giving approximately 10^7 cells per flask. Cells harvested and centrifuged in a 50mL Falcon tube and the pelle stored at -80°C prior to preparation of the membranes. In orc extract the cell membranes, the frozen pellet of 10^7 cells was th on ice and lysed by vortexing with 1mL of the lysis reagent M-F (Mammalian Protein Extraction Reagent, Thermo Scie containing EDTA-free Complete protease inhibitor cocktail (Ro The cell lysate was incubated on ice for 20 minutes and homogenised using a Polytron homogeniser at maximum spee two cycles at 20 seconds each. The lysate was then centrifug 1200X g at 4°C for 15 minutes in order to pellet cell debris. Afte step, the protocol was continued in different ways according t type of assay to be performed, as described below.

To prepare membrane extracts 0.5mL of M-PER solubilisation b containing suitable detergents and protease inhibitors, was add the supernatant, and the mixture was transferred into a 2mL s capped test tube ready for solubilisation. M-PER reagent proprietary detergent and, its solubilisation property was better other detergent test in trials (explained in Chapter 6). Therefor additional detergents were added to this buffer.

2.2.2.1 For radioligand binding assays

The resulting supernatant was transferred into an ultracentrifugation tube and spun at 55,000 rpm, 4°C for 60 minutes, in the Beckman bench-top ultracentrifuge using the TLA110 rotor. After centrifugation, the pellet was retained and resuspended in 1mL of M-PER reagent containing 1X protease inhibitors by passing 3-5 times through an 18G needle attached to a 2mL syringe. The partially-resuspended pellet was then treated further, by passing through a 25G needle several times, until completely dissociated. Samples were kept on ice throughout this process. They were aliquoted into 1.5mL Eppendorf test tubes and stored at -80°C.

2.2.3 Membrane Solubilisation

Solubilisation buffer was added to the supernatantin a 2mL screw-cap test tube and incubated on a rotator at 4°C, for 60 to 120 minutes to solubilise the membrane proteins. After this, the samples were spun in aBeckman bench-top ultracentrifuge using a TLA110 rotor, at 31,000 rpm, 4°C, for 60 minutes. The supernatant was transferred into a clean Falcon tube.

The solubilised membranes were pre-cleared of any non-specific proteins with protein G Sepharose™ (4 Fast Flow, GE Healthcare). Brielfy, 150μL of Protein G sepharose was transferred into a 1mL Eppendorf tube, and centrifuged at 1,000 rpm, 4°C for 2 minutes.

The supernatant was aspirated off, and replaced with the same amount of the solubilisation buffer (M-PER, 1X protease inhibitor cocktail). The wash step was repeated one more time. The membrane protein extract was divided into 300μL aliquots and transferred into clean 1.5mL Eppendorf tubes. To each aliquot, 40μL of washed Protein G Sepharose™ was added. The mixture was incubated at 4°C for at least 90 minutes on a rotor, followed by centrifuging at 1,000 rpm for 2 minutes. The supernatant was transferred to a new Falcon tube, and the protein concentration was determined before being frozen in aliquots at -80°C.

2.2.4 Immunoprecipitation

Immunoprecipitations were carried out using receptor-specific antibodies on the pre-cleared samples. Membrane preparation typically yielded approximately 3mg of proteins at an approximate concentration of 3mg/mL. Following solubilisation and pre-clearing of the sample, a protein concentration of 1.6mg/mL was typically obtained. This is roughly equivalent to 480μg of proteins per pre-cleared sample, as for each pre-clearing, the starting sample volume was 300μL per tube. To each of the tubes (480μg protein), 1μg of the primary antibody was added. The mixture was incubated at a 4°C rotator for at least 120 minutes. Afterward, 30μL of the Protein G Sepharose™, previously prepared and resuspended in the solubilisation buffer, was added, and incubated at 4°C using a rotator

for 60 to 120 minutes. The tubes were then spun at 1,000 rpm 4°C for 2 minutes, and the Sepharose beads were retained. These beads were further washed twice using 300μL per sample of M-PER solubilisation buffer containing 1X protease inhibitor cocktail. After the final wash, the beads were centrifuged at 1,000 rpm 4°C for 2 minutes. The supernatants were aspirated off, and the beads were resuspended in one volume of 2X Laemmli sample Buffer (Sigma) and stored at -20°C.

2.2.5 Sodium Dodecyl Sulphate Polyacrylamide Gel Electrophoresis (SDS-PAGE) and Western Blot Analysis

SDS-PAGE gels (10%) were made

using 30% ProtoGel® and buffers (stacking bufferand resolving buffer) as recommended by the manufacturer

Gelelectrophoresis and Western blot transfer were performed in aBIO-RAD Mini-PROTEAN® 3 Cell electrophoresis module and the Mini Trans-Blot® Electrophoretic Transfer Cell apparatus respectively following the manufacturer's instructions. To cast the gels, the glass plates and spacers were aligned and assembled in the casting frames. The 10% separating gel mixture was carefully poured into the space between the gel plates until about 5cm from the top. Any bubbles resulting from the transfer of the gel mixture were eliminated with butanol and the top of the layer was levelled with ddH_2O. The separating gel was left at room temperature to solidify. After

rinsingwith a small amount of distilled water, 4% of stacking gel was layered onto the top of the separating gel. A 10-well plastic comb was carefully inserted between the two gel plates and left to set.

After the stacking gel was set, the cassette was carefully assembled with the electrodes in the mini-tank; the inner chamber of the tank was filled with running buffer (1x Tris-Glycine Buffer (25mM Tris, 192mM Glycine, 0.1% SDS), pH 8.3 (BIO-RAD. The lower chamber of the mini-tank was also filled half-way with the running buffer. The plastic comb was carefully removed and the wells were flushed with buffer using a pipette..

Protein samples were denatured by adding equal volumes of 2x Laemmli sample buffer (Sigma) and boiled at 95°C for 15 to 20 minutes. The denatured samples were placed on ice for 5 to 10 minutes followed by the addition of 2 to 5μL of β-mercaptoethanol (20 to 25% v/v final; Sigma). The samples were loaded alongside a pre-stained protein marker (PageRuler™ Plus Prestained Protein Ladder, Fermentas). Electrophoresis was performed at 200V with Power Pac 200 (BIO-RAD) for 45 minutes.

After the electrophoresis, the gel was pre-equilibrated with transfer buffer and placed upside down three layers of pre-wetted 1mm filter paper (BIO-RAD); air bubbles were removed with a plastic roller. A piece of pre-wetted nitrocellulose membrane (Trans-Blot® pure

Nitrocellulose 0.45μm, BIO-RAD) was then placed on top of the gel with the aid of a pair of forceps, and air bubbles again removed. Another three layers of pre-wetted 1mm filter paper was placed onto the nitrocellulose membrane layer, and finally, one layer of pre-wetted fibre pad was added onto the 'sandwich'. The assembled cassette sandwich was placed into the buffer tankwhich was then filled with ice-cold transfer buffer (1x Tris-Glycine Buffer (25mM Tris, 192mM Glycine, 0.1% SDS), pH 8.3 (BIO-RAD), (10% solution, Fisher Scientific), and 20% Methanol (BDH). The tank was cooled by placing it inan icebox on a magnetic stirrer block. Proteins were transferred at 100V for 60 minutes using Power Pac 200 (BIO-RAD)..

2.2.6 Immunodetection

The research sought to identify heteromeric interactions between native receptors. Therefore, the immunodetection process used primary antibodies that directly targeted the receptor protein. These primary antibodies were all polyclonal antibodies raised from either rabbit or goat: Rabbit Anti-A_1R H-40 polyclonal IgG (Santa Cruz, SC-28995), Goat Anti-A_1R C-19 polyclonal IgG (Santa Cruz, SC-7500), Rabbit Anti-$P2Y_1$R H-120 Polyclonal IgG (Santa Cruz, SC-20123), Goat Anti-$P2Y_1$R N-16 Polyclonal IgG (Santa Cruz, SC-15203). The secondary antibodies used were conjugated with an infra-red dye (IRDye)- either IR680 or IR800: Donkey anti-goat IgG IRDye

800-conjugated (H+L) (Rockland, Lot # 14111), Goat anti-rabbit IgG IRDye 680-conjugated (H+L) (Alexa Fluor®, Molecular Probes).

After the gel transfer, the nitrocellulose membrane was removed with a pair of forceps, and immediately placed in 1X TBS (Tris buffered saline, 50mM Tris, pH8.0, 150mM NaCl) with gentle shaking at room temperature for 10 to 15 minutes. The TBS was then discarded and the membrane was blocked with minimum 0.4mL/ cm^2 membrane of Odyssey Blocking Buffer (LI-COR Biosciences) at room temperature for 30 to 60 minutes with gentle shaking.

The primary antibody was diluted in 1X TBS (minimum 0.2mL/ cm^2) to 1:500. The nitrocellulose membrane and the primary antibody dilutions were placed into a heat-sealed bag, carefully squeezed out air bubbles before sealing the opening side. It was then incubated at 4°C (cold-room) with gentle shaking overnight. Where an antibody-specific blocking peptide was used, the primary antibody was incubated with the blocking peptide prior to incubation with the membrane at 4°C overnight. The blocking peptide for $P2Y_1$ (sc-15203P, N-16, Santa Cruz) was added at the same dilution (1:500) as the primary antibody and incubated on a shaking-incubator at room temperature for 60 minutes.

After incubation, the membrane was washed gently with1X TBS for 15 minutes at room temperature. This wash cycle was repeated for three times. After this, the secondary antibodies were diluted in 1X

TBS and 0.005% SDS to a final concentration of 1:5000and added to the membrane in a heat-sealed bag wrapped in aluminium foil and incubated at room temperature with gentle shaking for 45 minutes.

After the incubation, the membrane was washed with adequate amount of 1X TBS for three cycles of 15 minutes. During the wash, the box containing the membrane was covered using aluminium foil. Finally, the membrane was briefly washed in 1X TBS, before taken for scanning using the Odyssey LI-COR infrared imaging system (LI-COR Biosciences), following the manufacturer's instructions. The machine optical system uses a diode laser and solid-state detector for dual channel detection. Secondary antibodies conjugated with the IRDye 680 and IRDye 800 are detected at 685nm and 785nm excitation channels respectively.

2.2.7 Quantification of Protein

Protein quantification was performed using the Bradford assay (BioRad Laboratories) according to the manufacturer's instructions. Bovine Serum Albumin (BSA) (Promega) was used to prepare a standard curve of known concentrations. In addition, a 'blank sample' with ddH_2O was also prepared as negative control. The samples were incubated at room temperature for 15 minutes before measuring absorbances at 595.00 nm in a CARY 50 Bio UV Visible

Spectrophotometer (VARIAN); the 'blank sample' was used to calibrate to zero before measuring the sample absorbances. For each sample, the readings were taken three times, and the (mean ± s.e.m.) values were calculated.

After 6 replicate experiments, a graph of absorbances (Y) against protein concentrations (X) was drawn using the GraphPad Prism® software (version 5.0b). The relationship between absorbance and protein concentration was determined as:

Y = 0.00118 X + 0.0212

In subsequent experiments, protein samples were diluted 1:10 dilutions before measuring the absorbances. Concentrations were then calculated from the equation above by substituting the absorbances (Y); the dilution factor was also taken into account.

2.3 TISSUE CULTURE TECHNIQUES

2.3.1 Cell Culture

Wild type CHO.K1 cells purchased from the European Collection for Cell Cultures (ECACC) and two stable clonal cell lines generated by Dr Andrea Townsend-Nicholson were used in this work. The two clonal cell lines were hA_1-CHO cells (hA_1-24) transfected with the

wild type human A_1R[176], and G14T-CHO cells (G14T-13), which were transfected with a constitutively-active mutant G14T A_1R. In addition, transient transfection of the cells was also performed in order to carry out the Bimolecular Fluorescent Complement (BiFC) assay for the visualisation of the receptor interactions in living cells.

. All cells were cultured in either T_{75} or T_{175} tissue cultured flasks using a 50:50 v/v mixed medium of Dulbecco's Modified Eagle's Medium (DMEM, Sigma) and the Hams F12 (Sigma) supplemented with 10% fetal bovine serum (FBS) and 2mM L-Glutamine (Sigma). The medium was stored in the 4°C fridge for a maximum length of 6 weeks before replenishing the L-Glutamine. All cell manipulations were carried out in a Class II Laminar flow safety cabinet (Heraeus) under sterile conditions; the cells were grown in 5% CO_2 at 37°C in a humidified tissue culture incubator (Heraeus).

2.3.2 Passaging and Cell Counting

The cells were split and passaged further when at 100% confluence. The cells were first washed with Dulbecco's Phosphate-Buffered Saline (DPBS, Sigma) and detached for 2 minutes at room temperature using DPBS-EDTA buffer (DPBS containing 0.5mM EDTA).

After the cells were detached from the flask, approximately 1mL of the suspension were transferred into a clean 1.5mL Eppendorf test tube and counted using CASY Cell Counter and Analyser System

(INNOVATIS) according to the manufacturer's instructions. The cell numbers were determined based on the resistance measurement of pulse area analysis. Cell density measurements were performed in triplicate and the results took into account of the dilution factor, and gave cell number and viability.

2.3.3 Transient Transfection

The protocol for transient transfection was a modified version of the calcium phosphate method previously described[204]. The plasmid DNA used for transfection was purified via a large-scale preparation by the CsCl gradient method described in the Section 2.1.8.

Approximately 300,000 cells were seeded into a 10cm Petri dish, with 10ml complete culture medium..

The transfection was carried out the next day when the cells were about 80-90% confluent. 20μg of plasmid DNA was mixed with 50μL of 2.5M $CaCl_2$ and an appropriate amount of sterile ddH_2O to a final volume of 500μL. 500μL of 2X BBS (composition?) was added drop-wise to the mixture with gentle vortexing, and left for a 30-minute room-temperature incubation, before being transferred drop-wise onto the cells. The plate was gently swirled for even distribution of the DNA complexes, then placed in a container filled with 3% CO_2,

sealed and placed inside the 37°C tissue culture incubator for 18 to 20 hours. After this time, the medium was replaced with fresh medium, and incubated for a furhter24 hours.

2.4 SIGNAL TRANSDUCTION ASSAYS

The techniques used for the functional characterisation of A_1R:$P2Y_1R$ receptor heteromers were mainly cAMP assays, for estimating the responses through the G_i-coupled pathway, and the Fluorescent Imaging Plate Reader (FLIPR) assay, which monitors the intracellular calcium mobilisation through the G_q-coupled signalling pathways.

2.4.1 cAMP Assay

The cAMP assay performed is a modified version of the protocols described previously[205-207]. The assay is designed to measure the level of *de novo* cAMP production using metabolic pre-labelling with ^{3}H-8-adenine to produce ^{3}H-ATP, the substrate for adenylyl cyclase.

Cells were grown until 100% confluent, and washed with DPBS buffer. The cells weredetached with DPBS-EDTA and counted; they were then seeded in 24-well plates at a density of 400,000 cells/well, and grown to confluence.

Confluent cells were metabolically labelled prior to the cAMP experiment. The radiolabelled medium was prepared in a 50mL Falcon tube by adding 50μL of ^{3}H-8-adenine (PerkinElmer) to 25mL of cell culture medium containing 10mM HEPES (Sigma) in order to maintain the pH of the medium. The spent medium from the 24-well plate was discarded and replaced with 1mL/well of the ^{3}H-8-adenine containing tissue-culture media. The plate was then incubated at 37°C. After 2hours, the medium was discarded carefully into the radioactive sink and the cells were washed 2X with 2mL of Hanks Balanced Salt Solution (Sigma).

Following loading with the ^{3}H-8-adenine solution, the cells were incubated in the presence of a phosphodiesterase inhibitor (10μM Ro20-1724; Tocris) at 37°C for 30 minutes. When experiments involved the use of antagonists, they were loaded at the same time as the phosphodiesterase inhibitor and incubated for 30minutes at 37°C, to allow the antagonists to reach equilibrium. Forskolin (Ascent Scientific) was used at a final concentration of 10 μM and was added simultaneously with agonists. The final volume of the reaction components added to each well was ~1000μL. All ligand stock solutions were prepared at 100X concentration. Stock solutions of Ro20-1724 and Forskolin (Ascent Scientific) were prepared in 100% EtOH, as was the A_1R antagonist, DPCPX (Tocris). All adenosine receptor agonists were dissolved in 100% DMSO, whilst nucleotides and the P2Y$_1$R antagonists MRS 2179 and MG 50-3-1 were prepared

in DPBS. The reactions were allowed to proceed at 37°C for 10 minutes, and stopped by addition of concentrated hydrochloric acid (HCl) at 50μL/well, in the fume cupboard. The samples were taken for further chromatography through columns, or stored at -20°C, if not used immediately.

Samples were removed from each well, placed in a 1.5mL Eppendorf tube and centrifuged at 13,200 rpm to pellet the cell debris. The supernatant was added to a new tube and 50μL was removed to a 20mL scintillation vial (Packard), to which, 5mL of Ultima-Gold (Perkin Elmer) scintillation fluid was added. These vials were counted for 1 minute to determine the total ^{3}H in each well, in order to compare the loading efficiency across the 24-well plate. To the remaining supernatant in each Eppendorf tube, 50μL of pre-diluted ^{14}C-cAMP (approximately 2775dpm/50μL) was added, and samples were subjected to dual Dowex/Alumina column chromatography.

Chromatographic columns were prepared and stored as follows: For the Dowex 50 columns, a 50:50 slurry of resin was prepared in distilled water. To each of the pre-wetted Bio-Rad columns, 2.4mL of the AG®50WX4 cation exchange resin (Bio-Rad) was applied, and the column was then filled with 10mL of distilled water. These were then washed with 5mL of 1M HCl, followed by two repeated washes using 10mL of distilled water. The Dowex 50 columns were stored in a sealed Tupperware box containing distilled water. For the Alumina

columns, 0.6g of pre-weighed neutral alumina was applied to each Bio-Rad Poly-Prep column. The columns were then washed twice with 10mL 0.1M imidazole and stored in a box containing 0.1M imidazole. The columns were regenerated after each experiment as follows: Dowex 50 columns were washed with 7.5mL 1M HCl, followed by 20mL of distilled water, which was added as two aliquots of 10mL each; Alumina columns were washed twice with 10mL 0.1M imidazole before being re-stored. After 10 uses, the columns were stripped of any bound nucleotides as follows: 5mL of NaOH (0.1N) were added to each Dowex 50 column followed by a 10mL wash using distilled water. The columns were then regenerated as described previously; Alumina columns were stripped with 5mL of 0.1N NaOH, and washed three times with 10mL of imidazole (0.1M).

Samples were loaded onto the Dowex 50 columns. After allowing the liquid to drain completely through these ion-exchange columns, they were then washed with 2mL of distilled water for the elution of non-cyclic nucleotides, before being placed carefully on top of the Alumina columns. Bound cAMP was eluted from the Dowex column with 4mL of distilled water, and collected by the Alumina column underneath. The Alumina columns were then placed over a set of pre-labelled scintillation vials that were carefully aligned with the Alumina columns. Four millilitres of 0.1M imidazole were added into each of the Alumina columns and the eluted ^{3}H-labelled cAMP was collected in the vials. Optiphase 'HiSafe'3 (Perkin Elmer) scintillation

fluid was added at 15mL volume to each vial and mixed thoroughly. These vials were taken for 5 minutes counting through ^{3}H and ^{14}C channel program to quantify ^{3}H-cAMP and column efficiency, respectively. For the latter, three vials containing 50μL of ^{14}C-cAMP (GE Healthcare) were filled with 15mL of Optiphase 'HiSafe'3 scintillation fluid and counted using the same program as the elution products above, for both ^{3}H and ^{14}C levels to determine the total ^{14}C counts applied to the column.

The vials were counted using a beta scintillation counter (Tri-CARB 2900TR, Packard) and the results were analysed using Microsoft Excel and GraphPad Prism®. All radioactive ligand usages, including scintillation, solid and liquid disposal, were carefully logged.

2.4.2 Calcium Mobilisation Assay

The Fluorometric Imaging Plate Reader (FLIPR) is used for the intracellular calcium mobilisation assays through the use of a calcium sensitive dye, which upon binding to Ca^{2+} emits fluorescent signals. All experiments performed in this project used the Fluo-4 NW Calcium Assay Kit (Starter Pack with Buffer, Invitrogen™/ Molecular Probes®, F36206). The Fluo-4 dye is supplied with pre-treatment of acetoxymethyl esters, which provide high permeability through the cell membrane, and absorbs strongly at 488nm of the spectrum when excited by an argon-ion laser. Because of this strong absorption,

Fluo-4 exhibits high fluorescence emission, and is able to detect calcium concentration at a Kd of 345nM[208]. In the FLIPR assay, the Fluo-4 dyes were loaded according to the manufacturer's instructions, in an assay buffer containing HEPES, to maintain the optimal pH level at 7.3, and probenecid, to avoid anion exchange protein extrusion of the dyes. Use of FLIPR provides a real-time measurement of intracellular calcium mobilisations, thus ideal for GPCR signalling through the $G_{\alpha q}$-coupled pathways.

CHO cells (wild type and mutant cell lines) were grown in either a T_{75} or T_{175} tissue culture flask until 100% confluent, washed with DPBS and detached using DPBS-EDTA, as described previously. The cells were counted and appropriate cell numbers were resuspended in culture medium. 100μL of the suspension was loaded onto each well of a Microtest™ 96-well Assay plate (Optilux™, black/ clear bottom, TC surface, BD Falcon™, BD Biosciences), so that approximately 40,000 cells/well were seeded. The plates were incubated at 37°C until the appropriate confluence level was reached. Depending on the purpose of the experiment, the plates were assayed at either sub-confluent (the monolayer of cells occupying approximately 80% of the surface in each well) or over-confluent levels (the cells were incubated for one day after 100% confluence was achieved). The culture medium was flicked off and the cells were loaded with 100μL/well of the calcium-sensitive dye, initially for 30 minutes at 37°C with a further 30-minute incubation at room temperature. The

cells were protected from light during the loading procedure, using aluminium foil.

Agonists and antagonists were prepared as 10X concentrated stocks in DPBS and were loaded into separate wells of a clear V-shape 96-well PP-Microplate (Greiner Bio-one). Each well of the drug plate maintains about 15-30μL of 'dead space', where the aspiration of the liquid became difficult. Therefore, a sufficient volume of the ligands was prepared for each well of the drug plate to ensure that the correct volumes of drug were added to the cell plate. When used, antagonists were added at the beginning of the second 30-minute incubation of the dye, in order to reach equilibrium.

Most of the assays were performed using the FLIPR-1 machine (Molecular Devices, Sunnyvale, California). During the end of the project, this machine was decommissioned and replaced with the FLIPR® Tetra (Molecular Devices, Sunnyvale, California). Comparative assays showed that both machines yielded the same EC_{50} results for each ligand, although the absolute level fluorescence generated from each machines differed.

In preparation for data collection using FLIPR, the agonist plate was aligned with the 96-well cell plate, and placed in the FLIPR machine with the lids removed. The ligands were added by the machine using the internal robotic system, a 96-channel multi-pipetter. The agonists

were aspirated from each well of the 96-well drug plate at the same time, and simultaneously dispensed into each of the corresponding wells on the cell plate. In FLIPR-1, the fluid dispensing was achieved by a gas pressure system connected to an O_2 cylinder. This pressure enables fluid to be dispensed without pipette tips being immersed into the medium in the recipient plate. In FLIPR® Tetra, the fluidics do not use the gas pressure system, and the pipette tips were immersed into the medium during dispensing. FLIPR-1 used an argon ion laser, which generated a 488nm wavelength light for the excitation of the calcium-sensitive dye. FLIPR® Tetra uses an LED excitation system. The fluorescent signals were emitted from the dye following excitation and were passed through an emission filter (510-570nm for FLIPR®-1 and 515-575nm for FLIPR® Tetra). These emission filters were connected to the CCD camera located underneath the cell plate and fluorescent signals were collected every second. Normally, experiments ran for 180 seconds; the first nine seconds established the assay baseline and the agonists were added at the tenth second. The change in the fluorescent levels in each of the 96 wells of the plate, following agonist stimulation, were recorded simultaneously by the CCD camera and the output was sent to a PC coupled to the FLIPR.

Depending on different machines, the CCD camera has a specific saturation level. Above this level, the camera will fail to resolve the fluorescence changes. For this reason, at the beginning of the assay,

the camera exposure length, shutter speed and the laser power were adjusted based on the initial fluorescence levels before the agonist activation, in order to obtain optimal signal detections. Experimental data were downloaded in Microsoft Excel format for analysis. The raw data generated by the PC give fluorescence in arbitrary units, as time sequences. The results, following analysis, were expressed as the ratio of the maximal fluorescence level change relative to the basal fluorescence (F/F_0 ratio).

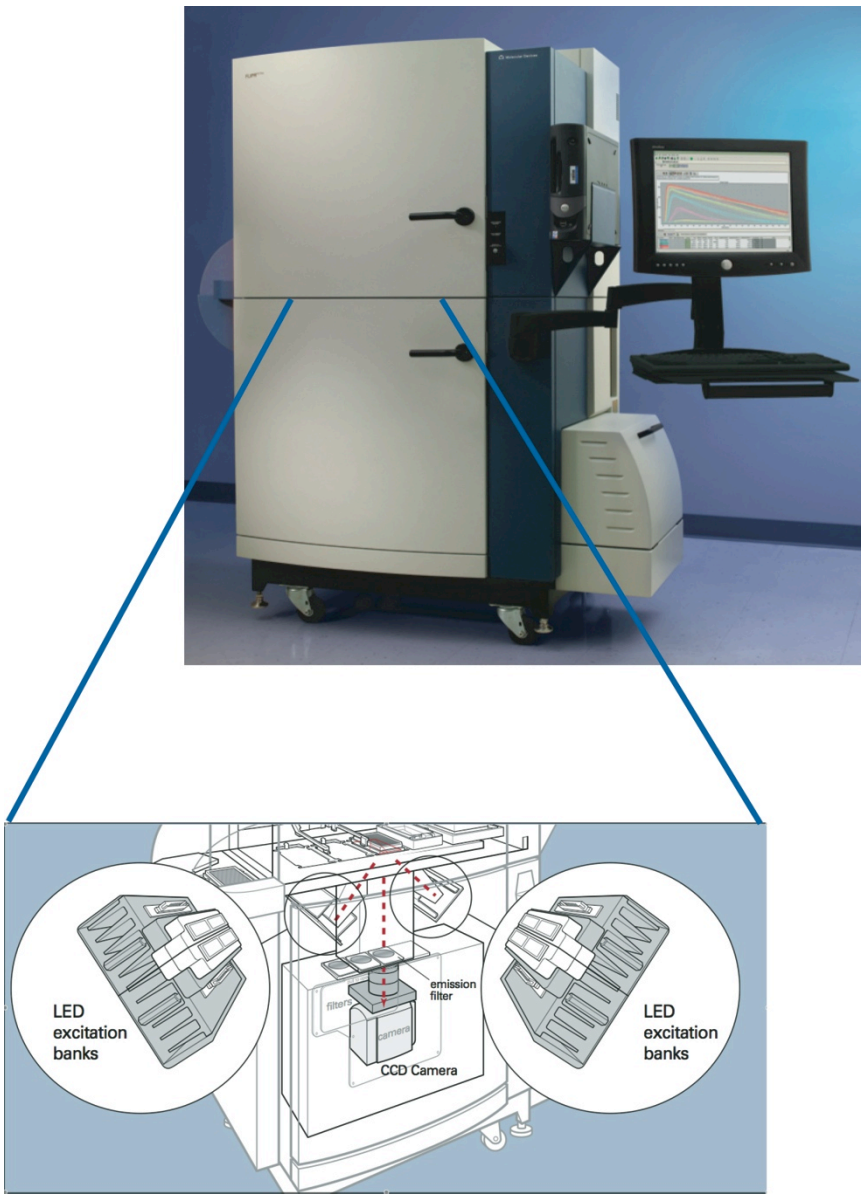

Figure 3. The image of a FLIPR® Tetra machine. (The modified picture resource was originally provide by Molecular Devices)

The upper chamber of FLIPR, where the drug and cell plates are placed, holds a platform for the assay. It also contains an internal robotic pipettor system, which automatically transfers fluids across the plates. The lower chamber of the machine is where the LED and camera are placed. During the experiment, the light source comes from the two LED diodes from the bottom of the plate, and the fluorescence emitted is then captured by the CCD camera located underneath.

2.5 DATA HANDLING

2.5.1 Pharmacological Analyses

The FLIPR assay data analyses were carried out using Microsoft Excel and GraphPad Prism® (V.5.0b). Excel was used for the primary calculations from the raw data obtained from the FLIPR machine, whereas Prism® was used for further pharmacological analysis, including the Hill transformations for EC_{50} analysis, and for plotting the figures. For most experiments, the data analysis was straightforward. However, the algorithm for the Hill transformations is based on the assumption of a monophasic concentration-response curve. For biphasic curves, an additional analysis was required, which involved isolating each of the two phases from the same curve, as described below.

When performing the Hill-transformation for the monophasic curves (CHO.K1 ADP concentration-response curve as an example, Figure 4a), the Y_{max} value was entered for the software calculations. This number was chosen as the calcium response at the highest concentration of agonist (Log [ADP] = -4) as, in theory, the highest concentration of ligand is expected to yield the greatest response. Occasionally, it was necessary to use a value from a lower concentration, typically -5.

The transformed data from a typical experiment are presented in Figure 4b. A linear regression line was plotted through the data

points located on the linear part of the concentration-response curve and the intercept with the X-axis represents the $logEC_{50}$ of the ligand (Figure 5). For all analyses, the ranges of linearity for transformed and untransformed data were compared to ensure that they matched, prior to calculating the EC_{50}, as discordance between these two sets of data would cause a shift in the slope of the linear regression line, giving a less accurate estimate of the EC_{50}. As can be seen in Figure 4b, the linear region of the transformed data (left panel) ranges from Log [ADP] = -5.5 to -8.5, whereas the linear portion of the concentration-response curve (Figure 4a) ranges between -6.5 and -8.5. Therefore, the linear regression line was drawn from -6.5 to -8.5 according to the original data.

This approach is valid for the estimation of single-site concentration-response curves because Prism uses an algorithm for the Hill transformation that is based on the assumption that the curve is monophasic. However, the analysis of biphasic-response curve requires a different approach. In the example shown in Figure 6, the biphasic curve can be considered to consist of two single monophasic curves, each of which has a Y_{max} value (Figure 6a). For the high affinity component, the Y_{max}-2 value was entered for the Hill-transformation, instead of Y_{max}-1. The linear region of this part of the curve was defined as described previously in Figure 4, and a linear regression line was plotted. Using this methodology, the $logEC_{50}$ value obtained for the high affinity component was -7.651, which was

consistent with that obtained by the curve estimation. For the low affinity part of the biphasic curve, the component was first extracted from the whole curve. These data were then normalised so that the largest value in the data set was set as 100% and the smallest value in the data was set as 0%. In case of errors, specific values were defined as either 100% or 0%. These were usually the mean value at a specific concentration point. The Hill-transformation and $logEC_{50}$ determination were carried out as described previously. The calculated $logEC_{50}$ of ADP at the low affinity site was -5.375, which was close to that estimated from inspecting the concentration-response curve.

The application of this methodology is necessary in order to obtain accurate calculations of EC_{50} values for the two components of a biphasic curve. If the Hill transformation was carried out using a Y_{max} value that corresponds to the response value at the highest ligand concentration, then, as shown in Figure 6b, the resulting $logEC_{50}$ values would be approximately -7.0 and -5.25 for the higher and lower affinity sites, respectively.

The reason for this is because the software needs to define a curve before performing any calculations. To do that, it always assumes a monophasic concentration-response curve and defines the curve based on the maximum and minimum response values. For the biphasic curve Hill-transformation, in order to perform a more

accurate calculation, Prism® extrapolates and extends both components for two complete curves, until both definitive values were satisfied for the equation. Therefore, for the high-affinity component of the curve, when the Y_{max}-1 value was used, the software extended the curve upwards until the Y_{max}-1 value was reached. Whereas, on the low-affinity component, although the Y_{max}-1 entered was true, the minimum response did not match the lowest point set by the software. It was extrapolated downwards as a theoretical curve, which has its minimal value same as the software default. In both cases, the $logEC_{50}$ values calculated from these two theoretical curves were shifted from the true values, hence inaccurate (Figure 7).

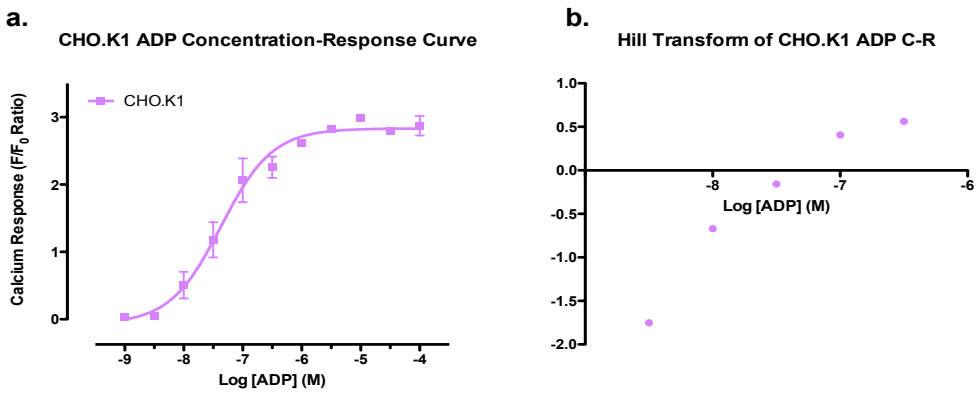

Figure 4. The Hill-transformation of the ADP concentration-response curve data revealed different linearity ranges from the untransformed data

a The ADP concentration-response curve in CHO.K1 cells. The curve showed a typical monophasic sigmoidal shape that has a linear concentration-dependent increase region between Log [ADP]= -6.5 and -8.5. ***b*** The Hill transformation calculated by GraphPad Prism® using the mean Ymax value at Log [ADP]= -4, which gives the maximal response. According to these transformed data, the linear part of the curve ranges between Log [ADP]= -5.5 to -8.5.

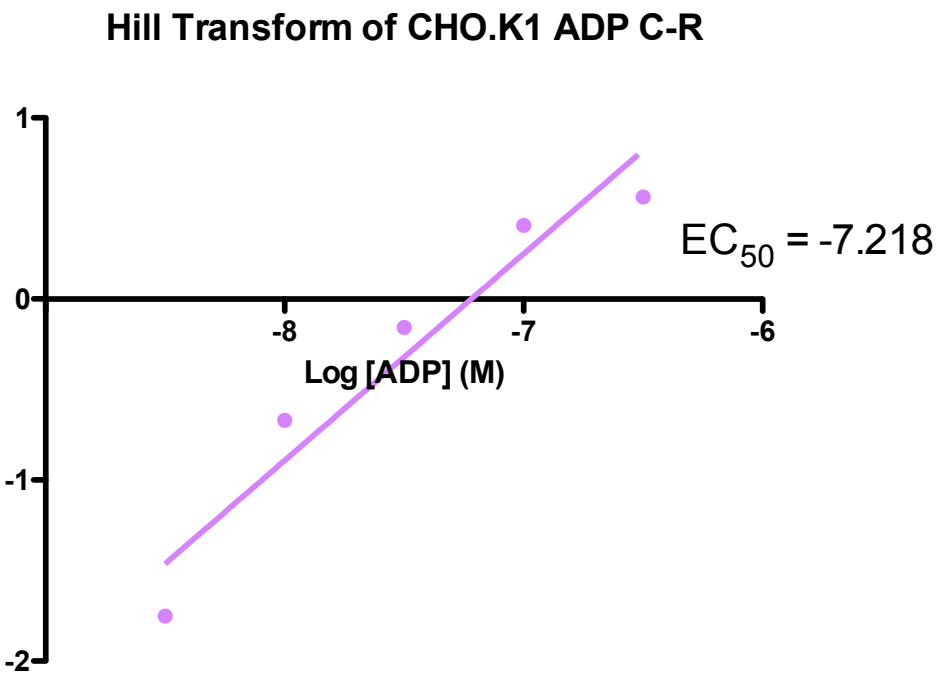

Figure 5. The definition of the linear region for the transformed data

The linearity was defined with comparison to the untransformed data, which confirmed on the region between Log [ADP] = -6.5 and -8.5. A linear regression line was draw for the logEC50 calculation. This number was represented by the intercept value on the X-axis.

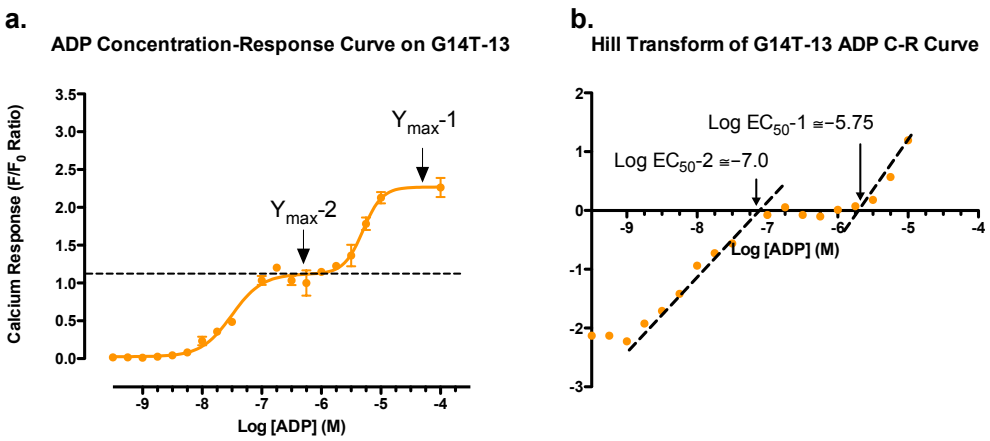

Figure 6. Hill-transformation for a biphasic curve needs to adapt a different methodology from the conventional method used for monophasic curves

a The biphasic concentration-response curve can be divided into two single mono-phasic curves each has their own Y_{max} values. ***b*** Hill transformations obtained using the Y_{max}-1 value at Log [ADP] = -4. The results resulted in incorrect logEC_{50} values of approximately -5.75 and -7.0 for the lower and higher affinity component of the curves, respectively.

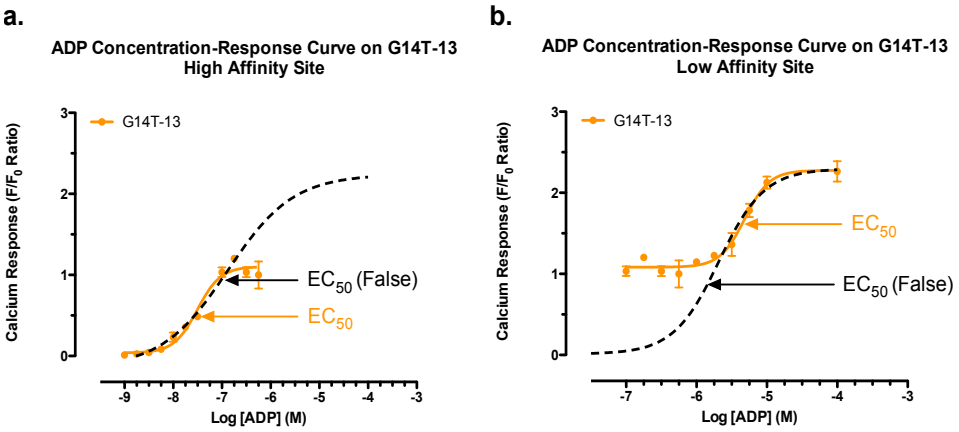

Figure 7. GraphPad Prism® software extent and extrapolate both component of the biphasic curve, result in the two complete theoretical curves

The software performs calculation upon a defined curve, which is characterised by its maximum and minimum values. When the Y_{max}-1 value (Figure 3a) was used, the two components of the biphasic curve were each extended into a complete curve.

a The high-affinity component was extrapolated upward when entered the Y_{max}-1 value, hence EC_{50} calculated from this theoretical curve was inaccurate. ***b*** The low-affinity component was extrapolated downwards until the minimum value defined by the software, therefore, the EC_{50} calculated was not accurate.

2.5.2 Statistical Analyses

All data represented a minimum of three experiments performed in triplicate, expressed as the mean $\pm$ s.e.m. Analyses of statistical significance were performed using GraphPad Prism. The Student-t test (two-tailed, 95% confidence interval) was primarily chosen as the most suitable model for comparing the differences in the mean values. Depending on the nature of each experiment, the paired t-test was performed where necessary.

Chapter 3

cAMP Responses via the A_1R:$P2Y_1R$ Receptor

3.1 INTRODUCTION

The $G_{\alpha i}$ – coupled pathway is stimulated via A_1 adenosine receptor activation, resulting in the inhibition of the enzyme adenylyl cyclase and leading to a decrease in the production of intracellular cAMP. The quantification of *de novo* cAMP synthesis and accumulation can be achieved by a cAMP assay based on the use of [8-^{3}H]-labelled radioactive adenine as a precursor. Foskolin, which directly activates adenylyl cyclase, is used to elevate the basal cAMP level in the cell line being studied in order to detect $G_{\alpha i}$-mediated inhibitory responses.

As described in Chapter 1, a physical interaction between the A_1 adenosine receptor and the $P2Y_1R$ has been identified in various tissues. Functional responses that may resulted from heteromeric A_1R:$P2Y_1R$ receptors have also been observed, whereby the $P2Y_1R$ agonist ADPβS is able to induce an A_1R-dependent pertussis toxin-sensitive $G_{\alpha i}$ response, significantly reducing the forskolin-stimulated

cAMP accumulation in a concentration-dependent manner. Further, this nucleotide-induced $G_{\alpha i}$ response can be blocked by DPCPX, an A_1R antagonist. These findings were based on a recombinant expression system, where both heteromeric partners were expressed at high levels in human embryonic kidney HEK293T cells, which lack A_1R, but endogenously express $P2Y_{1, 2}$ and $P2Y_4$ receptors.

This chapter aims to identify and characterise A_1R:$P2Y_1R$ heteromers activated by endogenous ligands that form when the two interacting receptor proteins are expressed at physiological levels of expression. This will be achieved using clonally-selected, stably-transfected cell lines established in the parental CHO.K1 cell line, which expresses endogenous $P2Y_1$ and $P2Y_2$ receptors but does not express any adenosine receptor subtypes. To provide a direct comparison between the results obtained from physiological and overexpressing receptor systems, the metabolic pre-labelling cAMP assay will be performed in the same buffer composition as used in the study that first reported the existence of functional A_1R:$P2Y_1R$ heteromers. These experiments will be carried out using two clonal CHO.K1 cell lines that were previously established in the laboratory: hA_1-24 (B_{max} = 45,800 $\pm$ 2,900 receptors/cell) and G14T-13 (B_{max} = 203,900 $\pm$ 5,300 receptors/cell).

In initial experiments performed in the laboratory (A. Townsend-Nicholson, personal communication), it was observed that hA_1-24

cells failed to respond to ADPβS, yet the constitutively-active cell line G14T-13, which expresses a form of the A_1R where the Glycine at position 14 has been replaced by Threonine, yielded a significant $G_{\alpha i}$ response. Since the original identification of the functional heteromer was conducted in a highly-expressed recombinant cell line, it is possible that there were constitutively active A_1R present. The G14T-13 cells were, therefore, pursued as the model system for the characterisation of the cAMP responses via the A_1R:$P2Y_1R$ heteromeric receptor and it was noted that constitutive activity of the A_1R may be required for the nucleotide signalling through the heteromeric receptors.

3.2 Forskolin Responses in the CHO.K1 and G14T-13 Cell Lines

As a starting point for the cAMP experiments, the constitutive activity of the G14T mutated form of the A_1R was investigated by comparing forskolin responses in the wild-type CHO.K1 cells with the forskolin responses obtained in the G14T-13 cells. The production of cAMP via direct stimulation of adenylyl cyclase should be significantly reduced in a cell line expressing constitutively-active $G_{\alpha i}$-coupled receptors. Therefore, a forskolin concentration-response curve was obtained for each cell line and the results were compared.

As shown in Figure 8, forskolin induced a concentration-dependent accumulation of cAMP in the CHO.K1 cell line (n=3 experiments, each performed in triplicate). Cyclic AMP production (8-[^{3}H]-cAMP) is expressed as the number of disintegrations per minute (DPM). The response takes effect from approximately 1μM forskolin (Log [Forskolin] = -6) and was still increasing at 100μM, the highest available concentration that could be applied to the assay. At this concentration, 12319 ± 720 DPM of cAMP were produced. The basal cAMP level (in DPM) of the cells was 48 ± 22 DPM. In CHO.K_1 cells, the calculated potency of forskolin is approximately 11.07μM ($logEC_{50}$ = -5.00 ± 0.04).

The response of G14T-13 cells to forskolin stimulation (n=3 experiments, each performed in triplicate) is shown in Figure 9, and the nature of the response is similar to that seen in CHO.K1 cells. The addition of increasing amounts of forskolin produced a sigmoidal concentration-response curve with 100μM forskolin generating 11677 ± 239 DPM of cAMP in G14T-13 cells. The EC_{50} was 8.11μM ($logEC_{50}$= -5.10 ± 0.04) in this cell line. The basal level is at 228 ± 113 DPM, approximately five times higher than CHO.K1 cells. There is no statistically significant difference in the forskolin potency (p= 0.2342) between the CHO.K1 and G14T-13 cell lines nor is there a significant difference in the maximum response obtained at 100μM forskolin (p= 0.4665).

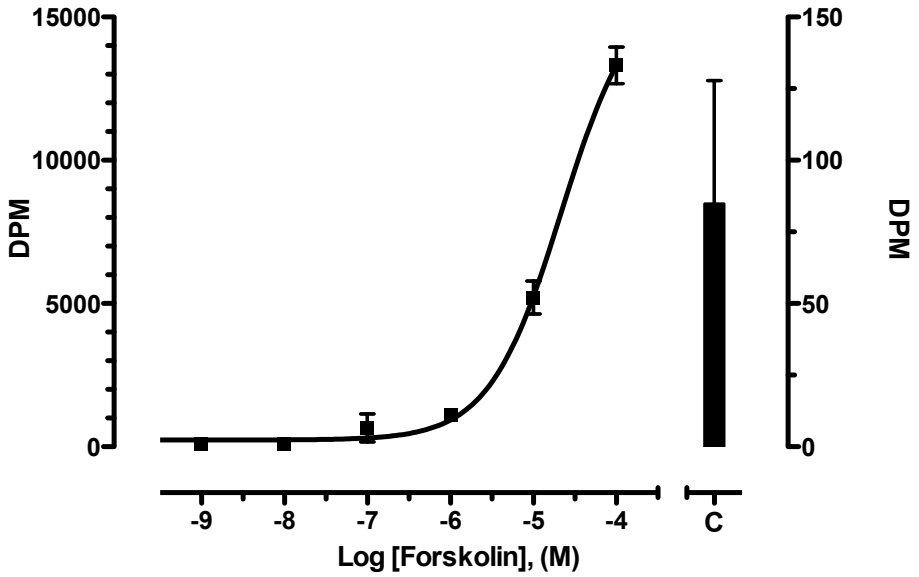

Figure 8. The forskolin concentration-response curve in CHO.K1 cells. A single representative experiment showing the response of CHO.K1 cells to increasing concentrations of forskolin. Left axis: cAMP production in response to forskolin (in disintegrations per minute (DPM)). Right axis: C = basal levels of cAMP in the absence of forskolin-stimulation. Three independent experiments were performed in triplicate, and the EC_{50} = 11.07μM ($logEC_{50}$ = -5.00 ± 0.04).

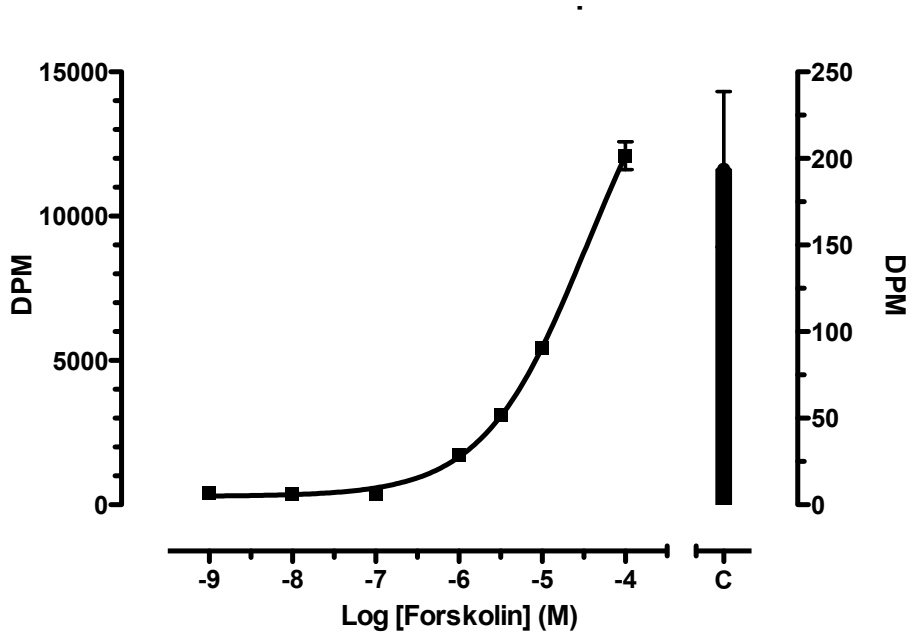

Figure 9. The forskolin concentration-response curve in G14T-13 cells

A representative experiment showing the response of G14T-13 cells to increasing concentrations of forskolin. Left axis: cAMP production in response to forskolin (in disintegrations per minute (DPM)). Right axis: C = basal levels of cAMP in the absence of forskolin-stimulation. Three independent experiments were performed in triplicate, and the EC_{50} = 8.11μM ($logEC_{50}$= -5.10 ± 0.04).

In order to carry out further comparisons between the two cell lines, the level of increase in the forskolin response over the basal cAMP concentration was adapted as an index, i.e. fold increase over basal, and analysed at each concentration point. As Figures 8 and 9 have shown, even in a single experiment (in triplicates) the value for the basal cAMP concentration carry a significant amount of error. Compared between all three experiments, the mean value of basal response also vary significantly, such that the s.e.m. is approximately 50%. For CHO.K1 and G14T-13, these are 48 ± 22 DPM and 228 ± 113 DPM respectively. The main reason to this phenomenon could be due to the contribution of residue cAMP in the Dowex 50 and Alumina columns. Since the basal cellular cAMP levels were expected to be very low, these extra amounts of cAMP bring variations, which would seem to be very large to a relatively small scale of total cAMP level. Therefore, statistically it seemed relatively more reliable to use the total mean basal cAMP level from all three independent experiments as a defined value for all three set of data, instead of using the value from each single experiment. In other words, the total mean basal cAMP level will be obtained from the three sets of data representing three independent experiments. The result of which serves as the mean cAMP level for all three experiment. Subsequent calculation of fold increase over basal at each concentration point should be reference to this figure.

As shown in Figure 10, it seemed that the CHO.K1 cells elicited a much higher level of response to forskolin between 1μM and 100μM concentrations. Table 4 showed the exact value at each concentration points. CHO.K_1 cells promoted a 257.4-fold increase in cAMP at 100μM forskolin, whereas there is only a 51.1-fold increase in cAMP produced by the G14T-13 cells: a difference between the cell lines of approximately five folds. However, such difference persisted only between concentration points that fall into the linear increasing region of the dose-response curve: between 10μM and 100μM. As mentioned previously, the basal cAMP in G14T-14 cells is approximately five times the level in CHO.K1. Therefore, it can easily be argued that the observed difference between the two dose-response curves may due to the difference in basal cAMP concentration.

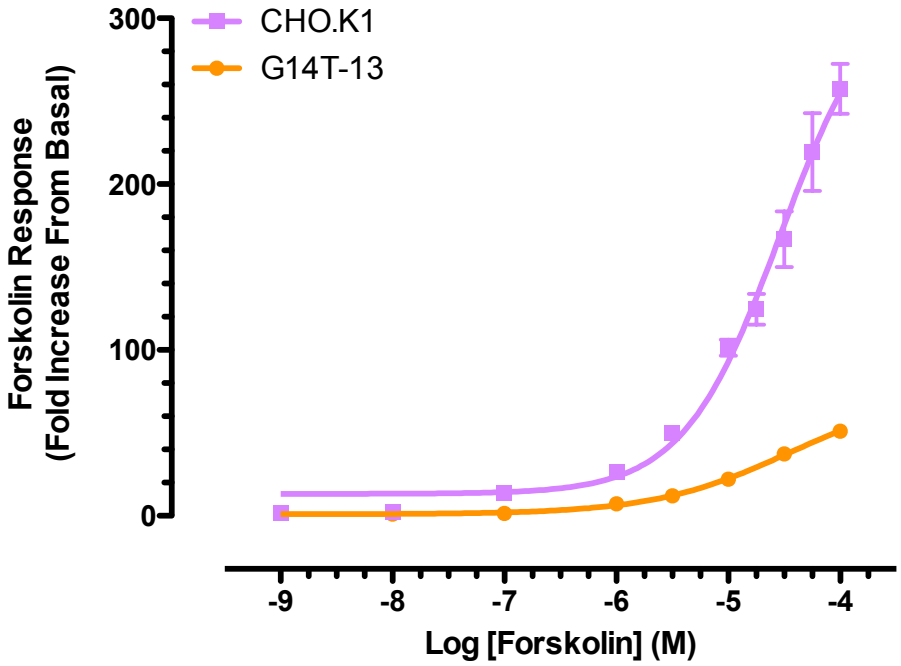

Figure 10. Forskolin responses in CHO.K1 compared with G14T-13.

The forskolin response is expressed as the fold increase of the cellular cAMP level over basal for each concentration of forskolin tested. The figure represents the mean of three independent experiments each performed in triplicate. There is no statistically significant difference in forskolin potency between the two cell lines shown.

Log [Forskolin] (M)	G14T-13		$CHO.K_1$	
	Mean	SEM	Mean	SEM
-4.00	51.12	1.047	257.4	15.04
-4.25	-	-	219.4	23.45
-4.50	37.27	2.303	166.9	16.78
-4.75	-	-	124.5	9.278
-5.00	22.01	1.214	101.4	4.783
-5.50	12.05	0.9574	49.79	4.064
-6.00	7.177	0.2510	26.67	2.819
-7.00	1.416	0.1976	13.75	0.0000
-8.00	1.059	0.3114	2.119	0.0000
-9.00	1.757	0.0000	1.709	0.0000

Table 4. Forskolin responses in CHO.K1 compared with G14T-13.

The numerical data plotted in Figure 10 are shown in this table and are expressed as the mean ± s.e.m.. The level of cAMP accumulation produced in $CHO.K_1$ cells was approximately 5-fold higher than that produced in G14T-13 cells, between Log [Forskolin]= -4 and -5 (10μM and 100μM). These concentration points are on the linear portion of the curve.

3.3 ADENOSINE RECEPTOR AGONISTS ELICIT A $G_{\alpha i}$ RESPONSE IN G14T-13 CELLS

In the previous experiments, the G14T-13 cell line did not display a significant constitutive activity of the G14T mutant A_1 adenosine receptor in comparison to the wild type CHO.K_1 cell line. This could be due to various reasons. Nevertheless, it is crucial to confirm whether this mutant receptor is functional to the A_1R agonist stimulations. As explained previously, the $G_{\alpha i}$ signalling pathway results into the reduction in the intracellular cAMP level; forskolin, which is a ligand that exerts direction stimulatory effect on the adenylyl cyclases, serves as a suitable elevator of the basal cAMP concentration in cells, which will then enable more accurate detection of the agonist-induced $G_{\alpha i}$ responses. The EC_{50} of forskolin was approximately 10μM (log EC_{50}= -5) in both cell lines. At this concentration, the response was on the linear portion of the concentration-response curve. Therefore, this concentration (10μM) was used in the subsequent experiments to elevate the basal control cAMP level for the characterisation of pharmacological responses.

In an initial characterisation, the responses of G14T-13 cells to several nucleoside agonists were determined (n=3 experiments, each performed in triplicate). The four adenosine receptor agonists used were CPA, NECA, R-PIA and 2-CADO. As shown in Figure 11, each agonist, when used at 1μM was able to inhibit the forskolin

response significantly (by approximately 82% in all cases) in G14T-13 cells. There was no significant difference between all of the four agonists tested. The basal cAMP level in the cell was 1.54 ± 0.50% of the 10μM forskolin response. The levels of cAMP produced in the presence of each of these agonists was 16.39 ± 1.84% (CPA), 14.37 ± 1.35% (NECA), 15.35 ± 2.12% (R-PIA) and 18.00 ± 0.50% (2-CADO), corresponding to inhibitions of 84%, 86%, 85% and 82% for CPA, NECA, R-PIA and 2-CADO, respectively.

In order to confirm the response was indeed through the $G_{\alpha i}$-coupled A_1R, the same experiment was repeated in the parental wild type CHO.K1 cell, which lacks A_1R. Figure 12 shows that at 100μM, the highest available concentration for the assay, none of the nucleoside agonists showed any significant effect on the forskolin-stimulated cAMP accumulation. This proved the agonist responses were indeed produced through A_1Rs

Even though in the previous section the G14T mutant receptors failed to display any significant constitutive activity to the forskolin-induce cAMP accumulation, it is necessary to scrutinise further in the agonist response compared to a wild-type A_1R. Such experiments will provide invaluable data for the level of G14T A_1R constitutive activity through a direct comparison with a wild-type A_1R, since in theory, it is expected that a cell line expressing the constitutively active A_1Rs may possess a higher potency and/ or efficacy level for

the same agonist. Amongst the agonists screened, CPA has frequently been used as a selective A_1R agonist, and there is a good amount of data on the effects of CPA on A_1 receptor activity in different species and cell types available for comparative purposes. In addition, the G14T constitutive actively was also tested using CPA, as published in the original paper. Based on this reason, the pharmacology of CPA was further examined in the G14T-13 and hA1-24 cells.

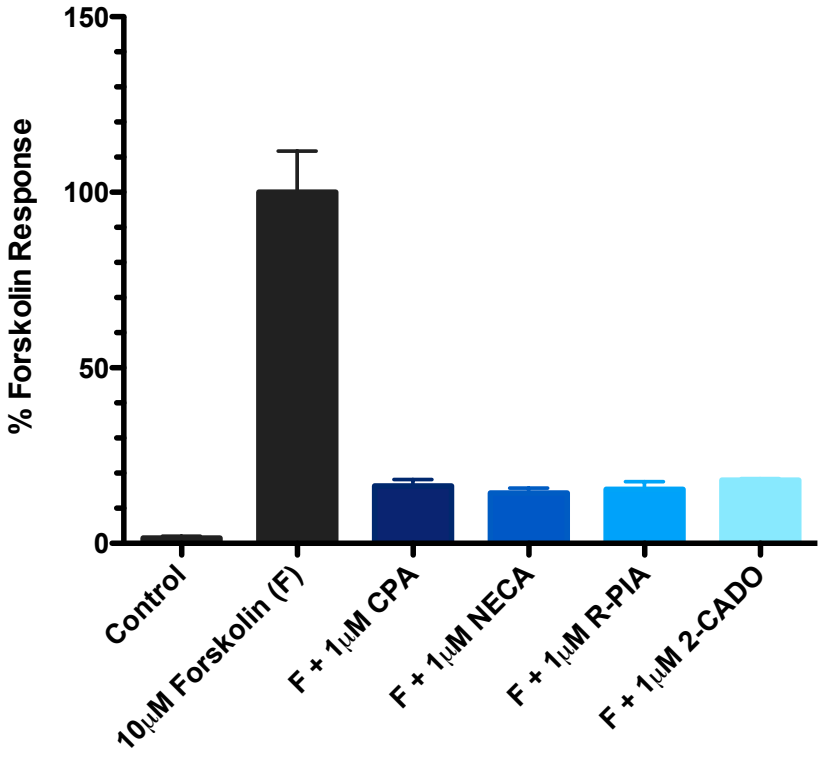

Figure 11. Inhibition of forskolin-stimulated cAMP accumulation by nucleoside analogues in G14T-13 cell

Four different adenosine receptor agonists were tested: CPA, NECA, R-PIA and 2-CADO, each at 1μM. The cAMP response has been expressed as a function of the response to 10μM forskolin. All of the four agonist induced inhibition to the forskolin response, indicating the G14T mutant receptor is functional. Data represent the mean $\pm$ s.e.m. of a representative experiment performed in triplicate.

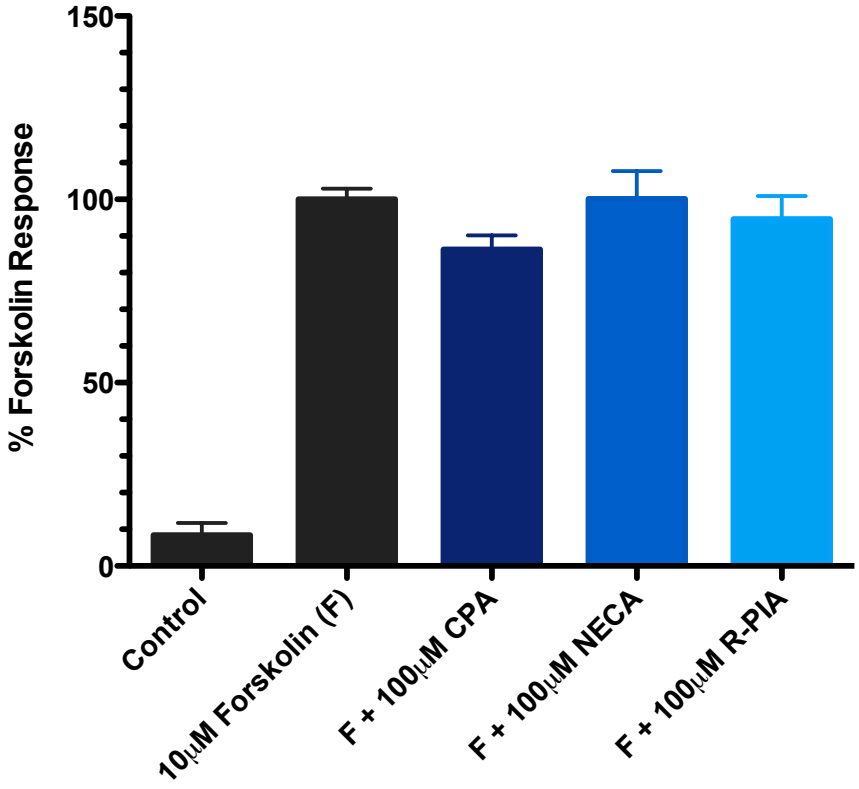

Figure 12. Inhibition of forskolin-stimulated cAMP accumulation by nucleoside analogues in CHO.K1 cells

Four different adenosine receptor agonists were tested: CPA, NECA, R-PIA and 2-CADO, each at the maximum final concentration possible, 100μM. The cAMP response has been expressed as a function of the response to 10μM forskolin. In the absence of A_1R, none of the agonists used induced any inhibitory response to forskolin. Data represent the mean $\pm$ s.e.m. of a representative experiment performed in triplicate.

Figure 13 shows the concentration-response curve for CPA on forskolin-stimulated adenylyl cyclase activity in G14T-13 cells (n=3 experiments, each performed in triplicate). The left side of the X-axis shows the 10μM forskolin stimulated cAMP response (F), which has been set to 100% and used for the normalisation of the data shown in the graph. The basal level of cAMP (C) is approximately 6.99 ± 1.37%, compared to the forskolin-stimulated level of cAMP (F), which means that 10μM forskolin elevated the cAMP approximately 14.3 folds. At the highest CPA concentration, 10μM, the cellular responses to forskolin were suppressed to 18.84 ± 0.87 % and the curve had plateaued; there was no further reduction in the cAMP level. The response to CPA at 1pM was 93.32 ± 4.59 % of the 10μM forskolin indicating the inhibitory effect was no longer significant. The CPA curve showed a monophasic concentration-dependent trend, with decreasing cAMP production (and, conversely, increasing adenylyl cyclase inhibition) as the agonist concentration increases. The potency of CPA is approximately 5.62nM ($\log EC_{50}$ =-8.28 ± 0.10).

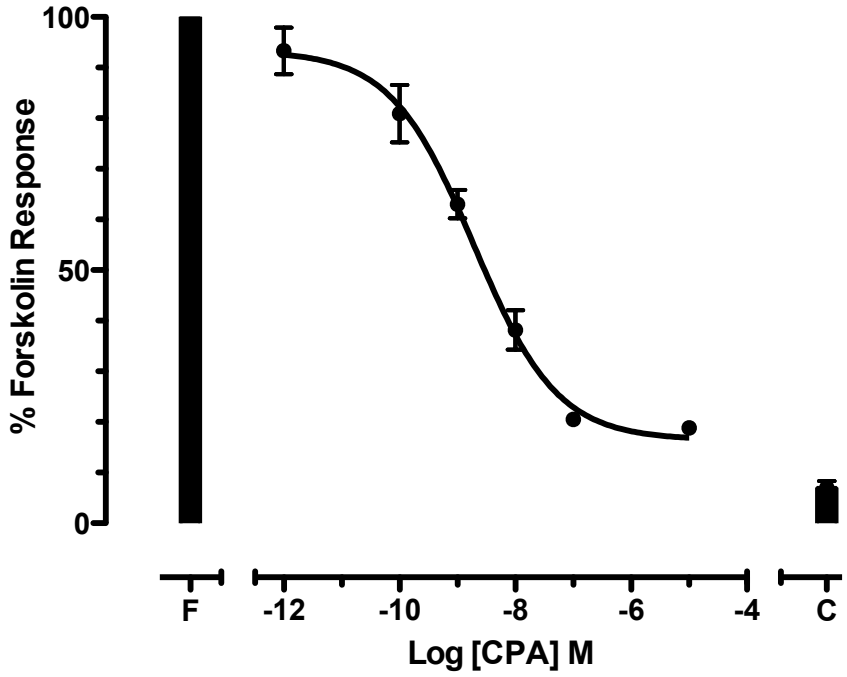

Figure 13. CPA inhibits forskolin-stimulated cAMP accumulation in G14T-13 cells

The accumulation of cAMP was stimulated by the addition of 10μM forskolin (F) and the effect of increasing concentrations of CPA was determined. The basal level of cAMP in un-stimulated cells is approximately 6.99 ± 1.37% of the forskolin responses, as shown in (c). The potency of CPA is approximately 5.62nM ($\log EC_{50}$ =-8.28 ± 0.10). Data represent the mean $\pm$ s.e.m. of three experiments, each performed in triplicate.

The same experiment was repeated in hA_1-24 cells, which express the wild-type A_1R and, as previously mentioned, did not appear to possess a 'functional heteromeric receptor' signalling properties ($P2Y_1R$ agonist ADPβS failed to elicit a $G_{\alpha i}$-coupled response).

Figure 14 showed the CPA concentration-response curves compared between the hA_1-24 cells (n=3 experiments, each performed in triplicate), and G14T-13 cells. The basal cAMP level (C) in the hA1-24 cells is not significantly different from the G14T-13, and is about 6.82 ± 0.77 % compared to the 10μM forskolin responses (F), which had elicited an approximately 14.6-fold increase in cAMP production. When applied at the highest concentration, 10μM, CPA resulted only 21.78 ± 3.44 % of response, which corresponds to a roughly 78% inhibition in the forskolin-stimulated cAMP elevation. When only 1pM of CPA was applied, the inhibitory effect was approximately 102.4 ± 8.0 % compared to the forskolin response i.e. the effect was no longer significant. The curve, like that of the G14T-13 cells, is a concentration-dependent monophasic curve and the potency level of CPA in hA_1-24 cells was approximately 10.2nM (Log EC_{50} =-7.991 ± 0.114). Compared between the two cell lines, CPA exhibited no significant difference in its potency levels. However, at Log [CPA]= -7 and -9, there is a statistically significant reduction in the percentage forskolin response in G14T-13 cells compared with hA_1-24. At 10nM (Log [CPA]= -8), the responses were not significantly different, but might due to the relatively larger errors. This is an experiment demonstrating the functional wild-type A_1R responses.

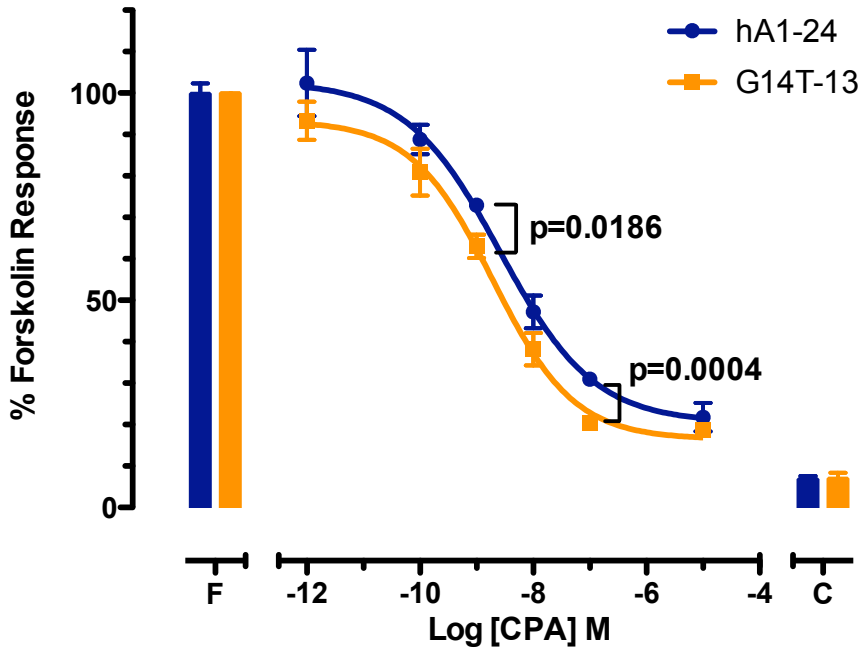

Figure 14. A comparison of the CPA inhibition of forskolin-stimulated cAMP accumulation in hA1-24 cells versus G14T-13 cells.

The accumulation of cAMP was stimulated by the addition of 10μM forskolin (F) and the effect of increasing concentrations of CPA was determined. The basal level of cAMP in un-stimulated cells is shown (C). Data represent the mean $\pm$ s.e.m. of three experiments, each performed in triplicate. The results for hA_1-24 are shown in orange and G14T-13 in blue. At Log [CPA]= -7 and -9, the CPA response in G14T-13 is statistically significantly different ($p<0.05$) from the response in hA_1-24 cells, as indicated by the p-values. The EC_{50} calculations showed the potency of CPA in both cells lines are approximately the same.

3.4 ADP/ ADPBS CONCENTRATION-RESPONSE CURVE

Previously, as first identified by the Nakata group, ADPβS the non-hydrolysable ADP analogue, had shown the signalling response via $G_{\alpha i}$ in an over-expressed recombinant cell system for both A_1R and $P2Y_1R$. Such effect was being referred to, in this project, as a 'functional A_1R:$P2Y_1R$ heteromeric receptor' response, since the result of which could most likely due to the heteromerisation process that creating a new receptor and pharmacology. Preliminary experiments performed in the laboratory (personal communication Dr Andrea Townsend-Nicholson) using ADPβS did not produce the same responses in the hA_1-24 cell line, but were obtained in the G14-13 cells, which were stably transfected with the constitutively-active G14T mutant A_1R. This has led to consideration of the possible effect of A_1R constitutive activity on the heteromeric receptor signalling. One reasonable argument being that the over-expressed recombinant system may result into the A_1R constitutive activity to certain extent, since the GPCRs are constantly in conformational changes between the active and inactive states.

In order to answer this question, further investigate in the functional heteromeric responses were conducted in G14T-13 cells. It was originally designed to examine the ADPβS concentration-response relationship prior to the analysis of antagonistic effects (both A_1R and $P2Y_1R$ antagonists). The experiments were started using various

concentrations of ADP β S, ranging from 10pM to 100μM (-8 to -4 in logarithmic scale), the responses of which were measured in the presence of 10μM (-5 log concentration scale) forskolin.

Unfortunately the experiments using the ADP β S ligands did not succeed. Figure 15 (A) had shown examples of two trial tests, both of which were performed in triplicates, attempted to determine the dose-response curve for this ligand. These data represents numerous repetitive trials. Responses of ADP β S were transformed and normalised to the 10μM forskolin response, and expressed as '% Response of 10μM Forskolin'. The results were not consistent such that: 1) it is not clear whether ADP β S exhibit any stimulatory effect on the A_1R-coupled pathways; 2) whether ADP β S response (if any) is concentration-dependent.

As the Trial-1 data ($n \geqslant 3$, each in triplicates) had revealed, ADP β S did not exert any significant effect to the forskolin-stimulated cAMP accumulation process at concentrations below 100μM (One-Way ANOVE, Tukey's Test): the levels of responses were very similar to 10μM forskolin. At 100μM, ADP β S significantly lowered the cAMP level for approximately 20% (One-Way ANOVE, Tukey's Test).

On the other hand, Trial-2 results ($n \geqslant 3$, each in triplicates) showed that ADP β S takes effect at all concentrations, that the levels of cAMP production were significantly reduced (One-Way ANOVE,

Tukey's Test). Despite of that, there was no clear concentration dependence of the inhibitory response by ADP β S (One-Way ANOVE, Tukey's Test).

The above data were the results of numerous trials and practices. It was initially attributed to the imperfect performance of the cAMP assay techniques, which might have led to large data errors and fluctuations (figures are not shown here). Therefore, subsequent intense practices were followed in order to enhance the technique, so that the magnitudes of errors for each triplicated sample were greatly reduces. In addition, at least three batches of the ADP β S ligand (from the same or different companies) had been screened in this project, due to the presence of very strong sulphurous odour, which might be owing to the possibility of sulphur liberation from the β-phosphate. Nevertheless, the results of the ADP β S examination did not yield any improvement after all these efforts.

A representative graph, in Figure 15 (B), illustrates the difficulties in producing consistent and reliable data. In this experiment, 100μM of ADP β S were selected as an example to test for its effect on 10μM forskolin-stimulated response of cAMP. The results of three paired tests, each of which was performed in triplicates, were presented. The agonist ADP β S used in all three trials came from the same batch of product. Despite of the minute scale of error, the results showed discrepancies in the effect of agonist: only one (out of three)

sample displayed significant inhibitory effect by ADP β S. Although in vast areas of science, probability and statistical analysis may be an essential reference, it is not possible in this case to draw a reliable and scientific conclusion purely based on the probability that two out of the three tested samples showed little ADP β S responses. Therefore, in order to scrutinise into the effect of functional heteromeric responses and proceed in this project, it was considered to attempt to use the natural-occurring $P2Y_1R$ agonist ADP, and whether it will produce any detectable and reliable responses.

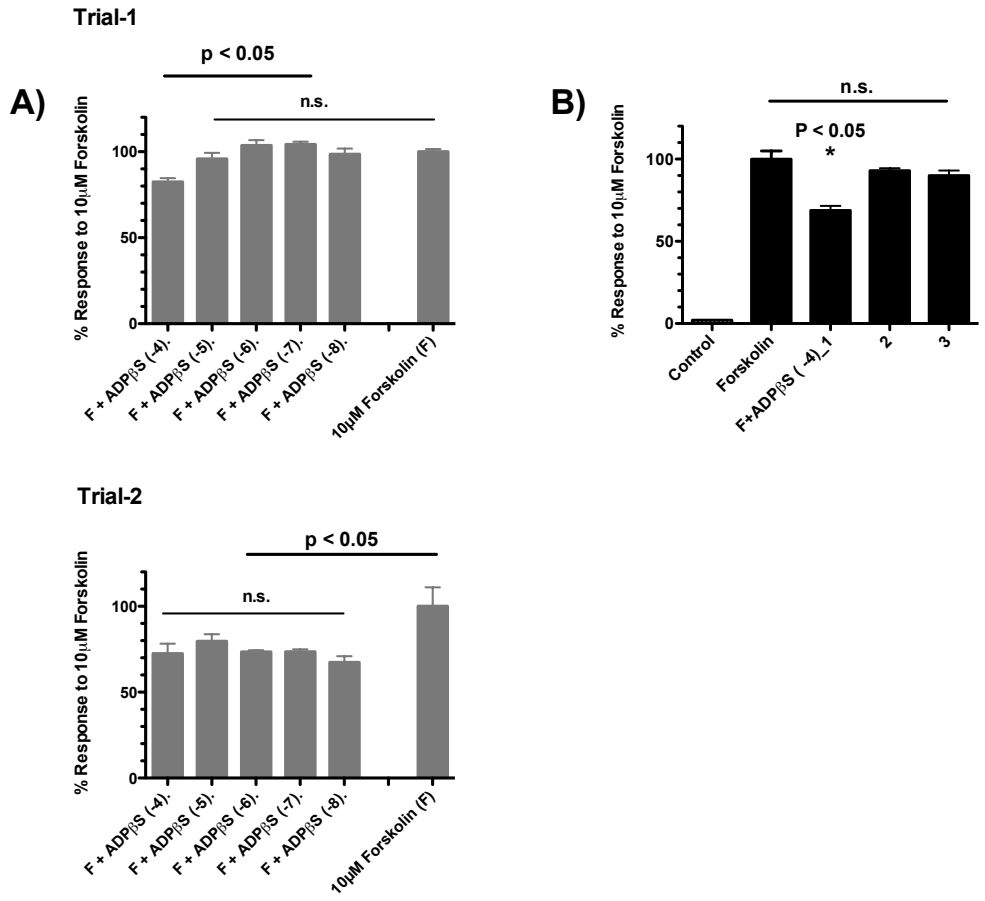

Figure 15. ADP β S response showed large discrepancies in various sample trials.

A) Trial-1 and Trial-2 are the two independent experiments (each in triplicate) representing many unsuccessful tests for determining the ADP β S concentration-response curves. All ADP β S responses were normalised against 10μM forskolin effect. Trial-1, the agonist failed to induce and significant inhibitory effect to the forskolin-induced cAMP production at all concentrations, except at 100μM (-4 logarithmic scale) (One-way ANOVA, Tukey's test). Trial-2, ADP β S exhibited inhibitory response to the forskolin-induced cAMP accumulation at all concentration levels, without any concentration-dependences.

B) A representative experiment testing the effect of 100μM ADP β S (of the same batch) on 10μM forskolin responses. Three independent samples were prepared and assayed in triplicates on the same cell plate. Only one sample revealed inhibitory responses to forskolin.

The natural-occurring $P2Y_1R$ receptor specific agonist ADP was used to characterise the $G_{\alpha i}$-coupled responses of G14T-13 cells. Figure 16 shows the results of these experiments (n=3 experiments, each performed in triplicate). The basal level of cAMP was approximately 4.10 ± 0.23% of the forskolin response. In the middle of the same axis, the partial concentration-response curve of ADP is shown. At 1mM, the highest available concentration, ADP induced over 50% reduction in the forskolin-induced cAMP production, leaving only 44.27 ± 2.79% of the original response. Despite of the incomplete concentration-response curve, the EC_{50} value could be estimated using the Hill transformation and linear regression: approximately 470μM ($\log EC_{50}$= -3.33 ± 0.01). During the course of these experiments, the laboratory supply of ^{14}C-cAMP tracer ran out and it proved impossible to obtain a new supply. It was highly doubted the compound, which was indeed labelled with the ^{14}C element was not cAMP, since this cannot be eluted through the Dowex 50 and Alumina columns (Chapter 2). Several complaints were made to the company, and acknowledged by the technical supporting team that the tracer contained problems. Two different batches of the compound were synthesised and ordered which, took more than 4 months; yet, neither of these was applicable. As a result, it was not possible to perform a more detailed pharmacological characterisation for the heteromeric receptor signal transduction properties.

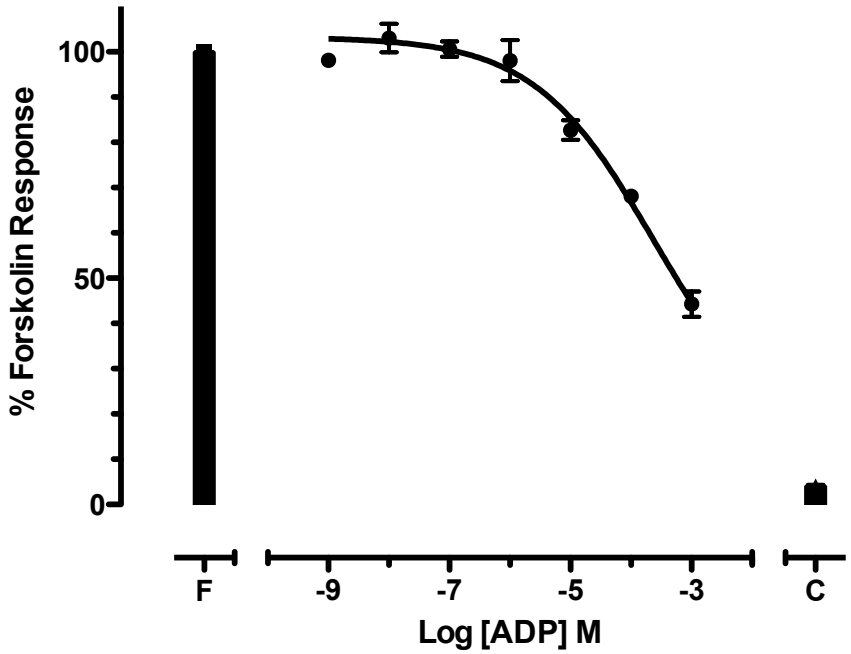

Figure 16. ADP inhibits forskolin-stimulated cAMP production in G14T-13 cells

The accumulation of cAMP was stimulated by the addition of 10μM forskolin (F) and the effect of increasing concentrations of CPA was determined and expressed as the percentage value compared to the 10μM forskolin responses. The basal level of cAMP in un-stimulated cells is shown (C). Data represent the mean $\pm$ s.e.m. of three experiments, each performed in triplicates. The EC_{50} was estimated by the software Prism from the incomplete concentration-response curve, and is approximately approximately 470μM ($\log EC_{50}$= -3.33 ± 0.01).

3.5 SUMMARY

The G14T mutant A_1R was proposed by one of the research groups being constitutively active. This receptor has a glycine residue substitution by threonine at position 14 on the transmembrane helix 1 (TM1), was used to generate the G14T-13 cell line. The G14T mutant A_1R was previously generated and characterised by Rivkees *et al*[209] and was shown to possess a 100-fold enhanced affinity for the A_1R agonist CCPA, with no significant difference in its DPCPX binding affinity. This mutant receptor was described later in a subsequent study to be a constitutively active A_1R[124] due to the constant level of [^{35}S]GTPγS specific binding level at varying concentrations of A_1R agonist CPA. In addition, cAMP assay results revealed a significant inhibition in the level of forskolin induced cAMP production in cells transfected with this G14T mutant A_1R, when compared with a wild type A_1R or a mock cell line.

In our lab, a preliminary experiment showed that the functional heteromeric receptor response, which was defined in this thesis as the functional $G_{\alpha i}$-coupled A_1R response activated by the $P2Y_1R$ agonist ADPβS, was only observed in a cell line co-expressing both $P2Y_1R$ and G14T mutant A_1R (G14T-13 cell line). In hA_1-24 cell line, which expresses the wild type A_1R and $P2Y_1R$, such response was not detected. Based on these, it was original hypothesised that the functional heteromeric receptor signalling response might require a

constitutively active A_1R, that the G14T-13 cell line might be a good model for studying the heteromeric receptor signal transduction properties. Therefore, in order to scrutinise it further, series of experiment were conducted, starting from the investigation of the level of constitutive actively of this mutant A_1R.

The constitutive activity of the G14T mutant A_1R was examined by comparing the forskolin response of CHO.K1 cells in the presence and absence of the G14T receptor (i.e. G14T-13 cell line). Whilst forskolin stimulated cAMP production in both CHO.K1 and G14T-13 with the same potency, the basal cAMP levels in the absence of forskolin, revealed large difference and the magnitude of errors. Such variation and error level in the basal cAMP counts might be due to the residue cAMP in the Dowex 50 and Alumina column from previous experiments. Even though the columns were washed after use, yet, comparing to the basal cAMP concentration in un-stimulated cells, contributions from the residual cAMP becomes relatively large. However, such scales of errors are negligible in comparison to the DPM count when being stimulated by forskolin. When the raw DPM data was transformed to the fold increase over basal, it seemed that the CHO.K1 cells generated much large forskolin responses to G14T-13 cell line: approximately five folds at concentration levels that fall within the linear region of the curve. Nevertheless, this figure coincides with the basal cAMP level difference between the two cell lines. Therefore, it is easily argued

that the observed fold increase over basal difference between the two cell lines might be the result of variation in the basal cAMP counts. This result does not support the G14T constitutively activity. Whereas, de Ligt *et al* had described the G14T response at 1μM forskolin stimulation as 54 ± 6% compared with a control mock-transfected cell line[124].

It has also been shown that G14T-13 cells are able to generate an inhibitory cAMP response following activation with a series of nucleoside analogues frequently used as adenosine receptor agonists. These responses were not observed in CHO.K1 cells, where A_1Rs are not expressed. One of the A_1R agonists, CPA, was then taken further for analysis, and the concentration-response was compared between hA1-24 and G14T-13 cells. Ten micromolar forskolin was used in order to elevate the basal cAMP level. At this concentration, G14T-13 cells gave an approximately 15.7 ± 2.3 folds increase in cAMP and hA1-24 cells 13.7 ± 2.3 folds; the responses of which are not significantly different (p= 0.5759, two-tailed Student t-test). The potency level of CPA in G14T-13 cells was not significantly different from hA_1-24 cells either. At 1nM and 100nM (Log [CPA] = -7 and -9), G14T-13 responses are significantly lower than hA_1-24 cells. For the remaining concentrations, the mean differences of the response were approximately 10% between the two cell lines. However, these appeared to be insignificant by the statistical analysis (two-tailed Student t-test), probably due to the relatively

large magnitudes of errors. The CPA response elicited in the G14T-13 cells suggested the G14T mutant A_1R is a functional receptor; yet, this had not been tested against antagonists or pertussis toxins, which exerts an inhibitory effect on the $G_{\alpha i}$-coupled signalling pathway.

It was unfortunate that ADPβS could not be used in the subsequent investigations. A huge amount of time had been spent on searching and testing for different batches of the ligand (Sigma and Torcris). The main problem encountered with this ligand was that the results showed inconsistency and large fluctuations, which was not due to the handling of the cAMP assay. The technique was confidently established after vast amount of practices in order to reduce the data errors and standard deviation levels. In addition, a strong sulphur odour was identified for some of the batches ordered from Sigma, which may indicates the liberation of the sulphur from the ligand. The natural-occurring agonist ADP was therefore used as a substitutes.

The ADP concentration-response was evaluated in the G14T-13 cells. The concentration-response curve did not reach a minimum due to the low potency level of the ligand. Despite of this, the concentration dependency of the agonist was unambiguous and the potency of ADP was estimated at approximately 470μM ($\log EC_{50}$ = -3.33 ± 0.01), even though it is much lower compared with the literature results 730 ± 35nM[103]. However, the maximum inhibition level (44.27 ± 2.79%

forskolin response) was 20% higher than the previous studies (62 ± 9% forskolin response). As preliminary data suggested that hA_1-24 cells did not respond to ADP β S stimulation, experiments to confirm the ADP effect to hA_1-24 cell were originally planed. These could not proceed due the lack of the ^{14}C-cAMP tracer. The lab stock was purchased from Amersham, which is now a part of PerkinElmer. The tracers purchased since failed to elute from the columns in the cAMP assay. When the compound was tested alone, it showed detectable ^{14}Carbon signal, which indicated that the ^{14}Carbon-labelled compound might not be cAMP. This problem was reported to the company who had made acknowledgement, and re-synthesised the product since. Two batches of the tracer compound had been test, which took at least four months, yet neither of these was desirable. In order to continue the investigation in the $G_{\alpha i}$-coupled signalling pathway, an alternative assay might be sought. The antagonist will be discussed in Chapter 5. However, due to the same reason, the results were not complete.

The differences observed in the properties of the G14T response are likely due to differences in the cAMP assay conditions. As described in the Material and Methods chapter, the cAMP assay I conducted quantified the *de novo* cAMP synthesis, whereas the assay method used by de Ligt *el al* quantifies changes in the total levels of cAMP in the cell. In addition, in their assay, adenosine deaminase (ADA) was used in order to eliminate the endogenous adenosine formed by the

cells. However, this was not used in my assay, which utilised conditions used by Yoshioka *et al*, who first identified the functional response through the heteromeric A_1R:$P2Y_1R$. These changes in experimental conditions may have influenced the results of the G14T mutation's activity. For the functional heteromeric receptor responses, a rightward shift of the ADP concentration-response curve, which leads to the difference in the potency level, may due to ADP hydrolysis, whereas ADPβS is a non-hydrolysable analogue of ADP. However, this more closely reflects the cellular reactions of A_1R:$P2Y_1R$ under physiological conditions. On the other hand, hydrolysis of ADP may also produce adenosine, which could elevate the level of the $G_{\alpha i}$ signalling, as ADA was not used in the assay.

Chapter 4

Calcium Responses via the A_1R:$P2Y_1R$ Receptor

4.1 Introduction

The $P2Y_1$ receptors are expressed endogenously in the Chinese Hamster Ovary CHO.K1 cells, coupled to the $G_{\alpha q}$ pathway, which leads to a release of calcium from intracellular stores. The agonists able to activate $P2Y_1$ receptors are the nucleotides ADP and ATP, and their synthetic analogues, namely 2-MeSADP, 2-MeSATP, ADPβS, and ATPγS. The EC_{50} of these ligands range from nanomolar to micromolar, depending on the cell type or tissue studies (references?). There are also characterised antagonists of this receptor, some of which are structural analogues of ADP such as MRS 2179 and MRS 2279. More intriguingly, ATP and its analogue 2-MeSATP can function as either partial agonists or antagonists at a much lowered potency level (approximately 10μM to 100μM). CHO.K1 cells also express an endogenous $P2Y_2$ receptor ($P2Y_2R$), which is the only other P2Y receptor the cell expresses in addition to the $P2Y_1R$. The $P2Y_2R$ is activated by UTP, ATP and their synthetic analogues, as well as by GTP and some synthetic dinucleotides. Suramin, as an antagonist, targets both the $P2Y_1R$ and $P2Y_2R$.

In the experiments focusing on the characterisation of the $G_{\alpha q}$-coupled pathway signalling in hA_1-24 and G14T-13 cells, co-expressing both an A_1R (wild type or constitutively active) and the $P2Y_1R$ at physiological levels, ADP was selected as the agonist in order to elicit a calcium response for the following reasons: (1) ADP is the naturally occurring agonist of the $P2Y_1R$, (2) ADP is a selective agonist for $P2Y_1R$, that does not exhibit any agonist effect on $P2Y_2R$, and (3) ADP was the agonist used in the cAMP assays, making it possible to compare the data from both signalling pathways.

4.2 THE TIME COURSE OF THE CALCIUM RESPONSE TO ADP

In initial experiments, the time course of the calcium response to ADP was investigated, in order to transform the raw FLIPR data to calcium response, which is also the first step of the FLIPR data analysis. An example of the time course curves and the definition of the important index points were demonstrated in Figure 17; data were collected from two single representative experiments, each performed in CHO.K1 and G14T-13 cells. As indicated in the figure, a complete time course curve is generated at each concentration of agonist, the baseline fluorescence was collected for 9 seconds and agonist (ADP) added at the 10^{th} second, with fluorescence signals collected every second over a total time period of 180 seconds. The blue curves represents the response detected from CHO.K1 cells

using 100nM (—) and 10μM (—) ADP, whereas the red curves indicate the response generated from G14T-13 cells, also by using 100nM (—) and 10μM (—) of ADP. In general, the response undergoes four phases including, chronologically: 1) the basal response (F_0), prior to agonist loading; 2) a signal drop to the minimum level (F_{min}) due to the addition of an agonist; 3) increases in the signal, to a maximum (F_{max}), indicating calcium release from the intracellular stores; 4) depletion of cytosolic calcium leading to a gradual decrease of fluorescence levels. For analysis, the F_0 was calculated as the average of nine data points, and the F_{max} and F_{min} values selected as the single-point data. The change in the fluorescent signal (F) was expressed as the difference between the maximum and minimum fluorescence, i.e. (F_{max} - F_{min}). In order for valid data comparisons, F value was normalised to the basal response, the final value F/F_0 represents the intracellular calcium response to agonist at a specific concentration.

After data transformation, the calcium response changes over the 180-second duration of the assay were reviewed and displayed (Figure 18). The figure shows a series of time course curves each corresponding to a specific concentration of ADP used in the assay. For both CHO.K1 and G14T-13 cells, the maximum calcium response showed a positive correlation with the concentrations of ADP. In other words, the concentration-dependent characteristic was not attenuated by the co-expression of an A_1R (G14T mutant) in the

cell line. Noticeably, the maximal response to ADP at 10nM, 100nM and 1μM (-8, -7 and -6 M in logarithmic scale) revealed levels of reduction in G14T-13 cells. In order to scrutinise the relationship between the agonist concentration and the $G_{\alpha q}$-coupled $P2Y_1R$ responses, further analysis was performed using the concentration-response curves. Therefore, the pharmacological profile of ADP in the wild-type CHO.K1 cells could be compared with the A_1R-expressing CHO cell lines (hA_1-24 and G14T-13).

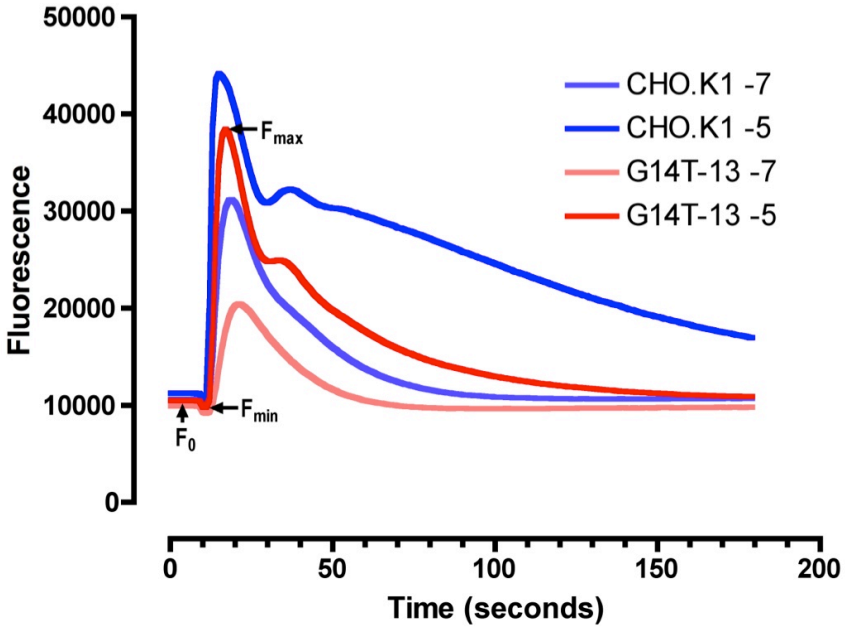

Figure 17. ADP induces fluorescent responses in CHO.K1 and G14T-13 cells.

A representative experiment showing the ADP-induced fluorescence level changes in CHO.K1 cells (blue) and in G14T-13 cells (red) over 180 seconds. The addition of 100nM (-7) (— / —) and 10μM (-5) (— / —) ADP resulted in differential effects on the fluorescence levels. The maximal signal (F_{max}) was reached in approximately ten seconds following the addition of the agonist, which generated a sudden drop in the signal (F_{min}). The F_0 is determined as the average fluorescence level before the addition of ligands.

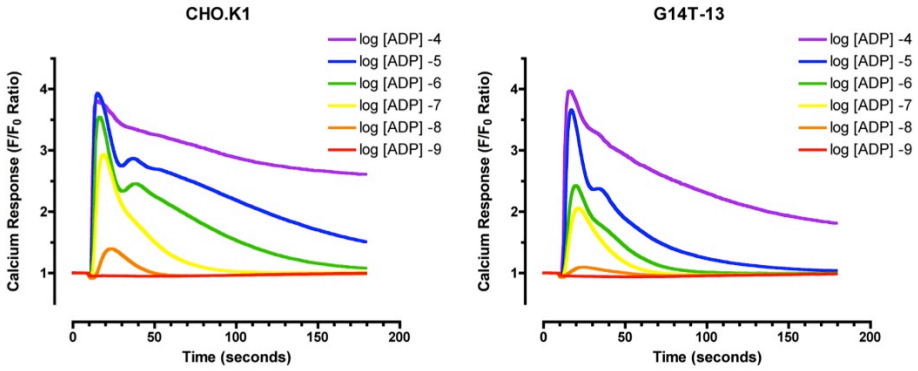

Figure 18. A concentration-dependent calcium response to ADP was observed in both CHO.K1 and G14T-13 cells.

The transformed calcium responses data were reviewed at various agonist concentration levels. The ADP concentrations used vary from 1nM to 100μM (-9 to -4 in logarithmic scale), and the calcium responses were displayed for the whole time course of 180 seconds. A larger response was obtained when a higher concentration of ADP was used. The peak responses at 10nM, 100nM and 1μM ADP concentration (-8, -7 and -6 in logarithmic scale) were significantly different for both cell lines.

4.3 ADP Concentration – Response Curves in Wild-type CHO.K1 and A_1R-expressing CHO Cells

Preliminary cAMP assays results from our lab had shown that the ADP-induced $G_{\alpha i}$-coupled response via the functional heteromeric A_1R:P2Y_1R receptor was only observed when a G14T mutant A_1R, which was previously reported as being constitutively active, was expressed; i.e. G14T-13 cells but not hA_1-24 cells. It was therefore questioned whether constitutive activity may be a requirement for the heteromeric $G_{\alpha i}$ response. This is an example that the P2Y_1Rs are able to influence the A_1R signalling, despite the fact that the G14T constitutive activity had not yet been confirmed. In light of these results, it is a possibility that the expression of A_1Rs (wild type and/ or G14T mutant) may also interfere with P2Y_1R responses. In the previous section, I have already demonstrated that the concentration-dependence of the ADP elicited calcium response change was not diminished by the co-expression of a G14T mutant A_1R. However, reductions in the responses were seen when ADP was applied at specific concentrations. Therefore, further detailed investigations are essential in order to understand the roles of the A_1R (G14T mutant and also in comparison with the wild type A_1R) to P2Y_1R signalling.

The first experiment performed on CHO.K1 and G14T-13 cell lines (Figure 19 and Figure 20), showed that the concentration-response curves had very different shapes. The CHO.K1 curve went from

minimum to maximum response over 3 log units, whereas G14T-13 curve spanned over 4 log units. Further, for G14T-13, neither three- or four-parameter non-linear regression equation resulted in a fit that included all of the points on the curve. With respect to Prism, the two curve fitting models were the (three-parameter) *log (agonist) vs. response* equation and the *log (agonist) vs. response – variable slope four-parameter* equation. The three-parameter (3-parameter) equation assumes the does-response curve fits the standard symmetrical sigmoidal shape, hence a hill-slope of 1.0. The equation calculates for the top and bottom plateaus, as well as the EC_{50} values, thus called 3-parameter model. It is useful if the curve does not contain a lot of data points. The four-parameter (4-parameter) equation, on the other hand, also assumes the curve being symmetrical and sigmoidal. However, it does not assume for a standard hill-slope of 1.0, instead the slope is calculated from the data points on the curve. This model is normally used when plenty of data points are available; the equation calculates four parameters: the top and bottom plateau, the EC_{50} values, as well as the hill-slope.

For CHO.K1 ADP concentration-response curve, both 3- and 4-parameter curves were compared. As the results revealed, both equations fit all data points, there is not a vast difference between the two curves. This was demonstrated by the very small discrepancy value between the two curves: F=1.430. Nevertheless, the 3-parameter model was preferred rather than the four-parameter

variable curve. The potency of ADP in CHO.K1 cells were calculated after at least 4 repeated experiments, EC_{50}= 72.4nM (log EC_{50}= 7.14 ± 0.11).

However, this was not the case for the G14T-13 cell line. A large discrepancy existed between the results generated by the two different models (F=20.48): the 4-parameter model is preferred over the 3-parameter curve. Even then, there is an ambiguous curve trend between the data points Log [ADP]= -6 and -7, which forms a small plateau at the middle of the curve. It was not certain at this stage if the 4-parameter model was indeed the best-fit equation for the data points. According to this model, the estimated ADP potency levels for the two cell lines were 10-fold different: 45nM ($logEC_{50}$ = -7.35) for CHO.K1 and 552nM($logEC_{50}$ = -6.26) for G14T-13 in this experiment. Despite these differences, the results confirmed the concentration-dependent ligand responses in both cell lines.

Interestingly, another phenomenon was observed. As the concentration-response curve shown, ADP took effect in CHO.K_1 cells from around 10nM (Log [ADP] = -8), and continues to a maximal level between 1μM and 10μM (Log [ADP] = -6 and -7), where the curve starts to enter the plateau. Whereas it is difficult to conclude, from the curve, whether the response in G14T-13 cells had reached a maximum at 100μM (Log [ADP] = -4) concentration based on the 4-

parameter variable curve. The fact that the G14T-13 response extended approximately 4 log units to achieve its maximum suggests the existence of a two-component system. In addition, as discussed above, the 4-parameter equation, which assumes the curve being symmetrical and sigmoidal, did not fit through the data points at Log [ADP]= -6 and -7 that appeared to form a plateau. Therefore, it is reasonable to hypothesise that the ADP response in G14T-13 cells may not be a simple sigmoidal relationship, instead, a biphasic curve that possesses two distinctive components that are most likely resulted from differential potency levels of ADP.

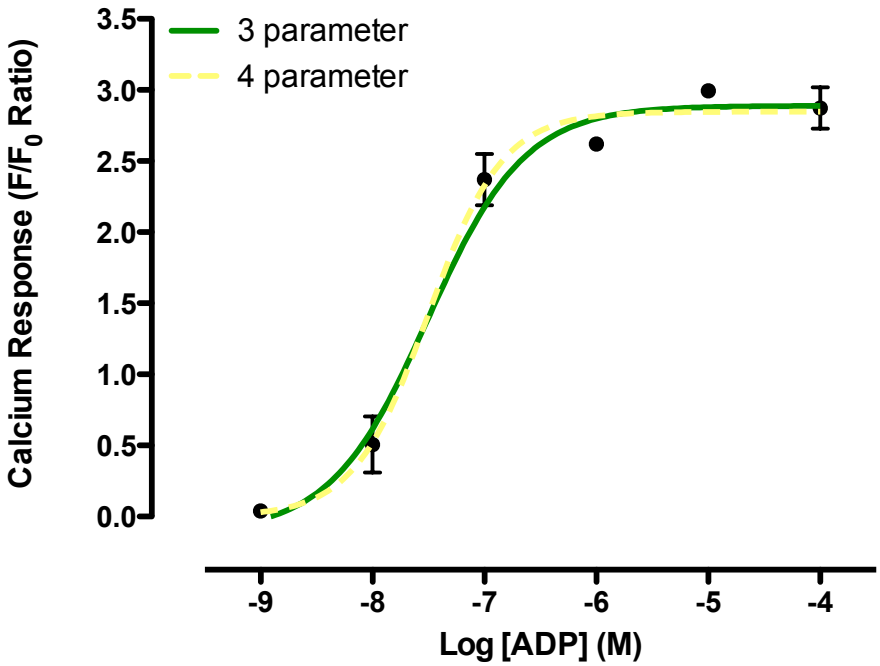

Figure 19. Fitting two different equations to the ADP concentration-response of CHO.K1 cells.

The (three-parameter) *log (agonist) vs. response* equation and the *log (agonist) vs. response – variable slope four-parameter* equation were compared. The F value, which represents the discrepancy level, was very small (F=1.430) indicating there is very little difference between the two curve-fitting models. However, the Prism software calculation showed the three-parameter model was preferred over the four-parameter curve, probably due to the small amount of data points. The concentration-dependent response of the receptor for the ligand ADP (n=5) has a calculated $\log EC_{50}$ = -7.35 (45nM).

- The (three-parameter) *log (agonist) vs. response* equation:

$Y=Bottom + (Top-Bottom)/(1+10^{((\log EC_{50}-X))})$

- The log (agonist) vs. response – variable slope four-parameter equation

$Y=Bottom + (Top-Bottom)/(1+10^{((\log EC_{50}-X)*HillSlope)})$

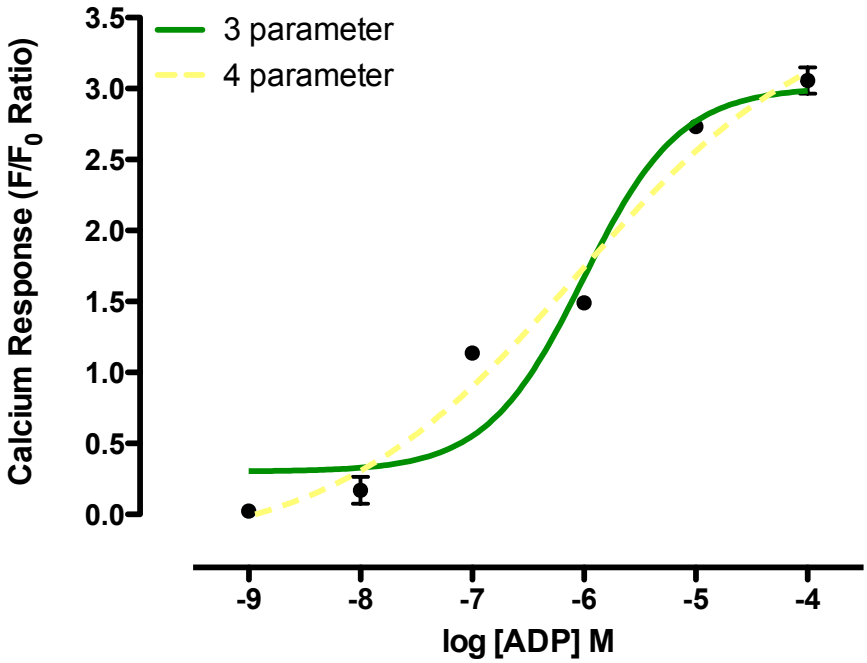

Figure 20. Fitting two different equations to the ADP concentration-response of G14T-13 cells

The (three-parameter) *log (agonist) vs. response* equation and the *log (agonist) vs. response – variable slope four-parameter* equation were compared. These two models generated very different results, as represented by the large F value for discrepancy level (F= 20.48). The four-parameter equation was preferred. According to the curve, the estimated potency level for ADP in G14T-13 is approximately 552nM ($logEC_{50}$= -6.258). The figure shows a representative experiment performed in triplicate.

In order to determine whether the response of G14T-13 cells to ADP was biphasic, the concentration-response curves were repeated at 0.25 log unit concentration intervals (Figure 21) and the results showed a clear biphasic concentration-response relationship. The data points were fitted smoothly to the biphasic curve. This biphasic model of the response was later proved by the 95% confidence intervals on each data point (Figure 22). Other equations, such as the (three-parameter) *log (agonist) vs. response* and the *log (agonist) vs. response – variable slope four-parameter* equations have been tested, and showed that the biphasic curve was the preferred curve model for the results generated. This implies that a heterogeneous population of $P2Y_1Rs$ exist in the G14T-13 cell line, which might be the cause of differential potencies of ADP.

The biphasic ADP response curve in this cell line involves a higher-potency phase between 10nM and about 100nM (Log [ADP] = -8 to -7), and a lower-potency phase from 1μM to 10μM (Log [ADP] = -6 to -5). Hill-Plot calculation showed the mean EC_{50} values (n=7) for the higher- and lower-potency components are approximately 59nM ($logEC_{50}$= -7.23 ± 0.23) and 2.0μM ($logEC_{50}$= -5.70 ± 0.07) respectively. The mean fraction ratio of the higher-potency phase compared to the whole curve is approximately 0.54 ± 0.05.

In comparison with the CHO.K1 responses, the EC_{50} value of the higher-potency phase is not significantly different from that obtained

from CHO.K1, which lack any A_1Rs. The upper-phase of the G14T-13 curve, on the other hand, is significantly less potent than the CHO.K1 ADP responses. Since the assay conditions were strictly controlled, the same ligand was used for both cell lines, and paired trial tests had also been carried out, the only difference that might have led to the distinctive results, were the type of receptors expressed in each cell line. In G14T-13 cells, a mutant A_1R was stably transfected and expressed; whereas the CHO.K1 cells, which was used to generate the G14T-13 cell line, does not endogenously express any A_1R. Therefore, it is most likely that the two phases correspond to the more potent non-heteromeric $P2Y_1$R, which showed similar EC_{50} levels with the CHO.K1 cells; and the lower-potency phase may due to the $P2Y_1$R heteromerisation with the G14T A_1R. Further, the fraction ratio mentioned above would indirectly suggest that approximately half of the $P2Y_1$Rs exit as heteromeric complex with A_1R.

The 95% confidence interval value was analysed for each data point on the curve, as shown in Figure 22. This value determines statistically the reliability of the calculation, which fits the biphasic curve through each data point. In other words, it estimates the confidence level of the shape of the curve determined at all concentrations. This confidence level is expressed as a range of mathematical values, represented in the figure with the error bars. The larger the error bar, the wider the confidence interval and the

less reliable the calculation is. Thus it is possible for the curve to be fitted in different ways. A tight range of confidence interval indicates the curve is more likely to go through the specific data point as predicted by the non-linear regression algorithm. In extreme cases, the confidence interval is too wide, so that the hypothesis is rejected. For curves such as that obtained from the response of the G14T-13 cell line to ADP, multiple models should be tested.

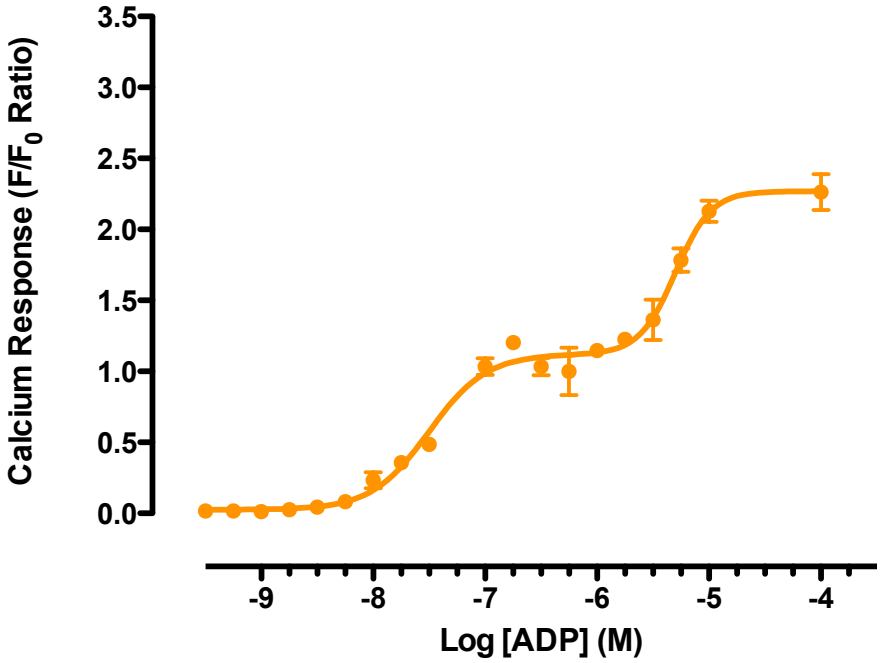

Figure 21. The ADP response in G14T-13 cells is biphasic.

The ADP concentration-response curve was obtained using 0.25 log unit concentration intervals. This figure is a representative of a single experiment performed in triplicates. The pharmacological data (mean ± s.e.m.) were calculated from at least 6 repeated experiments. The higher-potency component has a mean $\log EC_{50}$ of -7.23 ± 0.23, and the lower-potency phase site of -5.70 ± 0.07. The proportion of sites in the higher-potency phase is about 0.5 compared to the total curve, possibly indicating that approximately 50% of the $P2Y_1R$ exists in a non-heteromeric state.

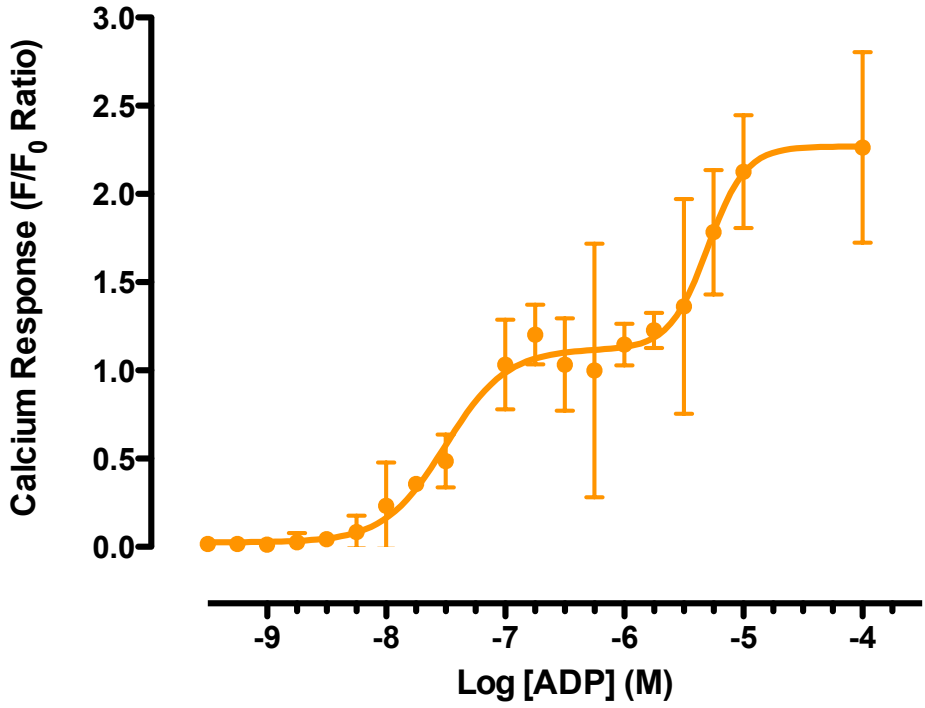

Figure 22. The ADP concentration-response curve in G14T-13 cells, with 95% confidence intervals indicated.

The error bar represents the 95% confidence interval values (CV) for each data point on the curve. The analysis showed that the small 95% CVs at the first plateau have confined the curve to a biphasic shape. The curve followed a tight trend with only a few exceptions, which do not oppose any alteration to the overall structure of the curve.

Having confirmed the biphasic concentration-response relationship of ADP in G14T-13 cells, whereby the lower-potency phase may correspond to the heteromeric receptor and the higher-potency response likely due to $P2Y_1R$, the ADP pharmacological profile was also characterised in hA_1-24 cells. The reason being that this cell line is stably transfected with the wild-type A_1R and serves as a comparative model to G14T-13 cells. As described in Chapter 3, the constitutive activity of G14T mutant A_1R had not yet been confirmed in this thesis, thus no evidence to prove whether the activity of A_1R is of a requirement enabling the functional heteromeric receptor signalling through the $G_{\alpha}i$-coupled pathway. Nevertheless, it is possible to conclude that the G14T A_1R forms a heteromeric complex with the endogenous $P2Y_1R$, creating a distinctive $G_{\alpha}i$-coupled signalling pathway that is not observed with the wild-type A_1R. Based on these understandings, questions have arisen concerning the $G_{\alpha}q$-coupled response whereby if the lower-potency phase, which has so far been attributed to the heteromerisation between the G14T A_1R and $P2Y_1R$, can also be detected in the hA_1-24 cell? Is a wild-type A_1R likely to exert the same effect on the $P2Y_1R$ response? Or is there a possibility that the reduced potency level could only be due to the presence of the G14T A_1R, of which the character resembles the $G_{\alpha}i$-coupled response?

Figure 23 shows the ADP response of the hA_1-24 cells when the agonist is applied at 0.25 logarithmic unit concentration intervals. The curve possesses a clear biphasic shape and the mean EC_{50} values (n=7) are 77.6nM and 2.45μM for the high and low-affinity sites respectively ($logEC_{50}$= -7.11± 0.09 and -5.61 ± 0.09). In addition, the fraction ratio of the two phases on the curve is approximately 0.41 ± 0.17. These results are consistent with the earlier findings in G14T-13. Further, they support the conclusion of differential ADP pharmacology, where the lower-potency phase most likely resulted from the heteromeric A_1R:$P2Y_1R$ receptors and that constitutive activity of the A_1R is not required for the heteromeric receptor's response.

The 95% CV analysis has also confirmed the trend of the biphasic curve. As shown by Figure 24, the CV ranges are quite tight, especially at the first plateau, which defines the end of the first phase as well as the starting of the second phase. Although there are a few exceptions with larger confidence intervals, they are not significant to change the overall shape of the curve. These data suggest that the ADP response in CHO.K1 cells is monophasic and biphasic in both G14T-13 and hA_1-24 cells. The results obtained from each cell line were normalised to their maximum response and graphed together for comparison, as shown in Figure 25.

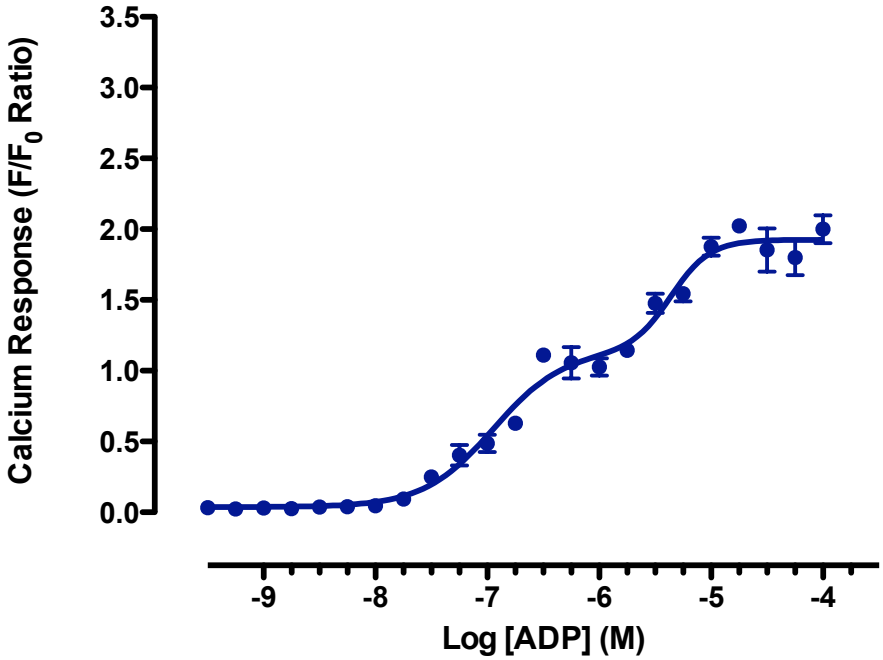

Figure 23. The ADP response in hA1-24 cells is biphasic.

The ADP concentration-response curve was obtained using 0.25 log unit concentration intervals. The figure represents a single experiment performed in triplicates. All data are expressed as the mean ± s.e.m. of the response ($n \geqslant 6$). The curve consists of two distinct phases corresponding to a high- and a low-potency phase ($logEC_{50}$ = -7.11 and -5.61 respectively). The fraction ratio of the higher-affinity site to the whole curve is approximately 0.41.

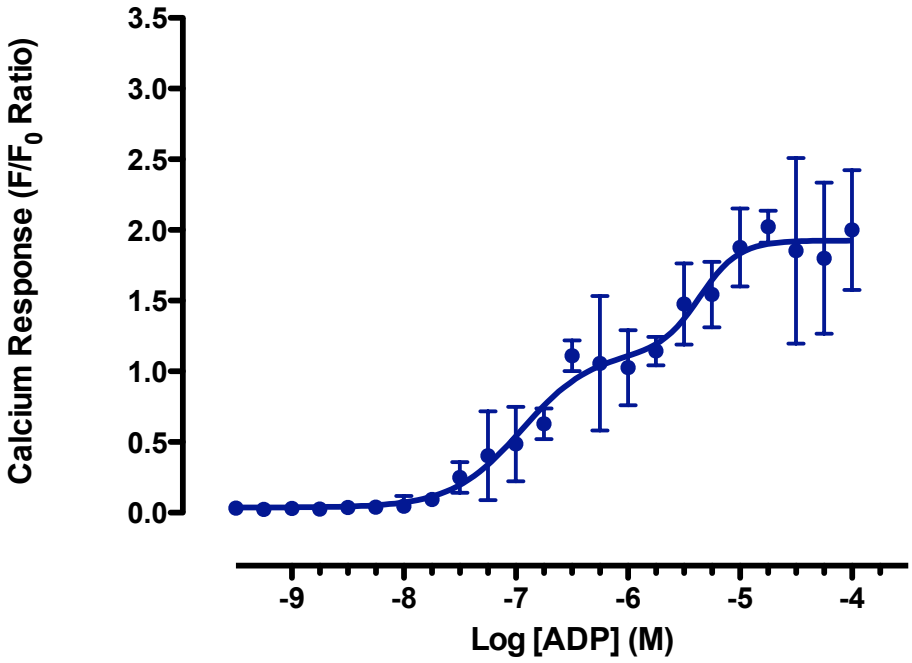

Figure 24. The ADP concentration-response curve in hA1-24 cells, with 95% confidence intervals indicated.

The data indicate the ADP response of hA_1-24 cells. The error bar represents the 95% confidence interval values (CV) for each data point on the curve.

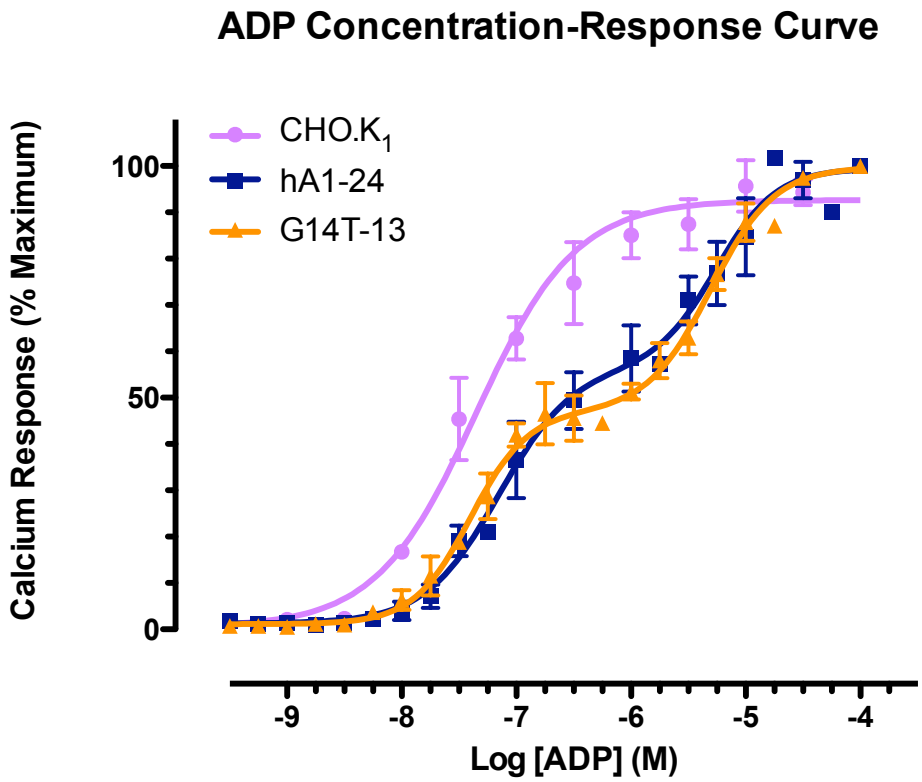

Figure 25. ADP concentration-response curves for CHO.K1, G14T-13 and hA_1-24 cells

The ADP concentration-responses in three different cell lines are represented as a percentage of the maximal response for each cell line. The data represent the mean ± s.e.m. for at least five experiments. The $logEC_{50}$ of the higher-potency phase for the G14T-13 and hA_1-24 curves are statistically the same as that of the CHO.K1 curve. There was no statistically significant difference in the proportion receptors present in the higher-affinity site of the G14T-13 curve, as compared with the hA_1-24 curve.

4.3.1 ADDITIOINAL CONSIDERATIONS

To ensure that there was no effect of pH upon the ADP response, the pH of various concentrations was compared with the PBS control, the vehicle used to prepare the ADP solutions used for the concentration-response curves. Figure 26 shows that the pH levels at all concentrations are relatively stable without any significant differences (n=3 experiments). The only exceptions were at log [ADP]= -3.0 and -3.5 ($p=0.0002$ and $p=0.0065$, respectively), which should not affect the previous data obtained, since the highest final concentration of ADP used was at -4.0 (on the logarithmic scale). The temperature at which the pH levels were measured was 22°C, the same as in the FLIPR machine, where the agonist was dispensed.

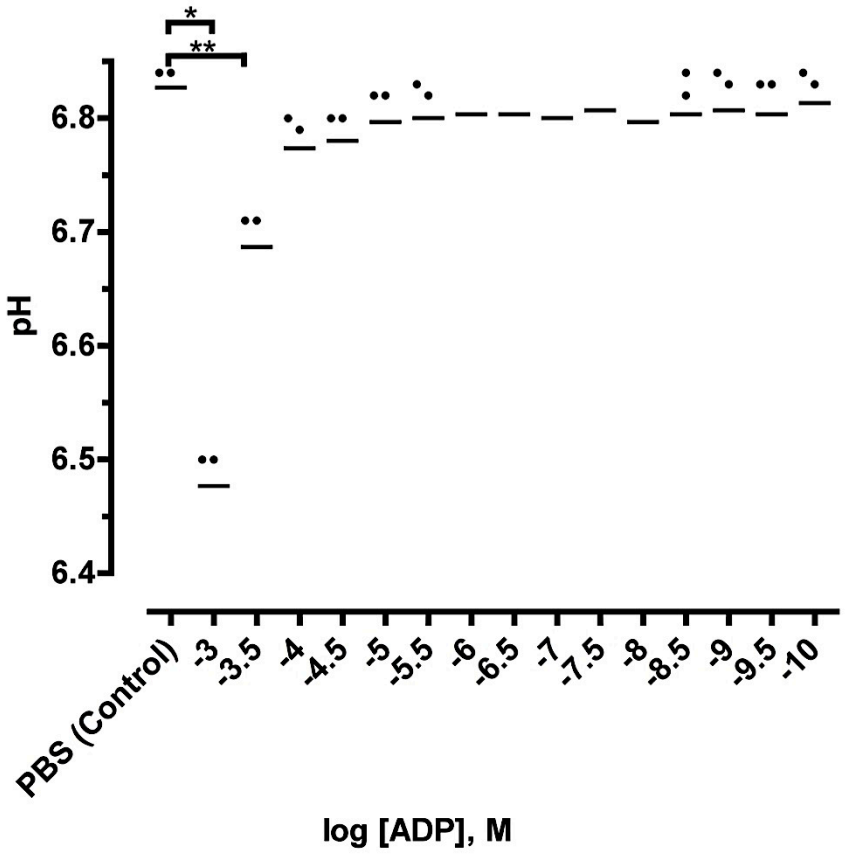

Figure 26. The pH of ADP at various concentrations compared with the PBS control.

The pH measurement of different concentrations of ADP was performed at 22°C, the same temperature as in the FLIPR assay. The results represent the mean $\pm$ s.e.m. of the pH value obtained at each concentration (n=3).

4.4 THE ROLE OF A_1R IN THE STIMULATION OF THE LOWER-POTENCY CALCIUM RESPONSE

In the previous section, it has been shown that the intracellular calcium responses to increasing concentrations of ADP exhibit differential relationships with respect to cell types: a sigmoidal concentration-response curve in the wild type CHO.K1 cells, compared with a biphasic curve, which is only observed when cells express A_1Rs (wild type and G14T mutant), i.e. hA_1-24 and G14T-13 cells. Since all experimental conditions were controlled, such phenomena is, therefore, most likely be caused by the difference in the receptor expressions and status in cell lines in which the co-expression of the A_1R leads to a heterogeneous population of $P2Y_1$Rs. It may be the formation of a heteromeric A_1R:$P2Y_1R$ that resulted in a reduced ADP potency level, which co-existed with the homomeric $P2Y_1R$ and response, hence the biphasic curve. This can easily be proved by the receptors' physical interactions, such as using co-immunoprecipitation and bimolecular fluorescence complementation assays. However, these methods were not available at the time of my project due to various reasons, pharmacological experiments were employed in advance, aiming to provide more direct confirmation on the heteromeric receptor signalling.

The object of this part of the project focuses on two questions: 1) will the changes in the number of A_1Rs lead to variations in the proportion of the second (top) phase of the curve, if positive, then; 2) will the activation (and inhibition) of A_1R facilitate (and impede) the formation of the second phase of the curve. To answer this first question, CHO cells with the G14T A_1R expressed at a range of levels (G14T cell lines) were used in FLIPR assays; the second, CPA (A_1R agonist) were tested on CHO.K1, hA_1-24, and G14T-13 cells. Unfortunately, these experiments did not yield reliable data due to over-confluent cell density at the time of assay, of which I was not aware at the time., This finding is indeed invaluable, as crucial cell and assay conditions that define a biphasic $G_{\alpha C}$ response in the A_1R-expressing CHO cell lines. In addition to the test of agonist CPA, the A_1R antagonist DPCPX will be described separately, in Chapter 5.

4.4.1 The A_1R expression level to the low-potency calcium response

In the lab, the G14T mutant cell line was produced at a range of expression levels. Six different G14T clones were cultured for FLIPR assays. Subsequent parallel experiments were originally planned in the wild type human A_1R transfected cells (hA_1 cell lines).

The ADP-induced calcium responses were analysed in all six clones. It is designed to reveal the possible consequence of the G14T

expression alteration on the proportion of the top part of the biphasic curve. Since the lower-potency phase is most likely due to the heteromeric A_1R:$P2Y_1R$ signalling, increasing or decreasing G14T expression may lead to augmentation or reduction in the ratio of the heteromeric receptors to the total $P2Y_1R$ population, hence elongate or shorten the top phase of the curve. On the other hand, if this correlation does exist, the results will further prove that the heteromeric receptor exhibits a lower-potency ADP pharmacology.

As described in Chapter 2, FLIPR assays were carried out for all six clones simultaneously to ensure the conditions are consistent. However, the results were not as expected (Figure 27). In this figure, curves represent one single experiment performed in triplicate. The top part showed the biphasic curve fitting results, and the bottom, data points connected by lines, where the scattering of the points are better reviewed. As an example, the G14T-13 cell did not produce the same biphasic concentration-response curve as previously seen, the curve is more scattered between log[ADP] of -4.75 and -5.25, which almost plateaus. In general, calcium responses at each concentration point are lowered, in addition to the sudden increase from log[ADP] of -4.75 to -4. When a biphasic curve was fitted, the first phase takes over only about 14.7% (estimation by GraphPad Prism) of the total response, which significantly differs from the results obtained earlier. The $logEC_{50}$ value for the second phase, as estimated by the software, is approximate -4.4. In other words, the

G14T-13 cell line, as a control in this experiment, failed to regenerate the same response. Therefore, not only that these G14T-13 data should not be used for comparison with the calcium responses from the other G14T cell lines, whether the rest of the data collected are reliable remains unclear.

Compared with the other curves, which have all showed varying degrees of scattering, tendencies for triphasic dose-response relationships were observed in all cases. The biphasic modelling showed that the relationship is ambiguous in G14T-5, 6 and 8 clones. In G14T-14 and 15, the $logEC_{50}$ of the lower-potency phases are approximately -4.93 and -4.43 respectively, these are close to the G14T-13 value obtained in this experiment, but much lower than the data analysed previously. Overall, it is impossible to determine the correlation between G14T A_1R expression level and the fraction ratio of the second lower-potency phase. The main reason being the inconsistent concentration-response relationship in these cell lines.

The same experiment was also repeated using another potent $P2Y_1R$ agonist 2MeSATP in all clones, so that both agonists could be screened in all G14T A_1R transfected clonal cell lines. This was the original design for these experiments. Unfortunately, as occurred in the ADP experiments, the results for 2MeSATP contained the same pattern of problems, and they were not conclusive (Figure 28). The experiment was performed only once in triplicates. Although the

concentration-response curve of 2MeSATP had not been determined in any of the CHO-based cell lines, it is clear that the curve obtained by all the G14T cell lines showed some similarities to the ADP responses described above. The G14T-13 curve reveals degrees of scattering (Figure 28 bottom) close to the ADP response, such that the biphasic curve fitting (Figure 28 top) was ambiguous and, the $logEC_{50}$ and fraction ratio (of the low-potency phase to the whole curve) could not be accurately determined. The other cell lines also produced varying degree of scattering and results differ slightly. Apart from the G14T-14 and 15 clones, for which the biphasic relationship were ambiguous; G14T-5, 6 and 8 cells were fitted with biphasic curves despite of the high level of data scatterings that almost led to three phases. All of these three curves showed a steep increase in the responses starting from 1μM concentrations (Log[2MeSATP]= -6), thus a large fraction ratio for the second phase, approximately 0.74, 0.77 and 0.89 respectively. The $logEC_{50}$ values estimated were about -3.49, -4.75 and -3.87.

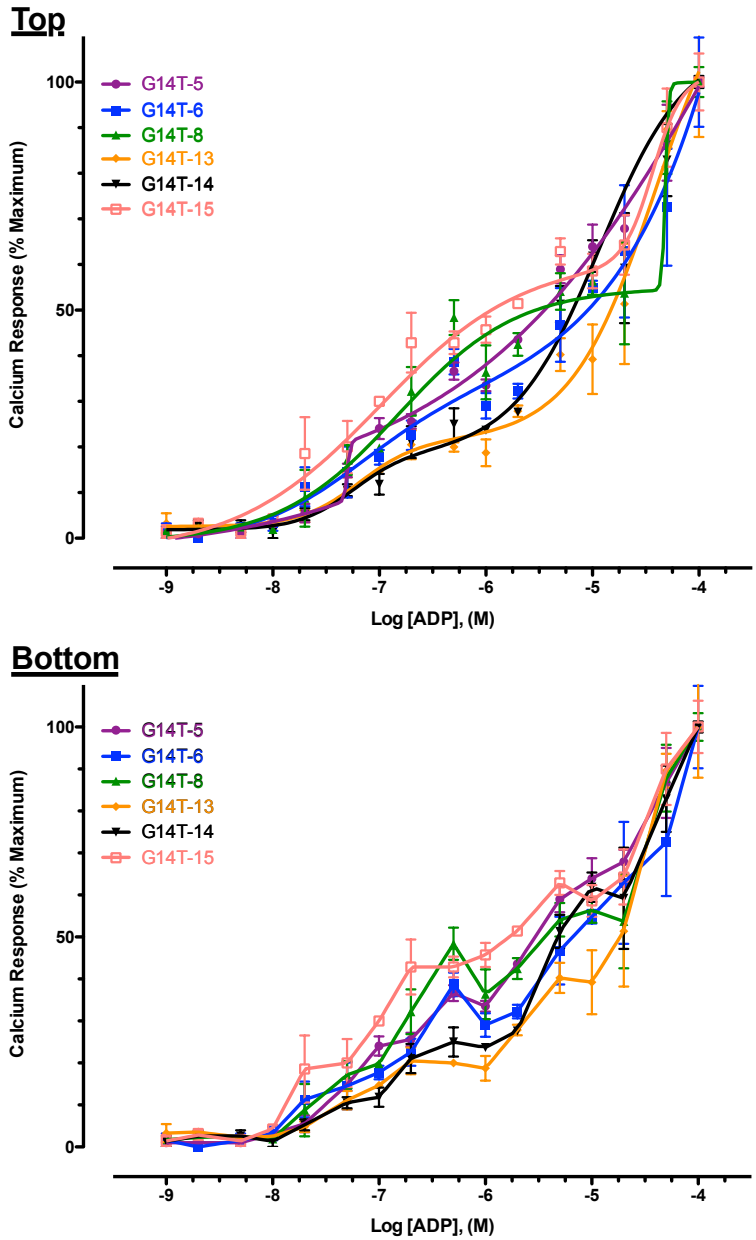

Figure 27. The comparisons for ADP concentration-responses in six G14T clonal cell lines.

The experiment was paired with the 2MeSATP test shown below, and performed once in triplicate. **Top**, Prism software modelling of biphasic does-response curves; **Bottom**, lines connecting each data points on the curve, revealing the degree of scattering. Curve fitting results showed the G14T-13 curve differs from previous results, a very small fraction of higher-potency phase and much larger fraction for the lowered potency second phase fragment. Biphasic model showed ambiguous result for G14T-5, 6 and 8 cells, probably because the data points are scattered. Line connections between points showed all curves may potentially result into a third phase component.

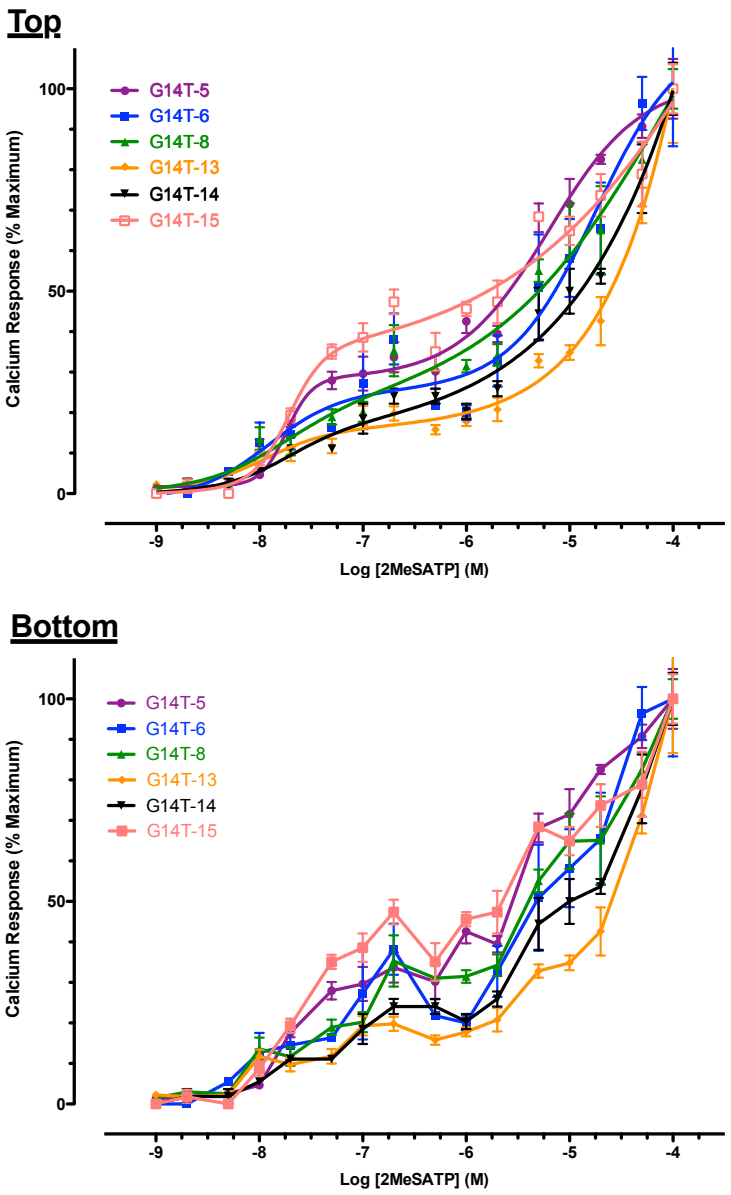

Figure 28. The comparisons for 2MeSATP concentration-responses in six G14T clonal cell lines.

The experiment was paired with the ADP test shown above, and performed once in triplicate. **Top**, Prism software modelling of biphasic does-response curves; **Bottom**, lines connecting each data points on the curve, revealing the degree of scattering. Curve fitting results showed the G14T-13 curve had a very small fraction of higher-potency phase and much larger fraction second phase fragment. Biphasic model showed ambiguous result for G14T-13, 14 and 15 cells, probably because the data points are scattering. Line connections between points showed all curves may potentially result into a third phase component.

Admittedly, it is not conclusive whether the 2MeSATP results were reliable, since the response was not previously confirmed in any of the CHO-based cell lines. Nevertheless, these data obey certain degree of similarity with the unreliable ADP results collected from the parallel experiment. Furthermore, in both ADP and 2MeSATP experiments, observations were made that are worth considering: 1) the degree of data scattering, which leads to the tendency for a triphasic curve as well as the ambiguous biphasic relationship; 2) the response experiences a sudden and sharp increase from a certain concentration point onwards, which had resulted into an extended low-potency phase. These phenomena were not seen before in either of the two A_1R-expressing cells (hA_1-24 and G14T-13). Since for these cell lines, the ADP concentration-response relationships were confirmed after numerous repeats, therefore, it became crucial to discover the cause of this altered response and be able to reproduce the same results.

Few attempts were made to resolve the case, first of which being the enhancement of the FLIPR technique, including the preparation of the agonist plate, controlling of the dye incubation time and the loading accuracy, which ultimately influences the standard deviation of basal fluorescent signals across the 96 wells in a plate. Secondly, use of a new aliquot of stock ADP solution to avoid ligand degradation.

The FLIPR assay enables the high throughput calcium response analysis, as each well of a 96-well plate generates 180 data points whilst the signal is being recorded once every second. Effectively, 17,280 data points per plate can be collected at the end of a single experiment. Such convenient technology encourages the user to screen a large amount of plates in a single use, forgetting that FLIPR is also very sensitive at differentiating fluorescent signals, thus revealing small differences that could probably be caused by experimental errors. In this particular experiment, when both ADP and 2MeSATP were screened in parallel in all six clonal cell lines, 12 plates were prepared simultaneously, which means an amplification of errors could have occurred, such as small pipetting imprecision when making serial dilution for the agonist, and time control for incubation at both 37°C and room temperatures. The larger the plate number, the higher the volume required for the agonist at each concentrations, especially when the experiments are paired and quarter log unit scale of concentrations are used. This inevitably induces a bigger chance of impaired accuracy in pipetting. It had also been noticed at a later stage of the project that thorough mixing and changing of pipet tips at each concentration of the serial dilution process reduces the data fluctuations and the magnitude of errors. Therefore, large-volume agonist preparation is not recommended, especially when the solvent volume exceeds 1ml and more than one pipetting might be necessary. On the other hand, the control of the dye incubation length is essential. In this experiment, a total of 12

plates were prepared simultaneously as a paired experiment. The incubations were carried out for 30 minutes at 37°C and further 30 minutes at room temperature. The process of dye-loading requires approximately 2 minutes for each plate; and in order to complete the FLIPR detection and data recording, about 5 minutes per plate are necessary. This means by the time the first plate had completed the FLIPR detection, the last plate would still have about 20 minutes remaining for room temperature incubation. As this proceeds, the final plate would have already been over-incubated for about 30 minutes before signals can be detected. For these reasons, it was decided that further experiments should aim to use adequate and minimum number of plates for a maximum amount of information. This will also serve as a valuable opportunity for the training of the technique as well as the experimental design. Secondly, degradation of the agonist ligand can also lead to unusual pharmacological behaviour. ADP was therefore, selected as an example performed repeated ($n>3$) trial test in G14T-13 cells using, not only a fresh aliquot of stock ADP solution, but also new ADP stocks were made from the original powder form as supplied by the company to ensure the results.

Even though all of the methods mentions above were tried, the biphasic response was still not observed (results not shown here). I then decided to look at this problem from a different aspect, which uses the other A_1R containing cell line, hA_1-24, to study the alteration

of the biphasic response, as well as to explore the effect A_1R activation on the extent of the lower-potency fragment of the curve.

4.4.2 The activation status of A_1R to the lower-potency fraction of the biphasic curve

As mentioned above, a series of experiments will be conducted in the hA_1-24 cell line, not only for the continuous observation of the biphasic dose-response relationship in the A_1R-expressing cells; more importantly, the confirmation of the nature of the low-potency phase of the curve, and the investigation into the role of A_1R activation status to the proportion of the heteromeric receptors. It was originally queried that activation of the A_1R might facilitate the heteromerisation of A_1R:$P2Y_1R$. A selective A_1R agonist (CPA) will be examined as to its effect on the ADP concentration-response curve. Prior to this, the CPA response alone to the $G_{\alpha e}$ pathway should be tested in all of the CHO base cell lines (CHO.K1, hA_1-24 and G14T-13) to exclude the possible synergistic effect resulting from the $G_{\beta\gamma o}$ subunit.

The CPA does-response curve was determined in three cell lines, CHO.K1, hA_1-24 and G14T-13, in a paired experiment. During this single trial test, various concentrations of CPA was prepared, and

detected in triplicate. The FLIPR assay was carefully conducted as described in Chapter 2, with improved techniques that were mentioned in the previous section. As Figure 29 shown, compared with the control test, CPA exhibited no significant effect (one-way ANOVA, Tukey's Multiple Comparison Test) on calcium response at most of the concentrations used (log[CPA] of -5 to -10), neither was any significant difference seen between the cell lines at a defined concentration. In the control sample, ligand added consists solely of 10% DMSO dissolved in DPBS, as CPA is soluble and stored in DMSO. Serial dilutions for CPA were prepared in DPBS in consistent with the ADP assay. Only at 100μM, was a large increase observed in all cell lines ($p < 0.05$, one-way ANOVA, Tukey's Multiple Comparison Test). Although the maximum response in hA_1-24 cells appeared to be greater than the other cell lines, statistical analysis revealed no significance. This could be explained by the relatively large magnitudes of errors in all three types of cell lines (one-way ANOVA, Tukey's Multiple Comparison Test). Overall, this increase in response could be simply due to a pH difference at the highest concentration of ligand, as well as a synergy between the receptors (A_1R and $P2Y_1R$). Since this was a single trial experiment, no firm conclusion could be made at this stage. Nevertheless, the purpose of this experiment was to determine whether a synergistic response could be induced through CPA activation. Therefore, as the data had revealed, 10μM seemed to be the highest concentration available, which will not result into a $G_{\alpha q}$ response. Such result, on the other

hand, should not be confused with the A_1R being inactive, as the cAMP assay had already shown a maximum A_1R response detected at this concentration of CPA (Chapter 3).

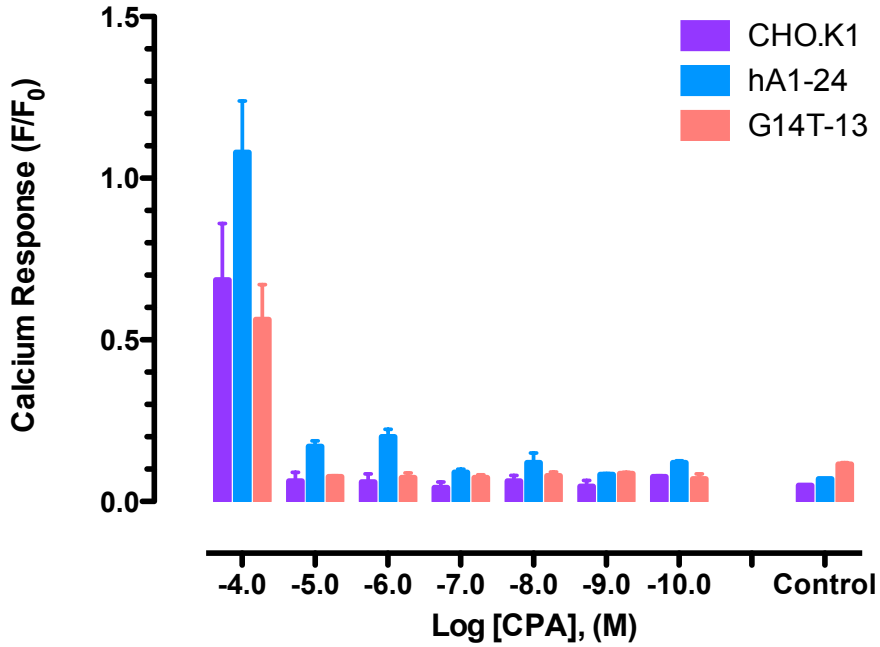

Figure 29. CPA concentration-response examination in CHO.K1, hA_1-24 and G14T-13 cell lines.

The experiment was conducted only once in triplicates. The results showed that the calcium response to CPA addition remained unchanged from Log [CPA] of -10 to -5 (100pM to10μM), with no significant difference from the control test (one-way ANOVA, Tukey's Multiple Comparison Test). At 100μM, CPA induced a significant calcium response in all cell lines ($p < 0.05$, one-way ANOVA, Tukey's Multiple Comparison Test).

Even though the experiment was only performed once, subsequent experiment of the effect of CPA on ADP dose-response relationship was performed based on the information obtained so far. This trial test was aimed only for a quick examination in aid of further planning for the project. In this experiment, ADP dose-response curves were determined in the presence and absence of 10μM CPA, which had been shown to be the highest possible concentration of ligand that will not induce a calcium response. The data shown in Figure 30 was also a single experiment performed in triplicate. In this figure, the ADP control response did not show the same curve as observed before: the biphasic response was no longer obvious. The hA_1-24 cell generated little responses between log[ADP] of -11 and -5.5, followed by a sudden increase in the calcium response from log[ADP] = -5.5 onwards. This curve differs slightly from the results obtained in section 4.4.2, where the G14T-13 cell also failed to produce a clear biphasic response. The G14T-13 cell response to ADP activation between log[ADP] of -8 and -4; showed a large degree of fluctuation between log[ADP] of -5.25 and -4.75, which looked like a second plateau phase; the response experienced a sudden steep increase as the log[ADP] increased from -4.75 to -4. Although these results differ from hA_1-24 data presented in Figure 30, evidently, in both cases the biphasic ADP concentration-response curve was no longer observable. The addition of 10μM CPA elevated the calcium responses between -8.5 and -4 of log[ADP]. However, due to the high degree of scattering, it is difficult to determine the dose-

response relationship from these data points. Moreover, the large magnitude of error renders the reliability of the data. In general, it is impossible to make conclusions about the effect of CPA on the ADP-induced calcium response pathway due to the failed control test in this paired experiment, despite the seemingly augmented ADP responses in the presence of CPA activation.

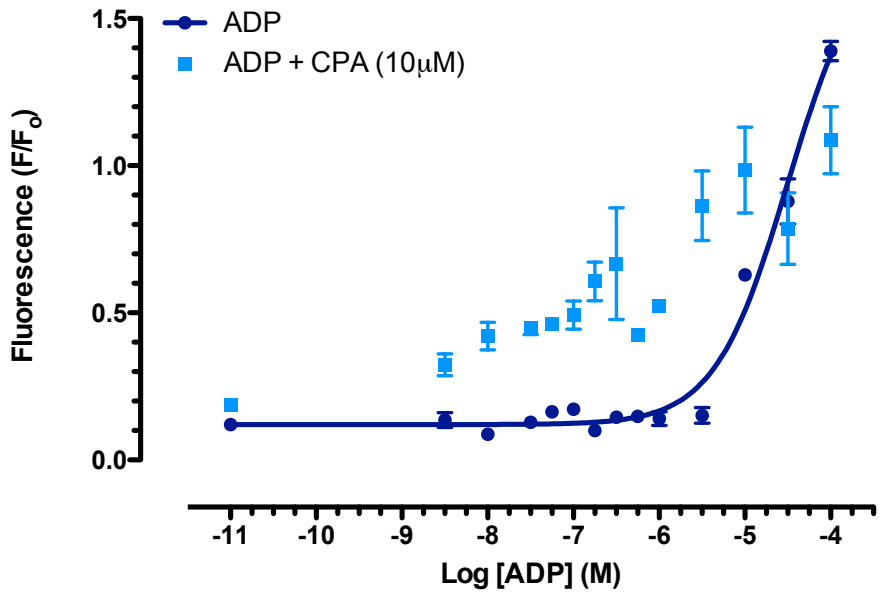

Figure 30. ADP concentration-response relationship change in the presence of CPA.

This is a single trial paired experiment, which was performed in triplicates. The biphasic ADP concentration-response relationship is no longer observable. ADP failed to elicit any calcium response between log[ADP] of -11 and -5.5; a sharp increase in the response was observed beyond log[ADP] of -5.5. In the presence of CPA, calcium responses were elevated at log[ADP] range between -8.5 and -4. The dose-response curve was not determined due to both high degree of data scattering and large magnitude of error bars. The true effect of CPA to the ADP concentration-response curve could not be concluded since the control ADP response differed largely from expectation.

4.5 INVESTIGATION INTO THE INCONSISTENT BIPHASIC ADP CONCENTRATION-RESPONSES

Previously I had observed a biphasic concentration-response curve for ADP in cells that co-express A_1R and $P2Y_1R$. This result had been confirmed by repetitive experiments ($n \geqslant 6$) in both hA_1-24 and G14T-13 cells, as was described in section 4.3. It was highly suspected that the high- and low-potency phases are the consequence of $P2Y_1R$ and A_1R:$P2Y_1R$ heterogeneous receptor populations. Subsequent experiments conducted based on such observations had been focused on the analysis of the pharmacological profiles for these two components, by which, further confirmation on the nature of the two potency sites may be possible in the absence of any physical interaction assays. However, it had occurred that the biphasic dose-response relationship was no longer detectable in both G14T-13 and hA_1-24 cells, instead, more scattered data points and delayed/ shifted responses were recorded in both cases. These directly affect the processing of other important data obtained in the paired experiments, hence results were incomparable. It is therefore, essential to find out the reason(s) for the inconsistency in the results obtained for the ADP concentration-response curve in order to progress in the project. The investigations looked into the problem at two main aspects: 1) experimental reagents and facilities; 2) cell culture techniques, which includes passaging number and cell conditions at the time of assay. For reasons that most of the results

collected from these trials and tests were negative, only the most significant findings will be presented below.

4.5.1 Reagents and Facilities

During the PhD, the FLIPR-1 machine was subjected to decommission and replacement with the latest FLIPR-TETRA. All experiments performed in this chapter were assayed using the FLIPR-1 machine, and all assay kits used, including the buffer, dye and probenecid contained, were of the same Lot number. These are least likely to cause the differences in the ADP concentration-response curves.

Another possible and more direct cause of the problem could be from the integrity of ADP. As previously tested, the pH of the ligand did not change through the serial dilution process. More assays were performed using a new tube of aliquot from the same stock solution as the ones used when the biphasic curves were first detected and confirmed in section 4.3, since, repeated cycles of freezing and thawing may lead to degradation of the ligand, especially the phosphate group on ADP. Subsequently, a separate tube of ADP stock solution was made from its powder form, and assays were repeated using aliquots of this newly made stock solution. However, neither of these methods had led to any improvement of the curves.

In addition, samples of ATP, ADP, AMP and adenosine were examined using the mass spectroscopy, by a trained specialist in the department, which proved no degradation for any of the ligands (results not shown).

From the above, the test results had helped to exclude almost all the possibilities that could be related to the use of ligand, assay reagents and machinery. It is thus worth investigating the cell systems; in other words, the culture techniques and cell conditions during the assays.

4.5.2 Cell Systems

4.5.2.1 Passaging Number

Cells cultured in the tissue culture flask were healthy. There was no contamination/ infection observed, neither was the growth rate changed. Cells were normally split at 1:10 ratio with respect to the tissue culture flask surface area. Before each assay, the 96-well cell plates were checked under microscope for cell confluence level as well as possible infections. These procedures were kept consistent throughout the entire PhD project.

Meanwhile, intensive literature researches were carried out, mainly focusing on the $P2Y_1R$ signalling and responses. A particular paper

had come to attention, which mentioned the loss of $P2Y_1R$ response after certain number of splittings and passagings[210]. According to the description, HEK 293 ceased to produce a clear calcium response to ADP β S activation, after more than 30 splittings. The paper indicated that such observation was not a result of the loss of $P2Y_1R$, as the immunocytochemical test confirmed the expression. Furthermore, it had also shown a retarded single-cell response after five times repeated addition of the ligand at 20 minutes intervals, whereby the calcium response was finally restored. Such findings were based on a different biological system, and the detection methods and conditions were significantly different from the FLIPR techniques. Nevertheless, in both cases the cells endogenously express the $P2Y_1R$, and demonstrated delayed calcium responses, which requires increasing concentration of agonists. Since the FLIPR experiments had been using cells passaged for over 20 times, it seems worth trying cells with lower passage numbers.

The hA_1-24 and G14T-13 cells were thawed from the freezing stocks, both of which had been splitted for less than five times. After repeating the same experiment using ADP, there was still no improvement on the results. Not only for the loss of ambiguous biphasic shape, more importantly, the intermittent observation of the largely scatter data points, which was similar to the (ADP + CPA) results shown in Figure 30, that made the results unreliable and

incomprehensible, thus unable to draw a conclusion for the exact dose-response relationship, if not biphasic.

4.5.2.1 Cell Confluence Level

So far, numerous experiments had been performed to characterise the calcium response profile in the A_1R co-expressing CHO cells, hA_1-24 and G14T-13. However, no further classical biphasic response was detectable, neither was it possible to conclude for the dose-response relationship based on the current results obtained.

The cell density/ confluence level at the assay had come to attention since the cAMP assays were performed whilst at the same time the investigation for the ADP calcium response was carried out. During which time, the cAMP assay had yielded good results for the forskolin responses from the G14T-13, implying standard cell properties. The experimental protocols for the FLIPR and cAMP assays were compared, and subsequently realised that the cell density level might be the cause of the problem. In the cAMP assay, cells were lysed after incubation and cAMP production level reached equilibrium; followed by a series of multiple procedures including solution transferring, centrifugation and cleaning for cell debris, washing, filtration and finally elution from the columns. All of which resulted in an inevitable loss of some of the cAMP products, without

further considering the loss by hydrolysis throughout the whole process. Mainly for this reason, the cells were cultured to a very confluent level in order to maximise the amount of cAMP production. On the other hand, this is not necessary for the FLIPR assay as the protocol required minimal steps: dye loading and incubation and the detection systems are efficient and highly sensitive. Cells prepared for the FLIPR assay were normally aimed for about 80% of growth area (here after referred to as 'sub-confluent'), at which state, the fibroblast cells exhibits the signified 'extended' morphology (Figure 33). However, there was no clear specification for cell densities at the time. As a result, cells for FLIPR assay were unintentionally cultured to very confluent levels (here after referred to as over-confluent) with the cAMP assay cell plates.

In order to test such hypothesis, FLIPR experiments were performed with cell plates prepared at different densities. The sub-confluent level, when the cells spread and occupy approximately 80% of the surface area (Figure 33), is the regular standard protocol by which the clear biphasic curves were observed. At over-confluent levels, the cells were grown for a full 24 hours beyond the 80% point, where there is no observable surface gaps remaining. Cells were grown tightly against each other at such dense level so that the 'extended' morphological shape was no longer maintained (Figure 33). Additional experiments showed that for optimal detections, a minimum of 50% confluence was required (data not shown). As

expected, the biphasic dose-response curves were observed once again at sub-confluent cell density, the $logEC_{50}$ values for both sites were not significantly different from the results describe previously; whereas, at over-confluent levels, the curves did not show biphasic shape (Figure 31 and 32).

At sub-confluent cell density, the biphasic concentration-response curve observed resembles the same pharmacological characteristic as the curves describe previously (Sub-Confluent, Figure 31 and 32). In hA_1-24 cells, the $logEC_{50}$ values for both higher and lower-potency sites were approximately -6.95 and -5.36 respectively, as calculated by Hill-plot. G14T-13 cells also yielded similar responses, that the higher-potency $logEC_{50}$ is approximately -7.18, and the lower being -5.27. The loss of the biphasic response was detected with over-growth of cells (Over-Confluent, Figure 31 and 32), shown by the connected lines. Such behaviour of response seemed the same as the ADP dose-response curve data presented in Figure 30 (hA_1-24) and 27 (G14T-13). The estimations modelled using the three-parameter equation (preferred over the four-parameter variable fit) showed the $logEC_{50}$ was approximately -4.48 and -4.95 for hA_1-24 and G14T-13 cell lines, respectively. This is an indication that the cell confluency level is a crucial condition for the detection of biphasic concentration-response pharmacology, and was proved by three repeated trials.

As a result of the investigation between different cell densities to the calcium response curves, the sub-confluent cell level was chosen as the most suitable condition for further experiments. During the project, the FLIPR machine was shared between departments, occasionally cells were cultured longer than scheduled due to the machine availability reason. It therefore appeared that the concentration-response had altered due to various extents when cells were being left for further growth to a density slightly higher than 80%. This was defined as the 'confluent' level of growth shown in Figure 33, while the 'extended' shape was maintained. The cell density may fluctuate throughout the experiments from slightly above 80% to just below 100%, since the incubation length was not strictly controlled; yet in each case, further growth was still possible for the cells to occupy the remaining visible surface areas. Such culture conditions opposed several effects on the concentration-response curve, depending on the cell line types. However, this observation did not cause any huge problems to the experiment, as it can be solved very easily, by booking on the FLIPR machine so that the length of cell growth can be controlled.

In the hA_1-24 cells (Confluent, Figure 31), the curve was more close to containing three components, i.e. triphasic curve. The data points were connected by segmented line, from where it is not difficult to notice that the first plateau is defined between -6.75 and -7.5 of log[ADP], and the second between -5.75 and -6.5; the third plateau

may be defined between -5.25 and -4.5. At concentration higher than -4.5 log units, the response showed a continuing tendency for increment, which made the curve more complex for analysis. In addition, the data points collected between -6 and -9 log[ADP] coincide with the higher-potency fragment of the biphasic curve obtained at sub-confluent levels, even though varying degrees of scattering made this part of the curve resemble a multi-component feature. It is difficult to conclude whether the lower-potency phase of the biphasic curve was significantly shifted towards the right, solely based on the data collected at the confluent level. However, compared with the 'over-confluent' result, it might be possible that the dose-response curve graduated shifts towards the right when cell density level increases.

Interestingly, the response detected from the G14T-13 cells did not yield the same curve as the hA_1-24 cells at confluent levels. As Figure 32 (Confluent) shows, the data produced revealed higher degrees of scattering compared with the hA_1-24 results. The segmented line connecting all data points best illustrated the relationship between the calcium responses to increasing ADP concentrations, that there is no strong evidence to conclude whether the curve bears biphasic or multi-component characteristics, the main reason being the repeated fluctuations of the responses. However, by evaluating the response spans across the concentration range, it seem clear that the calcium response was observed from

approximately log[ADP] of -8.5, which then continued throughout the entire range of concentrations tested; at -4 log[ADP], the highest available concentration, the response may have reached the maximal. The large scale (about 4 log units) of concentration range implies the possible existence of a dose-response curve, which may contain more than one phase. The Prism software modelled such concentration-response relationships, and showed the best-fit equation was four-parameter variable curve, and the logEC_{50} was approximately -6.98, similar to the value obtained for the higher-potency phase of the biphasic curve.

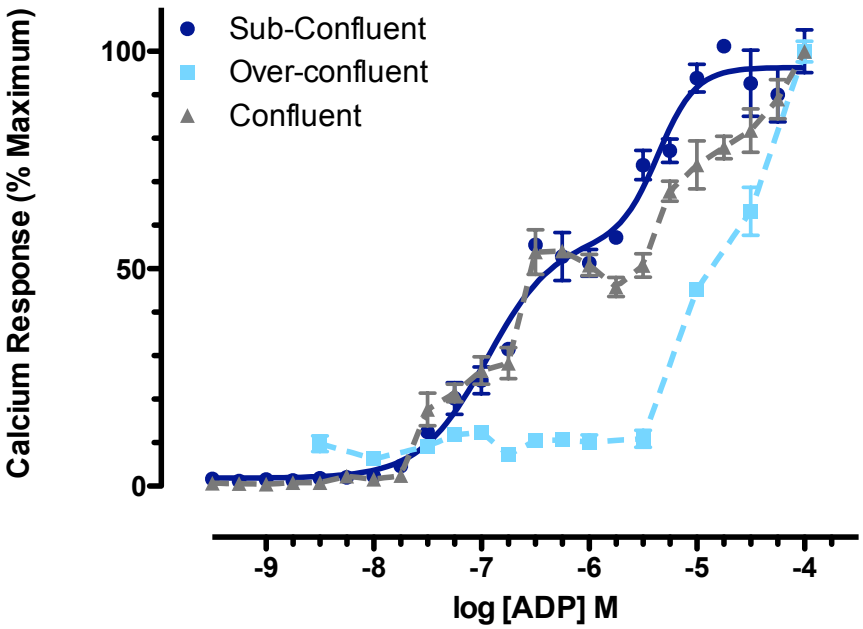

Figure 31. The ADP stimulated calcium response in hA_1-24 cell at sub- and over-confluent and confluent cell densities.

This is a representative figure for three repeated tests. Experiments between the sub-confluent and over-confluent conditions were paired. The effect of cell density and confluency level was being noticed and measured at a much later stage. All responses were normalised to the maximum fluorescence level for the purpose of comparison between all three conditions. It is only at a sub-confluent cell density, that a clear unequivocal biphasic curve was observed. At a confluent level, the dose-response curve was more close to having three components, whereas at over-confluent levels, only a single component was observed.

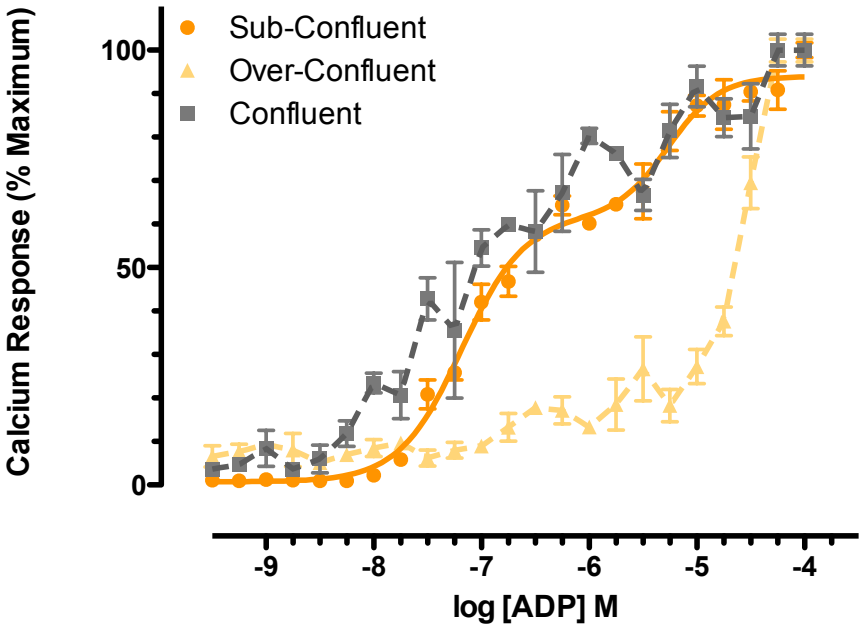

Figure 32. The ADP stimulated calcium response in G14T-13 cell at sub- and over-confluent and confluent cell densities.

This is a representative figure for three repeated tests. Experiments between the sub-confluent and over-confluent conditions were paired. The effect of cell density at confluent level was being noticed and measured in a much later stage. All responses were normalised to the maximum fluorescence level for the purpose of comparison between all three conditions. It is only at sub-confluent cell density, that a clear unequivocal biphasic curve was observed. At confluent and over-confluent levels, only a single component was observed from the dose-response curve, with higher degree of scattering at confluent density. The potency level decrease as cells were grown from confluent to over-confluent levels.

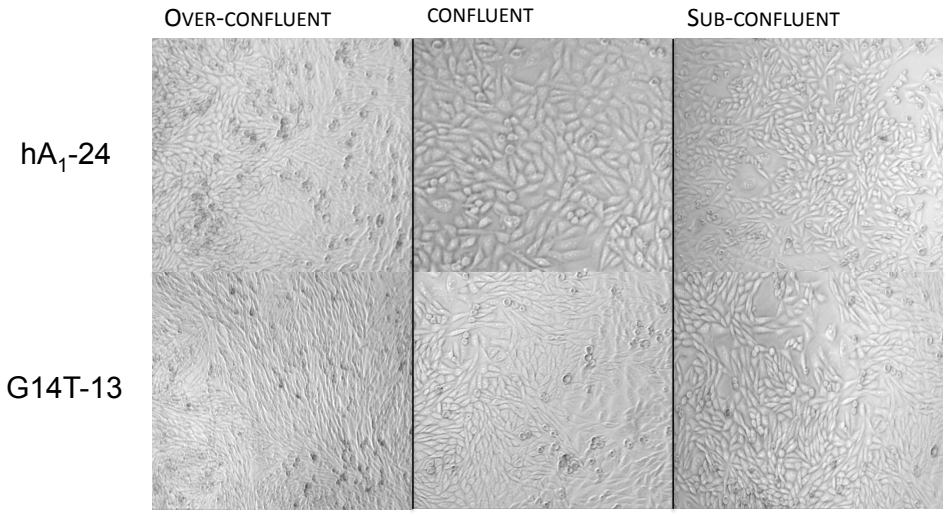

Figure 33. The pictorial presentation of the confluence levels of hA1-24 (Top) and G14T-13 (Bottom) cells used in the assays.

When the cells become over-confluent (left column), they grew tightly against each other, and become elongated. At sub-confluence level (right column), there were approximately 20% of the plating surface areas available for further growth of the cells. The cells were loosely in contact, and maintained the normal morphology. Confluent level (middle column) was defined as the cell density being slightly above sub-confluent, such that they occupy about 90% of the growth surface area, and are not yet arranged tightly in contact.

4.6 SUMMARY

Previously, series of investigations carried out by Yoshioka *et al* had shown the A_1R and $P2Y_1R$ form functional heteromers, that the $P2Y_1R$ agonist ADPβS induced a $G_{\alpha i}$-coupled response leading to inhibitions in the forskolin-stimulated cAMP accumulation. In Chapter 3, it was observed that the natural-occurring $P2Y_1R$ agonist ADP displayed a concentration-dependent $G_{\alpha i}$ response in G14T-13 cells. Therefore, it was necessary to examine the $G_{\alpha q}$-coupled signal transductions, whether the response will be altered or attenuated by the activation of $G_{\alpha i}$ responses.

In this chapter, I have shown that the ADP concentration-response revealed differential relationships in three cell lines. In CHO.K1 cells, ADP displayed a sigmoidal concentration response, whereas in cell lines that are stably transfected and express A_1R (wild-type and mutant), the dose-response curves were biphasic. The biphasic concentration-response curve had not been reported previously in the literature. Although the Yoshioka group identified the functional heteromeric receptor responses, little information was available for the $G_{\alpha q}$ response: the paper claimed that the potency of ADPβS was reduced in A_1R and $P2Y_1R$ co-transfected cells compared with those transfected with $P2Y_1R$ alone?; and the $G_{\alpha i}$-coupled response might

have been more sensitive to ADPβS stimulation than the $G_{\alpha q}$ response, which is indicated by the IP_3 production level[103]. However, there was no evidence for the concentration-response curve representing the $G_{\alpha q}$ signals.

The calcium response elicited by ADP in CHO.K1 cells is a sigmoidal dose-response curve with a potency of approximately 72.4nM ($logEC_{50}$= -7.14). In G14T-13 and hA_1-24 cells both curves are biphasic, with similar potency levels for each phase. Both phases of the dose-response curve share approximately equal proportions. The EC_{50} values calculated for the higher-potency phases were 59nM and 77.6nM for G14T-13 and hA_1-24 respectively ($logEC_{50}$= -7.23 and -7.11); for the lower-potency phase, the values were 2.0μM and 2.45μM ($logEC_{50}$ = -5.70 and -5.61). In addition, statistical analysis showed the potency level obtained in CHO.K1 cell was not significantly different from the higher-potency EC_{50} of both G14T-13 and hA_1-24 cells.

All experiments performed for ADP responses had used the same reagents and facilities. The experimental conditions were strictly under control. Test trials had also been carried out for both G14T-13 and hA_1-24 cells coupled with the CHO.K1 cells, which revealed a high degree of consistency in the results obtained. In addition, the pH level for all diluted ADP samples were measured, which showed no significant difference between the pH for all concentrations of ADP.

Therefore, the biphasic ADP response is most likely due to the differences in cell lines, that the G14T-13 and hA_1-24 cells express either the mutant or wild-type A_1R, whereas CHO.K1 cells lack any A_1R. It was postulated that the high-potency phase of the biphasic curve might be a representation of the non-heteromeric $P2Y_1R$ response to ADP, as displayed by the CHO.K1 cell; since the EC_{50} values remain the same. On the other hand, the lower-potency component probably corresponds to the heteromeric A_1R:$P2Y_1R$ complex, which may coincide with the findings by Yoshioka *et al*, (date?) that the ADPβS potency level showed reduction in the A_1R and $P2Y_1R$ co-transfected cells. Nevertheless, these experiments had answered a question that unlike the ADPβS-stimulated $G_{\alpha i}$ response, the ADP-activated $G_{\alpha q}$ calcium response can be observed in both G14T-13 and hA_1-24 cells.

The hypothesis proposed about the different potency components and the population of the receptor types needed to be confirmed. The most direct methods namely co-immunoprecipitation and bimolecular fluorescent complementation techniques were not available at the time for detection and receptor heteromerisation. Pharmacological tests were, therefore employed in order to focus on the signalling properties of the low-potency phase of the curve, which was postulated to correspond to the A_1R:$P2Y_1R$ heteromers. The analysis mainly aimed to determine whether any correlation existed between the G14T expression level (as well as the A_1R activation status) and

the proportion of the low-potency fraction of the curve. In other words: 1) if increasing G14T expression level will result in the extension in the upper-part of the biphasic curve, and reduction in the lower-part fraction; 2) if activation of the wild-type A_1R facilitates the formation of heteromeric receptors thus leading to the increase of the top fraction of the biphasic curve. Unfortunately, these experiments did not succeed, mainly due to the G14T-13 and hA_1-24 ADP concentration-response curves failing to reproduce the same results as previously characterised. The results lack any reliable and comparable controls.

Experiments performed in G14T cell lines included 6 G14T-transfected cell lines with varying expression levels, ADP and 2MeSADP responses were being examined. All curves showed a large degree of data scatterin, and the biphasic model fits became ambiguous. In some cases, the scattered points showed a tendency for a triphasic curve. Moreover, especially for the G14T-13 curve, a discrepancy in the two potency phases were also observed in some cell lines, such that the lower part of the curve was minimised and the upper section was largely extended as the response experienced a sharp increase from a certain concentration point onwards. On the other hand, the hA_1-24 cells were used to determine the ADP concentration-response relationship in the presence of CPA stimulation. The calcium responses to varying concentration of CPA were detected in CHO.K1, G14T-13 and hA_1-24 cells. The results

showed no significant induction of calcium signals at all concentrations except at 100μM (log[CPA]= -4), and there was no difference between the cell lines at any defined concentration. The sudden increase of calcium response at 100μM is unlikely due to any synergistic effect from the $G_{\beta\gamma}$ subunit release, since the CHO.K1 cell does not express any A_1R. The exact reason for this is unknown, but could be due to a change in the pH level at high ligand concentration. Nevertheless, it can be concluded from the experiment that 10μM (log[CPA]= -5) is the highest possible concentration, at which CPA will not results into any calcium responses, thus was used in subsequent experiments characterising the ADP concentration response whilst the A_1R is being activated. The later investigation of ADP response in the presence of CPA did not produce any desirable results either. The ADP concentration-response curve for hA_1-24 cells was no longer biphasic, and shifted greatly towards right. In the presence of 10μM CPA stimulation, the data collected contained high degree of scattering, and the curve modelling becomes very difficult. Even though the ADP response in the presence of CPA was elevated from the control, since neither set of results was reliable, no conclusion could be drawn from these.

To this point, the research direction was switched to the investigations for the loss in the biphasic feature of the ADP concentration-response curves. The curves were previously confirmed by at least 6 repeated experiments, and the research

objectives were built step by step based on these findings. It is therefore vital to be able to reproduce these biphasic concentration-response curves before further studies could be planned and carried out. Two aspects of the assay had been examined: 1) the reagents and FLIPR detection facilities; 2) cell systems. During the PhD project, the FLIPR-1 machine was decommissioned a few months before the new FLIPR-tetra machine was purchased and set up. However, all experiments and repeats that confirmed the biphasic dose-response curves were performed on FLIPR-1 machine. Since the loss of the biphasic feature was also identified when FLIPR-1 machine was in use, it is unlikely that the changes in response could be related to the detection facilities. In addition, all reagents used were supplied as a kit, although different kits may be used, all of which were of the same Lot number. In case of degradation, ADP stock solutions and aliquots were prepared from fresh powder form as originally supplied by the company, and its integrity was verified by mass spectroscopy, which was carried out by a trained specialist in the department (result not shown). Despite all, the curves could not retain the biphasic shape. On the other hand, after excluding the possibilities of cell passage number, culture condition that may exert effect on the ligand responses, it was finally identified that the cell confluence level at the time of assay played a key role in the ADP concentration-response relationship. It is worth stating that all these experiments were performed using the FLIPR-1 machine, before decommission.

The biphasic curves were obtained when cell densities were approximately 80% of the culture surface area, which was defined as 'sub-confluent' in this thesis. At 'over-confluent' level, where the cells were left in the incubator at least 24 hours exceeding the 'sub-confluent' states, growth occupied the entire tissue culture surface area, and cells where much elongated and contracted than the morphology observed at the sub-confluence level. The biphasic concentration-response curve was no longer obtained. Instead, the curve was shifted profoundly to the right. The EC_{50} values estimated by the three-parameter equations showed the potency levels of which were lower than for the upper-component of the biphasic curve. These were -4.48 and -4.95 ($logEC_{50}$) for hA_1-24 and G14T-13 respectively. At concentrations less than 10μM (log[ADP]= -5), the responses were very low and displayed levels of fluctuations. In particular, the response increased abruptly beyond 10μM ADP, and persisted so that it is could not be concluded straightforwardly if it had reached a plateau. It was also noted that when cell density levels exceeds 80%, the response becomes relatively unstable compared to the biphasic characteristic. As an example, at 'confluent' level, where the growth level is marginally above 'sub-confluent', the biphasic concentration response started to become ambiguous or even displayed monophasic trend. Data collected showedf degrees of scattering compared with the more steady and smooth biphasic curve, which was interested to my research.

Chapter 5

Antagonism of A_1R:$P2Y_1R$ Functional Responses

5.1 INTRODUCTION

In Chapter 3, I described that the ADP-induced cAMP reduction was thought to be due to the response of the A_1R:$P2Y_1R$ heteromeric receptor. This is thought to be caused by the heteromeric receptor complex inducing an A_1R response via activation by the $P2Y_1R$ agonist. Even though the evidence for the physical interaction between the two receptors was not confirmed in the work reported in this thesis, various literature reports show that the two receptors form a heteromer in the absence of any ligand. The literature reports are described in Chapter 1. In support of the heteromer formation, FLIPR assay results revealed biphasic ADP concentration-response curves in wild-type or G14T mutant A_1R-transfected cell lines (hA_1-24 and G14T-13). This response was not seen in untransfected wild type CHO.K1 cells,. Our results suggest that the $G_{\alpha q}$-coupled signalling pathway can involve a heterogeneous population of $P2Y_1R$. Data analysis reveals that the EC_{50} value for the more potent response (in both hA_1-24 and G14T-13 cell) is not significantly different from the ADP response induced in CHO.K1 cells. The less potent response is though to be due to the A_1R and $P2Y_1R$

heteromerisation. The agonist ADP, thus, seems to be able to elicit both $G_{\alpha i}$- and $G_{\alpha q}$-coupled responses simultaneously, most likely via the A_1R:$P2Y_1R$ heteromer. It was also noted that, the functional (heteromeric receptor) $G_{\alpha i}$ response was detected only when the G14T mutant, but not the wild type, A_1R was expressed. However, the biphasic ADP concentration-response curve was obtained regardless of the type of A_1R used to transfect the cells. In the absence of Co-IP and structural biological studies we will use antagonist pharmacological investigations to provide evidence for signalling profiles. This will indicate whether the response is induced via receptor activation or a response to downstream cross-talk events of a signalling pathway. This chapter describes experiments on the inhibition of heteromeric receptor signalling via cAMP and the calcium pathway by several purinergic receptor antagonists, Antagonists used include DPCPX (the most potent A_1R antagonist), MRS 2179 (a selective $P2Y_1R$ antagonist) and MG 50-3-1(a novel $P2Y_1R$ antagonist).

5.2 ANTAGONIST INHIBITION OF ADP-INDUCED $G_{\alpha i}$ RESPONSE

Primary experimental evidence in the lab suggests that the functional $G_{\alpha i}$ response, via the A_1R:$P2Y_1R$ heteromer, requires a G14T mutant A_1R. The mutant is reported to be constitutively active to present in

the cell line. To explore the pharmacology of the cAMP response we used the G14T-13 cell line as our model. Investigations carried out on this cell line did not reveal evidence for constitutive activity of G14T A_1R. Instead, a concentration-response curve for ADP was obtained. This result further supports the observation of an ADP-induced functional $G_{\alpha i}$ response. Arguably this response could be due to various indirect causes other than the receptor heteromerisation leading to a novel agonist pharmacology. For example, ADP hydrolysis and synergistic effect is sometimes observed in GPCRs. To determine if this was the case the ADP concentration response, detected in G14T-13 cells transfected with either A_1R or $P2Y_1R$ were subjected to antagonist inhibition. The effect of the antagonist on the parental CHO.K1 cells was used as a control for non heteromeric $P2Y_1R$ signalling events.

Forskolin (F, 10μM) was used to stimulate cAMP production above the basal levels and 1mM ADP to activate the A_1R:$P2Y_1R$ and inhibit the forskolin response (Fig. 34). This is the highest available concentration of ADP, which maximally inhibits the cAMP concentration. In addition an excess amount (100μM each) of DPCPX, MRS 2179 or MG 50-3-1 was applied to ensure the complete antagonisation of the forskolin-induced cAMP production. The results obtained are expressed as a percentage of the forskolin response (% Forskolin).

As shown in Figure 34, basal cAMP, in the absence of forskolin, was very low (14.98 ± 8.337 %). Forskolin stimulation induced about a 6.7-fold increase in cAMP. The addition of 1mM ADP significantly inhibited the forskolin-stimulated cAMP level by approximately 40% (57.92 ± 1.693% of forskolin response; p=0.0034), indicating a functional response. Varying degrees of antagonism of the ADP response were observed when cells were treated with either 100μM of DPCPX, MRS 2179 or MG 50-3-1 (80.25 ± 0.8914%, 72.46 ± 6.287% and 94.83 ± 0.3221% of the forskolin response, respectively). Although, the inhibitory effects of both DPCPX and MG 50-3-1 upon the ADP response were statistically significant (p= 0.0010 and 0.0022 respectively), the effect of MRS 2179 was not significant; this likely resulted from the relatively increased variation. Of the three antagonists, MG 50-3-1 had a greater effect than DPCPX (p= 0.0011).

The finding that an A_1R antagonist is able to inhibit the functional response of the heteromeric receptor suggests that A_1R activation is an essential requirement for functional response and, the signal transduction process through the A_1R. Given that the functional response was evoked with ADP, it is not surprising to find that the $P2Y_1R$ was able to inhibit the heteromeric receptor activation. However, the data presented here are only preliminary and are data derived from a single experiment. Unfortunately, the experiment could not be repeated because the supplier of the ^{14}C-labelled cAMP,

which is used in the assay as a tracer element to measure the efficiency rate of the Dowex and Alumina columns, discontinued the product line. The product from a new supplier proved unuseable. Three separate syntheses were tested in the cAMP assay, none were found to be cAMP. Subsequently, this was acknowledged by the supplier. Trial experiments carried out in the absence of the tracer produced invalid and unreliable data.

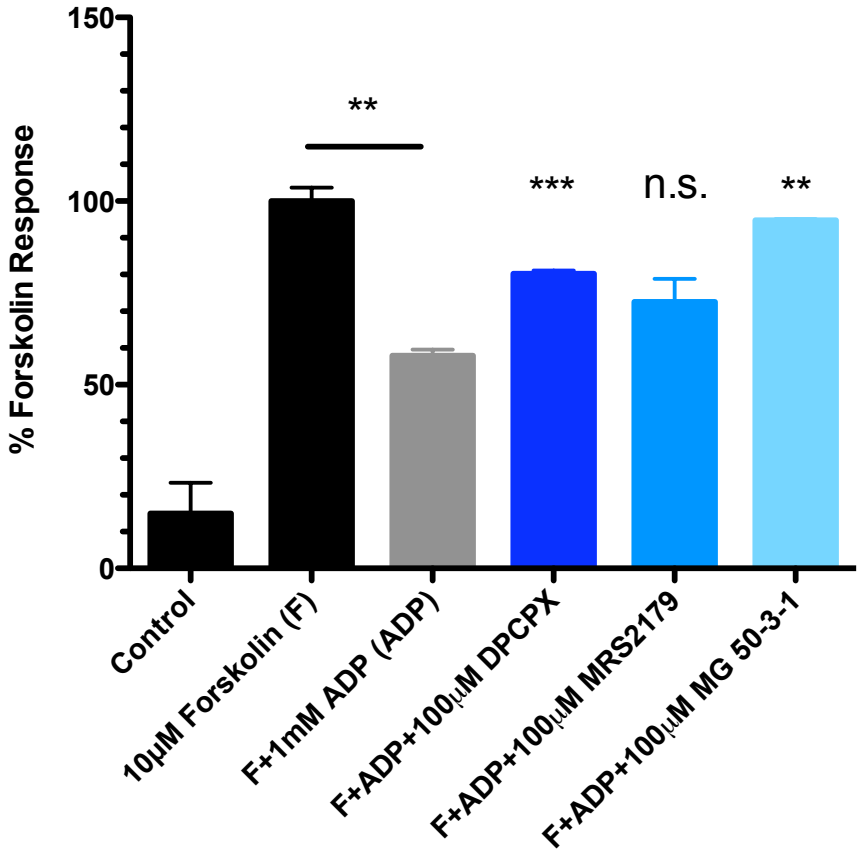

Figure 34. The antagonistic effects of DPCPX, MRS 2179 or MG 50-3-1 on the ADP-mediated inhibition of forskolin-induced cAMP production

10μM forskolin was used to stimulate cAMP production above the basal level. The addition of 1mM ADP inhibited the forskolin-stimulated cAMP response. Inhibition of the ADP-mediated functional response was observed for both DPCPX and MG 50-3-1, but not for MRS 2179.

5.3 ANTAGONIST INHIBITION OF ADP-INDUCED $G_{\alpha q}$ RESPONSE

In Chapter 4, we describe the biphasic ADP concentration-response curve obtained for the $G_{\alpha q}$-coupled response in hA_1-24 cells and in G14T-13 cells. The distinctive ADP potency components, compared with the sigmoidal CHO.K1 curves, suggested a heterogeneous population of receptors in the cell line, probably comprised of non-heteromeric forms of the $P2Y_1R$ and A_1R:$P2Y_1R$ heteromers. Due to the difference in the types of A_1R expressed in hA_1-24 and G14T-13 cell lines, it is postulated that the mutant G14T A_1R receptor may not be a requirement for the $G_{\alpha q}$-coupled response through A_1R:$P2Y_1R$ heteromers, as it was found for the functional $G_{\alpha i}$-coupled response. To test this hypothesis, the A_1R antagonist DPCPX, which was found to inhibit the ADP-activated cAMP reduction in the preliminary data (Figure 34), was examined in G14T-13 cells for its effect, especially on the lower-potency calcium response. The $P2Y_1R$ antagonists MRS 2179 and MG 50-3-1 were also evaluated to characterise their antagonistic profile on the biphasic ADP concentration responses. The same experiments were repeated in CHO.K1 cells and the responses were expressed as the percentage maximum of the fluorescent signal obtained, as described in the Chapter 4.

5.3.1 The Activity of MRS2179 and MG 50-3-1 on Calcium Responses Elicited by ADP in the CHO.K1 Cell Line

The pharmacological profile of MRS 2179 and MG 50-3-1 was first characterised in CHO.K1 cells, as this cell line does not express any A_1Rs. DPCPX was not used for the same reason. The results from these experiments will provide a baseline of $P2Y_1R$ function to use for comparison with the responses obtained in the G14T-13 cell line.

Each of the antagonists was pre-incubated to achieve equilibrium, as described in Chapter 2, at 1μM, 10μM and 100μM final concentration before addition of agonists to the plate and capture for the changes in fluorescence upon agonist addition. In addition, and in a paired experiment, a control ADP concentration-response curve, in the absence of antagonist, was also obtained. For both MRS2179 and MG 50-3-1, a concentration-dependent increase of fluorescence was observed in the control ADP response, as seen previously. However, a parallel rightward shift of the ADP concentration-response curve was obtained for both antagonists, with the extent of the rightward shift corresponding to an increase in the antagonist concentration.

In the case of MRS 2179 (Figure 35), the agonist ADP potency level decreased from $\log EC_{50}$ = -6.659 ± 0.014 (control) to -6.516 ± 0.097, -5.986 ± 0.022 and -5.467 ± 0.092, when incubated 1μM, 10μM and 100μM of the antagonist, respectively. These values were calculated using Hill-Plot analysis on GraphPad® Prism, and are expressed as

the (mean ± s.e.m.) values of three independent and paired experiments, each performed in triplicate. The Schild analysis for competitive antagonism was carried out using GraphPad Prism, and resulted in a Schild slope = 0.767 ± 0.003, showing that MRS 2179 may be a competitive antagonist of the endogenous $P2Y_1R$ in CHO.K1 cells. Therefore, the pA_2 value was calculated, which is approximately -5.490 ± 0.031.

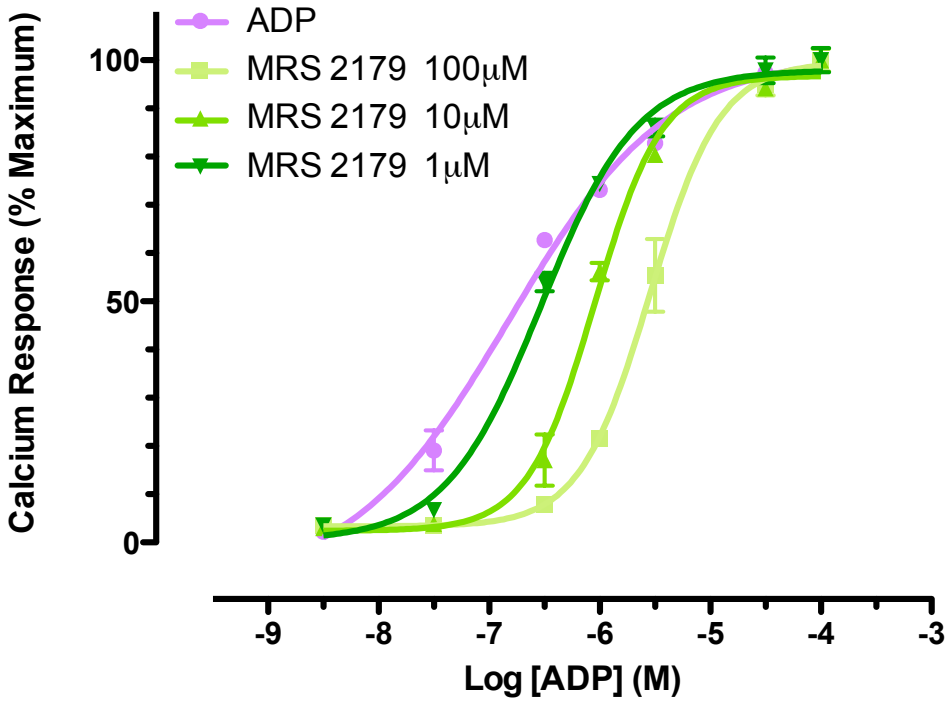

Figure 35. MRS 2179 acts as a competitive antagonist at the $P2Y_1R$

Application of increasing concentrations of MRS2179 shift the ADP response curve towards right in a parallel, concentration-dependent manner (n=3, in triplicates). The ADP potency level is reduced from $logEC_{50}$ = -6.659 ± 0.014 (control) to -6.516 ± 0.097, -5.986 ± 0.022 and -5.467 ± 0.092, when MRS 2179 was applied at 1μM, 10μM and 100μM, respectively. A representative experiment is shown. Data points represent the mean ± s.e.m. of a response determined in triplicate. Potencies represent the mean ± s.e.m. of a minimum of three experiments, each performed in triplicate.

In experiments performed using MG 50-3-1, similar results were obtained (Figure 36). MG 50-3-1 elicited a parallel rightward shift of the ADP concentration-response curve. The ADP potency was reduced from $\log EC_{50}$ = 6.602 ± 0.035 to -6.517 ± 0.015, -6.101 ± 0.026 and -5.259 ± 0.036 with increasing MG 50-3-1 concentration, from 1μM, 10μM to 100μM. All potency values were calculated using Hill-Plot analysis. MG 50-3-1 is also a competitive antagonist at the $P2Y_1R$ receptor, as the results from Schild slope reveal: 1.379 ± 0.0575. The MG 50-3-1 has a pA_2 value of -5.412 ± 0.102. These results were calculated from three independent and paired experiments performed in triplicate.

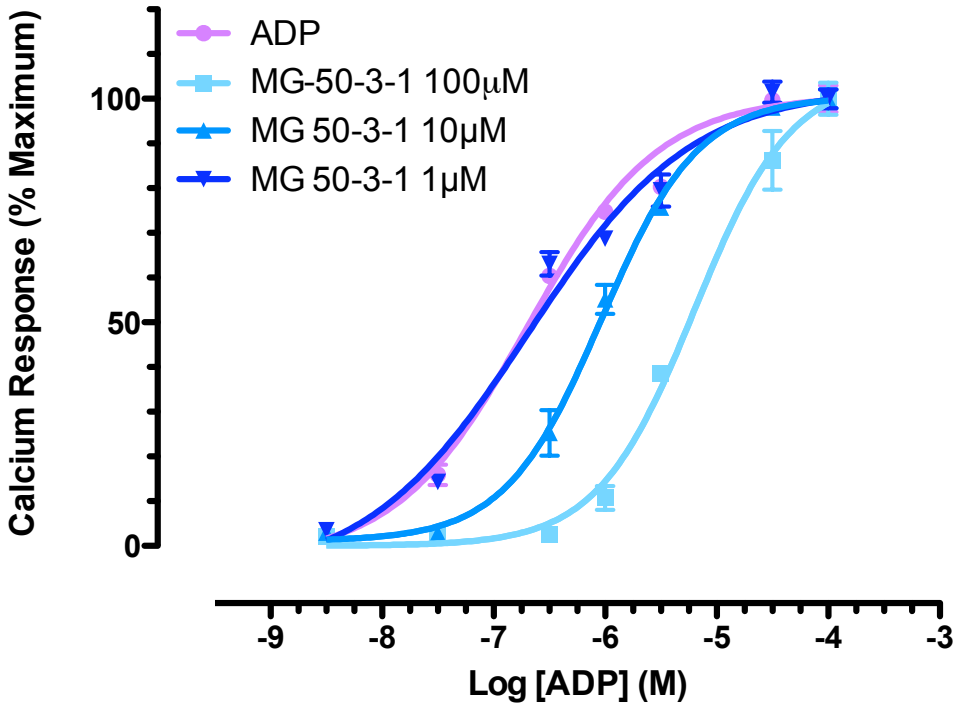

Figure 36. MG 50-3-1 acts as a competitive antagonist at the $P2Y_1R$

Application of increasing concentrations of MG 50-3-1 shifts the ADP response curve towards right in a parallel, concentration-dependent manner (n=3, in triplicates). The potency of ADP in the absence of MG 50-3-1 was $logEC_{50}$ = 6.602 ± 0.035. This value gradually increased to -6.517 ± 0.015, -6.101 ± 0.026 and -5.259 ± 0.036 as 1μM, 10μM and 100μM of MG 50-3-1 were applied. A Schild slope of 1.379 ± 0.0575 indicates a competitive nature of this antagonist, with pA_2 = -5.412 ± 0.102. A representative experiment is shown. Data points represent the mean ± s.e.m. of a response determined in triplicate. Potencies represent the mean ± s.e.m. of a minimum of three experiments, each performed in triplicate.

5.3.2 The Activity of MRS2179, MG 50-3-1 and DPCPX on Calcium Responses Elicited by ADP in G14T-13 Cells

Three antagonists were tested in the G14T-13 cell line, including MRS2179 and MG50-3-1, which were also examined using the CHO.K1 cells, and also DPCPX, which is an A_1R antagonist. The use of the two $P2Y_1R$ antagonists provides understandings of the nature of the biphasic $G_{\alpha q}$ signalling profiles. In particular into the role of $P2Y_1R$ that results in distinctive potency responses to ADP. Despite the lack of evidence for G14T A_1R constitutive activity reported in this thesis, DPCPX application will answer if A_1R activity is obligatory for the less potent $G_{\alpha q}$ signals.

The antagonists were applied as described above, at a final concentration of 1μM, 10μM and 100μM, as a paired experiment for the agonist ADP. For each antagonist, the change in the ADP concentration-response was used as a major estimation for the inhibitory effect. Each antagonist was tested in three independent experiments and triplicate samples were analysed in each experiment.

5.3.2.1 MRS 2179

Application of 1μM MRS2179 yields a biphasic ADP concentration-response curve with a slight difference in the fraction ratio to the

control. In contrast, sigmoidal curves were obtained when 10μM and 100μM antagonists were used (Figure 37). For the control ADP concentration-response curve, the calculated logEC_{50} values were -- 5.21 ± 0.13 and -7.10 ± 0.10 for the lower and higher potency phases, respectively. The addition of 1μM MRS 2179 resulted a minor change to the curve, such that the higher-potency response seems to take a higher proportion. However, the logEC_{50} values obtained for the two distinctive responses were -5.11 ± 0.16 and -6.81 ± 0.15, which showed statistical significance only for the higher-potency response ($p=0.0055$, Table 5). With increasing antagonist concentrations, a substantial parallel rightwards shift was observed, accompanied by the loss of the biphasic characteristic. At 10μM MRS 2179, the logEC_{50} was -5.73 ± 0.240, significantly different from both the higher- and lower-potency responses ($p= 0.0263$ compared with the upper phase, and $p< 0.0001$ for the lower phase). At 100μM, MRS 2179 resulted in a further reduction in the logEC_{50} (-5.11 ± 0.16) and showed no difference from that for the less potency ADP response, but significantly smaller compared with the high potency value ($p<0.0001$).

In addition, as demonstrated in the figure (Figure 37), the antagonist concentration increment is accompanied by a rightward shift of the curve, mainly on the higher-potency fraction for approximately 1.6 log units (100μM MRS 2179 from the control logEC_{50} point), compared with about 0.5 log-unit shifts on the upper phase of the curve.

Despite these results, it is difficult to conclude whether the loss of the biphasic nature of the curve is the sole result of a shift in the first-phase of the curve. To confirm whether this is the case the changes to the second phase of the curve need to be confirmed. This phase was discussed in the earlier chapter and may result from the heteromeric A_1R:$P2Y_1R$. The global curve fitting analysis provides much clearer illustrations to such observations.

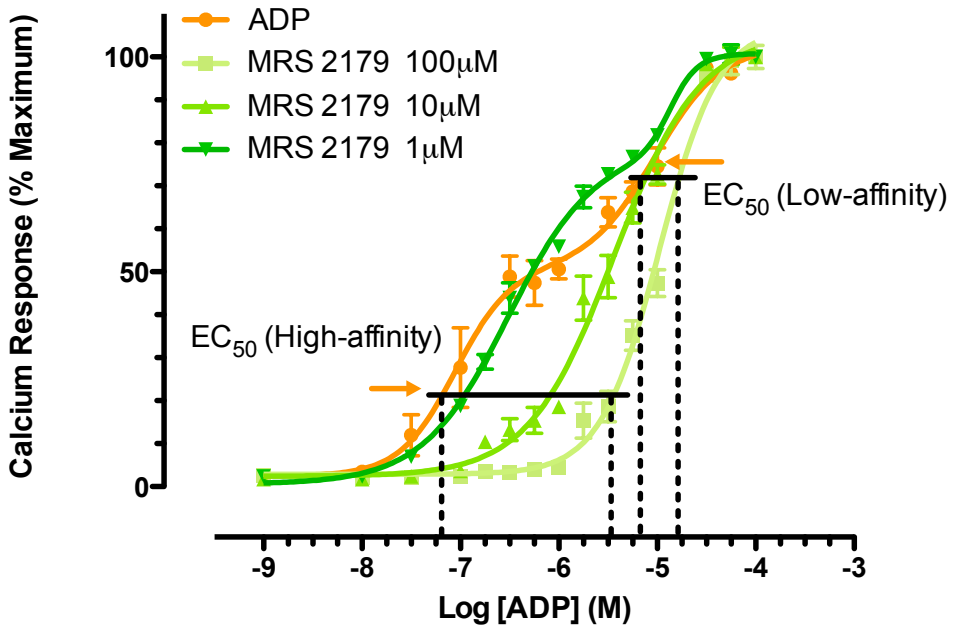

Figure 37. The effect of MRS 2179 on the ADP response in G14T-13 cells.

The calcium response to ADP in the presence of increasing concentrations of MRS2179 (n=3, in triplicates). Horizontal bars indicate the shift in EC_{50} for the two affinity sites. The high-potency part corresponds to the $P2Y_1$ receptor and the low-potency component corresponds to the A_1R:$P2Y_1R$ heteromeric receptor. The logEC_{50} values are expressed as mean ± s.e.m. from three independent experiments, each performed in triplicate.

The global curve fitting analysis was performed using the Graphpad Prism software. This allows constraints to be placed on specific parameters, and enables comparisons to be made between a group of curves or data sets. In this case, constraints were set on the two Hill slope values (nH1 and nH2) for both sections of the biphasic ADP concentration response curve. By constraining the Hill slopes for all conditions to the control ADP response, an assumption is made that the antagonist MRS 2179 induces a parallel shift of the ADP curve at both phases, whether proportional or not. In section 5.3.1, the Schild slope for MRS 2179 was determined to be roughly equal to 1.0, thus it may be acting as a competitive antagonist. The software was used to calculate the other parameters, such as the logEC50 values for both phases and the fraction ratio of the higher-potency phase of the curve.

The mean ADP concentration-response data (n=3) was analysed using the 'Biphasic' curve function. The software estimation for the potency levels of the responses was approximately -7.10 and -5.21 (logEC50, Table 6). The proportion of more potent calcium response is indicated by the fraction ratio (of the first phase to the whole curve), which is 0.56. In addition, the Hill slopes are 1.66 and 1.02 for the high- and low-potency phases respectively. These values were set as constraints for further curve analysis at varying MRS 2179 concentrations. Under such conditions, the analysis revealed a decreasing potency level for approximately 1.3 log units with

increasing antagonist concentration. The logEC50 for the second phase reaction showed little change (Table 6). On the other hand, the fraction ratio changed dramatically from 0.56 to 0.17, this may be due to the decrease in the higher-potency logEC50 values.

5.3.2.2 MG 50-3-1

The effect of MG 50-3-1 on the ADP response resembles the characteristics of MRS 2179 (Figure 38, Table 5). In the absence of antagonist, the ADP concentration-response curve showed a clear biphasic relationship, with the $\log EC_{50}$= -5.18 ± 0.60 and -6.98 ± 0.03 for the upper and lower part of the curve. The addition of antagonist induced a loss of the high-potency phase, and a concentration-dependent rightward shift of the curve. At 1μM of MG 50-3-1 the biphasic relationship was not different from control. When the concentration increases to 10μM and 100μM, MG 50-3-1 inhibited the more potent ADP reaction ($p < 0.0001$ for both case), with $\log EC_{50}$= -5.59 ± 0.08 and -5.23 ± 0.01 values respectively.

These results correspond to the global analysis (Table 6), which showed that the second phase $\log EC_{50}$ remains constant, whereas the first phase of the curve experienced a significant rightwards shift. Although the $\log EC_{50}$ at 10μM MG 50-3-1 only increased for about 0.3 log unit, the fraction ratio had decreased . On the other hand, at a concentration of 100μM, the $\log EC_{50}$ value became anonymous (-

5811), which may due to the dramatic loss of the first phase such that the biphasic assumption is no longer valid.

These results suggest that MG 50-3-1 has a significant impact on the early phase of the ADP concentration-response curve, where ADP potency level is the same as with the reactions to the non-heteromeric $P2Y_1R$. The antagonist may not have an effect on the second phase, where the ADP potency level is significantly lower, and the response is suspected to result from the presence of heteromeric A_1R:$P2Y_1R$ receptors.

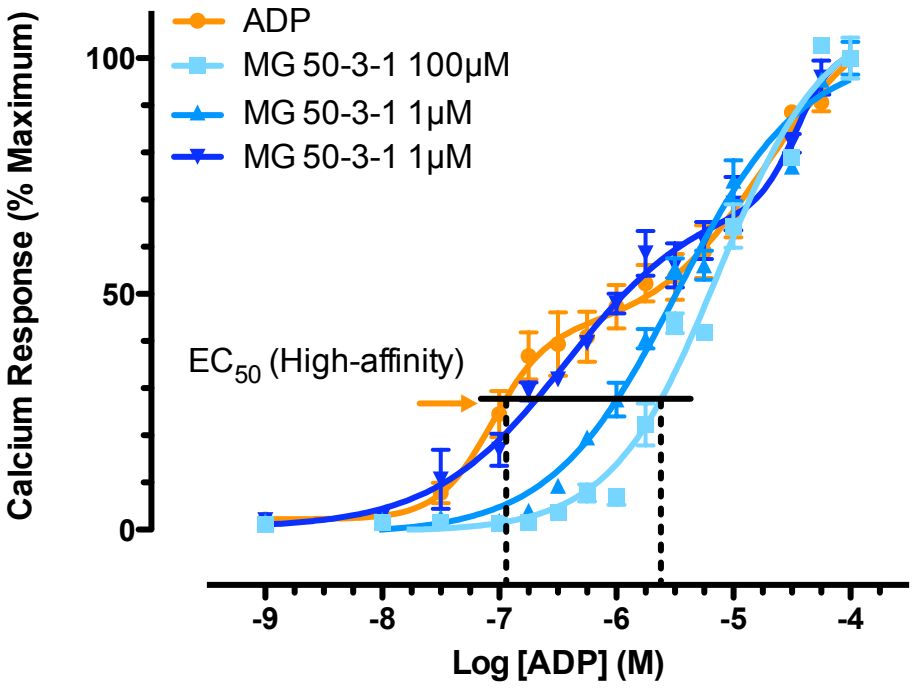

Figure 38. The effect of MG 50-3-1 on the ADP response in G14T-13 cells

The calcium response to ADP in the presence of increasing concentrations of MG 50-3-1 (n=3, in triplicates). Horizontal bars indicate the shift in EC_{50} for the two affinity sites. The high affinity site corresponds to the $P2Y_1$ receptor and the low affinity site corresponds to the A_1R:$P2Y_1R$ heteromeric receptor. The logEC_{50} values are expresses as mean ± s.e.m. from three independent experiments, each performed in triplicate.

5.3.2.1 DPCPX

All concentrations of DPCPX used yield biphasic ADP concentration-response curves with two distinct affinity sites for the agonist (Figure 39, Table 5, 6). Although the curve seems to have a slight rightward shift after the antagonist application at 1μM, 10μM or 100μM, the EC_{50} for both high- and low-potency curve component showed no significant differences. This was further supported by the global analysis (Table 6). DPCPX, an A_1R antagonist, was not expected to exhibit any effect on the calcium response, and indeed, neither part of the curved displayed any significant change to DPCPX. Nevertheless, G14T-13 cells, in which a mutant G14T A_1R, was stably expressed may be sensitive to DPCPX inhibition (Figure 34),. The ADP concentration-response curves were biphasic nature when G14T-13 compared with the wild type CHO.K1 cells, under the same conditions. From these results it is postulated that the low-potency phase might due to the presence of the A_1R, most likely through A_1R and $P2Y_1R$ heteromerisation. The results shown in Figure 39 implicate that the low-potency ADP response, possibly due to the A_1R:$P2Y_1R$ heteromeric receptor $G_{\alpha q}$ signal, is independent of A_1R activation or inhibition.

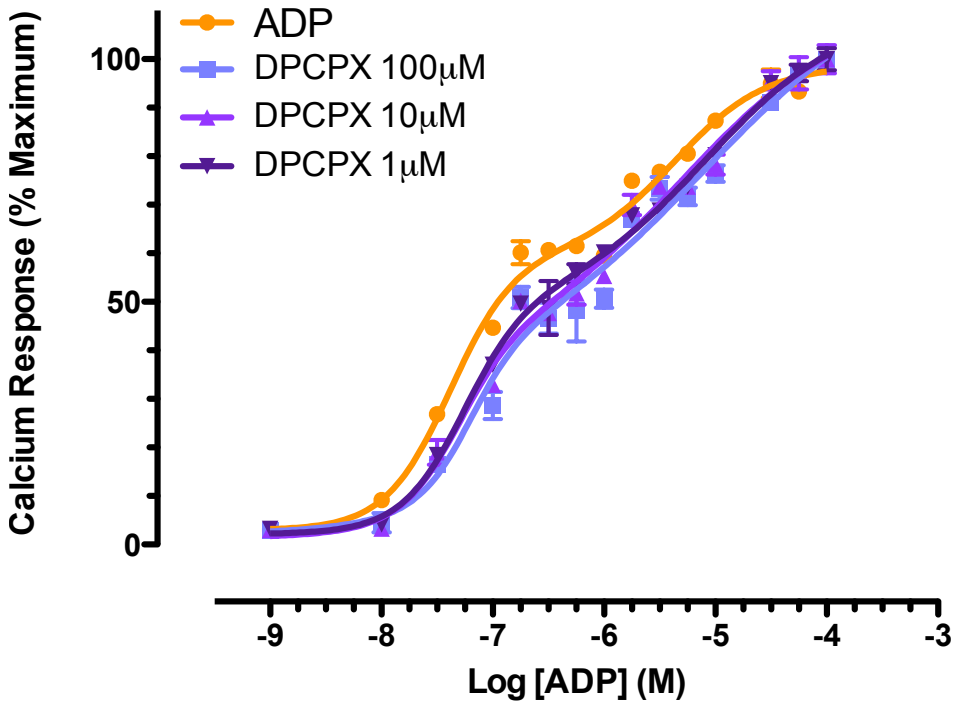

Figure 39. The effect of DPCPX on the ADP response in G14T-13 cells.

The calcium response to ADP in the presence of increasing concentrations of DPCPX (n=3, in triplicates). The high affinity site corresponds to the $P2Y_1$ receptor and the low affinity site corresponds to the A_1R:$P2Y_1R$ heteromeric receptor. The $logEC_{50}$ values are expresses as mean ± s.e.m. from three independent experiments, each performed in triplicate.

Agonist/ Antagonist		Receptor Sites			
		$P2Y_1R$		A_1R:$P2Y_1R$	
ADP		-7.10 ± 0.10	**p value**[a]	-5.21 ± 0.13	**p value**
MRS 2179	1μM	-6.81 ± 0.16	0.0055	-5.11 ± 0.16	-
	10μM	-5.73 ± 0.24	<0.0001	-	0.0263
	100μM	-5.11 ± 0.16	<0.0001	-	-
ADP		-6.98 ± 0.03	**p value**	-5.18 ± 0.60	**p value**
MG 50-3-1	1μM	-6.84 ± 0.15	-	-4.97 ± 0.23	-
	10μM	-5.59 ± 0.08	<0.0001	-	-
	100μM	-5.23 ± 0.01	<0.0001	-	-
ADP		-5.35 ± 0.09	**p value**	-7.39 ± 0.05	**p value**
DPCPX	1μM	-5.28 ± 0.08	-	-7.32 ± 0.02	-
	10μM	-5.32 ± 0.04	-	-7.17 ± 0.01	-
	100μM	-5.41 ± 0.00	-	-7.24 ± 0.04	-

a. statistic analysis was carried out with respect to the control (ADP) for either $P2Y_1R$ or A_1R:$P2Y_1R$ site.

Table 5. Summary table for the antagonistic effects on the $G_{\alpha q}$ response signalled through both $P2Y_1R$ and A_1R:$P2Y_1R$ receptor sites.

MRS 2179, MG 50-3-1 and DPCPX were tested for the antagonistic responses. The $\log EC_{50}$ from three independent experiments were calculated and are expressed as the mean ± s.e.m. value. All data are compared to the control (ADP), and the variations in the mean values are stated when a difference is significant, except DPCPX, for which the responses are not significantly different.

Antagonists		Control	Antagonist Concentrations		
		ADP	1μM	10μM	100μM
MRS 2179	$LogEC_{50}$_1	-7.10 ± 0.10	-6.89 ± 0.03	-6.80 ± 0.11	-5.80 ± 0.22
	$LogEC_{50}$_2	-5.21 ± 0.13	-5.11 ± 0.13	-5.60 ± 0.07	-4.94 ± 0.20
	Fraction	0.56	0.68	0.26	0.17
MG 50-3-1	$LogEC_{50}$_1	-6.98 ± 0.03	-6.84 ± 0.03	-6.65 ± 0.09	~ -5811
	$LogEC_{50}$_2	-5.18 ± 0.60	-4.97 ± 0.06	-5.50 ± 0.06	-5.18 ±0.04
	Fraction	0.40	0.37	0.17	~ 0.00
DPCPX	$LogEC_{50}$_1	-7.39 ± 0.05	-7.20 ± 0.05	-7.21 ± 0.08	-7.14 ± 0.09
	$LogEC_{50}$_2	-5.35 ± 0.09	-5.10 ± 0.08	-5.23 ± 0.10	-5.15 ± 0.12
	Fraction	0.59	0.53	0.51	0.50

Table 6. Summary table for the global curve fitting analysis results.

The hill slope values for both higher- and lower-potency phase (nH_1 and nH_2) were constrained to the control ADP response. The $logEC_{50}$ values and the fraction ratio were calculated and compared at varying antagonist concentrations. The $logEC_{50}$ values were express as mean ± s.e.m. (n=3, in triplicate). The $logEC_{50}$_1 and $logEC_{50}$_2 values are for higher- and lower potency response respectively, and the fraction ratio represents the proportion of the first phase to the whole concentration-response curve.

5.4 ANTAGONIST RESPONSES ARE NOT A FUNCTION OF pH

The pH value of each antagonist at four different concentrations was measured. The dilution samples were prepared at 22°C, which is the same as the temperature of the FLIPR assay when the calcium assay was carried out. 1μM, 10μM, 100μM and 1mM of each antagonist was tested. In the FLIPR assay, all ligands are loaded at 1:10 (v/v) ratio to each well of a 96-well cell plate. This means e.g. that a 1mM working concentration will bring the final ligand concentration in the assay to 100μM. Figure 36 shows that for each antagonist, there is no significant difference in the pH values between concentration ranges from 1μM to 100μM. At 1mM concentration, the pH value shows significant differences from the pH observed at the lower concentrations used for all three antagonists ($p<0.005$ for all comparisons). However, overall there is a relatively small change in the pH at the 1mM concentration, which should not affect the final results since the final concentration of the ligand in the cell plate takes into account the dilution factors, which makes the concentration effectively 100μM. At 100μM, the pH value does not show significant difference from the pH at other concentrations. Therefore, the concentration-dependent pharmacological response of the antagonist is not a result of variations in pH.

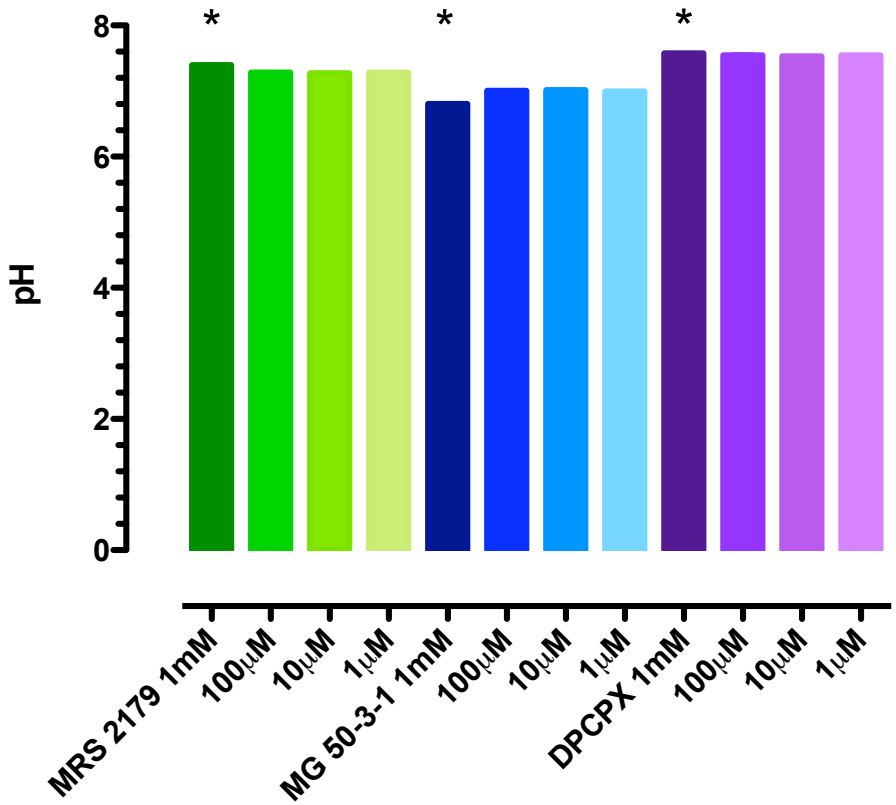

Figure 40. Determination of pH values for antagonist stocks.

The pH value of each antagonist used in the FLIPR assay is shown (n=3). Each antagonist has been tested at concentrations of stock solutions ranging from 1μM to 100μM. At 1mM, the pH level showed significant difference, although the relative change in pH was very small.

5.5 SUMMARY

The findings of the experiments described in this chapter show that the antagonist compounds investigated are able to exert varying degrees of inhibition on the $G_{\alpha i}$ pathway, indicating the activation of both receptors is essential in the $P2Y_1R$ agonist-initiated $G_{\alpha i}$ response. On the other hand, the calcium response through the $G_{\alpha q}$-coupled signalling pathway does not appear to be affected by inactivation of the A_1R constitutive activity, which correlates with the findings presented in the previous chapters. However, the $P2Y_1R$ antagonists, especially with respect to the high-affinity ADP-binding sites, significantly inhibited the calcium responses evoked by ADP. Further, MRS 2179 and MG 50-3-1 may be competitive antagonists of the endogenous $P2Y_1$ receptor expressed in the parental CHO.K1 cell line. The results obtained were not due to a variation in pH at different antagonist concentrations.

Chapter 6

Detecting Physical Interactions Between A_1R and $P2Y_1R$

6.1 INTRODUCTION

Physical interactions between the A_1R and $P2Y_1R$ have been identified in various cell lines and tissue types and reported in the literature. Having observed, what we interpret, as novel functional properties of the heteromeric receptor in hA_1-24 and G14T-13 cells we sought to confirm a physical interaction between the A_1R and $P2Y_1R$ in these clonal cell lines. hA_1-24 and G14T-13 cells express untagged versions of each receptor subtype at physiological levels. The most common methods used for the detection of receptor heterodimerisation are co-immunoprecipitation and fluorescence techniques. In this Chapter I describe my attempts to identify A_1R and $P2Y_1R$ heteromers by co-immunoprecipitation of the two receptors using commercially available purinergic receptor antibodies and by Bimolecular Fluorescence Complementation (BiFC), a technique useful for detecting heteromeric receptor protein interactions in living cells.

6.2 MEMBRANE PROTEIN SOLUBILISATION AND NATIVE RECEPTOR DETECTION

In order to detect physical interactions between A_1R and $P2Y_1R$, the receptors must be solubilised from the plasma membrane. To do this, it was necessary to identify an appropriate solubilisation reagent that would possess a reasonably high solubilisation efficiency without denaturing the receptors or preventing their immunodetection. Previous published work revealed that a number of detergents have been used successfully to solubilise the A_1R, $P2Y_1R$, $P2Y_2R$ and other G protein-coupled receptors from tissues and cells (shown in Table 6). These observations were used as a basis for selecting detergents for preliminary solubilisation experiments in the hA_1-24 and G14T-13 cell lines.

Detergents known to possess denaturing effects or toxic detergents, such as digitonin, were avoided[200]. When the rat testicular A_1 adenosine receptors were purified[211], functional analysis showed that the guanine-nucleotide-dependent increase in antagonist binding was lost[211,212], implying an uncoupling of receptors from G-proteins. However, G protein-coupling is not required for co-IP experiments, since early work showed that A_1R:$P2Y_1R$ heterodimers could form in the absence of G protein-coupling[103]. Detergents such as Triton X-100 and CHAPS have become popular due to their mild, non-denaturing conditions[200] and Nakata, et al. have used Triton X-100[91,103,105] instead of digitonin and sodium cholate[211,213,214] to

analyse A_1R:$P2Y_1R$ [91,103] and A_1R:$P2Y_2R$ [105] heteromer formation. The functional properties of the receptors were preserved using this solubilisation protocol.

Membrane Receptors	Tissues / Cell Lines	Detergent(s)	Year	Ref
A_1R	Rat brain membrane	1% digitonin + 0.1% sodium cholate	1989	213
	Rat testes	1% digitonin + 0.1% sodium cholate	1990	211
	Bovine brain	25mM CHAPS + 0.1% sodium cholate	1991	212
	Human brain membrane	1% digitonin + 0.1% sodium cholate	1992	214
	CHO-K1	digitonin (2:1 ratio to membrane)	1999	215
A_1R/ $P2Y_1R$	HEK 293T	1% Triton X-100 + 300mM NaCl	2001	103
	Rat brain	1% Triton X-100 + 300mM NaCl	2002	91
A_1R/ $P2Y_2R$	HEK 293T	1% Triton X-100 + 300mM NaCl	2006	105
Muscarinic Acetylcholine Receptor	Porcine atrial membrane	0.4% digitonin + 0.08% cholate in 3-3.5mg/ml protein	1981	216
Serotonin$_{1A}$ (5-HT$_{1A}$)	CHO	5mM CHAPS + 1M NaCl	2003	217
μ - δ opioid Receptor	HEK 293T	10% CHAPS +100mM NaCl	2006	218

Table 7. Examples of detergents used in the solubilisation and purification of the A_1R, $P2Y_1R$, $P2Y_2R$, and other G-protein coupled receptors from tissues or cells.

Detergents were used either solely or in combination, with a defined salt concentration. The use of more toxic detergents, such as digitonin and sodium cholate, was avoided and mild and non-denaturing detergents, such as Triton X-100 and CHAPS were used instead.

The following four conditions were initially tested for their ability to solubilise the $P2Y_1$ receptors from the parental CHO.K1 cell line:

- 1% Triton in 1x Tris-ion buffer*, 150mM NaCl (final), protease inhibitors
- 1% Triton in 1x Tris-ion buffer, 300mM NaCl (final), protease inhibitors
- 12.5mM CHAPS in 1x Tris-ion buffer, 150mM NaCl (final), protease inhibitors
- 5mM CHAPS in 1x Tris-ion buffer, 150mM NaCl (final), protease inhibitors

* Tris-ions buffer: 50mM Tris HCl pH7.4, 120mM NaCl, 5mM KCl, 2mM $CaCl_2$, 10mM $MgCl_2$

Unfortunately none of the conditions outlined above proved effective at solubilising the $P2Y_1R$. A commercially available cell lysis reagent, M-PER, was used for the cell lysis prior to membrane preparation. M-PER contains an unidentified and proprietary detergent and it was decided to test the efficacy of this detergent in the solubilisation process. Western blot and immunodetection of the $P2Y_1R$ were used

as a mean of comparing the extent of solubilisation using M-PER and the results can be seen in Figure 41. M-PER reagent solubilised 51.34 $\pm$ 1.38% of the $P2Y_1$ receptor protein (n=3). M-PER was thus the detergent of choice in all subsequent experiments.

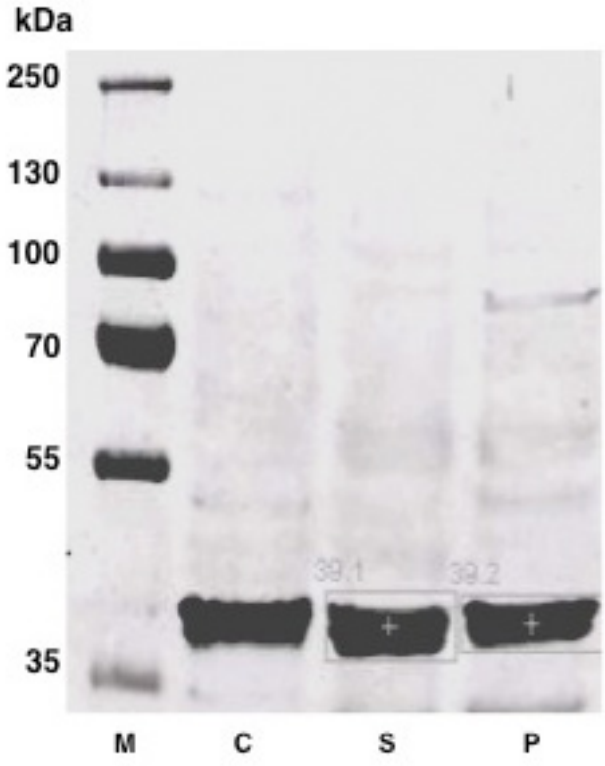

Figure 41. Solubilisation of $P2Y_1R$ receptors using M-PER.

CHO.K1 membranes were purified and solubilised using M-PER reagent and the intensity of the $P2Y_1$ receptor signal in solubilised membrane fractions (S) and the non-solubilised pellet (P) was quantified using SDS-PAGE and western blotting. The positive H4 lysate control (C) and a protein molecular weight ladder (M) were included on the gel. The solubilisation efficiency was calculated to be the ratio of S against (S+P) for the $P2Y_1$-immunoreactive signal. A representative experiment is shown.

Since I could effectively solubilise $P2Y_1$ receptors from the parental CHO.K1 cell line I attempted similar experiments on the G14T-13 and hA_1-24 cell lines prior to attempting to co-immunoprecipitate A_1R:$P2Y_1R$ heterodimers. The first of these experiments investigated the $P2Y_1$ receptor signal obtained in the G14T-13 cell line following the solubilisation protocol outlined above.

The positive control H4 cell lysate and G14T-13 solubilised membranes were electrophoresed in parallel on an SDS-PAGE gel. Following transfer to a membrane, one set of the sample was incubated with blocking buffer which minimises any non-specific protein interaction, prior to primary antibody adsorption. The other half of the membrane was incubated with the same blocking buffer in the presence of a blocking peptide, which was supplied with the primary antibody to specifically block the goat anti-$P2Y_1R$ antibody/$P2Y_1R$ interaction.

Figure 42 reveals that, consistent with the results obtained in the parental CHO.K1 cell line, a specific $P2Y_1R$ signal is detected at approximately 37kDa following solubilisation of membranes derived from the G14T-13 cell line. The left hand panel in Figure 42 shows an intense positive signal was observed (arrow) in the G14T-13 lysate, at the approximately the same position as the signal seen in the H4 cell lysate control. This is the $P2Y_1R$ band. There is a slight shift in the size of the bands between the two samples, which could be due

to differential glycosylation. This $P2Y_1R$ signal is greatly reduced in the right hand panel, when the experiment was performed in the presence of the blocking peptide, showing that the $P2Y_1R$ signal detected is indeed a specific one. The blot is clear with very little background.

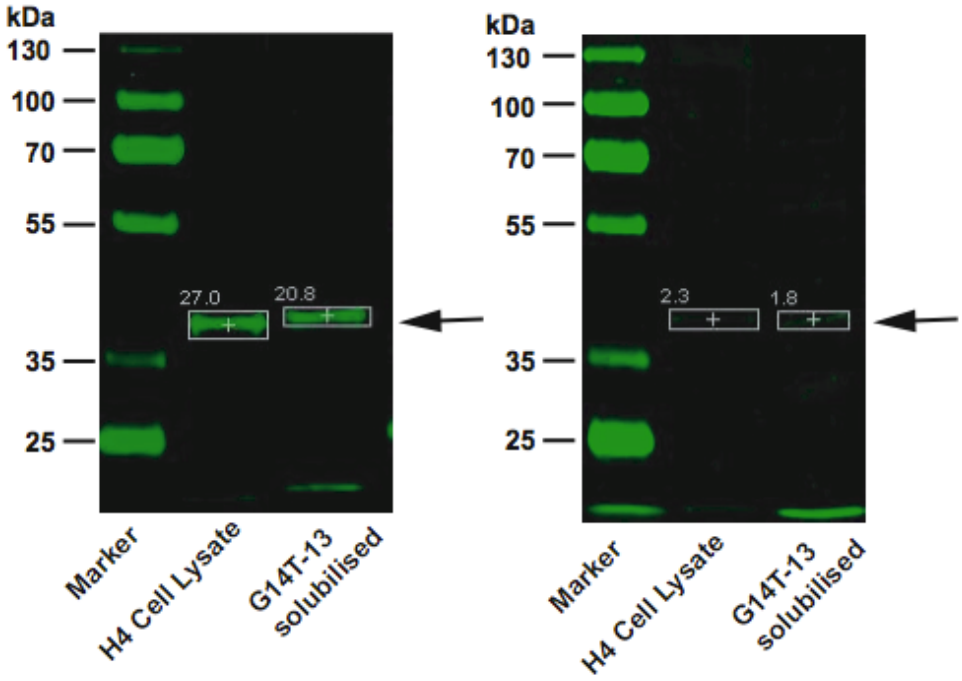

Figure 42. Immunodecection of $P2Y_1$ from M-PER solubilised G14T-13 membrans.

Left, a 37kDa protein (arrow) was detected in the G14T-13 solubilised membrane and in the positive control H4 cell lysate, using the goat $P2Y_1R$ polyclonal primary antibody. Right, the 37kDa signal was significantly reduced when the primary antibody was pre-incubated with its specific blocking peptide.

6.3 CO-IMMUNOPRECIPITATION OF A_1R AND $P2Y_1R$

Following on from the solubilisation experiments described in section 6.1, co-immunoprecipitation experiments were then conducted in order to identify a potential interaction between A_1R and $P2Y_1R$. Since the goat anti-$P2Y_1R$ primary antibody and the IR800 conjugated donkey anti-goat secondary antibody gave a very clear signal in the previous experiment, these were used for detection of the $P2Y_1R$ in co-immunoprecipitated samples.

The immunoprecipitation was achieved using a polyclonal anti-A_1R primary antibody raised from in rabbit. The samples were incubated with the antibody allowing sufficient time for interaction with the A_1Rs, after which, they were precipitated by adsorption to the Protein G sepharose beads. The Protein G sepharose beads binds to the Fc region of the IgG from a large variety of species. Therefore, the anti-A_1R antibody, which is bound to the A_1R, as well as the proteins interact with the A_1R ($P2Y_1R$), are precipitated with the Protein G sepharose. The anti-A_1R primary antibody used was raised in rabbit, a different species from the anti-$P2Y_1R$ primary antibody, in order to minimise the antibody heavy and light-chain signals obtained on the Western blot.

As Figure 43 shows, solubilised proteins from CHO.K1 and G14T-13 membranes were immunoprecipitated using rabbit anti-A_1R antibodies, and a rabbit IgG protein, followed by immunodetection of

$P2Y_1R$ on Western blots using the specific goat primary antibodies described previously. The CHO.K1 sample serves as the negative control for G14T-13 test samples, as the CHO.K1 cells do not express A_1R. A rabbit IgG protein was used in order to act as a negative control for the anti-A_1R antibodies.

The left side of the figure (A) shows $P2Y_1R$ detection using the goat antibody, which had previously been shown to be specific (see Figure 42). However, the results in Figure 43 reveal an intense signal at 37kDa in all samples, including the negative controls. This suggests a non–specific signal, since the CHO.K1 cell line lacks A_1R, and the rabbit IgG proteins should not bind to the A_1R even when it is expressed in G14T-13 cell. Therefore, under these conditions, it is unlikely that the signal corresponds to co-immunoprecipitated $P2Y_1R$ protein. In addition, there is a significantly higher amount of background noise level in this blot compared to the previous results, especially the bands at approximately 55kDa and 25-35kDa, which represent the antibody heavy and light chains. Furthermore, when the blocking peptide was used to pre-adsorb the anti-$P2Y_1R$ antibody, the 37kDa band failed to reduce its intensity significantly (Figure 43, B). These results suggest that the A_1 receptor antibody lacks specificity and because it was not possible to find another A_1 receptor antibody that was specific, the co-immunoprecipitation experiments and thus attempts to detect a A_1R:$P2Y_1R$ were abandoned.

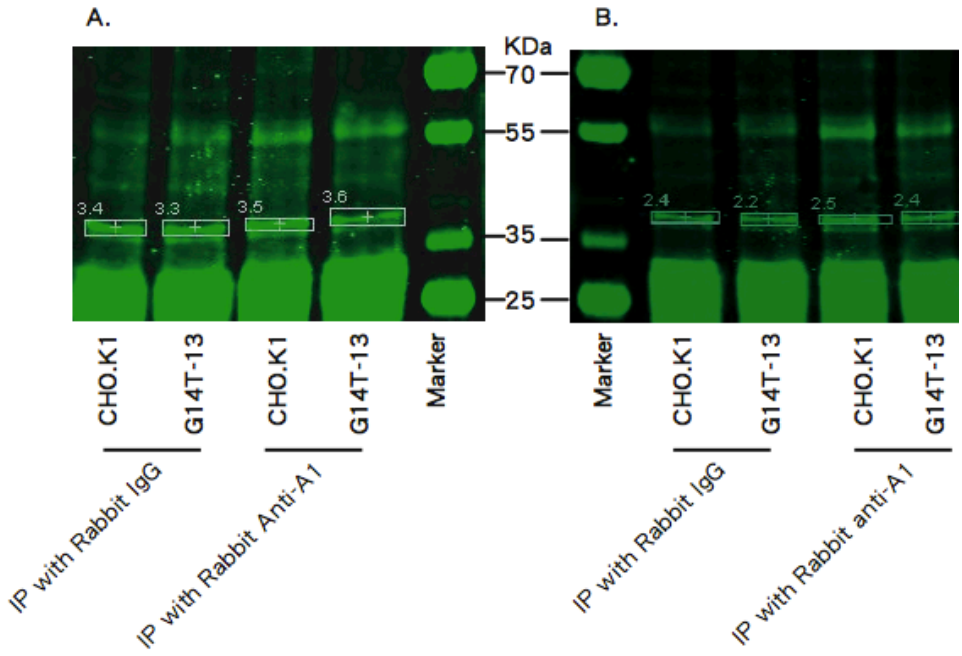

Figure 43. Co-immunoprecipitation of A_1R and $P2Y_1R$ from G14T-13 cells.

A representative figure showing the Western blot detection of $P2Y_1R$ using goat anti-$P2Y_1R$ primary antibodies following immunoprecipitation of AT_1R from $CHO.K_1$ and G14T-13 solubilised membranes using rabbit anti-A_1R antibody or control rabbit IgG.

A) A 37kDa band was detected in all samples, including the negative controls: *Lane 1* and *Lane 2*, CHO.K1 and G14T-13 solubilised membrane samples immunoprecipitated with rabbit IgG proteins; *Lane 3* and *Lane 4*, CHO.K1 and G14T-13 solubilised membranes immunoprecipitated with rabbit anti-A_1R primary antibodies.

B) A parallel experiment performed as in A) but the Western blot shown was incubated with anti-$P2Y_1R$ antibodies pre-adsorbed to the blocking peptides. The signal intensity for all bands reduced approximately the same amount but not significantly.

6.4 SUMMARY

Initial attempts to solubilise the A_1R and $P2Y_1R$ using detergents previously reported to be effective at solubilising these two receptors proved unsuccessful. In contrast, a commercially available cell lysis reagent (M-PER) was found to be efficient in solubilising the receptors, although the exact composition of this buffer is not clear. This reagent was originally tested for it's ability to solubilse $P2Y_1R$ and was demonstrated to solubilise ~50% of the membrane located receptor.

The initial Western blot experiments performed during the solubilisation trials were very encouraging with a specific 37kDa $P2Y_1R$ band detected in the solubilised membrane samples and in the positive control H4 lysate. These signals were significantly reduced by a blocking peptide specifically targeting the primary antibody, which appeared to confirm the specificity of the antibody. Unfortunately, subsequent co-immunoprecipitation in which A_1R was immunoprecipitated and $P2Y_1R$ detected showed a significant amount of non-specific signal, with the 37kDa band being detected in both positive and negative control samples and not reduced in intensity by pre-incubation with the blocking peptide.

Since the specificity of the anti-A_1R antibody was in question for the co-immunoprecipitation experiments, the anti-A_1R antibody was characterised further. Unfortunately, this also gave signals of the

expected size in the negative control samples. Due to the lack of a blocking peptide for the A_1 antibody, it was not possible to determine the amount of non-specific binding for this antibody, however, it can be concluded that this antibody exhibited a significant level of non-specificity, making the characterisation of the native receptor $A_1R/P2Y_1R$ dimer technically impossible.

Chapter 7

The Bimolecular Fluorescence Complementation: Constructs and Cloning

7.1 INTRODUCTION

As previously presented in Chapter 6, the process for the co-immunoprecipitation experiment for the native A_1R and $P2Y_1R$ interaction was impeded by the lack of antibody specificities. Although the technique provides fast and direct proof of protein-protein interactions, it is not the only method for detecting receptor interactions. In many studies, techniques involving fluorescent proteins (FPs) have been greatly adapted to visualise the receptor interactions, in *vivo*. In order to circumvent the antibody specificity problem, I had, therefore, focused on the establishment of a new technique, which will allow the detection of A_1R and $P2Y_1R$ in living cells.

The bimolecular fluorescence complementation (BiFC) assay is a recently developed technique designed for the visualisation of in *vivo* protein-protein interactions[219-222]. The use of this method is primarily based on the unique feature of the green fluorescent proteins (GFPs) and its large number of variants such as yellow (YFP), cyan (CFP)

and red fluorescent (RFP) proteins, all of which showed the ability to reconstitute into a functional protein when their N- and C-terminal fragments are brought into close proximity[219,221,223]. The fluorescent proteins (FPs) consist of 11 strands of β-barrel surrounding an α-helix in the centre of the protein[224]. It has been shown that the chromophore is probably located near the N-terminal end, since the truncated N-terminal 1-173 amino acid (aa) YFP fragment (YFP_{1-173}) was still able to reform a functional protein with its C-terminal complementary fragment containing aa residues 156-239 ($YFP_{156-239}$). In addition, YFP_{1-173} also formed a functional YFP with the $CFP_{156-239}$[221]. The advantage of BiFC over fluorescence resonance energy transfer (FRET) is that a high level of receptor expression is not a requirement; therefore, it allows detection of weak interactions between proteins. In addition, the simple detection method using a fluorescent microscope under circumstances where agonists and antagonists can be applied and the results on protein-protein interactions observed also makes this technique more favourable[223].

Previously, numerous GPCR interactions have been detected using BiFC, including a more recent experiment, which investigated the membrane diffusion of the human A_1R and $A_{2A}R$ homomers and heteromers in CHO cells[225]. The results proved that the C-terminal tagging of the YFP, full length or fragments, does not affect the homomeric receptor signalling properties as well as the membrane expression levels. Further, the results also demonstrated the

fluorescent signals detected are resulted from specific receptor interactions. In addition to this, a rat brain $P2Y_1R$ tagged with an eGFP (enhanced GFP) revealed an unaffected signal transduction property when compared with the wild-type receptor, as well as a predominant localisation to the cell membrane[226]. These results provided positive supporting evidence for the feasibility of adapting such a technique in visualisation of the A_1R and $P2Y_1R$ interactions.

In this chapter, I will present the designing of the BiFC constructs for both A_1R and $P2Y_1R$, and the cloning strategies. During the process of building these constructs, the laboratory notebook was stolen, which then resulted into subsequent complications in the cloning. Loss of these notes made it impossible to refer to previous work and determine the cause of problems for the first BiFC constructs cloned, where the inserted DNA fragment size did not meet expectation. Due to this reason, all the existing work and results achieved were abolished, and the whole process had to be started from the beginning. This had greatly affected the progress of the project.

Few attempts were carried out initially in order to identify the cause of the problem for the BiFC constructs, none of which produced desirable findings. However, it was noticed, for the first time, that a pair of restriction enzymes, NheI and EcoRV, which were both upstream of the inserted fluorescent proteins, were able to remove the FP fragments from the construct. Such phenomenon was

observed again following re-starting of the BiFC cloning project. After the cloning of FPs into an expression vector, the same pair of restriction endonuclease enzymes was used in order for ligation of the GPCR fragments. Nevertheless, the newly inserted FP fragments were excised unexpectedly after these reactions. This led to investigations into the properties of the restriction enzymes and BiFC constructs, and determined that the problem was caused by the design of the constructs, which had created a Dam methylation site. Series of experiments were carried out in order to overcome such problem, and repeated trials were conducted. Despite of a few unanticipated problems encountered during the process, sequence analysis had finally confirmed the successful generation of HA-A_1R-YFP_{1-239} and Myc-$P2Y_1$R-YFP_{1-239} constructs.

7.2 CLONING STRATEGIES AND PLANS

The generation of suitable A_1R and $P2Y_1$R FP fusion proteins and the constructs schematics are shown in Figure 44. cDNAs encoding the G protein-coupled receptor proteins were tagged on their 5'-terminal end with either a Haemagglutinin (HA-A_1R) or a Myc (Myc-$P2Y_1$R) tag immediately downstream of a consensus Kozak sequence to facilitate translation. The stop codon was removed from the GPCR so that all downstream sequences could be fused in-frame. A 'linker' sequence was inserted in-frame to the 3' of the GPCR, using the polylinker of the mammalian expression vector pcDNA3.1+.

Immediately behind this linker, cDNAs encoding cyan or yellow FP protein sequences, either full-length (encoding amino acids 1-239) or partial (encoding either amino acids 1-173 or 156-239), were fused in-frame. The resulting construct is a chimeric fusion, from N-terminal end to C-terminal end, of the epitope tag, GPCR and FP fragment. The experimental design was created by a final year project student in the laboratory, who amplified the necessary DNAs using a proofreading polymerase and cloned the resulting amplicons into the TOPO-Blunt PCR cloning vector (Invitrogen). I sequenced all of these constructs and used them to build the BiFC constructs in the mammalian expression vector pcDNA3.1^{+}(Neo). For future convenience in the molecular cloning works, all of the six GPCR and FP fragments were transferred and cloned into the pcDNA3.1^{+} (Neo) expression vector; these include HA-A_1R, Myc-P2Y_1R, $YFP_{1\text{-}239}$, $YFP_{1\text{-}173}$, $YFP_{156\text{-}239}$, and $CFP_{1\text{-}173}$. The constructs were purified by the CsCl gradient maxi-prep (Chapter 2) and stored. The FP fragment was ligated behind the GPCR into the vector, in order to generate the final BiFC constructs.

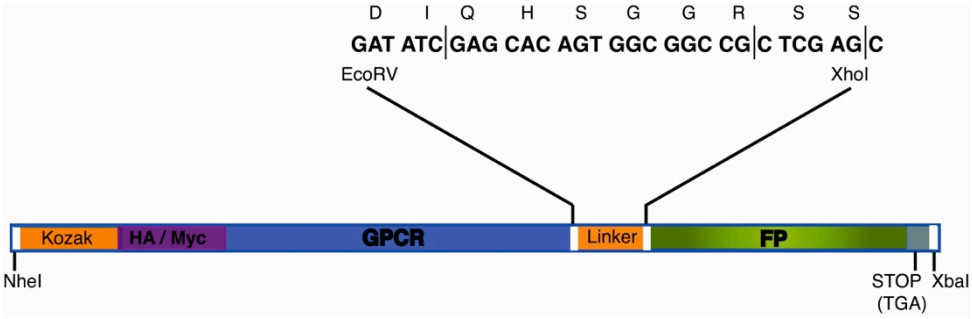

Figure 44. Schematic representation of the BiFC construct design.

The GPCR and FP fragments were excised from the TOPO-PCR vector and sequentially inserted into the polylinker of pcDNA3.1^{+}(Neo). The GPCR sequence is cloned between the NheI and EcoRV sites and is fused to an epitope tag (HA/Myc) at the 5' end of the receptor sequence. It lacks a stop codon. The FP sequence is cloned between the XhoI and XbaI sites. The linker sequence encodes a peptide that is 10 amino acids in length (DIQHSGGRSS) and is part of the polylinker of the mammalian expression vector.

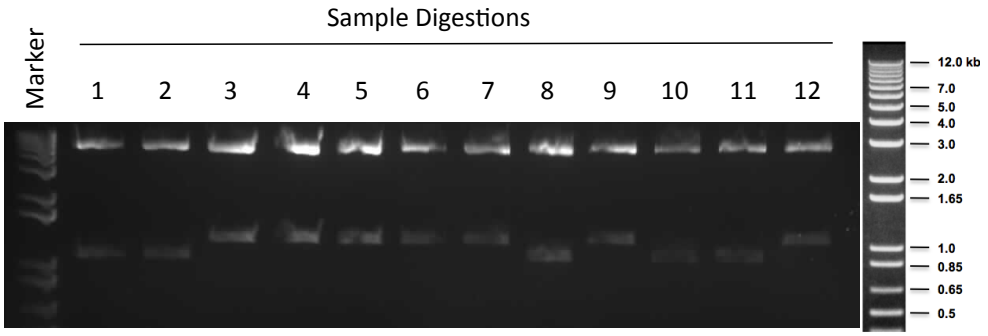

Figure 45. Restriction endonucleases digestion of the HA-A_1R-YFP_{1-239} construct using NheI and XbaI.

Twelve construct samples extracted and purified from the mini-prep were digested with the pair of restriction enzymes, and revealed DNA bands with varying sizes. The reaction mixture was electrophoresed in 1% agarose gel containing ethedium bromide, along side a DNA marker. A standard DNA ladder after electrophoresis was obtained from the company's website (right), the sizes of each band were indicated. According to the DNA ladder, all extracted bands were between 1.0 and 1.65kb.

7.3 BUILDING BIFC CONSTUCTS

7.3.1 The Existing Constructs

Following transfer of all the GPCR and FP DNA fragments into the pcDNA3.1^{+}(Neo) expression vector (hereafter referred to as either GPCR/ pcDNA3.1^{+}(Neo) or FP/ pcDNA3.1^{+}(Neo)), the HA-A_1R BiFC constructs were cloned by inserting the YFP_{1-239} full-length protein downstream of the GPCR part. As mentioned previously, both HA-A_1R and Myc-$P2Y_1$R were amplified and cloned with C-terminal stop codon deletion, so that the fluorescent protein moiety will be in-frame. The construct HA-A_1R-YFP_{1-239} was digested with a pair of restriction endonuclease enzymes (RE) NheI and XbaI, both of which flank the 5' and 3'-terminal end of the DNA constructs. The digestion reaction was designed to confirm that the cloning results match the size expectation, before being further proved by sequencing reactions.

As the results show, the enzyme pair exited the inserted fragments with varying sizes, which were not as expected (Figure 45). The constructs were extracted and purified by the mini-scale DNA preparation (mini-pre) methods. After the enzyme digestion, all twelve samples were loaded onto the 1% agarose gel for electrophoresis alongside a DNA marker/ ladder. The DNA ladder on the right side of the figure was obtained from the company's website, which showed the standard bands separation, after electrophoresis. According to the marker sizes, it can be estimated that excised

bands by NheI and XbaI were between 1.0 and 1.65kb. These bands were smaller than the HA-A_1R-YFP_{1-239} fragment, which is 1.725kb as calculated. In other words, the HA-A_1R-YFP_{1-239} fragment should be between 1.65 and 2.0kb position of the marker bands. It was not clear why the inserted fragment was smaller and of differential size, since the original laboratory notebook, which contained all the entire records of the cloning process was stolen. Therefore, it became impossible to identify the cause of this problem. Nevertheless, a few tests involving restriction enzyme digestions were performed which endeavoured to check for the validity of the construct.

These tests focused primarily on the HA-A_1R/ pcDNA3.1$^+$(Neo) and YFP_{1-239}/ pcDNA3.1$^+$(Neo) individually before the ligation reaction. The HA-A_1R/ pcDNA3.1$^+$(Neo) was first analysed by a series of RE digestions, including: 1) XbaI; 2) BamHI; 3) XbaI and BamHI pair; and 4) NheI and BamHI pair (Figure 46, 1)). NheI, EcoRV and XbaI sites are located on the multiple cloning site region of the pcDNA3.1$^+$(Neo) vector. Following the insertion of HA-A_1R between the NheI and EcoRV site, the distance between the two RE sites increased to 1725bp, which is equivalent to the length of the DNA inserted. The XbaI site is 27bp downstream of the EcoRV site. In addition, the enzyme BamHI cut the HA-A_1R only at 461bp downstream of the NheI site (Figure 46, 2)).

Therefore, to summarise the above, RE reaction with either XbaI or BamHI should yield a linearised HA-A_1R-containing plasmid of approximately 7100bp, that is the sum of the HA-A_1R fragment (1725bp) and the pcDNA3.1$^+$(Neo) vector plasmid (5428bp), neglecting the very small fraction excised between the NheI and EcoRV sites within the multiple cloning region, prior to HA-A_1R ligation. The XbaI and BamHI pair should produce a 544bp band, and the NheI and BamHI pair 461bp (Figure 46, 2)). However, as shown in the results (Figure 46, 1)), the XbaI and BamHI pair had excised a DNA fragment of approximately 1kb. Moreover, the NheI and BamHI reaction did not produce any visible DNA band. It was difficult to explain the reason for these results without any DNA sequencing analysis. Yet, it was clear that the HA-A_1R/ pcDNA3.1$^+$(Neo) plasmid contained major faults, hence was discarded.

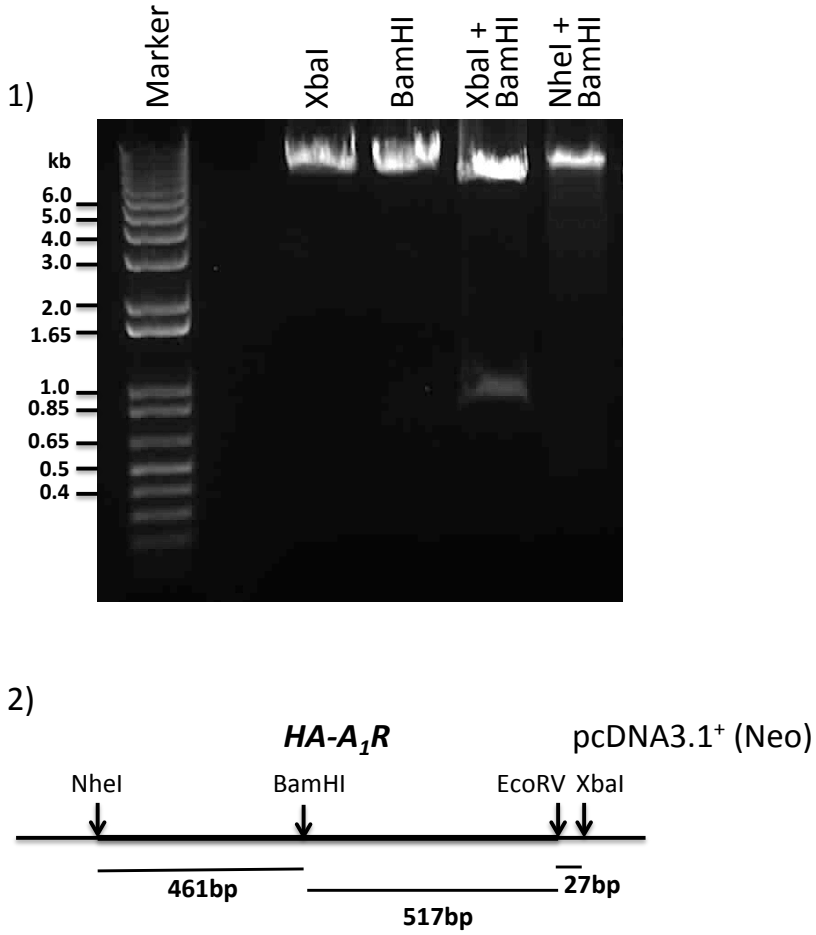

Figure 46. Series of RE reactions for the HA-A_1R/ pcDNA3.1$^+$(Neo) construct.

1) The construct was digested with XbaI, BamHI, XbaI + BamHI (pair), and NheI + BamHI (pair). The reaction mixtures were electrophoresed on 1% agarose gel containing ethedium bromide. The XbaI + BamHI reaction yielded a DNA fragment of approximately 1.0kb, which is almost twice the size expected, 544bp. No visible band was detected from the NheI + BamHI digestion.

2) A simplified map of HA-A_1R/ pcDNA3.1$^+$(Neo) construct, revealing some key RE sites. The HA-A_1R fragment was inserted between the NheI and EcoRV sites in the multiple cloning region of the pcDNA3.1$^+$(Neo) vector plasmid. The distance between the two sites is 1725bp, the length of the HA-A_1R fragment. The XbaI site, which is also located within the multiple cloning site region, is only 27bp downstream of EcoRV site. The HA-A_1R fragment contained a single BamHI RE site, 461bp downstream of NheI, and 517bp upstream of EcoRV site.

On the other hand, the YFP constructs including YFP_{1-239}, YFP_{1-173}, and $YFP_{156-239}$, which were previously built in the pcDNA3.1^{+}(Neo) plasmid, were also examined and all contained major problems. As explained earlier, these YFP DNA fragments were inserted between the XhoI and XbaI RE sites in the multiple cloning region of the vector. In order to re-construct the HA-A_1R-YFP in pcDNA3.1^{+}(Neo) plasmids, the HA-A_1R moiety was extracted directly form the TOPO-Blunt plasmid, and ligated in front of the YFP fragments, which are already inserted in the pcDNA3.1^{+}(Neo) plasmids. Such method bypasses the standard planning and procedures, where the valid HA-A_1R/pcDNA3.1^{+}(Neo) and FP/ pcDNA3.1^{+}(Neo) plasmids are usually constructed in advance. This ensured the accuracy of the GPCR fragments and, more importantly, reduced the time-scale for the whole cloning process.. Therefore, all three YFP plasmids were digested first using a pair of RE, NheI and EcoRV, which are located at the two terminals of the HA-A_1R fragment.

As the results have shown in Figure 47 a, restriction enzyme digestion using the pair of enzymes excised a DNA band from each of the plasmids. In Figure 47a, lane 1 to 3 represents the pcDNA3.1^{+}(Neo) plasmids containing YFP_{1-239}, YFP_{1-173}, and $YFP_{156-239}$ fragments. The results of the RE reaction was loaded onto a 1% ethidium bromide containing agarose gel alongside a DNA ladder (M), for electrophoresis to ensure the complete digestion of the plasmid DNA. The standard DNA ladder on the right side of the figure

revealed the sizes and positions of the DNA bands after electrophoresis. By estimation, the excised fragments are approximately between 650bp and 850bp in lane1, between 500bp and 650bp in lane 2, and almost 300bp in lane 3. These coincide with the sizes of the FP fragments (including the 3' end stop codon): 720bp for YFP_{1-239}, 522bp for both YFP_{1-173} and CFP_{1-173}, and 255bp for $YFP_{156-239}$. It was, therefore, suspected that the NheI and EcoRV enzyme pair might have excised the YFP fragments that were previously cloned into the pcDNA3.1^{+}(Neo) plasmids, even though in theory this seemed impossible.

In order to confirm the findings and to exclude the possibility of enzyme contamination (by XhoI and XbaI), all four YFP/ pcDNA3.1^{+}(Neo) constructs were examined using NheI and EcoRV enzymes borrowed from a different lab. After the RE reaction, the digestion mixtures were electrophoresed and analysed in 1% agarose gel. The results confirmed the potential problems within the constructs (Figure 47b). Lane 1 to 4 corresponds to the YFP_{1-239}, YFP_{1-173}, CFP_{1-173}, and $YFP_{156-239}$ containing plasmids. RE digestion extracted DNA bands approximately the same sizes as the inserted FP fragments. In lane 4, due to the small size, the band is much less intense than the others.

In addition, it was further proved that these bands electrophoresed at the same distance as the ones extracted by the XhoI and XbaI enzyme pair; and the uncut plasmids did not contain such fragments (Figure 47c). In Figure 47c, the YFP_{1-239}, YFP_{1-173}, CFP_{1-173}, and $YFP_{156-239}$ containing plasmids (1 to 4, 5 to 8, and 9 to 12 as corresponding orders) were analysed and compared. The uncut plasmids did not produce any additional DNA bands, whereas, the NheI and EcoRV digestions yielded the same DNA bands as the XhoI and XbaI pair. The excised DNA fragments migrated the same distance in both types of digested samples. This confirmed that the plasmids are undamaged closed circular DNA, yet the constructs contained major faults.

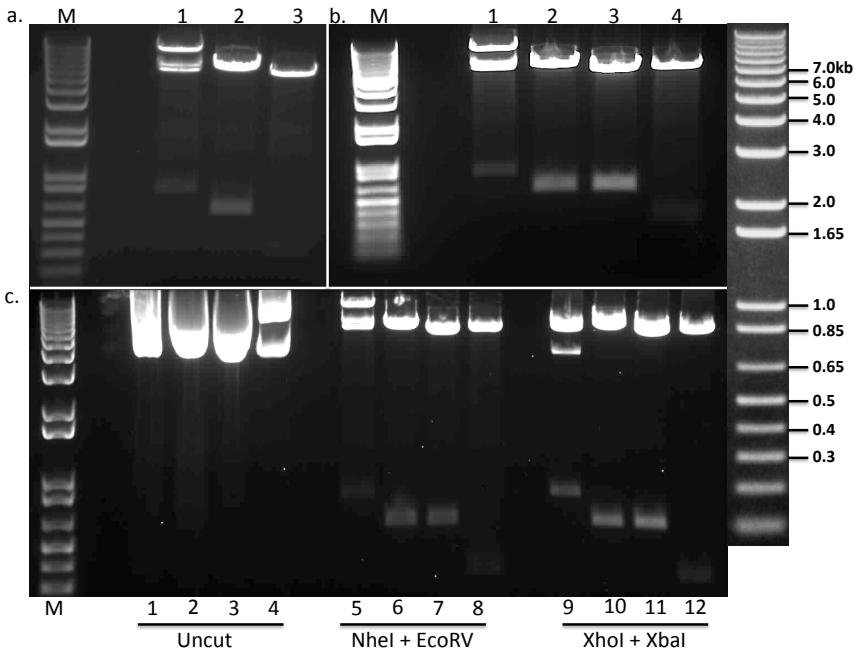

Figure 47. YFP/pcDNA3.1^{+}(Neo) construct analysis by RE digestion.

NheI and EcoRV digestion of the YFP (a, b and c) and CPF (b and c) containing plasmid produced DNA fragments of the approximate sizes as purified FP fragments. The XhoI and XbaI reaction yielded the same results as the NheI and EcoRV pair. The reaction mixtures were electrophoresed on 1% agarose gel containing ethidium bromide, alongside a DNA marker (M).

a. NheI and EcoRV digestion of $YFP_{1\text{-}239}$ (lane 1), $YFP_{1\text{-}173}$ (lane 2), and $YFP_{156\text{-}239}$ (lane 3) containing pcDNA3.1^{+}(Neo) plasmids produced the DNA bands unexpectedly. The sizes of these bands coincide with the purified YFP fragments.

b. Lane 1 to 4, $YFP_{1\text{-}239}$, $YFP_{1\text{-}173}$, $CFP_{1\text{-}173}$ and $YFP_{156\text{-}239}$ constructs in pcDNA3.1^{+}(Neo). RE digestion performed using the NheI and EcoRV enzymes borrowed from another lab. A DNA band was excised from each of the four constructs, and the sizes are approximately the same as the purified FP fragments.

Lanes 1 to 4 (uncut DNA), 5 to 8 (NheI + EcoRV), and 9 to 12 (XhoI + XbaI) each corresponds to $YFP_{1\text{-}239}$, $YFP_{1\text{-}173}$, $CFP_{1\text{-}173}$ and $YFP_{156\text{-}239}$ constructs in pcDNA3.1^{+}(Neo), in orders. The NheI + EcoRV and XhoI + XbaI pairs produced the same digestion results. The uncut DNA does not contain any smaller DNA fragments.

7.3.2 NheI and EcoRV Digestions and Dam Methylation

Restriction endonuclease reaction analysis had identified problems in the HA-A_1R/pcDNA3.1$^+$(Neo) construct, that the sizes of DNA fragments excised from the digestion did not match expectations. Since then, a series of RE digestions using the NheI and EcoRV, and XhoI and XbaI enzymes pairs had also confirmed potential faults existed in the previously cloned FP/pcDNA3.1$^+$(Neo) constructs. Unfortunately, it was not possible to examine the planning and process of these cloning steps, which took place over 6 months ago, as the laboratory notebook was stolen. As a result, the existing constructs were discarded, and the constructs cloning works were re-commenced from the beginning.

The GPCR and FP fragments were originally synthesised by PCR reactions into the TOPO Blunt vectors. These constructs were sequenced to confirm their accuracies and reliabilities. As planned, all four types of the FP fragments will be cloned into the pcDNA3.1$^+$(Neo) expression plasmid, followed by the insertion of corresponding GPCR parts upstream the FPs. After a series of experiments and problem solving processes, all of the FP fragments were successfully cloned into the pcDNA3.1$^+$(Neo) plasmids; the constructs were purified by large-scale DNA preparations, and stored for further use.

In order to ensure the accuracy of the GPCR DNAs, the fragments were digested and purified from the TOPO Blunt plasmids, where

they were originally synthesised and cloned. These were then directly inserted in front of the FPs in the pcDNA3.1$^+$(Neo) vector. The GPCR fragment is located upstream the FPs between the NheI and EcoRV sites. When digested by this enzyme pair, the FP/pcDNA3.1$^+$(Neo) constructs revealed the same problem as previously observed in Figure 47: the FP fragments were excised after the reaction (Figure 48).

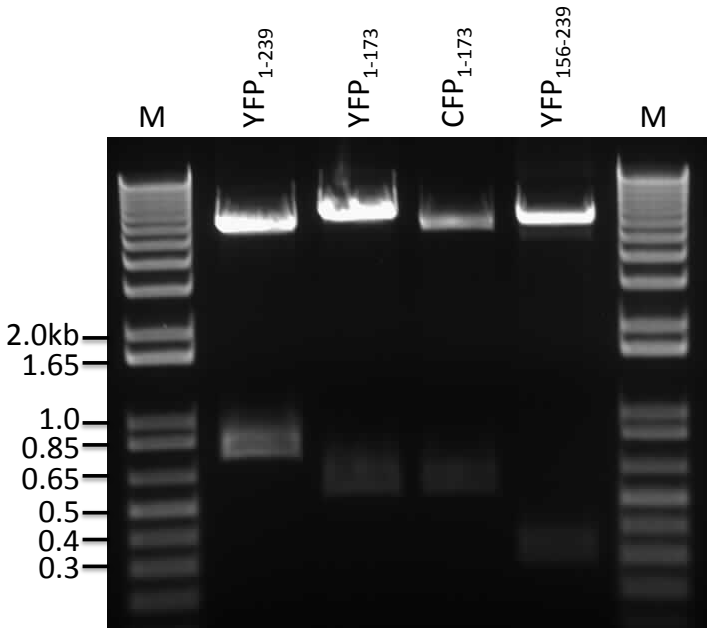

Figure 48. NheI and EcoRV digestion of the newly constructed FP/ pcDNA3.1$^+$(Neo) plasmids resulted into DNA fragments of the approximately the same size as the purified FPs.

The reaction mixtures were electrophoresed on 1% agarose gel containing ethidium bromide alongside the markers (M). The constructs digested were indicated by the FP fragments contained: from left to right, YFP_{1-239}/pcDNA3.1$^+$(Neo) (YFP_{1-239}), YFP_{1-173}/pcDNA3.1$^+$(Neo) (YFP_{1-173}), CFP_{1-173}/pcDNA3.1$^+$(Neo) (CFP_{1-173}), and $YFP_{156-239}$/pcDNA3.1$^+$(Neo) ($YFP_{156-239}$). Small DNA fragments were excised unexpectedly, and were approximately the same size as the purified FP fragments.

The reoccurrence of such phenomena is a firm indication of a potential problem in the construct design. Further investigations,

therefore, were carried out using the YFP_{1-239} containing plasmids as an example. Both TOPO Blunt and pcDNA3.1^{+}(Neo) constructs were analysed in pairs, focusing on the NheI and EcoRV reactions and the subsequent products. The results of an RE digestion can usually provide primary information on the differences between DNA sequences, and thus answer the question as to the extent of to damage and alterations in the DNA fragments during the cloning process.

In this experiment, an equal amount of YFP_{1-239}/TOPO Blunt and YFP_{1-239}/pcDNA3.1^{+}(Neo) plasmid DNAs were digested using both NheI and EcoRV, each in an independent reaction. All four reactions took place simultaneously, for the same reaction length. The resulting digest mixtures were analysed by electrophoresis on a 1% agarose gel containing ethidium bromide. As shown in Figure 49, EcoRV alone excised a band of approximately 700bp from the pcDNA3.1^{+}(Neo) plasmid, which most likely corresponds to the full-length YFP fragments inserted. TOPO Blunt plasmid digestion using the same enzyme did not yield the same band; neither did the NheI reaction on both the TOPO Blunt and pcDNA3.1^{+}(Neo) plasmids. The full-length YFP fragment was designed with the XhoI and XbaI enzyme pair flanking both terminals, following ligation into the TOPO Blunt vector, which contained unique EcoRV and NheI sites. Therefore, it was expected that the pair of enzymes, when working alone, should each cut the plasmid once, thus produce a single

large-sized band representing the linear plasmid. This is the same for the pcDNA3.1^{+}(Neo) plasmid that the EcoRV and NheI sites are only on the multiple cloning site region. As explained, in theory, the EcoRV enzyme was not expected to exise the YFP fragment through a single digestion. The results obtained in Figure 49, therefore, are a clear indication of serious problem occurring during the cloning process.

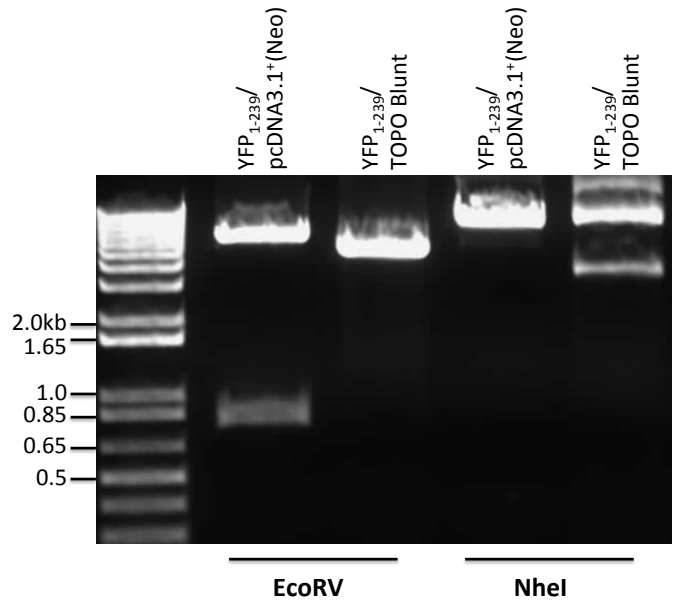

Figure 49. EcoRV and NheI restriction endonuclease analysis of plasmid DNAs.

Equal amount of pcDNA3.1^{+}(Neo) and the TOPO Blunt plasmids containing the full length YFP (YFP_{1-239}) were analysed using the EcoRV and NheI restriction enzymes, in independent digestion reactions simultaneously for the same reaction length. The resulting DNA mixtures were electrophoresed on 1% agarose gel containing ethidium bromide. EcoRV alone exised a band approximately 700bp from the pcDNA3.1^{+}(Neo) plasmid, but not the TOPO Blunt plasmid. NheI reaction did not yield any visible small DNA fragment from either of the plasmids investigated.

In order to understand the problems, both plasmids were prepared for sequencing. However, careful examination of the plasmids restriction sites and the designing strategy of the constructs had helped to identify the problem. As the FPs were attached downstream the GPCR, a stop codon was inserted at the 5' end of the FP fragments followed by the XbaI restriction enzyme site. It was solely unanticipated that a Dam methylation site was formed between this chosen stop codon and the XbaI sequences.

The DNA methylation reaction is a crucial stage which takes place during cellular division process, keeps the accuracy of DNA through the replication steps, and protect against mutations. The Dam methylation refers to the *E coli* DNA adenine methyltransferase (Dam) reaction, which is a part of the bacterial inert restriction modification system that introduces a methyl group to the N6 position adenine in the GATC sequence, thus prevent cleavage by restriction enzymes. Foreign un-methylated DNAs may be digested by restriction endonucleases.

In this case, the stop codon (TGA) is immediately upstream of the XbaI site (TCTAGA), forming the GATC sequences (TGATCTAGA). The methylation process will, therefore, prevent the cleavage by XbaI enzyme from the specific site. As a consequence, when excising the FP fragment from the TOPO Blunt vector using the XhoI and XbaI

enzyme pairs, the XbaI failed to cleave at the designated site that was primed into the FP DNA fragment; instead, it cuts at the XbaI site on the TOPO Blunt vector. This site is 53 base pairs downstream of the XbaI on the FP fragments; it is impossible to differentiate between the two types of fragments by electrophoresis. More importantly, this fragment will contain an additional EcoRV site (Figure 50 a)). As illustrated in the Figure 50 a) below, the full-length YFP fragment with XhoI and XbaI sites primed at the 5' and 3' ends were ligated into the Blunt PCR Product region of the TOPO Blunt vector. Restriction endonuclease digestion using the XhoI and XbaI pair should normally produce Fragment 1, which is approximately 720bp. Unfortunately, the XbaI site on the YFP fragment was disabled by formation of a methylation site with the stop code immediate upstream the restriction site ($XbaI^{Met}$). The fragment excised is approximately 773bp (Fragment 2), which would not be distinguished from the right structured fragment (Fragment 1) by electrophoresis since the difference between the two fragments is only 53bp. In addition, this fragment will contain an EcoRV site downstream the YFP_{1-239} gene. When this fragment was ligated into the pcDNA3.1^{+}(Neo) plasmid, it inevitably introduced an addition (either an additional EcoRV site or additional EcoRV sites (not sure there was one or more) EcoRV sites into the construct, such that it possesses two EcoRV sites, one of which intrinsically located in the multiple cloning site of the plasmid. Restriction enzyme digestion using EcoRV cleaves at both sites, thus producing a 760bp DNA

band visualised on the agarose gel (Figure 50 b)). This explains why EcoRV alone was able to remove a fragment approximately the same size as the full-length YFP, or other FP fragments inserted.

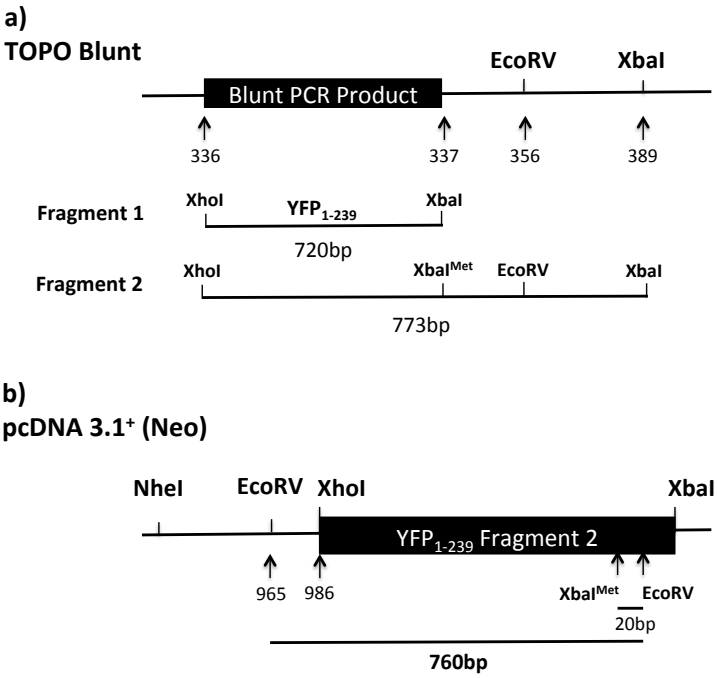

Figure 50. Illustrative figure for the locations of the restriction endonuclease sites and the reaction products.

a) XhoI and XbaI RE digestion of the YFP_{1-239}/ TOPO Blunt plasmids results into two different fragments.

Fragment 1: The right structured DNA fragment from XhoI and XbaI digestions. For YFP_{1-239}, the fragment is approximately 720bp, ligated into the 'Blunt PCR Product'. The XbaI enzyme cleaves twice at both sites. The enzyme cleavage sites are indicated by arrows with numbers. Fragment 2: The alternative products when the first XbaI site ($XbaI^{Met}$) is blocked by formation of a methylation site between the stop codon and the RE site. The product of approximately 773bp, contains an EcoRV site.

b) Ligation of Fragment 2 into the pcDNA3.1$^+$ Neo, the resulting constructs contained two EcoRV sites.

RE digestion using EcoRV is able to excise a 760bp fragment in a single reaction. The arrows and numbers refer to the enzymes cleavage sites on the pcDNA3.1$^+$ (Neo).

To overcome this problem, a Dam negative strain (Dam^-) of competent *E. coli* cells can be used, the GPCR fragment being inserted prior to the FPs. Alternatively, site-directed mutagenesis procedures can also be employed to change the stop codon sequence, thus eliminate the methylation site. However, the later approach was not adapted in this project for the main reason that the Dam methylation site and introduction of an additional EcoRV site should not affect the protein translation and functions. It was, therefore, not favourable to carry out an extra experimental step considering that the remaining time scale of the project is relatively short.

As already mentioned, a Dam^- strain of competent *E. coli* was transformed with the existing FP/pcDNA3.1$^+$(Neo) constructs. These constructs carry the extra EcoRV site downstream the FP fragments. In theory, the newly synthesised constructs should be un-methylated such that RE digestion using the XhoI and XbaI enzymes will be able to generate the right FP fragments. These fragments will subsequently be ligated into the pcDNA3.1$^+$(Neo) plasmid behind the GPCR gene, which was already cloned into the vector. In order to select and amplify these, the final constructs will be transformed into the Dam^- bacteria to avoid re-methylation. Nevertheless, in practice, although the HA-A_1R and Myc-P2Y_1R were successfully cloned into the pcDNA3.1$^+$(Neo), amplification of the FP/pcDNA3.1$^+$(Neo) constructs in the Dam^- did not entirely solve the problem. The XhoI

and XbaI enzymes, each were able to exise the FP, or the same-sized fragment in a single digestion (results not shown).

Such results were not anticipated, and could not be explained. Yet, it is important to confirm on the accuracy of these transformed FP constructs. Therefore, the Dam$^-$ strain amplified constructs were prepared for sequencing (Chapter 2). In this project, DNA sequence analysis was performed on campus, the constructs were amplified by sequencing PCR and purified in the lab before being loaded onto the sequencer by a specialised technician. The sequence analysis did not proceed effectively, several trials had shown problems such as contaminated DNA samples; crystal formation, which may come from the reagents; or even loss of DNA samples during purifications. These were not seen previously. Whilst endeavouring to identify and solve the problems for sequencing reactions, it was decided to abandon these constructs built using the Dam$^-$ bacteria, as unknown errors might have occurred, which serves an important implication that the chosen cloning strategy may be imperfect. This directly influences the quality of the resulting constructs generated. As mentioned earlier, all constructs produced by PCR into the TOPO vectors were confirmed by sequence analysis at the beginning of this PhD project. Therefore, in order to avoid any unexpected problems, these constructs will be used to transform into the Dam$^-$ bacteria directly, even though the TOPO Blunt plasmid is not an expression vector, in other words, not the most suitable plasmid for DNA

amplification. The constructs will be purified and fragment exised, and ligated into the pcDNA3.1^{+}(Neo) vector. This method not only ensures the accuracy of the GPCR and the FP DNAs, more crucially, eliminates the Dam methylation process so that the FP gene fragments will be excised from the correct XbaI site.

In the first step, the results of transformation were encouraging: all GPCR and FP constructs were successfully purified. After RE cleavage and extraction of the DNA fragments, GPCR were cloned into the pcDNA3.1^{+}(Neo) plasmid followed by the corresponding FPs. The HA-A_1R-YFP_{1-239} and Myc-P2Y_1R-YFP_{1-239} constructs were cloned first as trial experiments. Primary confirmation by RE were carried out, and results were positive (Figure 51 a)).

The two constructs were digested using two pairs of RE, NheI and EcoRV, and NheI and XbaI. The NheI and EcoRV pair flanking the GPCR moiety of the constructs will, thus, extract the fragment; whereas the later pair, NheI and XbaI, enzyme sites are located at both terminals of the entire constructs, digestions of which will excise the complete GPCR-YFP_{1-239} constructs (Figure 44). From Figure 51 a), it is not difficult to realise that the fragments removed by the NheI and EcoRV enzymes are around 1kb and slightly above 1kb for HA-A_1R and Myc-P2Y_1R respectively. These correspond to the more accurate size estimations from their DNA sequences, that the HA-

A_1R is approximately 1kb, and the Myc-$P2Y_1R$ 1.2kb. In addition, the full length YFP_{1-239} is about 720bp with the 3' end stop codon. Therefore, it is expected that the bands correspond to both HA-A_1R-YFP_{1-239} and Myc-$P2Y_1R$-YFP_{1-239} DNA fragments (i.e. after NheI and XbaI digestion) should have migrated at a much shorter distance compared with the GPCR alone, between the 1.65kb and 2.0kb bands as represented by the standard DNA ladder.

In Figure 51 b), HA-A_1R-$YFP_{156-239}$ and Myc-$P2Y_1R$-YFP_{1-173} cloned using the same method were analysed by the NheI and XbaI RE digestion reaction. The cleavage by these two enzymes generated DNA fragments slightly larger than 1.0kb and 1.65-2.0kb for HA-A_1R-$YFP_{156-239}$ and Myc-$P2Y_1R$-YFP_{1-173} respectively. These are approximately equivalent to the sequence-based size estimation: around 1.2kb and 1.7kb for each.

More accurate proof for the sequences was obtained by DNA sequencing analysis. The results showed that it was not clear whether the FP part of the construct was accurate for both HA-A_1R-$YFP_{156-239}$ and Myc-$P2Y_1R$-YFP_{1-173}, since the amplification of DNA seemed to be incomplete. The HA-A_1R-YFP_{1-239} construct was successfully cloned. Unfortunately, for the Myc-$P2Y_1R$-YFP_{1-239} construct, another GPCR DNA fragment, $P2Y_2R$ was mistaken for $P2Y_1R$, during the cloning process. Subsequent experiments were

carried out in order to ligate the purified Myc-$P2Y_1R$ fragment into the Myc-$P2Y_2R$-YFP_{1-239}, where the Myc-$P2Y_2R$ gene was exised by NheI and EcoRV enzymes, and the remaining part of the construct purified. The final Myc-$P2Y_1R$-YFP_{1-239} was sequenced again and confirmed the accuracy, prior to the large-scale DNA preparations by CsCl gradient (Chapter 2).

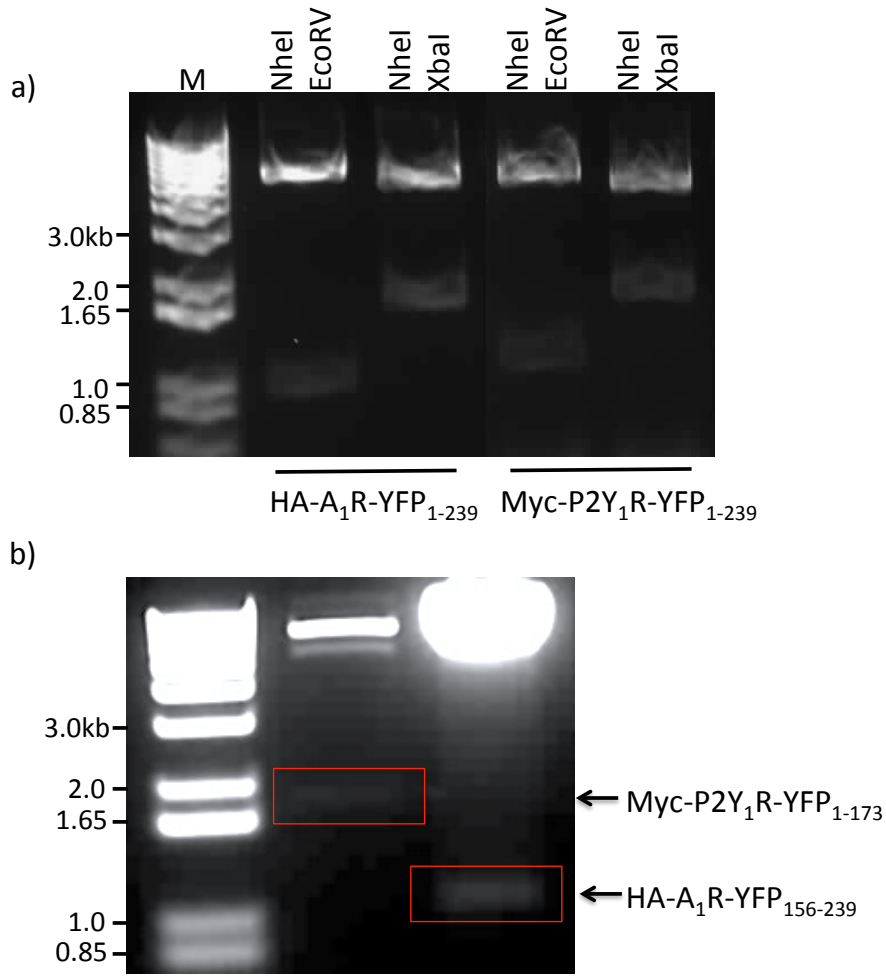

Figure 51. Restriction endonuclease analysis for the cloned constructs.

a) Confirmation of the HA-A_1R-YFP_{1-239} and Myc-$P2Y_1$R-YFP_{1-239} constructions using two pairs of RE.

Digestion using the NheI and EcoRV pair exised a DNA fragment of approximately 1.0kb and slightly larger than 1.0kb for the HA-A_1R-YFP_{1-239} and Myc-$P2Y_1$R-YFP_{1-239} constructions respectively. NheI and XbaI pairwise reaction yielded similar-sized fragment for both constructs, between 1.65 and 2.0kb.

b) Confirmation of the HA-A_1R-$YFP_{156-239}$ and Myc-$P2Y_1$R-YFP_{1-173} constructions using NheI and XbaI RE digestion.

A fragment of approximately 1.65 to 2.0kb was obtained from Myc-$P2Y_1$R-YFP_{1-173} after the RE reaction. For HA-A_1R-$YFP_{156-239}$, the excised fragment size is just above 1.0kb.

7.4 SUMMARY

This chapter focused on the descriptions of the molecular cloning work conducted in order to build up the DNA constructs for the BiFC assay. As discussed in Chapter 6, the antibody specificity problem had become a great issue impeding the progress of the co-IP experiments. In order to provide the evidence for the heteromeric receptor physical interactions, as well as a complementation to the co-IP work, an adaptation to the BiFC assay was planned. This technique had been advantageous in detection of receptor interactions, as discussed in the beginning of this chapter; in particular, it was used to investigate on the A_1R and $A_{2A}R$ homomeric and heteromeric oligomerisations in CHO cells. The results of these experiments showed that the fluorescent signals were specific from the receptor interactions, and C-terminal tagging of the FP fragments does not affect the homomeric receptor signalling properties, as well as the membrane expression. In addition, eGFP attachment to the C-terminal tail of the $P2Y_1R$ had also provided positive supporting evidence for the use of the FP in receptor detections, that the signal transduction property and the membrane localisation of the receptor were not affected.

The design of these constructs involves the GPCR ligated upstream of the FP fragments into the multiple cloning site (MCS) region of the pcDNA3.1$^+$(Neo) expression vector, approximately 20bp apart, thus a linker by the plasmid's intrinsic DNA sequence. The GPCR and the

FP sequences are each synthesised by PCR and cloned into the TOPO-Blunt vector. For the GPCR fragments, epitope tags (HA or Myc) were attached directly in front of the receptor, in order for use of the Co-IP assays in the future experiments. In addition, for both GPCR and FP, specific restriction endonuclease sequences were attached to the two terminals of the protein. This enables the receptor and fluorescent protein to be excised and ligated into the designated sites in the pcDNA3.1^{+}(Neo) vector plasmid's MCS region. Pairs of RE sites flanking the GPCR are NheI and EcoRV, and, XhoI and XbaI for the FP. Nevertheless, for the purpose of future experiments, before constructing into the complete GPCR-FP sequence, all GPCR and FP DNAs were each cloned into the pcDNA3.1^{+}(Neo) vector in the first step, and the products were amplified and purified by the large-scale DNA preparations.

Originally, four GPCRs were synthesised by PCR reactions, including HA-A_1R, HA-A_{2A}R, Myc-P2Y_1R, and Myc-P2Y_2R, all of which were subjected to stop codon deletion. FP fragments were inserted with a stop codon at their C-terminal tail, upstream adjacent to the XbaI RE site. These include the full-length $YFP_{1\text{-}239,}$ N-terminal fragment $YFP_{1\text{-}173}$ and $CFP_{1\text{-}173}$, as well as the C-terminal fragment $YFP_{156\text{-}239}$. All of the eight constructs were built into the pcDNA3.1^{+}(Neo) vector, which took almost six months to acquire fine molecular cloning techniques and establishment of the complicated CsCl-gradient large-scale DNA preparation method. Unfortunately, the laboratory notebook, which

contained a very detailed record of the cloning processes, was stolen. This resulted in a huge negative impact on future work: when problems were observed using RE digestions of the constructs, it became impossible to identify the possible cause of the problem, and at which the stages this may have occurred, as well as to check for further issues that may have arisen. Therefore, all of the constructs built into the pcDNA3.1^{+}(Neo) vector had to be discarded and the work recommenced from the beginning.

The question raised initially was that RE digestion excised HA-A_1R-YFP_{1-239} constructs from the pcDNA3.1^{+}(Neo) plasmid did not match the size expectation. This implied the constructs may contain certain errors, for example, inaccurate DNA fragments. Subsequent investigations were carried out using RE in order to check the integrity of both HA-A_1R and YFP_{1-239} fragments that were independently cloned into the pcDNA3.1^{+}(Neo) vector. The results of which were not promising, both GPCR and FP constructs may have acquired errors during the process of cloning, since the original constructs synthesised by PCR did not display any problem from DNA sequencing analysis. In addition, a more serious issue was identified, that the EcoRV enzyme on its own was able to exise all the FP fragments from the pcDNA3.1^{+}(Neo) vector, whilst the two RE sites designed flanking the FPs were NheI and EcoRV. On the other hand, NheI alone was not able to produce the same results. These,

therefore, brought concerns to the design of the constructs as well as the cloning strategy.

After careful examination of the sequence and design of the GPCR and FP constructs, it was discovered that the choice of the stop codon sequence at the 3' end of FPs, had indirectly caused the problems observed with the FP constructs. As a consequence, the error extends and might have led to faults in the HA-A_1R-YFP_{1-239} construct. The stop codon sequence TGA formed a Dam methylation site (GATC) with the sequences encoding the XbaI RE site directly adjacent to it, resulted into the XbaI being 'inactive' ($XbaI^{Met}$). In theory, this should have prevented the XhoI and XbaI enzyme pair extraction of the FPs from the TOPO blunt vector. However, the TOPO blunt vector itself contained XbaI site only about 50bp downstream the PCR cloning region, where the FP constructs were being ligated. It therefore provided an XbaI recognition site, in conjunction with the XhoI reaction, allowing the excision of an extended FPs fragment. Such fragment could not easily be distinguished from the true desirable FP fragment via DNA electrophoresis on a 1% agarose gel. In addition, an EcoRV site was identified approximately 20bp downstream the $XbaI^{Met}$, upstream of the vector-contained XbaI site, in this extend part of the construct. This provides the answer to the question why EcoRV alone was able to extract the FPs constructs from the pcDNA3.1$^+$(Neo) plasmid. It is because this EcoRV served as the second site in addition to the one,

which is approximately 20bp upstream above the 5' end of the FP construct, in the MCS region of the plasmid. As mentioned above, the extra 40bp of DNA sequence will hardly result into any difference by electrophoresis separation, thus EcoRV DNA fragments that were the almost the same sizes as the FPs.

Although additional EcoRV and XbaI sites were downstream of the stop codon, these should not affect the protein folding, and hence function. Nevertheless, it seemed important to avoid confusion that may cause misunderstanding of the results from RE digestions, since this is the main method for checking the integrity of DNA constructs, before proceeding to the large-scale amplification. One of the solutions to this Dam methylation problem is to perform a site-directed mutagenesis reaction. However, by adapting such technique, all of the FP/ TOPO blunt constructs would have to be re-synthesised, including design and synthesis of a pair of primers for PCR and ligation into the vector, as well as performing the large scale DNA purifications; all of which are quite time-consuming. Based on these reasons, I chose to use a Dam^- strain of competent E. *coli* cells. Transformation of the FP/ pcDAN3.1$^+$ (Neo) constructs into the Dam^- cells should produce mostly the un-methylated plasmids. Following XhoI and XbaI extraction, FPs can be ligated into the GPCR/ pcDAN3.1$^+$ (Neo), thus generate the complete GPCR-FP constructs. Unfortunately, it was not entirely understood why this method did not produced the expected results. Sequencing for these constructs was

attempted several times. Due to problems that might have occurred at the PCR steps as well as the subsequent purification steps, the quality of these results was not sufficient for analysis. Meanwhile, instead of using the FP/ pcDAN3.1^{+} (Neo) plasmids, the TOPO plasmids containing the FPs were directly transformed into the Dam^{-} cells, albeit a non-expression vector. Such strategy aimed to produce the un-methylated plasmids at the initial step of cloning, which, as a result, was successful.

The final sequenced and confirmed constructs were HA-A_1R-YFP_{1-239} and My-$P2Y_1$R-YFP_{1-239}, despite of the confusion that the $P2Y_2$R was mistaken for $P2Y_1$R, which was solve by simple RE digestion and ligation to exchange for both receptor constructs. For HA-A_1R-$YFP_{156-239}$ and Myc-$P2Y_1$R-YFP_{1-173}, the YFP moiety of the construct was not clear from the sequencing results; therefore, requires further confirmation.

Chapter 8

Discussion

In this thesis, I have investigated the signal transduction profiles in a heterogeneous mammalian cell system, the functional characteristics of which might be the result of a heteromeric receptor complex formed between A_1R and $P2Y_1R$, as previously identified in the literature. The previous study[103] was based on an over-expressed recombinant system from which the novel '$P2Y_1R$-like' signalling response through the heteromeric A_1R:$P2Y_1R$ was first identified. However, this is an amplified cell system with high receptor expression numbers. Since mammalian cells under physiological conditions may not exhibit such high level of receptors, it remains unclear how such a finding can relate to a biological system. Therefore, in order to establish the link between the functional heteromeric receptor signalling response and biological relevance, as well as to determine a functional profile through both receptor coupled pathways, a series of experiments were conducted in a clonal heterologous expression system with a significantly reduced receptor expression levels. The cell system was based on CHO.K1 cells, which express an endogenous $P2Y_1R$, that were then transfected with either a wild type or a constitutively active mutant A_1R.

The experimental results have been described in detail in chapters 3-6. In this chapter, I will focus on a discussion of these results in the context of previous findings and will suggest possible future experiments that might provide a better understanding of the A_1R:$P2Y_1R$ heteromeric receptor.

8.1 PHYSIOLOGICAL EXPRESSION LEVELS OF THE A_1 AND $P2Y_1$ RECEPTORS

Yoshioka *et al* identified the A_1R:$P2Y_1R$ functional response in HEK293T cells, where both HA-A_1R and Myc-$P2Y_1R$ were co-transfected, and compared their findings with HEK293T cells transfected with either A_1R or HA-A_1R, alone. Radio-ligand binding assay using [^{3}H]DPCPX on these transfected cells showed that the epitope tag did not affect expression efficiency, as the B_{max} value for both A_1R and HA-A_1R expressing cells revealed no significant differences (3.5 ± 0.12 pmol/mg and 3.6 ± 0.11 pmol/mg respectively). However, when compared with cells only expressing HA-A_1R, co-transfection of HA-A_1R and Myc-$P2Y_1R$ induced an approximately 50% reduction in B_{max} (1.9 ± 0.05 pmol/mg) whilst the K_D remained constant. Unfortunately, the expression level of $P2Y_1R$ in this system was unknown, since there was no commercially available radioligand for $P2Y_1$ receptor.

I have used two recombinant clonal cell lines previously established in the laboratory by Dr Andrea Townsend-Nicholson. These are based on CHO.K1 cells, which express $P2Y_1R$ endogenously, hence, at physiological level. Transfections using either a wild type human A_1R, or a constitutively active mutant human A_1R (the G14T mutation) were made and the B_{max} values were determined for different clones using [^{3}H]DPCPX (Table 7). The B_{max} values are expressed as the number of receptors per cell (receptors/cell). The theoretical conversion rate between the receptors/cell and pmol/mg (of membrane) is 1pmol/mg equivalent to 10^5 receptor/cell [227,228]. According to this conversion, in Yoshioka's study, the HA-A_1R expression level is about 190,000 receptors/cell, which is approximately the same as G14T A_1R of the G14T-13 cell line and is approximately 4-fold higher than the hA_1R expressed in the CHO cells in my project.

To determine what constitutes a "physiological level of expression", A_1R expression levels from different organisms and tissues were compared and found to range from approximately 2 fmol/mg in the rat cerebellum to about 5 pmol/mg in the guinea pig cortex (Shown in Table 8). In addition, the findings differ between research groups. All results in Table 8 were obtained from radioligand saturation binding assays using [^{3}H]DPCPX.

At 45,800 ± 2,890 receptors/cell, the hA_1-24 cell line has an A_1R expression level corresponding to approximately 460fmol/mg of protein, which lies within the physiological range shown in Table 6. The G14T-13 cell line has an A_1R expression level corresponding to approximately 2pmol/mg of protein, which also lies within physiological expression levels. It should also be noted that the expression levels obtained by Yoshioka *et al* also fall within this range.

CELL LINE	A_1R		$P2Y_1R$
	K_D (nM)	B_{MAX}(RECEPTOR/CELL)	
CHO.K1 (WILD TYPE)	-	-	Endogenous
CHO-hA_1 (CLONE-24)	0.65 ± 0.16	45,800 ± 2,890	Endogenous
CHO-G14T (CLONE-13)	1.30 ± 0.06	204,000 ± 5,260	Endogenous

Table 8. Quantification of A_1R expression levels in hA_1-24 and G14T-13 cells.

The affinity (K_D) for [^{3}H]DPCPX and the A_1 adenosine receptor density (B_{max}) were determined using a saturation radioligand binding assay (Dr Andrea Townsend-Nicholson, personal communication).

Species	Organs/ Tissue	B_{MAX} (fmol/mg)	Reference
Human	Astroglial cells	1340 ± 139	[229]
	Cortex	4960 ± 4220	[230]
	Lung parenchyma tissue	230 ± 25	[231]
Rat	Cerebellum (astrocyte culture)	≈ 2	[232]
	Cortex	2380 ± 490	[230]
	Cortex (astrocyte culture)	≈ 28	[232]
	Cerebral cortex (whole membrane)	917 ± 60	[233]
	Hippocampus	3860 ± 1230	[230]
	Hippocampus (astrocyte culture)	≈ 25	[232]
	Nodose ganglia	39.6 ± 1.2	[234]
	Renal membrane	19.9	[235]
	Striatum (astrocyte culture)	≈ 3	[232]
	Tegmentum (astrocyte culture)	≈ 24	[232]
	Thalamus (astrocyte culture)	≈ 23	[232]
	Whole brain (astrocyte culture)	≈ 14	[232]
	Whole brain (Young age)	204.79 ± 26.22	[236]
	Whole brain (old age)	101.09 ± 10.10	[236]
Guinea Pig	Cortex	5260 ± 1680	[230]
	Hippocampus	4500 ± 1750	[230]
Mouse	Cortex	3410 ± 730	[230]

Table 9. A_1R expressions levels in different tissues.

A_1 adenosine receptor density from different species and tissues are compared. Values range from 2fmol/mg to 5.3pmol/mg of protein.

8.2 CONSTITUTIVE ACTIVITY OF THE A_1R AND THE A_1R:$P2Y_1R$ CAMP RESPONSE

The purpose of these investigations was to characterise the signal transduction properties of the functional heteromeric A_1R:$P2Y_1R$ complex previously described by Yoshioka *et al*[103], where the $P2Y_1R$ agonist ADPβS elicited a $G_{\alpha i}$-coupled A_1R response that can be blocked by pertussis toxins. These experiments were conducted on a highly expressed recombinant cell system. In order to gain a greater understanding of the signalling profile of these heteromeric receptors, as well as to confirm whether such '$P2Y_1R$-like'[103] response takes place at physiological conditions, further studies were carried out.

A G14T mutant A_1R was previously and was shown to possess a 100-fold enhanced affinity for the A_1R agonist CCPA, with no significant difference in its DPCPX binding affinity by a research group, and was described later in a subsequent study to be a constitutively active A_1R[124] due to the constant level of [^{35}S]GTPγS specific binding level at varying concentrations of A_1R agonist CPA. In addition, cAMP assay results revealed a significant inhibition in the level of forskolin induced cAMP production in cells transfected with this G14T mutant A_1R, compared with a wild type A_1R or a mock cell line. This receptor was thought to be a model, thus the G14T-13 cell line.

In the lab, a preliminary trial assay had confirmed that the functional heteromeric receptor signalling process was only observed in G14T-13 cells, which expresses the constitutively active G14T A_1R, but not in the wild-type A_1R transfected hA_1-24 cells. It was, therefore, suspected that the A_1R constitutive activity might be a requirement for the heteromeric receptor to respond to ADPβS, the $P2Y_1R$ agonist. A report by Shryock *et al*[237] showed the observation of the spontaneous A_1R activity when the receptor was expressed at relatively high levels (4-8pmol per milligram of membrane proteins). This suggested the possibility of a natural-occurring constitutive activity, which can be explained by the constant conformational change of the GPCRs between the active and inactive states. Even though the expression level in Yoshioka's experiments was not as high as 4-8pmol/mg, it was indeed 4 times higher than the hA_1-24 cells, which could probably be one of the reasons why the functional response by ADPβS activation was not observed in hA_1-24 cells.

All experiments carried out had followed the same assay condition adapted by the Yoshioka group, which did not contain ADA. In addition, the cAMP assay method used in this thesis focused on the *de novo* synthesis of ^{3}H-cAMP, of which the results may be dependent on the amount of ^{3}H-adenine precursor integrated into the biochemical pathway of cAMP synthesis. This might have played a crucial role in the differential data compared with the previous literatures.

Overall, the constitutive activity of the receptor could not be firmly proved. The ability of G14T-13 cells to suppress the cAMP accumulation induced by forskolin was only assessed against the CHO.K1 cells, which do not express any A_1R. The response of the G14T receptor, as expressed by fold increase (of the cAMP) over basal level, showed significant reduction from the CHO.K1 cells; yet, most likely due to the large differences between the basal levels. Both cell lines yielded basal cAMP levels baring large magnitudes of errors almost 50% the mean values. The most significant cause of which could be from the minute amount of residual cAMP contained in the Dowex 50 and Alumina columns even after washing. Comparatively, these contribute to a large extent to the basal cAMP level, which is at minimal. Therefore, this serves as a clear indication that basal cAMP levels (in the absence of forskolin stimulation) should not be used as a normalisation figure for evaluating results between the two cell lines. Instead, an inverse agonist such as DPCPX can be used, and the results compared with the hA_1-24 cells, which express the wild-type A_1Rs. Regrettably, these experiments could not be improved due to the lack of time and resources (^{14}C-cAMP tracer).

The G14T-13 cell line responds to the A_1R agonists suggesting the G14T mutant receptor is a functional A_1R. A negative experiment with the CHO.K1 cells had supported this finding: the forskolin

responses did not show any significant change with the addition of A_1R agonists. The selective agonist CPA was taken for further analysis in both G14T-13 and hA_1-24 cells, the results of which revealed very little differences. CPA had the same potency level in both cell lines, although the level of response generated at each concentration point might contain certain level of variations. Only at 1nM and 100nM was a significant reduction detected in G14T-13 cells. For the remaining concentrations of CPA, even though the mean response level seemed to be approximately 10% lower than hA_1-24, because of the scale of errors, statistical analysis did not prove any significant difference demonstrated by the G14T-13. Therefore, it could only be concluded that at 1nM and 100nM CPA, G14T-13 cells express a functional A_1R, which displayed greater degree of inhibition to the forskolin-induced cAMP production compared to the hA_1-24 cells. However, it is not sufficient to serve as a supportive evidence for the G14T constitutive activity.

As mentioned in Chapter 3, the functional heteromeric response was analysed using ADP instead of the non-hydrolysable analogue ADPβS. The results produced an incomplete concentration-response curve, such that the potency of ADP had to be estimated under the assumption that the curve spans from 0 to 100% response. This had generated an ADP EC_{50} value of approximately 470μM. Such number might be significantly higher than the physiological concentrations of ADP in CHO cells. As some examples, in

vertebrate skeletal muscle cells, ADP concentration varies from 1-10μM at resting states to about 50-300μM at extreme conditions[238]; whereas in bovine aortic endothelia cells, the physiological ADP concentration is below 200μM[239]. These figures imply that the functional heteromeric response may not be physiological, and requires extracellular supply of ADP. Nevertheless, a certain proportion of ADP may have been subjected to hydrolysis, hence a rightward shift of concentration-response curve. Despite all, the unique property of these heteromeric receptors' activation by ADP and analogues provides great potential for pharmaceutical developments. On the other hand, hydrolysis of ADP may produce adenosine, which in turn is able to induce the $G_{\alpha i}$-coupled responses.

Since the ADA was excluded from the assay, it leaves a question whether ADP hydrolysis and adenosine exert any effect to the heteromeric receptor concentration response.

Another interesting finding was that the maximum inhibitory effect of ADP was 20% greater compared to ADPβS as shown by Yoshioka *et al*. Arguably, such phenomenon might be explained by the stimulation of adenosine from ADP hydrolysis, yet it could not fully support the observation that the EC_{50} level estimated from the concentration-response curve was profoundly reduced. The reason being that subjected to the stimulation of ADP and its hydrolysis product adenosine, the curve would very much likely bare a leftward shift, or even display multi-component features. Alternatively,

provided that the G14T receptor was indeed constitutively active, for which there has not been any firm evidence so far, the observations might be explained. The reduced potency level might be due to a differential ADP binding site formed between the A_1R and $P2Y_1R$, as well as an altered G-protein coupling; and the elevated efficacy level probably being the much higher level of constitutive activity in G14T-13 cells compared with the HEK293T cells, for which the potential constitutive activities may only be the result of high receptor density leading to greater possibilities of active-state receptor conformations.

8.3 The Biphasic Calcium Response Elicited By ADP

Although the heteromeric receptor signalling response via the cAMP-pathways has previously been published, very little information on the calcium response elicited by the $G_{\alpha q}$-coupled pathway was known.

In this project, I aimed to characterise the $G_{\alpha q}$-signalling properties of the A_1R:$P2Y_1R$ receptor heteromer by looking at the ADP-stimulated increase in the intracellular calcium concentrations. In these experiments, the calcium response was measured using the FLIPR assay. The use of ADP as the agonist is consistent with the use of this ligand to quantify cAMP production in the same cell lines. FLIPR is a fast and sensitive high throughput technique (that can be used to

generate a large amount of data efficiently) method a large amount of data is generated efficiently. However, since the detection of fluorescent signal is very sensitive, it becomes vital to have a strict control on the experimental conditions across the samples being assayed. Therefore, the use of a large number of plates (more then 5 plates) in a single experiment is not recommended, in particular when more than one drug plates are required.

From these experiments a biphasic calcium concentration-response relationship to ADP was found in the hA_1-24 and G14T-13 cell lines. This is a novel finding, and the results were compared against a wild-type CHO.K1 cell line response, which showed a sigmoid relationship to increasing agonist concentrations. These paired experiments differ only in the receptor expressions, such that the CHO.K1 cells lack any A_1R, whilst the G14T-13 and hA_1-24 cells were stably transfected with either a G14T mutant or a wild-type A_1R. As the functional data revealed differential ADP potency levels, it is thus most likely due to heterogeneous $P2Y_1R$ population in the hA_1-24 and G14T-13 cell lines. The lower-potency component of the curve might be the results of the heteromeric A_1R:$P2Y_1R$, whereas the ligand ADP might be more potent to the non-heteromeric $P2Y_1R$, hence no significant difference in the EC_{50} compared to the CHO.K1 cell response. In combination with the previous laboratory data that the functional heteromeric response was only observed in G14T-13 cells but not hA_1-24, it is thus intriguing that the constitutive activity (or at least the

G14T mutation) on the A_1R moiety might only be required for the functional $G_{\alpha i}$ signalling, but not for the $G_{\alpha q}$ pathway. This could serve as an implication that the A_1R and $P2Y_1R$ may be forming distinctive ADP binding sites by heteromerisation, such that the ligand activates the heteromeric receptor that signals through both $G_{\alpha i}$ and $G_{\alpha q}$ pathway simultaneously. As a result, the agonist potency level to the heteromeric receptor is greatly reduced through the $G_{\alpha q}$-coupled pathway. In the $G_{\alpha i}$ signalling pathway, the response was only observed when the mutant G14T A_1R was expressed, probably because the receptor bares potential constitutive activities. In the absence of any structural biological studies, pharmacological analysis of the antagonist responses might provide better understandings to such hypothesis. All antagonist pharmacology will be discussed in section 8.4.

Interestingly, the phenomenon that ADP can have differential affinity sites was first reported in 1995, with a chick brain $P2Y_1R$ expressed in *Xenopus* oocytes[240]. The agonist response was determined by the means of measuring the voltage change across the cell membrane that resulted from the opening of a Ca^{2+}-activated chloride channel. The EC_{50} of the high-potency site was determined to be approximately 258 ± 40nM, which is similar to the EC_{50} I obtained with -7.111 ± 0.09165 for G14T-13 cells and -7.229 ± 0.1294 for hA_1-24 cells. However, the authors concluded that the presence of the

low-affinity site was not clear and might be due to the presence of a contaminant. This was later reviewed by King & Townsend-Nicholson[241], who suggested that such a observation might be related to receptor densities and conformations of receptors that can exist as monomers and dimers. Another example of a low-potency ADP site was reported by Filtz *et al* in 1994[242], who showed the a native $P2Y_1R$ expressed in the turkey erythrocytes respond to ADP activation at 8μM potency, approximately -5.10 in a logarithmic scale, which also coincides with the values I obtained for the low-potency site. This information should not serve as supporting evidence for A_1R and $P2Y_1R$ heteromerisation purely based on the numerical values, however, in the *Xenopus* oocytes experiment above, possibilities of receptor heteromerisation should not be excluded, since the cells express an endogenous $P2Y_{11}R$ which can transduce signals via both cAMP and calcium pathways and is able to form heteromers with the $P2Y_1R$.[243] In addition, there is strong evidence supporting the existence of an adenosine receptor in this cell line[244,245] and, it was also pointed out by the authors that: an adenosine receptor response was found to be present in some batches of *Xenopus* oocytes used in the study by Simon *et al*.

As initially thought, the mutant G14T A_1R activity (whether being constitutively active or other potential activity as the constitutive activity was not confirmed by cAMP assays in this thesis) might facilitate the formation of heteromeric receptor. This can be reflected

on the curve by an increase in the proportion of the low-potency ADP response (i.e. the top phase of the curve) compared with hA_1-24 cells. However, this ratio (the proportion of the low-potency component relative to the entire curve) showed significant variability, such that the mean values for both curves were approximately 50%, not statistically significantly different from one another. On the other hand, in these cells, the $P2Y_1$Rs are endogenously expressed. Therefore, the $P2Y_1$R expression level will be the limiting factor in the heteromeric receptor's formation. In other words, if the transfected A_1R/ G14T A_1R expression exceeds the endogenous $P2Y_1$R level, then the formation of heteromeric receptors will be hindered by the smaller amount of $P2Y_1$R expression levels. It is not clear why the proportion of receptors in the low-potency phase, i.e. the A_1R:$P2Y_1$R, did not remain stable, but a possible explanation might be related to the cell density at the time of the FLIPR assay. Several pharmacological approaches were attempted to prove this hypothesis: by using the A_1R agonist in conjunction with ADP; or the comparison of ADP concentration responses between CHO cell lines expressing varying concentrations of G14T mutant A_1R. Nevertheless, these experiments were not successful partly because the ADP concentration-response curve in both G14T-13 and hA_1-24 cells failed to reveal the biphasic shape as previously proved by at least six repeated experiments. Due to the lack of valid reference and control results, all data obtained were incomparable, even though the quality of these data was not reliable.

Although it remains unsolved whether the activation of A_1R might increase the observation of low-potency ADP response, it was noted that the cell confluence clearly has a significant impact on the calcium response. A stable ADP concentration-response relationship was only observed when the assay was performed at sub-confluent cell densities. The concentration-response curve shifts even when the confluence level experiences a marginal change. It seems that as the confluence level increases, such change becomes more significant. The biphasic characteristic of the curve was ambiguous (hA_1-24, multi-component-like curve) or completely diminished (G14T-13, sigmoidal curve) at 'confluent'. Only at 'over-confluent level' was a significant rightward shift of the curve observed. The concentration response to ADP at this confluence level was monophasic, the maximum response of which was undefined as the curves revealed tendency of continuous increase beyond the highest available concentration of the ligand. The EC_{50} estimation by the Prism software showed the value is even lower than the upper component of the biphasic curve, which might be due to the formation of A_1R:$P2Y_1R$ heteromers. However, this low EC_{50} value does not necessary indicate an extremely shifted equilibrium towards the A_1R:$P2Y_1R$ in the total $P2Y_1R$ population. It could be an implication of a decreased $G_{\alpha q}$ protein coupling property at higher confluence levels, and thus a reduced potency level of the ligand. Another possible explanation is that at different cell density level, the

cells may enter a different growth cycle. The cells grow in the tissue culture flask in a monolayer; in other words, further proliferation is inhibited or restricted by the limited growth surface area. It is frequently observed in cell culture practice that prolonged incubation exceeding the maximal growth surface area results in cell apoptosis. Floating cell debris and change in the pH of the medium are the most direct indications for cell death. Therefore, compared with 'sub-confluent' density, at 'confluent' level the majority of the cells enter the G_0 phase, where the cells rest and cease to divide. There might be a very subtle difference between the receptors membrane expression levels, which then leads to the change in the ADP concentration response. On the other hand, at 'over-confluent' cell density, floating detached cells or debris are always observed. Decrease in the medium pH level is indicated by changes in the colour of medium from red (phenol red indicator contained) to yellow. Under such conditions, the release of intracellular content and the drop in the pH level might bring significant impact, either directly or indirectly, to the receptors and responses to ADP. Despite all, at 'sub-confluent' level, a biphasic concentration-response relationship of ADP is always observed.

8.4 ANTAGONISM AND THE cAMP AND CALCIUM SIGNALLING PATHWAYS

The antagonist analysis was performed using the same set of ligands for the heteromeric receptor signalling responses through both the $G_{\alpha i}$ and $G_{\alpha q}$-coupled pathways. The comparison between the two different, but interdependent pathways, provides important information on the possible signalling mechanisms utilised by the heteromeric receptors.

When considering the cAMP response, the ADP inhibition of the forskolin-induced cAMP production levels, was blocked by A_1R (DPCPX) and $P2Y_1R$ (MG 50-3-1) antagonists. MG 50-3-1 is structurally related to Reactive Blue 2, and is the most potent antagonist at the $P2Y_1$-like-receptor of the guinea-pig taenia coli[246]. MRS 2179, on the other hand, was not able to exert an effect on ADP, which may be due to the large error that resulted from significant variations in the mean. However, this only represents one single experiment, due to the problems of ^{14}C-cAMP tracer supply. The most significant outcome from this experiment is the conclusion that both A_1R and $P2Y_1R$ activation are required for the functional cAMP response, as the pharmacological block of either receptor inhibits the A_1R:$P2Y_1R$ $G_{\alpha i}$ response.

In contrast, signalling through the $G_{\alpha q}$-coupled pathway revealed a slightly different response to antagonists. DPCPX was not effective at inhibiting $G_{\alpha q}$ responses in any of the cell lines tested. MRS 2179 and MG 50-3-1 showed competitive antagonism of the ADP response in CHO.K1 cells, but the antagonistic effect is only seen on the high-affinity ADP binding site (homomeric $P2Y_1R$) but not on the A_1R:$P2Y_1R$ heteromeric receptor site in hA_1-24 and G14T-13 cells. These results indicate that although signalling through the $G_{\alpha i}$-pathway requires a constitutively active A_1R, it is not a requirement for the $G_{\alpha q}$-coupled signalling; as DPCPX did not inhibit the ADP-evoked calcium response. Phospholipase Cβ (PLCβ) plays a pivotal role in this transduction pathway as hydrolysis of PIP_2 to produce IP_3 leading the intracellular calcium mobilisation. The G_i-protein βγ subunit ($G_{i\beta\gamma}$) is able to activate PLCβ-3 enzyme as a cross-talk mechanism. Since CHO.K1 cells exclusively express PLCβ-3, which can be regulated by $G_{i\beta\gamma}$, this may influence the calcium signals that are detected. This cross-talk pharmacology has been studied to a great extent, in the past years by Hill *et al*[188,247-249], especially in the hA_1-transfected CHO cells, which has similar expression levels as the hA_1-24 cells. These studies confirmed that the $G_{i\beta\gamma}$ subunit release from the A_1R activation induced a concentration-dependent increase in IP_3 levels, which then causes mobilisation of intracellular calcium. Most of the A_1R agonists tested, including CPA, NECA and

APNEA had significant effect on the activation of the $G_{i\beta\gamma}$-induced IP_3 production. In particular, the synergistic stimulation by CPA and UTP on A_1R and $P2Y_2R$, which is also endogenously expressed in the CHO.K1 cell line, showed an IP_3 response much greater than the additive response of both signalling pathways. Based on these findings, it is reasonable to argue that the low-affinity ADP site may receive contributions from the $G_{i\beta\gamma}$-stimulation of PLCβ-3 rather than the sole affect of $P2Y_1R$-coupled $G_{\alpha q}$ proteins. However, the antagonism data suggested that the calcium response is independent of $G_{\alpha i}$ signalling. Furthermore, although synergy between A_1R and $P2Y_2R$ was confirmed in an hA_1R-expressing cell line, the $P2Y_2R$ is not activated by ADP.

Having discussed that the low-affinity site most likely corresponds to the A_1R:$P2Y_1R$, it is now possible to hypothesise that the reason the response from A_1R:$P2Y_1R$ is not inhibited by a $P2Y_1R$ antagonist may be because the two receptors form a shared novel agonist binding site for ADP. For example, the adenosine moiety of ADP may be shared between the receptors, and the diphosphate group may interact primarily with the $P2Y_1R$. Such ligand binding may bypass the conventional $P2Y_1R$ receptor antagonism, especially in a receptor conformation required for signalling via the $G_{\alpha q}$ pathway. It has been shown that in A_1R the N^6-adenine of adenosine analogues tend to

orientate towards the top of TM3, with the ribose group interacting with the bottom half of TM3 and TM7[209,250]. For $P2Y_1R$, the ATP binding site is believed to be located between TM3, 6 and 7. The adenine group is close to TM6 and 7, the ribose group is close to TM3 and 7, and the adenosine and α-phospohate interact with the exofacial side of TM3 and 7, which implies the binding site for the adenosine group may not be completely buried within the transmembrane domains, making it possible to form a novel site for the adenosine group between the two different receptors.

8.5 CONCLUSION

In conclusion, a unique $G_{\alpha i}$-coupled response was observed, which corresponds to the functional A_1R:$P2Y_1R$ heteromeric receptor pharmacology as described in previous literature. The work conducted in this thesis was primarily base on clonal CHO.K1 cell lines, hA_1-24 that stably-expresses wild-type human A_1R and, G14T-13, stably-transfected with a G14T mutant A_1R reported by the literature to possess constitutive activity. However, such constitutive activity could not be confirmed in this thesis. In hA_1-24 cells, A_1R is expressed at a level comparable to that seen under the physiological conditions, and revealed previously unidentified information about the conditions required for signalling via the A_1R:$P2Y_1R$ heteromeric receptor.

At physiological expression levels, the $G_{\alpha i}$-coupled cAMP response was not observed with a wild-type A_1R but was seen with a constitutively active A_1R. However, the calcium mobilisation response to ADP stimulation on the $G_{\alpha q}$-coupled PLCβ activation pathway showed two separate potencies for ADP. Strict control of the conditions indicated a heterogeneous population of $P2Y_1Rs$, and that the high- and low-potency reactions mostly like correspond to homomeric $P2Y_1R$ and heteromeric A_1R:$P2Y_1R$ receptor signalling. This response is independent of the A_1R activity, as the same signalling profile was detected in the G14T-13 cells and further, was not inhibited by the A_1R selective DPCPX. In contrast, calcium responses elicited by the more potent ADP response were blocked by the $P2Y_1R$ competitive antagonists MRS 2179 and a novel antagonist MG 50-3-1. Co-activation of both A_1R and $P2Y_1R$ is crucial for signal transduction of the A_1R: $P2Y_1R$ heteromeric receptor through the $G_{\alpha i}$-coupled pathway.

8.6 FUTURE WORK

8.6.1 Functional Characterisation

8.6.1.1 cAMP Signalling

Further characterisation of the $G_{\alpha i}$ response will require resolution of the problem encountered in the cAMP assays due to the unavailability of the ^{14}C-cAMP tracer. As mentioned in Chapter 3, this tracer element is important for the estimation of column efficiency rate, without which, the results become unreliable. A batch of a new synthesis of the product was tested. The results suggested this ^{14}C-labelled substance was not cAMP, as it failed to elude from the Dowex and alumina columns. Therefore, in order to continue the research, a new and alternative method of quantifying cAMP needs to be developed. Secondly, the antagonist experiments should be repeated to confirm the MRS 2179 and MG 50-3-1 response in G14T-13 cells. The differences, if any exist, between these two ligands will provide valuable information about the ADP binding properties of the heteromeric A_1R:$P2Y_1R$ complex. In addition, the response to adenosine can be investigated since it is the naturally-occurring agonist for the A_1R. Furthermore, although it is only a hypothesis, GTPγS-binding experiments will help to analyse and compare the G protein-coupling properties between cells expressing A_1R or $P2Y_1R$ alone, and cells co-expressing both receptors, to see whether the heteromerisation process influences the G14T A_1R coupling to $G_{\alpha i}$. For example, whilst CHO.K1 cells do not express

A_1R, the 1321N1 cells lack $P2Y_1R$, and could be used to establish new cell lines for such experiments.

8.6.1.2 Calcium Signalling

The calcium response through the receptor heteromer can also be studied further, mainly focusing on the low-affinity ADP site, which corresponds to the A_1R:$P2Y_1R$ heteromers. Although it has been shown that DPCPX will not inhibit the response produced by a constitutively-active A_1R-coupled $P2Y_1R$ heteromer, this inhibitory response was not studied in the hA_1-24 cells, which express the wild-type A_1R:$P2Y_1R$ heteromers. Therefore, it can only be concluded, so far, that the low-affinity heteromeric receptor signalling process does not require the A_1R constitutive activity. Whether this response will persist when the wild-type A_1R is blocked by DPCPX remains to be determined. In addition, co-activation of both receptors can also be tested in both G14T-13 and hA_1-24 cells. It would be difficult, at this stage, to suggest a ligand that enhances or suppresses the formation of this heteromeric receptor complex. On the other hand, it is possible that in both G14T-13 and hA_1-24 cells, the levels of $P2Y_1R$ might be limiting the level of heteromerisation. Therefore, it would be of interest to use 1321N1 cells to vary $P2Y_1R$ expression levels in the presence of an endogenous A_1R. The drawback of such an approach is that the levels of $P2Y_1R$ expression level cannot presently be determined by radioligand binding. However, the extent of receptor

heteromerisation can be revealed by the proportion of the calcium responses to ADP in the low-potency sites. In addition, a question that remains to be asked is whether the decrease in the ADP potency level seen with antagonist inhibition on the homomeric $P2Y_1R$ also facilitates the formation of the heteromeric receptor, since the rightward shift in the high-potency phase eventually merges with the low-potency site, making it impossible to distinguish between $P2Y_1R$ antagonism and an increase in the number of A_1R:$P2Y_1R$ receptors. This question might be better answered by using the BiFC technique, which was discussed in 7.6.2.

8.6.2 Physical Interactions

Currently, detection using the native receptor-specific antibody showed the specific signal for $P2Y_1R$. However, due to specificity problems with the commercially available antibody for A_1R, a non-specific band approximately the same size is also detected in western blots. This may be caused by impurities that are intrinsically present in the cells and membranes. It was not within the scope of this project to develop a specific antibody for the A_1. Therefore, the BiFC technique was chosen as an alternative method for detections for physical interactions, since if native receptor interactions were not able to be characterised, visualisation of receptor interactions in living cells would provide important information about conditions under which A_1R:$P2Y_1R$ form. The heteromerisation process intrinsic

to BiFC brings the two fluorescent protein fragments into close proximity, allowing alignment and reconstitution of a functional fluorescent protein. This process can also take place between complementary fragments of different fluorescent proteins so, for example, YFP and CFP fragments can re-associate, making competition assays possible, for example to further study the formation of A_1R:$P2Y_1R$ and A_1R:$P2Y_2R$ in CHO.K1 cells. The constructs for this assay are being cloned at the moment. BiFC will also identify if the complex is formed intracellularly or on the membrane and will be useful for studying desensitisation and other properties of the heteromers. The example of this is demonstrated previously by Briddon *et al*, who looked into the membrane expression and transport of the A_1R and $A_{2A}R$ homomers and heteromers[225] and showed that homomers of both receptors were detected on the cell membrane as well as in the intracellular space, suggesting that the oligomers may be formed before being transported to membrane surface or that receptor trafficking may take place. A_1R and $P2_1R$ homomeric and heteromeric formations have been observed to be facilitated by both receptors selective agonists[251,252]. Therefore, in future experiments, the use of agonists in a BiFC assay might assist in identifying cellular compartmentations in which oligomerisation takes place. As mentioned earlier, BiFC may also provide more precise information regarding the effect of ligands, both agonist and antagonist, on the level of heteromerisation. Finally, the A_1R preferential binding partner between the $P2Y_1R$ and $P2Y_2R$

may be determined. Since the chromophore of the fluorescent protein is at the N-terminal fragment, therefore, by tagging N-terminal fragments of different fluorescent proteins to $P2Y_1R$ and $P2Y_2R$, the competitive binding between the two receptors can be identified.

References

1 Gurevich, V. V. & Gurevich, E. V. GPCR monomers and oligomers: it takes all kinds. *Trends Neurosci* **31**, 74-81 (2008).

2 Pierce, K. L., Premont, R. T. & Lefkowitz, R. J. Seven-transmembrane receptors. *Nat Rev Mol Cell Biol.* **3**, 639-650. (2002).

3 George, S. R., O'Dowd, B. F. & Lee, S. P. G-protein-coupled receptor oligomerization and its potential for drug discovery. *Nat Rev Drug Discov* **1**, 808-820 (2002).

4 Milligan, G. G protein-coupled receptor dimerisation: molecular basis and relevance to function. *Biochim Biophys Acta* **1768**, 825-835, doi:10.1016/j.bbamem.2006.09.021 (2007).

5 Schertler, G. F., Villa, C. & Henderson, R. Projection structure of rhodopsin. *Nature* **362**, 770-772 (1993).

6 Schwartz, T. W. Locating ligand-binding sites in 7TM receptors by protein engineering. *Curr Opin Biotechnol* **5**, 434-444 (1994).

7 Baldwin, J. M. The probable arrangement of the helices in G protein-coupled receptors. *Embo J* **12**, 1693-1703 (1993).

8 Okada, T. *et al.* X-Ray diffraction analysis of three-dimensional crystals of bovine rhodopsin obtained from mixed micelles. *J Struct Biol* **130**, 73-80 (2000).

9 Bourne, H. R. How receptors talk to trimeric G proteins. *Curr Opin Cell Biol* **9**, 134-142 (1997).

10 Iiri, T., Farfel, Z. & Bourne, H. R. G-protein diseases furnish a model for the turn-on switch. *Nature* **394**, 35-38, doi:10.1038/27831 (1998).

11 Palczewski, K. *et al.* Crystal structure of rhodopsin: A G protein-coupled receptor. *Science* **289**, 739-745 (2000).

12 Stenkamp, R. E., Teller, D. C. & Palczewski, K. Crystal structure of rhodopsin: a G-protein-coupled receptor. *Chembiochem* **3**, 963-967, doi:10.1002/1439-7633(20021004)3:10<963::aid-cbic963>3.0.co;2-9 (2002).

13 Pierce, K. L., Premont, R. T. & Lefkowitz, R. J. Seven-transmembrane receptors. *Nat Rev Mol Cell Biol* **3**, 639-650, doi:10.1038/nrm908 (2002).

14 Leff, P. The two-state model of receptor activation. *Trends Pharmacol Sci* **16**, 89-97 (1995).

15 Henderson, R. *et al.* Model for the structure of bacteriorhodopsin based on high-resolution electron cryo-microscopy. *J Mol Biol* **213**, 899-929, doi:10.1016/s0022-2836(05)80271-2 (1990).

16 Pardo, L., Ballesteros, J. A., Osman, R. & Weinstein, H. On the use of the transmembrane domain of bacteriorhodopsin as a template for modeling the three-dimensional structure of guanine nucleotide-binding regulatory protein-coupled receptors. *Proc Natl Acad Sci U S A* **89**, 4009-4012 (1992).

17 Crystal structure of rhodopsin: a G protein-coupled receptor. Palczewski K,*(1) kumasaka T, hori T, behnke CA, motoshima H, fox BA, trong IL, teller DC, okada T, stenkamp RE, yamamoto M, miyano M. Science 2000;289:739-745. *Am J Ophthalmol* **130**, 865 (2000).

18 Pin, J. P. *et al.* International Union of Basic and Clinical Pharmacology. LXVII. Recommendations for the recognition and nomenclature of G protein-coupled receptor heteromultimers. *Pharmacol Rev* **59**, 5-13 (2007).

19 Gearing, K. L. *et al.* Complex chimeras to map ligand binding sites of GPCRs. *Protein Eng* **16**, 365-372 (2003).

20 Jaakola, V. P. *et al.* The 2.6 angstrom crystal structure of a human A2A adenosine receptor bound to an antagonist. *Science* **322**, 1211-1217, doi:10.1126/science.1164772 (2008).

21 Del Castillo, J. & Katz, B. Interaction at end-plate receptors between different choline derivatives. *Proc R Soc Lond B Biol Sci* **146**, 369-381 (1957).

22 Colquhoun, D. The relation between classical and cooperative models for drug action. *In Drug Receptors, ed. Rang, H. P., pp. 149-182. Macmillan Press, London.* (1973).

23 Samama, P., Cotecchia, S., Costa, T. & Lefkowitz, R. J. A mutation-induced activated state of the beta 2-adrenergic receptor. Extending the ternary complex model. *J Biol Chem* **268**, 4625-4636 (1993).

24 GPCRDB. http://www.gpcr.org/7tm.

25 Cobanoglu, M. C., Saygin, Y. & Sezerman, U. Classification of GPCRs Using Family Specific Motifs. *IEEE/ACM Trans Comput Biol Bioinform*, doi:10.1109/tcbb.2010.101 (2010).

26 Peng, Z. L., Yang, J. Y. & Chen, X. An improved classification of G-protein-coupled receptors using sequence-derived features. *BMC Bioinformatics* **11**, 420, doi:10.1186/1471-2105-11-420 (2010).

27 Worth, C. L., Kreuchwig, A., Kleinau, G. & Krause, G. GPCR-SSFE: a comprehensive database of G-protein-coupled receptor template predictions and homology models. *BMC Bioinformatics* **12**, 185, doi:10.1186/1471-2105-12-185 (2011).

28 Conklin, B. R. & Bourne, H. R. Structural elements of G alpha subunits that interact with G beta gamma, receptors, and effectors. *Cell* **73**, 631-641 (1993).

29 Lambright, D. G. *et al.* The 2.0 A crystal structure of a heterotrimeric G protein. *Nature* **379**, 311-319, doi:10.1038/379311a0 (1996).

30 Lambright, D. G., Noel, J. P., Hamm, H. E. & Sigler, P. B. Structural determinants for activation of the alpha-subunit of a heterotrimeric G protein. *Nature* **369**, 621-628, doi:10.1038/369621a0 (1994).

31 Coleman, D. E. *et al.* Structures of active conformations of Gi alpha 1 and the mechanism of GTP hydrolysis. *Science* **265**, 1405-1412 (1994).

32 Noel, J. P., Hamm, H. E. & Sigler, P. B. The 2.2 A crystal structure of transducin-alpha complexed with GTP gamma S. *Nature* **366**, 654-663, doi:10.1038/366654a0 (1993).

33 Clapham, D. E. & Neer, E. J. G protein beta gamma subunits. *Annu Rev Pharmacol Toxicol* **37**, 167-203 (1997).

34 Dhanasekaran, N. & Dermott, J. M. Signaling by the G12 class of G proteins. *Cell Signal* **8**, 235-245 (1996).

35 Kurose, H. Galpha12 and Galpha13 as key regulatory mediator in signal transduction. *Life Sci* **74**, 155-161 (2003).

36 Milligan, G. & Kostenis, E. Heterotrimeric G-proteins: a short history. *Br J Pharmacol* **147 Suppl 1**, S46-55 (2006).

37 Wedegaertner, P. B., Chu, D. H., Wilson, P. T., Levis, M. J. & Bourne, H. R. Palmitoylation is required for signaling functions and membrane attachment of Gq alpha and Gs alpha. *J Biol Chem* **268**, 25001-25008 (1993).

38 Kleuss, C., Scherubl, H., Hescheler, J., Schultz, G. & Wittig, B. Different beta-subunits determine G-protein interaction with transmembrane receptors. *Nature* **358**, 424-426, doi:10.1038/358424a0 (1992).

39 Kleuss, C., Scherubl, H., Hescheler, J., Schultz, G. & Wittig, B. Selectivity in signal transduction determined by gamma subunits of heterotrimeric G proteins. *Science* **259**, 832-834 (1993).

40 Gomes, I. *et al.* G protein coupled receptor dimerization: implications in modulating receptor function. *J Mol Med* **79**, 226-242 (2001).

41 Jahangeer, S. & Rodbell, M. The disaggregation theory of signal transduction revisited: further evidence that G proteins are multimeric and disaggregate to monomers when activated. *Proc Natl Acad Sci U S A* **90**, 8782-8786 (1993).

42 Agnati, L. F., Fuxe, K., Zoli, M., Rondanini, C. & Ogren, S. O. New vistas on synaptic plasticity: the receptor mosaic hypothesis of the engram. *Med Biol* **60**, 183-190 (1982).

43 Yan, K., Greene, E., Belga, F. & Rasenick, M. M. Synaptic membrane G proteins are complexed with tubulin in situ. *J Neurochem* **66**, 1489-1495 (1996).

44 Angers, S., Salahpour, A. & Bouvier, M. Dimerization: an emerging concept for G protein-coupled receptor ontogeny and function. *Annu Rev Pharmacol Toxicol* **42**, 409-435 (2002).

45 Agnati, L. F., Ferre, S., Lluis, C., Franco, R. & Fuxe, K. Molecular mechanisms and therapeutical implications of intramembrane receptor/receptor interactions among heptahelical receptors with

examples from the striatopallidal GABA neurons. *Pharmacol Rev* **55**, 509-550 (2003).

46 Mercier, J. F., Salahpour, A., Angers, S., Breit, A. & Bouvier, M. Quantitative assessment of beta 1- and beta 2-adrenergic receptor homo- and heterodimerization by bioluminescence resonance energy transfer. *J Biol Chem* **277**, 44925-44931 (2002).

47 Issafras, H. *et al.* Constitutive agonist-independent CCR5 oligomerization and antibody-mediated clustering occurring at physiological levels of receptors. *J Biol Chem* **277**, 34666-34673 (2002).

48 Salahpour, A. *et al.* Homodimerization of the beta2-adrenergic receptor as a prerequisite for cell surface targeting. *J Biol Chem* **279**, 33390-33397 (2004).

49 Wilson, S., Wilkinson, G. & Milligan, G. The CXCR1 and CXCR2 receptors form constitutive homo- and heterodimers selectively and with equal apparent affinities. *J Biol Chem* **280**, 28663-28674 (2005).

50 Law, P. Y. *et al.* Heterodimerization of mu- and delta-opioid receptors occurs at the cell surface only and requires receptor-G protein interactions. *J Biol Chem* **280**, 11152-11164 (2005).

51 Wang, D., Sun, X., Bohn, L. M. & Sadee, W. Opioid receptor homo- and heterodimerization in living cells by quantitative bioluminescence resonance energy transfer. *Mol Pharmacol* **67**, 2173-2184 (2005).

52 Ramsay, D., Kellett, E., McVey, M., Rees, S. & Milligan, G. Homo- and hetero-oligomeric interactions between G-protein-coupled receptors in living cells monitored by two variants of bioluminescence resonance energy transfer (BRET): hetero-oligomers between receptor subtypes form more efficiently than between less closely related sequences. *Biochem J* **365**, 429-440 (2002).

53 Zeng, F. Y. & Wess, J. Identification and molecular characterization of m3 muscarinic receptor dimers. *J Biol Chem* **274**, 19487-19497 (1999).

54 Harikumar, K. G., Morfis, M. M., Lisenbee, C. S., Sexton, P. M. & Miller, L. J. Constitutive formation of oligomeric complexes

between family B G protein-coupled vasoactive intestinal polypeptide and secretin receptors. *Mol Pharmacol* **69**, 363-373 (2006).

55 Hebert, T. E. *et al.* A peptide derived from a beta2-adrenergic receptor transmembrane domain inhibits both receptor dimerization and activation. *J Biol Chem* **271**, 16384-16392 (1996).

56 AbdAlla, S., Zaki, E., Lother, H. & Quitterer, U. Involvement of the amino terminus of the B(2) receptor in agonist-induced receptor dimerization. *J Biol Chem* **274**, 26079-26084 (1999).

57 Rodriguez-Frade, J. M. *et al.* The chemokine monocyte chemoattractant protein-1 induces functional responses through dimerization of its receptor CCR2. *Proc Natl Acad Sci U S A* **96**, 3628-3633 (1999).

58 Horvat, R. D., Roess, D. A., Nelson, S. E., Barisas, B. G. & Clay, C. M. Binding of agonist but not antagonist leads to fluorescence resonance energy transfer between intrinsically fluorescent gonadotropin-releasing hormone receptors. *Mol Endocrinol* **15**, 695-703 (2001).

59 Cheng, Z. J. & Miller, L. J. Agonist-dependent dissociation of oligomeric complexes of G protein-coupled cholecystokinin receptors demonstrated in living cells using bioluminescence resonance energy transfer. *J Biol Chem* **276**, 48040-48047 (2001).

60 Latif, R., Graves, P. & Davies, T. F. Ligand-dependent inhibition of oligomerization at the human thyrotropin receptor. *J Biol Chem* **277**, 45059-45067 (2002).

61 Milasta, S. *et al.* Interactions between the Mas-related receptors MrgD and MrgE alter signalling and trafficking of MrgD. *Mol Pharmacol* **69**, 479-491 (2006).

62 George, S. R. *et al.* Oligomerization of mu- and delta-opioid receptors. Generation of novel functional properties. *J Biol Chem* **275**, 26128-26135, doi:10.1074/jbc.M000345200 (2000).

63 Lee, S. P. *et al.* Dopamine D1 and D2 receptor Co-activation generates a novel phospholipase C-mediated calcium signal. *J Biol Chem* **279**, 35671-35678, doi:10.1074/jbc.M401923200 (2004).

64 Fan, T. *et al.* A role for the distal carboxyl tails in generating the novel pharmacology and G protein activation profile of mu and delta opioid receptor hetero-oligomers. *J Biol Chem* **280**, 38478-38488, doi:10.1074/jbc.M505644200 (2005).

65 So, C. H. *et al.* D1 and D2 dopamine receptors form heterooligomers and cointernalize after selective activation of either receptor. *Mol Pharmacol* **68**, 568-578, doi:10.1124/mol.105.012229 (2005).

66 Rios, C. D., Jordan, B. A., Gomes, I. & Devi, L. A. G-protein-coupled receptor dimerization: modulation of receptor function. *Pharmacol Ther* **92**, 71-87 (2001).

67 Ng, G. Y. *et al.* Identification of a GABAB receptor subunit, gb2, required for functional GABAB receptor activity. *J Biol Chem* **274**, 7607-7610 (1999).

68 Guo, W., Shi, L., Filizola, M., Weinstein, H. & Javitch, J. A. Crosstalk in G protein-coupled receptors: changes at the transmembrane homodimer interface determine activation. *Proc Natl Acad Sci U S A* **102**, 17495-17500 (2005).

69 Meyer, B. H. *et al.* FRET imaging reveals that functional neurokinin-1 receptors are monomeric and reside in membrane microdomains of live cells. *Proc Natl Acad Sci U S A* **103**, 2138-2143 (2006).

70 Jastrzebska, B. *et al.* Functional and structural characterization of rhodopsin oligomers. *J Biol Chem* **281**, 11917-11922 (2006).

71 Zhou, F., Filipeanu, C. M., Duvernay, M. T. & Wu, G. Cell-surface targeting of alpha2-adrenergic receptors -- inhibition by a transport deficient mutant through dimerization. *Cell Signal* **18**, 318-327 (2006).

72 Pfeiffer, M. *et al.* Homo- and heterodimerization of somatostatin receptor subtypes. Inactivation of sst(3) receptor function by heterodimerization with sst(2A). *J Biol Chem* **276**, 14027-14036 (2001).

73 Hilairet, S., Bouaboula, M., Carriere, D., Le Fur, G. & Casellas, P. Hypersensitization of the Orexin 1 receptor by the CB1 receptor: evidence for cross-talk blocked by the specific CB1 antagonist, SR141716. *J Biol Chem* **278**, 23731-23737 (2003).

74 Chabre, M. & le Maire, M. Monomeric G-protein-coupled receptor as a functional unit. *Biochemistry* **44**, 9395-9403 (2005).

75 Ciruela, F. *et al.* Presynaptic control of striatal glutamatergic neurotransmission by adenosine A1-A2A receptor heteromers. *J Neurosci* **26**, 2080-2087 (2006).

76 Rios, C., Gomes, I. & Devi, L. A. mu opioid and CB1 cannabinoid receptor interactions: reciprocal inhibition of receptor signaling and neuritogenesis. *Br J Pharmacol* **148**, 387-395 (2006).

77 Hillion, J. *et al.* Coaggregation, cointernalization, and codesensitization of adenosine A2A receptors and dopamine D2 receptors. *J Biol Chem* **277**, 18091-18097 (2002).

78 Drury, A. N. & Szent-Gyorgyi, A. The physiological activity of adenine compounds with especial reference to their action upon the mammalian heart. *J Physiol* **68**, 213-237 (1929).

79 Winbury, M. M., Papierski, D. H., Hemmer, M. L. & Hambourger, W. E. Coronary dilator action of the adenine-ATP series. *J Pharmacol Exp Ther* **109**, 255-260 (1953).

80 Wolf, M. M. & Berne, R. M. Coronary vasodilator properties of purine and pyrimidine derivatives. *Circ Res* **4**, 343-348 (1956).

81 Forrester, T. & Williams, C. A. Release of adenosine triphosphate from isolated adult heart cells in response to hypoxia. *J Physiol* **268**, 371-390 (1977).

82 Holton, F. A. & Holton, P. The capillary dilator substances in dry powders of spinal roots; a possible role of adenosine triphosphate in chemical transmission from nerve endings. *J Physiol* **126**, 124-140 (1954).

83 Holton, P. The liberation of adenosine triphosphate on antidromic stimulation of sensory nerves. *J Physiol* **145**, 494-504 (1959).

84 Burnstock, G., Campbell, G., Satchell, D. & Smythe, A. Evidence that adenosine triphosphate or a related nucleotide is the transmitter substance released by non-adrenergic inhibitory nerves in the gut. *Br J Pharmacol* **40**, 668-688 (1970).

85 Burnstock, G. Purinergic nerves. *Pharmacol Rev* **24**, 509-581 (1972).

86 Burnstock, G. Do some nerve cells release more than one transmitter? *Neuroscience* **1**, 239-248 (1976).

87 Smith, A. D. Cellular control of the uptake, storage and release of noradrenaline in sympathetic nerves. *Biochem Soc Symp*, 103-131 (1972).

88 Lagercrantz, H. On the composition and function of large dense cored vesicles in sympathetic nerves. *Neuroscience* **1**, 81-92 (1976).

89 von Kugelgen, I. & Starke, K. Noradrenaline and adenosine triphosphate as co-transmitters of neurogenic vasoconstriction in rabbit mesenteric artery. *J Physiol* **367**, 435-455 (1985).

90 Forsyth, K. M., Bjur, R. A. & Westfall, D. P. Nucleotide modulation of norepinephrine release from sympathetic nerves in the rat vas deferens. *J Pharmacol Exp Ther* **256**, 821-826 (1991).

91 Yoshioka, K., Hosoda, R., Kuroda, Y. & Nakata, H. Hetero-oligomerization of adenosine A1 receptors with P2Y1 receptors in rat brains. *FEBS Lett* **531**, 299-303 (2002).

92 Ralevic, V. & Burnstock, G. Receptors for purines and pyrimidines. *Pharmacol Rev* **50**, 413-492 (1998).

93 Fredholm, B. B., AP, I. J., Jacobson, K. A., Klotz, K. N. & Linden, J. International Union of Pharmacology. XXV. Nomenclature and classification of adenosine receptors. *Pharmacol Rev* **53**, 527-552 (2001).

94 van Calker, D., Muller, M. & Hamprecht, B. Adenosine inhibits the accumulation of cyclic AMP in cultured brain cells. *Nature* **276**, 839-841 (1978).

95 van Calker, D., Muller, M. & Hamprecht, B. Adenosine regulates via two different types of receptors, the accumulation of cyclic AMP in cultured brain cells. *J Neurochem* **33**, 999-1005 (1979).

96 Londos, C., Cooper, D. M. & Wolff, J. Subclasses of external adenosine receptors. *Proc Natl Acad Sci U S A* **77**, 2551-2554 (1980).

97 Daly, J. W., Butts-Lamb, P. & Padgett, W. Subclasses of adenosine receptors in the central nervous system: interaction with caffeine and related methylxanthines. *Cell Mol Neurobiol* **3**, 69-80 (1983).

98 Bean, B. P. Pharmacology and electrophysiology of ATP-activated ion channels. *Trends Pharmacol Sci* **13**, 87-90 (1992).

99 Dubyak, G. R. & el-Moatassim, C. Signal transduction via P2-purinergic receptors for extracellular ATP and other nucleotides. *Am J Physiol* **265**, C577-606 (1993).

100 North, R. A. P2X receptors: a third major class of ligand-gated ion channels. *Ciba Found Symp* **198**, 91-105; discussion 105-109 (1996).

101 Volonte, C., Amadio, S., D'Ambrosi, N., Colpi, M. & Burnstock, G. P2 receptor web: complexity and fine-tuning. *Pharmacol Ther* **112**, 264-280 (2006).

102 King, B. F. & Townsend-Nicholson, A. Nucleotide and Nucleoside Receptors. *Tocris Reviews* (2003).

103 Yoshioka, K., Saitoh, O. & Nakata, H. Heteromeric association creates a P2Y-like adenosine receptor. *Proc Natl Acad Sci U S A* **98**, 7617-7622, doi:10.1073/pnas.121587098 (2001).

104 Ecke, D. *et al.* Hetero-oligomerization of the P2Y11 receptor with the P2Y1 receptor controls the internalization and ligand selectivity of the P2Y11 receptor. *Biochem J* **409**, 107-116 (2008).

105 Suzuki, T., Namba, K., Tsuga, H. & Nakata, H. Regulation of pharmacology by hetero-oligomerization between A1 adenosine receptor and P2Y2 receptor. *Biochem Biophys Res Commun* **351**, 559-565 (2006).

106 Gines, S. *et al.* Dopamine D1 and adenosine A1 receptors form functionally interacting heteromeric complexes. *Proc Natl Acad Sci U S A* **97**, 8606-8611 (2000).

107 Ciruela, F. *et al.* Metabotropic glutamate 1alpha and adenosine A1 receptors assemble into functionally interacting complexes. *J Biol Chem* **276**, 18345-18351 (2001).

108 Carriba, P. *et al.* Striatal adenosine A2A and cannabinoid CB1 receptors form functional heteromeric complexes that mediate the motor effects of cannabinoids. *Neuropsychopharmacology* **32**, 2249-2259 (2007).

109 Khan, M. M. & Martell, A. E. Thermodynamic quantities associated with the interaction of adenosine triphosphate with metal ions. *J Am Chem Soc* **88**, 668-671 (1966).

110 Cockcroft, S. & Gomperts, B. D. The ATP4- receptor of rat mast cells. *Biochem J* **188**, 789-798 (1980).

111 Jin, X., Shepherd, R. K., Duling, B. R. & Linden, J. Inosine binds to A3 adenosine receptors and stimulates mast cell degranulation. *J Clin Invest* **100**, 2849-2857, doi:10.1172/jci119833 (1997).

112 Fredholm, B. B., Irenius, E., Kull, B. & Schulte, G. Comparison of the potency of adenosine as an agonist at human adenosine receptors expressed in Chinese hamster ovary cells. *Biochem Pharmacol* **61**, 443-448 (2001).

113 Schubert, P., Komp, W. & Kreutzberg, G. W. Correlation of 5'-nucleotidase activity and selective transneuronal transfer of adenosine in the hippocampus. *Brain Res* **168**, 419-424 (1979).

114 Broch, O. J. & Ueland, P. M. Regional and subcellular distribution of S-adenosylhomocysteine hydrolase in the adult rat brain. *J Neurochem* **35**, 484-488 (1980).

115 Zimmermann, H., Braun, N., Kegel, B. & Heine, P. New insights into molecular structure and function of ectonucleotidases in the nervous system. *Neurochem Int* **32**, 421-425 (1998).

116 Carswell, H. V., Graham, D. I. & Stone, T. W. Kainate-evoked release of adenosine from the hippocampus of the anaesthetised rat: possible involvement of free radicals. *J Neurochem* **68**, 240-247 (1997).

117 Delaney, S. M., Shepel, P. N. & Geiger, J. D. Levels of endogenous adenosine in rat striatum. I. Regulation by ionotropic glutamate receptors, nitric oxide and free radicals. *J Pharmacol Exp Ther* **285**, 561-567 (1998).

118 Brundege, J. M., Diao, L., Proctor, W. R. & Dunwiddie, T. V. The role of cyclic AMP as a precursor of extracellular adenosine in the rat hippocampus. *Neuropharmacology* **36**, 1201-1210 (1997).

119 Dunwiddie, T. V., Diao, L. & Proctor, W. R. Adenine nucleotides undergo rapid, quantitative conversion to adenosine in the extracellular space in rat hippocampus. *J Neurosci* **17**, 7673-7682 (1997).

120 Olah, M. E., Jacobson, K. A. & Stiles, G. L. Role of the second extracellular loop of adenosine receptors in agonist and antagonist binding. Analysis of chimeric A1/A3 adenosine receptors. *J Biol Chem* **269**, 24692-24698 (1994).

121 Tucker, A. L., Jia, L. G., Holeton, D., Taylor, A. J. & Linden, J. Dominance of G(s) in doubly G(s)/G(i)-coupled chimaeric A(1)/A(2A) adenosine receptors in HEK-293 cells. *Biochem J* **352 Pt 1**, 203-210 (2000).

122 Xu, F. *et al.* Structure of an agonist-bound human A2A adenosine receptor. *Science* **332**, 322-327, doi:10.1126/science.1202793 (2011).

123 Klotz, K. N. *et al.* Comparative pharmacology of human adenosine receptor subtypes - characterization of stably transfected receptors in CHO cells. *Naunyn Schmiedebergs Arch Pharmacol* **357**, 1-9 (1998).

124 de Ligt, R. A., Rivkees, S. A., Lorenzen, A., Leurs, R. & AP, I. J. A "locked-on," constitutively active mutant of the adenosine A1 receptor. *Eur J Pharmacol* **510**, 1-8, doi:10.1016/j.ejphar.2005.01.007 (2005).

125 von Kugelgen, I. Pharmacological profiles of cloned mammalian P2Y-receptor subtypes. *Pharmacol Ther* **110**, 415-432, doi:10.1016/j.pharmthera.2005.08.014 (2006).

126 Jiang, Q. *et al.* A mutational analysis of residues essential for ligand recognition at the human P2Y1 receptor. *Mol Pharmacol* **52**, 499-507 (1997).

127 Moro, S. *et al.* Human P2Y1 receptor: molecular modeling and site-directed mutagenesis as tools to identify agonist and antagonist recognition sites. *J Med Chem* **41**, 1456-1466 (1998).

128 Waldo, G. L. & Harden, T. K. Agonist binding and Gq-stimulating activities of the purified human P2Y1 receptor. *Mol Pharmacol* **65**, 426-436 (2004).

129 Abbracchio, M. P. *et al.* International Union of Pharmacology LVIII: update on the P2Y G protein-coupled nucleotide receptors: from molecular mechanisms and pathophysiology to therapy. *Pharmacol Rev* **58**, 281-341, doi:10.1124/pr.58.3.3 (2006).

130 Leon, C. *et al.* The P2Y1 receptor is an ADP receptor antagonized by ATP and expressed in platelets and megakaryoblastic cells. *FEBS Lett* **403**, 26-30 (1997).

131 Hechler, B. *et al.* ATP derivatives are antagonists of the P2Y1 receptor: similarities to the platelet ADP receptor. *Mol Pharmacol* **53**, 727-733 (1998).

132 Sak, K. & Jarv, J. Adenosine triphosphate is full antagonist at human P2Y(1) purinoceptors. *Neurosci Lett* **284**, 179-181 (2000).

133 Boyer, J. L., Adams, M., Ravi, R. G., Jacobson, K. A. & Harden, T. K. 2-Chloro N(6)-methyl-(N)-methanocarba-2'-deoxyadenosine-3',5'-bisphosphate is a selective high affinity P2Y(1) receptor antagonist. *Br J Pharmacol* **135**, 2004-2010 (2002).

134 King, B. F. 2-Chloro-N6-methyl-(N)-methanocarba-2'-deoxyadenosine-3',5'-bisphosphate is a selective high affinity P2Y1 receptor antagonist: commentary on Boyer et al. *Br J Pharmacol* **135**, 1839-1840 (2002).

135 Charlton, S. J. *et al.* PPADS and suramin as antagonists at cloned P2Y- and P2U-purinoceptors. *Br J Pharmacol* **118**, 704-710 (1996).

136 Halls, M. L. & Cooper, D. M. Regulation by Ca2+-signaling pathways of adenylyl cyclases. *Cold Spring Harb Perspect Biol* **3**, a004143 (2011).

137 Antoni, F. A. Molecular diversity of cyclic AMP signalling. *Front Neuroendocrinol* **21**, 103-132, doi:10.1006/frne.1999.0193 (2000).

138 Fagan, K. A. *et al.* Adenovirus-mediated expression of an olfactory cyclic nucleotide-gated channel regulates the endogenous Ca2+-inhibitable adenylyl cyclase in C6-2B glioma cells. *J Biol Chem* **274**, 12445-12453 (1999).

139 Straub, S. V., Wagner, L. E., 2nd, Bruce, J. I. & Yule, D. I. Modulation of cytosolic calcium signaling by protein kinase A-mediated phosphorylation of inositol 1,4,5-trisphosphate receptors. *Biol Res* **37**, 593-602 (2004).

140 Dai, S., Hall, D. D. & Hell, J. W. Supramolecular assemblies and localized regulation of voltage-gated ion channels. *Physiol Rev* **89**, 411-452 (2009).

141 Cooper, D. M., Karpen, J. W., Fagan, K. A. & Mons, N. E. Ca(2+)-sensitive adenylyl cyclases. *Adv Second Messenger Phosphoprotein Res* **32**, 23-51 (1998).

142 Wu, Z., Wong, S. T. & Storms, D. R. Modification of the calcium and calmodulin sensitivity of the type I adenylyl cyclase by mutagenesis of its calmodulin binding domain. *J Biol Chem* **268**, 23766-23768 (1993).

143 Beavo, J. A. Cyclic nucleotide phosphodiesterases: functional implications of multiple isoforms. *Physiol Rev* **75**, 725-748 (1995).

144 Soderling, S. H., Bayuga, S. J. & Beavo, J. A. Cloning and characterization of a cAMP-specific cyclic nucleotide phosphodiesterase. *Proc Natl Acad Sci U S A* **95**, 8991-8996 (1998).

145 Danchin, A. Phylogeny of adenylyl cyclases. *Adv Second Messenger Phosphoprotein Res* **27**, 109-162 (1993).

146 Tesmer, J. J., Sunahara, R. K., Gilman, A. G. & Sprang, S. R. Crystal structure of the catalytic domains of adenylyl cyclase in a complex with Gsalpha.GTPgammaS. *Science* **278**, 1907-1916 (1997).

147 Zhang, G. *et al.* Characterization and crystallization of a minimal catalytic core domain from mammalian type II adenylyl cyclase. *Protein Sci* **6**, 903-908 (1997).

148 Taussig, R., Iniguez-Lluhi, J. A. & Gilman, A. G. Inhibition of adenylyl cyclase by Gi alpha. *Science* **261**, 218-221 (1993).

149 Dessauer, C. W., Tesmer, J. J., Sprang, S. R. & Gilman, A. G. Identification of a Gialpha binding site on type V adenylyl cyclase. *J Biol Chem* **273**, 25831-25839 (1998).

150 Ashkenazi, A. *et al.* An M2 muscarinic receptor subtype coupled to both adenylyl cyclase and phosphoinositide turnover. *Science* **238**, 672-675 (1987).

151 Seamon, K. B., Padgett, W. & Daly, J. W. Forskolin: unique diterpene activator of adenylate cyclase in membranes and in intact cells. *Proc Natl Acad Sci U S A* **78**, 3363-3367 (1981).

152 Perkins, J. P. Adenyl cyclase. *Adv Cyclic Nucleotide Res* **3**, 1-64 (1973).

153 Neer, E. J. Physical and functional properties of adenylate cyclase from mature rat testis. *J Biol Chem* **253**, 5808-5812 (1978).

154 Londos, C., Lad, P. M., Nielsen, T. B. & Rodbell, M. Solubilization and conversion of hepatic adenylate cyclase to a form requiring MnATP as substrate. *J Supramol Struct* **10**, 31-37 (1979).

155 Bradham, L. S., Holt, D. A. & Sims, M. The effect of Ca2+ on the adenyl cyclase of calf brain. *Biochim Biophys Acta* **201**, 250-260 (1970).

156 Moss, J. & Vaughan, M. Activation of adenylate cyclase by choleragen. *Annu Rev Biochem* **48**, 581-600 (1979).

157 Tang, W. J. & Gilman, A. G. Type-specific regulation of adenylyl cyclase by G protein beta gamma subunits. *Science* **254**, 1500-1503 (1991).

158 Tang, W. J. & Gilman, A. G. Construction of a soluble adenylyl cyclase activated by Gs alpha and forskolin. *Science* **268**, 1769-1772 (1995).

159 Ishikawa, Y. Regulation of cAMP signaling by phosphorylation. *Adv Second Messenger Phosphoprotein Res* **32**, 99-120 (1998).

160 Yoshimura, M., Ikeda, H. & Tabakoff, B. mu-Opioid receptors inhibit dopamine-stimulated activity of type V adenylyl cyclase but enhance dopamine-stimulated activity of type VII adenylyl cyclase. *Mol Pharmacol* **50**, 43-51 (1996).

161 Sunahara, R. K., Dessauer, C. W. & Gilman, A. G. Complexity and diversity of mammalian adenylyl cyclases. *Annu Rev Pharmacol Toxicol* **36**, 461-480 (1996).

162 Varga, E. V. *et al.* Identification of adenylyl cyclase isoenzymes in CHO and B82 cells. *Eur J Pharmacol* **348**, R1-2 (1998).

163 Bhat, S. V., Bajqwa, B. S., Dornauer, H., do Scusa, N. J. & Fehlhaber, H. W. Structures and stereochemistry of new labdane diterpiniods from coleus forskohlii briq. *Tetrahedron Letters* **18**, 1669 (1977).

164 Boyajian, C. L., Bickford-Wimer, P., Kim, M. B., Freedman, R. & Cooper, D. M. Pertussis toxin lesioning of the nucleus caudate-putamen attenuates adenylate cyclase inhibition and alters neuronal electrophysiological activity. *Brain Res* **495**, 66-74 (1989).

165 Scholich, K., Barbier, A. J., Mullenix, J. B. & Patel, T. B. Characterization of soluble forms of nonchimeric type V adenylyl cyclases. *Proc Natl Acad Sci U S A* **94**, 2915-2920 (1997).

166 Willoughby, D. & Cooper, D. M. Organization and Ca2+ regulation of adenylyl cyclases in cAMP microdomains. *Physiol Rev* **87**, 965-1010 (2007).

167 Lai, H. L. *et al.* Protein kinase C inhibits adenylyl cyclase type VI activity during desensitization of the A2a-adenosine receptor-mediated cAMP response. *J Biol Chem* **272**, 4970-4977 (1997).

168 Lin, T. H. *et al.* Protein kinase C inhibits type VI adenylyl cyclase by phosphorylating the regulatory N domain and two catalytic C1 and C2 domains. *J Biol Chem* **277**, 15721-15728 (2002).

169 Rhim, J. H., Jang, I. S., Yeo, E. J., Song, K. Y. & Park, S. C. Role of protein kinase C-dependent A-kinase anchoring proteins in lysophosphatidic acid-induced cAMP signaling in human diploid fibroblasts. *Aging Cell* **5**, 451-461 (2006).

170 Taylor, S. S., Buechler, J. A. & Yonemoto, W. cAMP-dependent protein kinase: framework for a diverse family of regulatory enzymes. *Annu Rev Biochem* **59**, 971-1005 (1990).

171 Taylor, S. S., Knighton, D. R., Zheng, J., Ten Eyck, L. F. & Sowadski, J. M. Structural framework for the protein kinase family. *Annu Rev Cell Biol* **8**, 429-462 (1992).

172 Taylor, S. S., Knighton, D. R., Zheng, J., Ten Eyck, L. F. & Sowadski, J. M. cAMP-dependent protein kinase and the protein kinase family. *Faraday Discuss*, 143-152 (1992).

173 Chen, Y. *et al.* Adenylyl cyclase 6 is selectively regulated by protein kinase A phosphorylation in a region involved in Galphas stimulation. *Proc Natl Acad Sci U S A* **94**, 14100-14104 (1997).

174 Milligan, G., Mullaney, I., Kim, G. D. & MacEwan, D. Regulation of the stoichiometry of protein components of the stimulatory adenylyl cyclase cascade. *Adv Pharmacol* **42**, 462-465 (1998).

175 Drmota, T. *et al.* Agonist-induced internalization of the G protein G11alpha and thyrotropin-releasing hormone receptors proceed on different time scales. *J Biol Chem* **273**, 21699-21707 (1998).

176 Townsend-Nicholson, A. & Shine, J. Molecular cloning and characterisation of a human brain A1 adenosine receptor cDNA. *Brain Res Mol Brain Res* **16**, 365-370 (1992).

177 Houslay, M. D. Adaptation in cyclic AMP signalling processes: a central role for cyclic AMP phosphodiesterases. *Semin Cell Dev Biol* **9**, 161-167 (1998).

178 Spence, S., Rena, G., Sullivan, M., Erdogan, S. & Houslay, M. D. Receptor-mediated stimulation of lipid signalling pathways in CHO cells elicits the rapid transient induction of the PDE1B isoform of Ca2+/calmodulin-stimulated cAMP phosphodiesterase. *Biochem J* **321 (Pt 1)**, 157-163 (1997).

179 Klingler, C. *et al.* Angiotensin II potentiates vasopressin-dependent cAMP accumulation in CHO transfected cells. Mechanisms of cross-talk between AT1A and V2 receptors. *Cell Signal* **10**, 65-74 (1998).

180 Bruzzone, R. The molecular basis of enzyme secretion. *Gastroenterology* **99**, 1157-1176 (1990).

181 Berridge, M. J., Lipp, P. & Bootman, M. D. The versatility and universality of calcium signalling. *Nat Rev Mol Cell Biol* **1**, 11-21, doi:10.1038/35036035 (2000).

182 Harnett, K. M. & Biancani, P. Calcium-dependent and calcium-independent contractions in smooth muscles. *Am J Med* **115 Suppl 3A**, 24S-30S (2003).

183 Fukami, K., Inanobe, S., Kanemaru, K. & Nakamura, Y. Phospholipase C is a key enzyme regulating intracellular calcium and modulating the phosphoinositide balance. *Prog Lipid Res* **49**, 429-437, doi:10.1016/j.plipres.2010.06.001 (2010).

184 Streb, H., Irvine, R. F., Berridge, M. J. & Schulz, I. Release of Ca2+ from a nonmitochondrial intracellular store in pancreatic acinar cells by inositol-1,4,5-trisphosphate. *Nature* **306**, 67-69 (1983).

185 Essen, L. O., Perisic, O., Cheung, R., Katan, M. & Williams, R. L. Crystal structure of a mammalian phosphoinositide-specific phospholipase C delta. *Nature* **380**, 595-602, doi:10.1038/380595a0 (1996).

186 Williams, R. L. Mammalian phosphoinositide-specific phospholipase C. *Biochim Biophys Acta* **1441**, 255-267 (1999).

187 Camps, M. *et al.* Isozyme-selective stimulation of phospholipase C-beta 2 by G protein beta gamma-subunits. *Nature* **360**, 684-686, doi:10.1038/360684a0 (1992).

188 Dickenson, J. M. & Hill, S. J. Involvement of G-protein betagamma subunits in coupling the adenosine A1 receptor to phospholipase C in transfected CHO cells. *Eur J Pharmacol* **355**, 85-93 (1998).

189 Selbie, L. A. & Hill, S. J. G protein-coupled-receptor cross-talk: the fine-tuning of multiple receptor-signalling pathways. *Trends Pharmacol Sci* **19**, 87-93 (1998).

190 Bosanac, I. *et al.* Structure of the inositol 1,4,5-trisphosphate receptor binding core in complex with its ligand. *Nature* **420**, 696-700, doi:10.1038/nature01268 (2002).

191 Bosanac, I., Michikawa, T., Mikoshiba, K. & Ikura, M. Structural insights into the regulatory mechanism of IP3 receptor. *Biochim Biophys Acta* **1742**, 89-102, doi:10.1016/j.bbamcr.2004.09.016 (2004).

192 Evenas, J., Malmendal, A. & Forsen, S. Calcium. *Curr Opin Chem Biol* **2**, 293-302 (1998).

193 Guerini, D., Coletto, L. & Carafoli, E. Exporting calcium from cells. *Cell Calcium* **38**, 281-289, doi:10.1016/j.ceca.2005.06.032 (2005).

194 Catterall, W. A. From ionic currents to molecular mechanisms: the structure and function of voltage-gated sodium channels. *Neuron* **26**, 13-25 (2000).

195 Kamp, T. J. & Hell, J. W. Regulation of cardiac L-type calcium channels by protein kinase A and protein kinase C. *Circ Res* **87**, 1095-1102 (2000).

196 Liu, M. & Simon, M. I. Regulation by cAMP-dependent protein kinease of a G-protein-mediated phospholipase C. *Nature* **382**, 83-87 (1996).

197 Muallem, S., Schoeffield, M. S., Fimmel, C. J. & Pandol, S. J. Agonist-sensitive calcium pool in the pancreatic acinar cell. II. Characterization of reloading. *Am J Physiol* **255**, G229-235 (1988).

198 Williamson, J. R. & Monck, J. R. Signal transduction mechanisms involved in hormonal Ca2+ fluxes. *Environ Health Perspect* **84**, 121-136 (1990).

199 Kalipatnapu, S. & Chattopadhyay, A. Membrane protein solubilization: recent advances and challenges in solubilization of serotonin1A receptors. *IUBMB Life* **57**, 505-512 (2005).

200 Schimerlik, M. I. Overview of membrane protein solubilization. *Curr Protoc Neurosci* **Chapter 5**, Unit 5 9 (2001).

201 Chattopadhyay, A. & Harikumar, K. G. Dependence of critical micelle concentration of a zwitterionic detergent on ionic strength: implications in receptor solubilization. *FEBS Lett* **391**, 199-202 (1996).

202 Chattopadhyay, A., Harikumar, K. G. & Kalipatnapu, S. Solubilization of high affinity G-protein-coupled serotonin1A receptors from bovine hippocampus using pre-micellar CHAPS at low concentration. *Mol Membr Biol* **19**, 211-220 (2002).

203 Schurholz, T. Critical dependence of the solubilization of lipid vesicles by the detergent CHAPS on the lipid composition. Functional reconstitution of the nicotinic acetylcholine receptor into preformed vesicles above the critical micellization concentration. *Biophys Chem* **58**, 87-96 (1996).

204 Chen, C. & Okayama, H. High-efficiency transformation of mammalian cells by plasmid DNA. *Mol Cell Biol* **7**, 2745-2752 (1987).

205 Johnson, R. A. & Salomon, Y. Assay of adenylyl cyclase catalytic activity. *Methods Enzymol* **195**, 3-21 (1991).

206 Salomon, Y., Londos, C. & Rodbell, M. A highly sensitive adenylate cyclase assay. *Anal Biochem* **58**, 541-548 (1974).

207 White, A. A. & Zenser, T. V. Separation of cyclic 3',5'-nucleoside monophosphates from other nucleotides on aluminum oxide columns. Application to the assay of adenyl cyclase and guanyl cyclase. *Anal Biochem* **41**, 372-396 (1971).

208 Gee, K. R. *et al.* Chemical and physiological characterization of fluo-4 Ca(2+)-indicator dyes. *Cell Calcium* **27**, 97-106, doi:10.1054/ceca.1999.0095 (2000).

209 Rivkees, S. A., Barbhaiya, H. & AP, I. J. Identification of the adenine binding site of the human A1 adenosine receptor. *J Biol Chem* **274**, 3617-3621 (1999).

210 Fischer, W., Franke, H., Groger-Arndt, H. & Illes, P. Evidence for the existence of P2Y1,2,4 receptor subtypes in HEK-293 cells: reactivation of P2Y1 receptors after repetitive agonist application. *Naunyn Schmiedebergs Arch Pharmacol* **371**, 466-472, doi:10.1007/s00210-005-1070-6 (2005).

211 Nakata, H. A1 adenosine receptor of rat testis membranes. Purification and partial characterization. *J Biol Chem* **265**, 671-677 (1990).

212 Freissmuth, M., Selzer, E. & Schutz, W. Interactions of purified bovine brain A1-adenosine receptors with G-proteins. Reciprocal modulation of agonist and antagonist binding. *Biochem J* **275 (Pt 3)**, 651-656 (1991).

213 Nakata, H. Purification of A1 adenosine receptor from rat brain membranes. *J Biol Chem* **264**, 16545-16551 (1989).

214 Nakata, H. Biochemical and immunological characterization of A1 adenosine receptors purified from human brain membranes. *Eur J Biochem* **206**, 171-177 (1992).

215 Gao, Z., Robeva, A. S. & Linden, J. Purification of A1 adenosine receptor-G-protein complexes: effects of receptor down-regulation and phosphorylation on coupling. *Biochem J* **338 (Pt 3)**, 729-736 (1999).

216 Cremo, C. R., Herron, G. S. & Schimerlik, M. I. Solubilization of the atrial muscarinic acetylcholine receptor: A new detergent system and rapid assays. *Analytical Biochemistry* **115**, 331 (1981).

217 Chattopadhyay, A., Jafurulla, M. & Kalipatnapu, S. Solubilization of serotonin1A receptors heterologously expressed in Chinese hamster ovary cells. *Cell Mol Neurobiol* **24**, 293-300 (2004).

218 Snook, L. A., Milligan, G., Kieffer, B. L. & Massotte, D. Mu-delta opioid receptor functional interaction: Insight using receptor-G protein fusions. *J Pharmacol Exp Ther* **318**, 683-690 (2006).

219 Ghosh, I., Hamilton, A. D. & Regan, L. Antiparallel Leucine Zipper-Directed Protein Reassembly: Application to the Green Fluorescent Protein. *J. Am. Chem. Soc.* **122**, 5658-5659 (2000).

220 Hu, C. D., Chinenov, Y. & Kerppola, T. K. Visualization of interactions among bZIP and Rel family proteins in living cells using bimolecular fluorescence complementation. *Mol Cell* **9**, 789-798 (2002).

221 Hu, C. D. & Kerppola, T. K. Simultaneous visualization of multiple protein interactions in living cells using multicolor fluorescence

complementation analysis. *Nat Biotechnol* **21**, 539-545, doi:10.1038/nbt816 (2003).

222 Kerppola, T. K. Visualization of molecular interactions by fluorescence complementation. *Nat Rev Mol Cell Biol* **7**, 449-456, doi:10.1038/nrm1929 (2006).

223 Vidi, P. A., Przybyla, J. A., Hu, C. D. & Watts, V. J. Visualization of G protein-coupled receptor (GPCR) interactions in living cells using bimolecular fluorescence complementation (BiFC). *Curr Protoc Neurosci* **Chapter 5**, Unit 5 29, doi:10.1002/0471142301.ns0529s51 (2010).

224 Ormo, M. *et al.* Crystal structure of the Aequorea victoria green fluorescent protein. *Science* **273**, 1392-1395 (1996).

225 Briddon, S. J. *et al.* Plasma membrane diffusion of G protein-coupled receptor oligomers. *Biochim Biophys Acta* **1783**, 2262-2268, doi:10.1016/j.bbamcr.2008.07.006 (2008).

226 Vohringer, C., Schafer, R. & Reiser, G. A chimeric rat brain P2Y1 receptor tagged with green-fluorescent protein: high-affinity ligand recognition of adenosine diphosphates and triphosphates and selectivity identical to that of the wild-type receptor. *Biochem Pharmacol* **59**, 791-800 (2000).

227 Gebhard F.X, S. Overproduction of membrane proteins. *Current Opinion in Structural Biology* **2**, 534-544, doi:10.1016/0959-440x(92)90083-j (1992).

228 Grisshammer, R. & Tate, C. G. Overexpression of integral membrane proteins for structural studies. *Q Rev Biophys* **28**, 315-422 (1995).

229 Tonazzini, I., Trincavelli, M. L., Montali, M. & Martini, C. Regulation of A1 adenosine receptor functioning induced by P2Y1 purinergic receptor activation in human astroglial cells. *J Neurosci Res* **86**, 2857-2866, doi:10.1002/jnr.21727 (2008).

230 Maemoto, T. *et al.* Species differences in brain adenosine A1 receptor pharmacology revealed by use of xanthine and pyrazolopyridine based antagonists. *Br J Pharmacol* **122**, 1202-1208, doi:10.1038/sj.bjp.0701465 (1997).

231 Varani, K. *et al.* Alteration of adenosine receptors in patients with chronic obstructive pulmonary disease. *Am J Respir Crit Care Med* **173**, 398-406, doi:10.1164/rccm.200506-869OC (2006).

232 Biber, K., Klotz, K. N., Berger, M., Gebicke-Harter, P. J. & van Calker, D. Adenosine A1 receptor-mediated activation of phospholipase C in cultured astrocytes depends on the level of receptor expression. *J Neurosci* **17**, 4956-4964 (1997).

233 Rebola, N. *et al.* Long-term effect of convulsive behavior on the density of adenosine A1 and A 2A receptors in the rat cerebral cortex. *Epilepsia* **46 Suppl 5**, 159-165, doi:10.1111/j.1528-1167.2005.01026.x (2005).

234 Middlekauff, H. R. *et al.* Localization and functional effects of adenosine A1 receptors on cardiac vagal afferents in adult rats. *Am J Physiol* **274**, H441-447 (1998).

235 Gould, J., Morton, M. J., Sivaprasadarao, A., Bowmer, C. J. & Yates, M. S. Renal adenosine A1 receptor binding characteristics and mRNA levels during the development of acute renal failure in the rat. *Br J Pharmacol* **120**, 947-953, doi:10.1038/sj.bjp.0700980 (1997).

236 Castillo, C. A. *et al.* Age-related expression of adenosine receptors in brain from the senescence-accelerated mouse. *Exp Gerontol* **44**, 453-461, doi:10.1016/j.exger.2009.04.006 (2009).

237 Shryock, J. C., Ozeck, M. J. & Belardinelli, L. Inverse agonists and neutral antagonists of recombinant human A1 adenosine receptors stably expressed in Chinese hamster ovary cells. *Mol Pharmacol* **53**, 886-893 (1998).

238 Chase, P. B. & Kushmerick, M. J. Effect of physiological ADP concentrations on contraction of single skinned fibers from rabbit fast and slow muscles. *Am J Physiol* **268**, C480-489 (1995).

239 Van Coevorden, A. & Boeynaems, J. M. Physiological concentrations of ADP stimulate the release of prostacyclin from bovine aortic endothelial cells. *Prostaglandins* **27**, 615-626 (1984).

240 Simon, J., Webb, T. E., King, B. F., Burnstock, G. & Barnard, E. A. Characterisation of a recombinant P2Y purinoceptor. *Eur J Pharmacol* **291**, 281-289 (1995).

241 King, B. F. & Townsend-Nicholson, A. Recombinant P2Y receptors: the UCL experience. *J Auton Nerv Syst* **81**, 164-170 (2000).

242 Filtz, T. M., Li, Q., Boyer, J. L., Nicholas, R. A. & Harden, T. K. Expression of a cloned P2Y purinergic receptor that couples to phospholipase C. *Mol Pharmacol* **46**, 8-14 (1994).

243 Devader, C. *et al.* A novel nucleotide receptor in Xenopus activates the cAMP second messenger pathway. *FEBS Lett* **581**, 5332-5336, doi:10.1016/j.febslet.2007.10.024 (2007).

244 Lotan, H., Dascal, N., Cohen, S. & Lass, Y. ATP-evoked membrane responses in Xenopus oocytes. *Pflugers Arch* **406**, 158-162 (1986).

245 Kobayashi, T., Ikeda, K. & Kumanishi, T. Functional characterization of an endogenous Xenopus oocyte adenosine receptor. *Br J Pharmacol* **135**, 313-322, doi:10.1038/sj.bjp.0704475 (2002).

246 Glanzel, M., Bultmann, R., Starke, K. & Frahm, A. W. Structure-activity relationships of novel P2-receptor antagonists structurally related to Reactive Blue 2. *Eur J Med Chem* **40**, 1262-1276, doi:10.1016/j.ejmech.2005.07.007 (2005).

247 Megson, A. C., Dickenson, J. M., Townsend-Nicholson, A. & Hill, S. J. Synergy between the inositol phosphate responses to transfected human adenosine A1-receptors and constitutive P2-purinoceptors in CHO-K1 cells. *Br J Pharmacol* **115**, 1415-1424 (1995).

248 Cordeaux, Y., Ijzerman, A. P. & Hill, S. J. Coupling of the human A1 adenosine receptor to different heterotrimeric G proteins: evidence for agonist-specific G protein activation. *Br J Pharmacol* **143**, 705-714, doi:10.1038/sj.bjp.0705925 (2004).

249 Baker, J. G. & Hill, S. J. A comparison of the antagonist affinities for the Gi- and Gs-coupled states of the human adenosine A1-receptor. *J Pharmacol Exp Ther* **320**, 218-228, doi:10.1124/jpet.106.113589 (2007).

250 AP, I. J., Von Frijtag Drabbe Kunzel, J. K., Kim, J., Jiang, Q. & Jacobson, K. A. Site-directed mutagenesis of the human adenosine A2A receptor. Critical involvement of Glu13 in agonist recognition. *Eur J Pharmacol* **310**, 269-272 (1996).

251 Yoshioka, K., Saitoh, O. & Nakata, H. Agonist-promoted heteromeric oligomerization between adenosine A(1) and P2Y(1) receptors in living cells. *FEBS Lett* **523**, 147-151 (2002).

252 Choi, R. C., Simon, J., Tsim, K. W. & Barnard, E. A. Constitutive and agonist-induced dimerizations of the P2Y1 receptor: relationship to internalization and scaffolding. *J Biol Chem* **283**, 11050-11063, doi:10.1074/jbc.M709266200 (2008).

4)